



Delft University of Technology

Scaling a spin qubit quantum processor from two to six qubits

Philips, S.G.J.

DOI

[10.4233/uuid:62dcc7a6-df92-43e1-b40c-9879f97eabb6](https://doi.org/10.4233/uuid:62dcc7a6-df92-43e1-b40c-9879f97eabb6)

Publication date

2023

Document Version

Final published version

Citation (APA)

Philips, S. G. J. (2023). *Scaling a spin qubit quantum processor from two to six qubits*. [Dissertation (TU Delft), Delft University of Technology]. <https://doi.org/10.4233/uuid:62dcc7a6-df92-43e1-b40c-9879f97eabb6>

Important note

To cite this publication, please use the final published version (if applicable).
Please check the document version above.

Copyright

Other than for strictly personal use, it is not permitted to download, forward or distribute the text or part of it, without the consent of the author(s) and/or copyright holder(s), unless the work is under an open content license such as Creative Commons.

Takedown policy

Please contact us and provide details if you believe this document breaches copyrights.
We will remove access to the work immediately and investigate your claim.

SCALING A SPIN QUBIT QUANTUM PROCESSOR FROM TWO TO SIX QUBITS

SCALING A SPIN QUBIT QUANTUM PROCESSOR FROM TWO TO SIX QUBITS

Proefschrift

ter verkrijging van de graad van doctor
aan de Technische Universiteit Delft,
op gezag van de Rector Magnificus Prof. Dr. Ir. T. H. J. J. van der Hagen,
voorzitter van het College voor Promoties,
in het openbaar te verdedigen op
vrijdag 23 juni 2023 om 10:00 uur

door

Stephan Georges Jozef PHILIPS

Master in de nanowetenschappen, nanotechnologie en nano-engineering,
KU Leuven, België
geboren te Leuven, België.

Dit proefschrift is goedgekeurd door de promotor.

Samenstelling promotiecommissie bestaat uit:

Rector Magnificus

voorzitter

Prof. dr. ir. L. M. K. Vandersypen

Technische Universiteit Delft, promotor

Onafhankelijke leden:

Prof. Dr. D.P. DiVincenzo

Technische Universiteit Delft

& Forschungszentrum Jülich

& RWTH Aachen University

Prof. Dr. J.J.L. Morton

University College London & Quantum Motion

Prof. Dr. A. Morello

University of New South Wales

Prof. Dr. L. DiCarlo

Technische Universiteit Delft

Dr. S. Goswami

Technische Universiteit Delft



Geprint door: proefschriftenprinten.nl

Cover:

Schets van een spin qubit device gefabriceerd op een silicium wafer. De blauwe, gele en rode structuren stellen de metalen gates voor waarmee we elektronen aantrekken. Door de voltages op de metalen gates te veranderen, kunnen we het potentiaallandschap beïnvloeden. Een schets van het gewenste potentiaallandschap wordt getoond door het gebogen vlak onder de gates. De zwarte punten stellen elektronen voor, gevangen in dit potentiaallandschap. Qubits worden gemaakt door gebruik te maken van de spin van deze elektronen.
Delen van de schets zijn gemaakt met DALL·E 2 en neuralstyle.art.

Copyright © 2023 by Stephan Philips

ISBN 978-90-833330-5-2

Een elektronische versie van dit proefschrift is te vinden op
<http://repository.tudelft.nl/>.

CONTENTS

1	Introduction	1
1.1	A brief history	2
1.2	Calculating with classical and quantum computers	2
1.3	Building quantum computers	4
1.4	Thesis Outline	6
2	Quantum Dots as Spin Qubits : Fundamentals	11
2.1	From free electron to quantum dot	12
2.2	From quantum dot to qubit	19
3	A programmable two-qubit quantum processor in silicon	33
3.1	Introduction	34
3.2	Single and two-qubit gate implementation	34
3.3	Universal control	37
3.4	Conclusion	40
3.5	Methods	40
3.6	Supplementary information	48
3.6.1	Frequency shifts on Q2 due to off-resonant frequency pulses	48
3.6.2	Calibration of single-qubit gates	54
3.6.3	State tomography of Bell states	55
4	Radio frequency reflectometry in silicon-based quantum dots	63
4.1	Introduction	64
4.2	RF Reflectometry	64
4.3	The ohmic Approach	66
4.4	Split-Gate Approach	69
4.5	Conclusion	71
5	Universal control of a six-qubit quantum processor in silicon	75
5.1	Introduction	76
5.2	Defining initialization, readout, single and two-qubit gates on a six-qubit quantum processor	77
5.3	Generating entangled states	82
5.4	Conclusion	84
5.5	Methods	84
5.6	Considerations on scaling	98
5.6.1	Scaling limitations of the methods used in the present work	98
5.6.2	Path forward to larger systems	99

5.7	Micromagnet design	100
5.8	Different samples tested for this experiment	103
5.9	Sample design	105
5.10	Entanglement Witnesses	109
5.11	Quantum state tomography	109
5.12	Error channels in the experimental data: dephasing and “heating”	111
5.12.1	State tomography simulations	111
5.12.2	Discussion	112
6	Defining control architectures for spin qubit experiments	121
6.1	Introduction	122
6.2	Characterizing spin qubit devices	122
6.2.1	Dipstick device characterization	122
6.3	Spin qubit device operation and instrumentation	125
6.4	Software	131
6.4.1	DM_solver	132
6.4.2	Core_tools	139
6.4.3	PulseLib	148
6.4.4	SpinQubitTemplates	151
6.4.5	Micromagnet simulator	152
6.4.6	Next generation software?	153
6.5	Extra : choosing an AWG	154
7	Conclusion and outlook	159
7.1	Conclusions	159
7.2	Outlook	161
7.2.1	Fidelity	162
7.2.2	Connectivity	167
7.2.3	Measurement and Speed	169
7.3	Looking ahead, from a personal perspective	170
Summary		181
Samenvatting		183
Acknowledgements		185
Curriculum Vitae		191
Publications		193

1

INTRODUCTION

*In theory, there is no difference between theory and practice.
But, in practice, there is.*

Benjamin Brewster

1.1. A BRIEF HISTORY

The first conceptualization of a quantum computer was proposed in the early eighties by Richard Feynman and Yuri Manin [7, 15]. Richard Feynman argued one can only simulate a quantum system using another well controlled quantum system. A simulation with a classical computer gets exponentially harder as the problem size increases, whereas for a quantum computer this increase is polynomial. These ideas inspired many physicists to start developing quantum algorithms.

The first 'useful' algorithm¹ was developed by Peter Shor in 1994. He showed that a quantum computer can factor integers exponentially faster [22] than any known classical algorithm. This was an important result, as many encryption schemes rely on this problem.

At the same time several scientists doubted if a quantum computer could ever be built, as unimaginably precise quantum operations² are needed to run e.g. Shor's factorization algorithm.

Reliable operations in the presence of errors can be performed on classical computers, as it is easy to detect errors during the calculation (e.g. one could make a copy of the bits and perform the calculation twice). Quantum mechanics does not allow one to make copies of qubits (a measurement collapses the quantum state [16]), which prevents the usage of classical error correction in quantum computers.

This problem was solved by Peter Shor³ and Andrew Steane in 1995, who designed error correcting codes [24, 25, 23] that distribute the information of a single state over many qubits. The measurement problem is avoided by measuring symmetries between the qubits, rather than the state of the qubits themselves. These correction schemes significantly lower the fidelities that need to be achieved by the experimental physicist [8] and give good hope that we can one day build a large scale quantum computer!

1.2. CALCULATING WITH CLASSICAL AND QUANTUM COMPUTERS

Traditional (classical) computers solve many everyday problems, e.g. they count up bills for cashiers, make a car drive on its own, predict the weather and much more. All computations with traditional computers rely on 'classical' (Newtonian) physics, which means the computer is in one state at a time (e.g. current or no current). A quantum computer is different in this respect, as it can be in multiple states at once. This non-intuitive phenomenon implies that it is possible to perform many computations at once. These new capabilities allow one to solve a subset of problems much more efficiently. For example, the simulation of molecules [14, 29] with applications in medicine and energy or solving linear equations [11] with applications in financing and machine learning. In the following sections we investigate why classical and quantum computers are different and

¹Many other persons made important contributions[19] that led to this algorithm (e.g. David Deutsch, Daniel Simon, Umesh Vazirani).

²A quantum operation is an operation performed on the qubit, this could be for example an initialization, a readout, a bit flip, a conditional gate,

³Fun fact, the idea of the bit flip code (basis for Shor's code) was already discovered (unknowingly) in 1985 by Asher Peres [17].

explore how a quantum computer can help to solve complex problems.

On a classical computer, a function evaluation can be defined as:

$$y = f(x_1, x_2, \dots) \quad (1.1)$$

Where f is a logical function and x_1, x_2 and y are the input and output variables. Each variable can be represented by a string of bits (e.g. 0001, 1000, ...).

For a quantum computer, we can make a similar construct:

$$|y\rangle = f(|x_1\rangle, |x_2\rangle, \dots) \quad (1.2)$$

Where the variables are placed within a ket, $| \rangle$, which describes a quantum state (as a vector). Quantum states are 'special' as they can be in multiple states at once, i.e. a superposition of states. To illustrate how this works, we consider the following states for $|x_1\rangle$ and $|x_2\rangle$:

$$|x_1\rangle = \alpha_0 |0\rangle + \alpha_1 |1\rangle \quad (1.3)$$

$$|x_2\rangle = |00\rangle \quad (1.4)$$

Where $|x_1\rangle$ is a single and $|x_2\rangle$ a two qubit register. The first register is initialized in a superposition of the $|0\rangle$ and $|1\rangle$ state, where each state has an amplitude α_i .

Suppose our function f adds the value of $|x_1\rangle$ to $|x_2\rangle$. Then we could write classically, $|y\rangle = f(|0\rangle, |00\rangle) + f(|1\rangle, |00\rangle)$. Where $|y\rangle$ is a quantum state (vector) that collects the state amplitudes of each input,

$$|y\rangle = \alpha_0 |0\rangle |00\rangle + \alpha_1 |1\rangle |01\rangle \quad (1.5)$$

The output state $|y\rangle$ has the same number of qubits as the input states as a quantum calculation needs to be reversible. If we were to measure the outcome of our calculation, we would measure either the state $|0\rangle |00\rangle$ or $|1\rangle |01\rangle$ with a probability α_i^2 . At first sight this might look troubling, as we may be able to parallelize the calculation, but if we can only measure one answer at a time, we are not gaining much over the classical calculation.

As it is only possible to measure one outcome at a time, it is clear something smart needs to be done after the calculation, which returns the wanted answer with a high probability. Shor's factoring algorithm is a good example for this. This algorithm factors a large integer number N ($N = pq$) into two prime numbers (p and q). It is known from number theory[22] that p and q can be found efficiently if one can find the period of the following function:

$$f(x) = a^x \mod N \quad (1.6)$$

where a is a number coprime with N [22]. The factoring algorithm consists (Fig. 1.1a) out of four parts, (1) make a superposition, (2) perform the modular exponentiation, (3) perform a quantum Fourier transform and (4) measure the input state.

At the start of the algorithm, two registers⁴ are initialized in the $|0\rangle$ state, ($|\psi\rangle = |\psi_1\rangle |\psi_2\rangle = |0\rangle |0\rangle$). As a next step, we want prepare the first register (m-qubits) in a full superposition ($M = 2^m$),

$$|\psi\rangle = \frac{1}{\sqrt{M}} \sum_i^{M-1} |i\rangle |0\rangle \quad (1.7)$$

⁴Each register is a set of n qubits, where each register can hold up to 2^n input states. The states are written in a non-binary form, e.g., $|0\rangle, |1\rangle, |2\rangle, |3\rangle, \dots$.

We can now provide this input to the function $f(x)$ (eq. 1.6), which writes the outcome in the second register (Fig. 1.1b and c),

$$|\psi\rangle = \frac{1}{\sqrt{M}} \sum_i^{M-1} |\textcolor{teal}{i}\rangle |\textcolor{blue}{a}^i \bmod N\rangle \quad (1.8)$$

The values in the first register are now correlated (entangled) with the values in the second register. Suppose we perform a measurement⁵ on the second register, and measure $|\psi_2\rangle = |\textcolor{blue}{1}\rangle$. The wavefunction is now given by:

$$|\psi\rangle = \frac{1}{\sqrt{k}} \sum_i^{k-1} |\textcolor{teal}{c}_i\rangle |\textcolor{blue}{a}^{c_i} \bmod N = 1\rangle \quad (1.9)$$

Where c_i are all the input values for which $f(x) = 1$. The states present in the first register are now periodically spaced as shown in Fig. 1.1c. The logical next step is to take the quantum Fourier transform which can reveal the period as shown in Fig. 1.1d. With a high probability one can measure a multiple of the period, which allows one to find back the period, which is needed to calculate the prime factors.

This algorithm is a good example how quantum algorithms can outperform classical algorithms. When executing the quantum algorithm we only need to evaluate $f(x)$ once (requiring an effort of $O(n^3)$), whereas classically many function evaluations are needed to retrieve the period ($\mathcal{O}(2^{n^{1/3}})$), which makes the calculation impractical to execute for a large N .

It would be very exciting to be able to run algorithms like this. Currently we do not possess the hardware to execute 'useful' quantum algorithms. These types of algorithms require a large number of qubits (> 1000), with extremely high operational fidelity (error rate $< 1e-15$) [9].

1.3. BUILDING QUANTUM COMPUTERS

The quantum community works towards the goal of building a universal⁶ error corrected quantum computer. This is a very far reaching goal, that will take many years to realize.

The basic requirements of the components (qubits) of a such computer are defined by DiVincenzo's criteria [5], i.e. (shorted version) :

1. The system of qubits must be scalable (i.e. it must be easy to double the qubit count).
2. One must be able to measure, initialize and operate (universally) each qubit.
3. The coherence time of the qubits needs to be long compared to the time scale of the quantum operations.

⁵This is not needed in a real implementation

⁶*Universal* indicates the quantum computer can perform any operation (i.e. can run any algorithm).

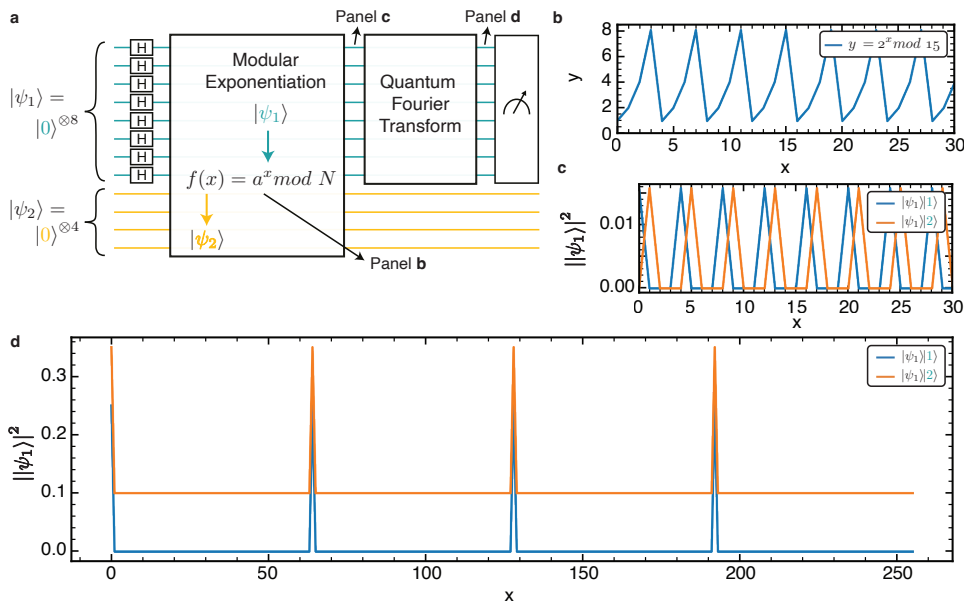


Figure 1.1: **Shor's factoring algorithm** | **a** Quantum circuit describing the operations that are needed to execute Shor's algorithm. $|\psi_1\rangle$ and $|\psi_2\rangle$ are two quantum registers used to perform the calculation. **b** Evaluation of the function $f(x)$ (eq. 1.6) with $a = 2$ and $N = 15$, revealing a period of 4. **c** Amplitudes of the first thirty states of $|\psi_1\rangle$ after the modular exponentiation with respect to a given value of the second register ($|2\rangle$). **d** Measurement probability of register 1 after the quantum Fourier transform has been performed. The possible measurement outcomes (m_s) are 0,64,128,192. These values can be related back to the original period by $\frac{256*n}{m_s}$, where n is an integer.

We can make these statements more quantitative using the hardware estimates for running 'useful' applications e.g. Shor's algorithm or the calculation of a molecule ground state [9, 20].

1. The minimal system size depends strongly on the fidelity of the qubit operations. Assuming a 99.9% fidelity, one needs to target a system size of 1 million to 1 billion qubits.
2. The minimal operation fidelity is set by the threshold fidelity of the error correcting code[8]. The threshold for e.g. a surface codes is ~99%, as a rule of thumb it is best to be at least one order of magnitude above this threshold [1].
3. A good qubit connectivity is required for the error correction. A minimal connectivity can be acquired using a two dimensional lattice (e.g. square grid).

At the time of writing we are quite far from these numbers, especially the number of qubits needs to be increased (only a few dozen of qubits have been demonstrated [2, 6, 3]). The central question for most qubit platforms seems not to be, "does it work?", but, "does it scale?".

Scientists and engineers are trying to answer this question for the different quantum computing platforms (e.g. superconducting qubits, trapped ions, neutral atoms , ...). In this work, we study spin qubits in silicon made by gate-defined quantum dots. This platform is less far along as the other platforms mentioned, but has some advantages which might help it scale more easily to a large qubit number. The following reasons make spin qubits in silicon an attractive platform [26]:

- Spin qubits are small, this is both a relief and burden. Small is nice as it allows one to integrate many qubits in a small area without the need for interchip connectivity. At the same time, it also means a lot of control electronics needs to reach a very small place on the chip. These challenges are treated in more detail in [4, 13].
- Spin qubits can be built using the same fabrication methods as the common transistor [30]. This allows for seamless integration[26, 10, 21, 27, 12] of the qubits with classical electronics avoiding the 'wiring' problem⁷. As millions of transistors can be integrated together on a chip, it is not too far of a stretch to assume it might be possible to do the same with spin qubits.
- Spin qubits can be operated at elevated temperatures [18, 28] (1-4 Kelvin range), which significantly increases the thermal budget available at the chip. It still has to be proven that is is possible to achieve high fidelities at these temperatures.

1.4. THESIS OUTLINE

In this thesis, we scale spin qubit systems in silicon from two to six qubits in an academic environment. We do this while maintaining the operation fidelity of the qubits. To make

⁷A common problem (except for atomic qubits) in the quantum community is that every qubit has its own properties, which means a different signal needs to be applied to each qubit. In practice this means at least one cable per qubit. – *you can only brute-force to a certain extend* –

this possible, we also investigate fast readout methods in silicon and create a software environment to easily operate a handful of qubits. In the following the different chapters of this thesis are introduced.

Chapter 2 introduces the theoretical concepts needed to understand how the quantum processor in chapter **3** and **6** is operated.

In **Chapter 3** the operation of a two qubit quantum processor in silicon is described. We show universal control by performing a state tomography of Bell states and executing Grover's and the Deutsch-Jozsa algorithm.

Chapter 4 describes methods for fast qubit readout. This work was part of the multi-qubit work, where we aimed at fast operation of the quantum chip. The execution speed of our experiment was most hindered by slow waveform uploads (chapter 7) and slow readout (ms timescales). In this chapter we show how a small modification to the design of the gates enables the usage of RF readout in accumulation mode devices.

Chapter 5 presents the main achievement of this work. We show that we are able to develop a 6-qubit quantum processor, which we operate universally. In addition we are able to achieve respectable fidelities for the quantum gates, state preparation and measurement.

Chapter 6 introduces the software and hardware developments that were needed to perform the experiments described in **Chapter 5**.

Chapter 7 provides an overview and conclusions for this work. This chapter puts this work in perspective and discusses next steps in scaling up spin qubits.

BIBLIOGRAPHY

- [1] G. Q. Ai. "Exponential suppression of bit or phase errors with cyclic error correction". *Nature* 595.7867 (2021), p. 383.
- [2] F. Arute *et al.* "Quantum supremacy using a programmable superconducting processor". *Nature* 574.7779 (2019), pp. 505–510.
- [3] D. Bluvstein *et al.* "A quantum processor based on coherent transport of entangled atom arrays". *Nature* 604.7906 (2022), pp. 451–456.
- [4] J. M. Boter *et al.* "The spider-web array—a sparse spin qubit array". *arXiv preprint arXiv:2110.00189* (2021).
- [5] D. P. DiVincenzo. "The physical implementation of quantum computation". *Fortschritte der Physik: Progress of Physics* 48.9-11 (2000), pp. 771–783.
- [6] L. Egan *et al.* "Fault-tolerant operation of a quantum error-correction code". *arXiv preprint arXiv:2009.11482* (2020).
- [7] R. P. Feynman. "Simulating Physics with Computers". *International Journal of Theoretical Physics* 21.6/7 (1982).
- [8] A. G. Fowler, S. J. Devitt, and C. Jones. "Surface code implementation of block code state distillation". *Scientific reports* 3.1 (2013), pp. 1–6.
- [9] C. Gidney and M. Ekerå. "How to factor 2048 bit RSA integers in 8 hours using 20 million noisy qubits". *Quantum* 5 (2021), p. 433.
- [10] M. F. Gonzalez-Zalba, S. de Franceschi, E. Charbon, T. Meunier, M. Vinet, and A. Dzurak. "Scaling silicon-based quantum computing using CMOS technology". *Nature Electronics* 4.12 (2021), pp. 872–884.
- [11] A. W. Harrow, A. Hassidim, and S. Lloyd. "Quantum algorithm for linear systems of equations". *Physical review letters* 103.15 (2009), p. 150502.
- [12] J. Hasler, N. Dick, K. Das, B. Degnan, A. Moini, and D. Reilly. "Cryogenic floating-gate CMOS circuits for quantum control". *IEEE Transactions on Quantum Engineering* 2 (2021), pp. 1–10.
- [13] R. Li *et al.* "A crossbar network for silicon quantum dot qubits". *Science advances* 4.7 (2018), eaar3960.
- [14] S. Lloyd. "Universal quantum simulators". *Science* 273.5278 (1996), pp. 1073–1078.
- [15] Y. Manin. "Computable and uncomputable". *Sovetskoye Radio, Moscow* 128 (1980).
- [16] J. L. Park. "The concept of transition in quantum mechanics". *Foundations of physics* 1.1 (1970), pp. 23–33.
- [17] A. Peres. "Reversible logic and quantum computers". *Physical review A* 32.6 (1985), p. 3266.

- [1] L. Petit, H. Eenink, M. Russ, W. Lawrie, N. Hendrickx, S. Philips, J. Clarke, L. Vandersypen, and M. Veldhorst. “Universal quantum logic in hot silicon qubits”. *Nature* 580.7803 (2020), pp. 355–359.
- [2] J. Preskill. “Quantum computing 40 years later”. *arXiv preprint arXiv:2106.10522* (2021).
- [3] M. Reiher, N. Wiebe, K. M. Svore, D. Wecker, and M. Troyer. “Elucidating reaction mechanisms on quantum computers”. *Proceedings of the national academy of sciences* 114.29 (2017), pp. 7555–7560.
- [4] S. Schaal, A. Rossi, V. N. Ciriano-Tejel, T.-Y. Yang, S. Barraud, J. J. Morton, and M. F. Gonzalez-Zalba. “A CMOS dynamic random access architecture for radio-frequency readout of quantum devices”. *Nature Electronics* 2.6 (2019), pp. 236–242.
- [5] P. W. Shor. “Algorithms for quantum computation: discrete logarithms and factoring”. *Proceedings 35th annual symposium on foundations of computer science*. Ieee. 1994, pp. 124–134.
- [6] P. W. Shor. “Fault-tolerant quantum computation”. *Proceedings of 37th Conference on Foundations of Computer Science*. IEEE. 1996, pp. 56–65.
- [7] P. W. Shor. “Scheme for reducing decoherence in quantum computer memory”. *Physical review A* 52.4 (1995), R2493.
- [8] A. M. Steane. “Error correcting codes in quantum theory”. *Physical Review Letters* 77.5 (1996), p. 793.
- [9] L. M. K. Vandersypen, H. Bluhm, J. Clarke, A. Dzurak, R. Ishihara, A. Morello, D. Reilly, L. Schreiber, and M. Veldhorst. “Interfacing spin qubits in quantum dots and donors—hot, dense, and coherent”. *npj Quantum Information* 3.1 (2017), pp. 1–10.
- [10] Y. Xu *et al.* “On-chip integration of Si/SiGe-based quantum dots and switched-capacitor circuits”. *Applied Physics Letters* 117.14 (2020), p. 144002.
- [11] C. H. Yang *et al.* “Operation of a silicon quantum processor unit cell above one kelvin”. *Nature* 580.7803 (2020), pp. 350–354.
- [12] C. Zalka. “Simulating quantum systems on a quantum computer”. *Proceedings of the Royal Society of London. Series A: Mathematical, Physical and Engineering Sciences* 454.1969 (1998), pp. 313–322.
- [13] A. M. J. Zwerver *et al.* “Qubits made by advanced semiconductor manufacturing”. *Nature Electronics* 5.3 (2022), pp. 184–190.

2

QUANTUM DOTS AS SPIN QUBITS : FUNDAMENTALS

An expert is a person who has made all the mistakes that can be made in a very narrow field.

Niels Bohr

In this work, we build qubits, the basic building block of a quantum computer. We do this by encoding its information in the spins of single electrons. These electrons are physically confined and controlled in quantum dots. The first part of this chapter introduces the concept of a quantum dot and explains the material properties of Silicon, the host material of the quantum dots. The second part discusses the physics of the spin angular momentum and how it can be controlled in a quantum dot context. An introduction will be given on the initialization, manipulation and readout of single electron spins. In further chapters, we will use this knowledge to further refine the theory and use it to operate spin qubits.

2.1. FROM FREE ELECTRON TO QUANTUM DOT

Taming a single electron: A free electron in vacuum can be well described by its momentum, which is given by the following Hamiltonian [32] :

2

$$\hat{H} = -\frac{\hbar^2 \nabla^2}{2m_e} \quad (2.1)$$

When solving¹ the Schrodinger equation, the electron can be found anywhere in space with equal probability. As we want to localize the electron in a quantum dot, we need to create an environment with a local potential minimum in all three directions, e.g. due to electric fields. We describe this by adding the potential $U(r)$ to the Hamiltonian:

$$\hat{H} = -\frac{\hbar^2 \nabla^2}{2m_e} + U(\mathbf{r}). \quad (2.2)$$

This Hamiltonian is sufficient to describe a single electron in a quantum dot. A particle in a box toy model for a quantum dot potential can be constructed by considering $U(x, y, z) = 0$ for $[0 < i < l_i]$; where i is a spatial dimension (x,y,z) and l_i is the size of the quantum dot in the direction i . Outside this region, the potential is infinitely large, as shown in Fig. 2.1a. At the boundaries, 0 and l_i , the probability of finding the electron is 0. A valid (normalized) solution is given by[32]:

$$\psi_n(x, y, z) = \sqrt{\frac{8}{l_x * l_y * l_z}} \sin\left(\frac{n\pi x}{l_x}\right) \sin\left(\frac{n\pi y}{l_y}\right) \sin\left(\frac{n\pi z}{l_z}\right) \quad (2.3)$$

for $n_i = 1, 2, 3, \dots$. The energy for each eigenstate is given by,

$$\epsilon_{n_x, n_y, n_z} = \frac{\pi^2 \hbar^2}{2m_e} \left(\frac{n_x^2}{l_x^2} + \frac{n_y^2}{l_y^2} + \frac{n_z^2}{l_z^2} \right) \quad (2.4)$$

For the quantum dots used in this work, $l_x, l_y >> l_z$.

Creating a quantum dot: In this work, two mechanisms are used to confine single electrons. We use the band structure of a semiconducting stack to confine electrons in the z-direction and use electric fields to confine them in the x,y-plane (see Fig. 2.1b). The semiconducting stack used in this work is a SiGe/Si/SiGe heterostructure (Fig. 2.1c). The electrons are confined in this structure as the conduction band energy in silicon is lower than in SiGe. Electrons can be accumulated in the Si quantum well by biasing a metallic gate on top of the quantum well positively (Fig. 2.1c). This accumulated sheet of electrons is called a two dimensional electron gas (2DEG).

The quantum dots are created by locally shaping the potential well (x,y direction) using gates[44, 17], as shown in Fig. 2.1b. The plunger gates (blue) control the number of electrons in the quantum dot. The barrier gates (yellow) control the strength of confinement and the screening gates (red) screen the electric fields from the gates on top. By changing

¹A valid solution is given by, $\psi(r) = Ae^{i\mathbf{k}\cdot\mathbf{r}}$, where \mathbf{k} is the wavevector and r the space coordinate

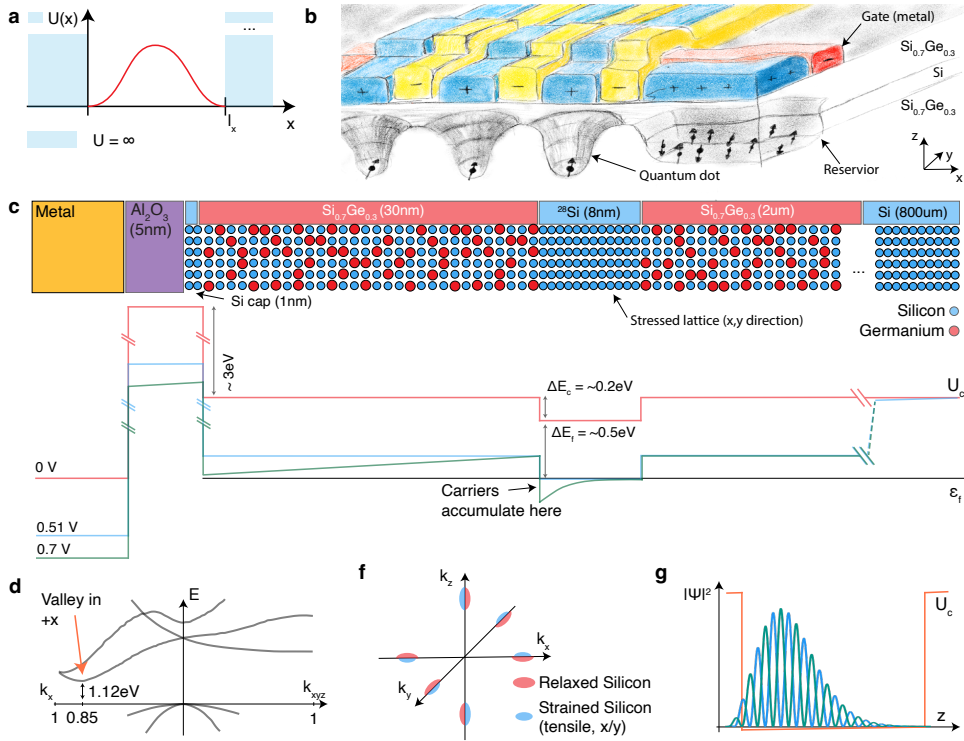


Figure 2.1: Confinement and the Silicon band structure | **a**, A quantum dot in one dimension. The potential $U(x)$ is indicated by the colored area and is infinite for $0 > x > l_x$. The ground state solution ($\psi_0(x)$) is plotted in red. **b**, Artistic impression of a quantum dot device in silicon. The blue, yellow and red colored structures represent metallic gates, which can be biased to control the density of electrons in the quantum well (silicon layer). The potential landscape $U(x, y)$ is shown for 3 quantum dots and one reservoir. **c**, Cross section along the z, x -plane of the heterostructure. The top panel shows the material stack, and the circles represent single atoms. The lattice constant in the x and z direction is different in the Si layer due to the lattice mismatch with the SiGe layer. The bottom panel shows the potential ($U(z)$) for different gate voltages (0, 0.5 and 0.7 V). The quantum well is expected to accumulate around 0.5 V (blue line) as the silicon conduction band crosses the Fermi level. The green line (0.7 V) illustrates the additional band bending originating from the accumulated charges inside the quantum well ($V^2 U = -\frac{\rho}{\epsilon}$). **d**, Dispersion relation of bulk silicon[1]. At $k_x = 0.85 \frac{2\pi}{a_0}$, one of the 6 valleys (energy minima) of the conduction band is shown, where a_0 is the lattice constant ($a_0 = 0.543\text{nm}$). The other valleys are located along the $\pm k_x, \pm k_y$ and $\pm k_z$ axes. **f**, The equipotential points around the 6 valleys are shown in case of relaxed Si and strained Si. The strain lifts the 6 fold degeneracy as the energy of the valleys in the x and y -direction is increased. Note that the equipotential surfaces are ellipsoids, indicating that the effective mass is different in the longitudinal and the transversal direction. **g**, Sketch of the wavefunction of a single electron in the z -direction, where the conduction band edge $U(z)$ is indicated by the orange line. The ground and excited valley state is plotted by the green and blue lines. The excited state has a larger overlap with the conduction band of the SiGe (high potential zone), causing the lifting of the valley degeneracy.

the bias of the screening gates, one can also control the y-confinement of the quantum dots.

Adding Silicon to the equation: As mentioned before, the electrons are confined in the conduction band of the silicon layer. The electrons inherit the properties of its host material (Si). The effective mass of the electron changes, in addition an extra quantum number needs to be added due to the degeneracies in the Si band structure. These degeneracies are called valleys, the $+x$ valley is shown in band structure sketch in Fig. 2.1d. The other valleys can be found in the $-x$, $\pm y$ and $\pm z$ direction.

The Si quantum well is stressed in the x and y-direction due the difference in lattice constant ($\sim 1\%$) between the Si and SiGe. This stress increases the energy of the valley in the $\pm x$ and $\pm y$ direction ($\Delta E_{v_{\pm z} \leftrightarrow v_{\pm x, \pm y}} = 200\text{meV}$ [45]). Two degenerate minima are left ($\pm z$ -direction), in which electrons can be populated.

When looking in more detail at the band structure, we observe that the effective mass ² of the electron is different in the x,y versus z direction. The Hamiltonian for the kinetic energy term in the z-valleys is then given by:

$$\hat{H} = -\frac{\hbar^2}{2} \left(\frac{1}{m_{x,y}^*} \frac{\partial^2}{\partial^2 x} + \frac{1}{m_{x,y}^*} \frac{\partial^2}{\partial^2 y} + \frac{1}{m_z^*} \frac{\partial^2}{\partial^2 z} \right) \quad (2.5)$$

where $m_{x,y}^* = 0.19m_e$ and $m_z^* = 0.98m_e$ ³. When adding this effect to our toy model (equation 2.2), the eigenenergies of the system are given by:

$$\epsilon_{n_x, n_y, n_z, v} = \frac{\pi^2 \hbar^2}{2m_{x,y}^*} \left(\frac{n_x^2}{l_x^2} + \frac{n_y^2}{l_y^2} \right) + \frac{\pi^2 \hbar^2 n_z^2}{2m_z^* l_z^2} \quad (2.6)$$

Notice that the extra quantum number v was added indicating the occupied valley state ($+/ - z$ valley) (see next section). If we fill in the equations with $l_{x,y} = 50\text{nm}$ and $l_z = 8\text{nm}$, we get the following:

n_x	n_y	n_z	v	Energy (meV)
1	1	1	$+z$	7.5
2	1	1	$+z$	9.9
1	2	1	$+z$	9.9
1	1	2	$+z$	25.5

Which corresponds well to the values measured in quantum dot devices[44]. When adding electrons a quantum dot ⁴, we expect to firstly occupy the valley states (see next section) and then the orbitals states in the x an y direction.

²The effective mass approximation (EMA) is used to simplify the description of the electron in its host (Si) material. The energy around the conduction band minima is well described by $E(\mathbf{k}) = E_0 + \frac{\hbar^2 \mathbf{k}^2}{2m^*}$, which is described by a Hamiltonian $\hat{H}(\mathbf{k}) = -\frac{\hbar^2 \nabla^2}{2m^*}$

³These are the bulk values.

⁴When solving for more than one electron, one should also include the Coulomb interaction between the different electrons in the Hamiltonian.

Until now, we considered the potential outside the quantum dot to be infinite. The real offset is determined by the difference in conduction band energy (ΔE_c) between the Si and SiGe layer, as illustrated in Fig. 2.1c. In reality this means that the wavefunction partially penetrates (exponential decay) in the SiGe substrate. In the next section we describe how this affects the quantum dots.

The valley splitting (ϵ_v) is defined as the energy difference between the ground and first excited valley state ($\pm z$ valleys). This parameter plays an important role for spin qubit experiments, as it can affect the fidelity of qubit operations.

An intuitive picture explaining the origin of the valley splitting is shown in Fig. 2.1g. Two wavefunctions have the same envelope, but oscillate with a different phase. The envelope is the solution of the particle in a box Hamiltonian⁵, and the Bloch oscillations originate from the $\pm k_z$ -vectors for each valley. When looking in detail at the interface, the integrated area of the exponentially decaying wavefunction in the SiGe part is not equal for both valleys, hence breaking the degeneracy (simplistic view). The derivation of the valley splitting can be found in [9].

The value of the valley splitting can be influenced by the following parameters:

- The conduction band offset of the SiGe and Si layer, as it controls how strongly the wavefunction is repelled from the SiGe substrate. This value is fixed at the stage of heterostructure growth (e.g. $Si^{0.7}Ge^{0.3}$ [5]).
- The shape of $U(z)$. When a stronger electric field⁶ is used to confine the quantum dot in the z direction, the wavefunction is pulled more strongly towards the interface, causing an increase in the valley splitting [20]. This parameter can also be influenced by changing the thickness of the Si quantum well.
- The quality of the interface. Atomic steps at the SiGe/Si interface reduce the valley splitting as the difference of overlap with the SiGe layer is reduced for the two wavefunctions[9, 26].

In our experiments typical values for the valley splitting range from $50\mu eV$ to $300\mu eV$, which, as we will show later, is large enough to enable good quality qubits.

Modelling multiple quantum dots: As it is impractical to calculate the properties for many particles using the previous models, a simplification[42] can be made by introducing the Fermi Hubbard (FH) model. The extended⁷ Fermi-Hubbard model is given by (see also Fig. 2.2a):

$$\hat{H}_{FH} = \sum_{i,j} -t_{ij} (\sigma_i^\dagger \sigma_j + \sigma_j^\dagger \sigma_i) + \sum_i U_i \hat{n}_i + \sum_{i,j} V_{ij} \hat{n}_i \hat{n}_j + \sum_i \mu_i \hat{n}_i \quad (2.7)$$

⁵Where $U(z)$ contains the contributions of the electric fields (→ Poisson equation) originating from the electrostatic gates and the potential originating from the band structure of the heterostructure.

⁶The strength of the electric field can be tuned by changing the difference between the plunger and barrier gates. The tunability also depends strongly on the depth of the quantum well and the gate pitch.

⁷Some additional terms are added which makes it a more complete description for quantum dots.

The first term of the Hamiltonian describes the rate (t_{ij}) at which an electron can tunnel from site i to site j. The operator σ_i (σ_i^\dagger) is the creation (annihilation) operator for an electron at site i. The tunnel rate between two quantum dots can be modified by changing the barrier gate voltage between dot i and j [37]. The second term describes the on-site interaction U_i , and is proportional to the number of electrons at site i. The third term describes the interaction between the electrons on dots i and j [16]. The last term describes the electrochemical potential μ_i which is controlled by the electrostatic gates (see Fig. 2.2a).

A sensing dot (SD) is a quantum dot used to sense the charge occupation of neighboring quantum dots[11]. A sketch is shown in Fig. 2.2b. Sensing dots are usually operated in the many electron regime, as it makes it easier to strongly tunnel-couple them with the reservoirs. The reservoirs are accumulated regions of the 2DEG which are connected via an ohmic contact to the measurement wires (just like a transistor). Fig. 2.2c shows the current running through the SD as a function of the applied SD plunger voltage. Each peak indicates the sequential transport of individual electrons through the sensing dot. The peak appears when there is an electrochemical potential level present between the Fermi level of the source and drain.

The location of each peak is a function of the addition energy and the local electric field. The local electric field is a function of the potentials on the electrostatic gates surrounding the sensing dot and also of the number of charges in the neighboring dots⁸. One can detect the addition of an electron in an adjacent quantum dot by staying at a fixed SD plunger voltage (e.g. on the slope of a peak) and monitoring the SD current. If the number/position of charges in the environment changes, the SD current will change as shown in Fig. 2.2c.

Cross talk of the plunger and barrier gates. In an ideal world one would be able to control both the electrochemical potential ($\mu_i \rightarrow P_i$ gate) and the tunnel coupling ($t_{ij} \rightarrow B_i$ gate) using single gates [39]. In reality multiple gates effect a single parameter, i.e. when changing P_1 , μ_1 is changed, but so will μ_2 (Fig. 2.2e) due to the capacitive coupling of QD2 with P_1 . The question is how we can circumvent this problem?

The effect of the gates on the electrochemical potential at the site of a dot can be described by [11]:

$$\Delta\mu_{QD} = \frac{e}{C_\Sigma} \left(\sum_i C_{QD,i} \Delta V_i \right) \quad (2.8)$$

where $C_{QD,i}$ is capacitance⁹ between the quantum dot and gate i. C_Σ is the sum of all the capacitances from the gates that surround the QD. V_i is the gate voltage applied to the i^{th} gate. For multiple quantum dots, we can rewrite equation 2.8 as (simplified):

$$\vec{U} = C \vec{V} \quad (2.9)$$

⁸This corresponds effectively to the the V_{ij} term in the Fermi Hubbard model (eq. 2.7)

⁹The quantum dot is considered to be a classical metallic dot coupled to the surrounding gates (e.g. $Q = CV$), where we assume that the quantum dot is grounded to the reservoir.

Where \vec{U} is a vector with the quantum dot electrochemical potentials, \vec{V} a vector with the applied gate voltages and C the capacitance matrix. When inverting this equation, $\vec{V} = C^{-1}\vec{U}$, one can supply a set of electrochemical potentials (wishlist) for the quantum dots and calculate the voltages that are needed to accomplish this. Each element in U is called a virtual gate [39], usually labeled $vP1$, $vP2$, Where $vP1$ is just the electrochemical potential of dot 1, but in different units. The inverted capacitance matrix is also called the virtual gate matrix [23].

One question remains: how to measure the elements $\left(\frac{C_{i,j}}{C_{\Sigma_i}}\right)$ of the capacitance matrix C ? The tuning strategy used for the 6 qubit experiments in chapter 5 is described in Fig. 2.2h-l. This strategy¹⁰ is based on [39] and [23].

1. Measure the sensing dot current as a function of the SD plunger and the plunger of the nearest quantum dot (Fig. 2.2e). From the slopes (green lines) we can extract $\frac{\delta\mu_{vSD}[mV]}{\delta V_{vP1}}$ and $\frac{\delta\mu_{vP1}[mV]}{\delta V_{vSD}}$, which can be directly dialed in the virtual gate matrix¹¹. The result is shown in Fig. 2.2f. Note the image is centered on the anti-crossing of the sensing dot and QD1. This is important as electrons will need to tunnel through the array in the next steps (if the anticrossings are not aligned at the same level (here 0mV), no transport will possible through the array). In this step it is also useful to measure the following entries of the virtual gate matrix ($\frac{\delta\mu_{vP1}[mV]}{\delta V_{vB0}}$, $\frac{\delta\mu_{vP1}[mV]}{\delta V_{vB2}}$, $\frac{\delta\mu_{vP1}[mV]}{\delta V_{vP2}}$ and $\frac{\delta\mu_{vSD}[mV]}{\delta V_{vB0}}$).
2. We follow the procedure of the previous step, but tune now for QD1 and QD2, as shown in Fig. 2.2g. After correcting the cross talk, aligning with the center of the anticrossing and adjustment of the tunnel-coupling, a textbook double dot charge stability diagram is obtained in Fig. 2.2h. When applying this procedure deeper into the array, e.g. for the third quantum dot, latching effects can occur as illustrated in Fig. 2.2i. This happens because sometimes it is hard to load/unload electrons as the coupling to the reservoir gets too low¹².
3. Return to step 2 for the next set of dots (e.g. Fig. 2.2 i).

¹⁰For the experimentalist : it is assumed that the sensing dot is tuned up and that the plungers and barriers of the array are biased with voltages around their pinch value (typ. a few 100mV less). The array should be close to the single electron regime. It is best to start the tune up procedure in the unaccumulated regime, as for accumulated array the dot locations are likely to shift during the tune up procedure (larger voltage changes needed and 2DEG that is moving), which changes the tunnel couplings and measured capacitances of the capacitance matrix during the experiments.

¹¹We choose here to to fill the virtual gate matrix, as virtual gates are used be on the axis of the sweeps (and it allows for easily updating the matrix).

¹²TIP : in case only diagonal lines are visible, go back in the tuning and make sure all the anticrossings are well aligned.

2

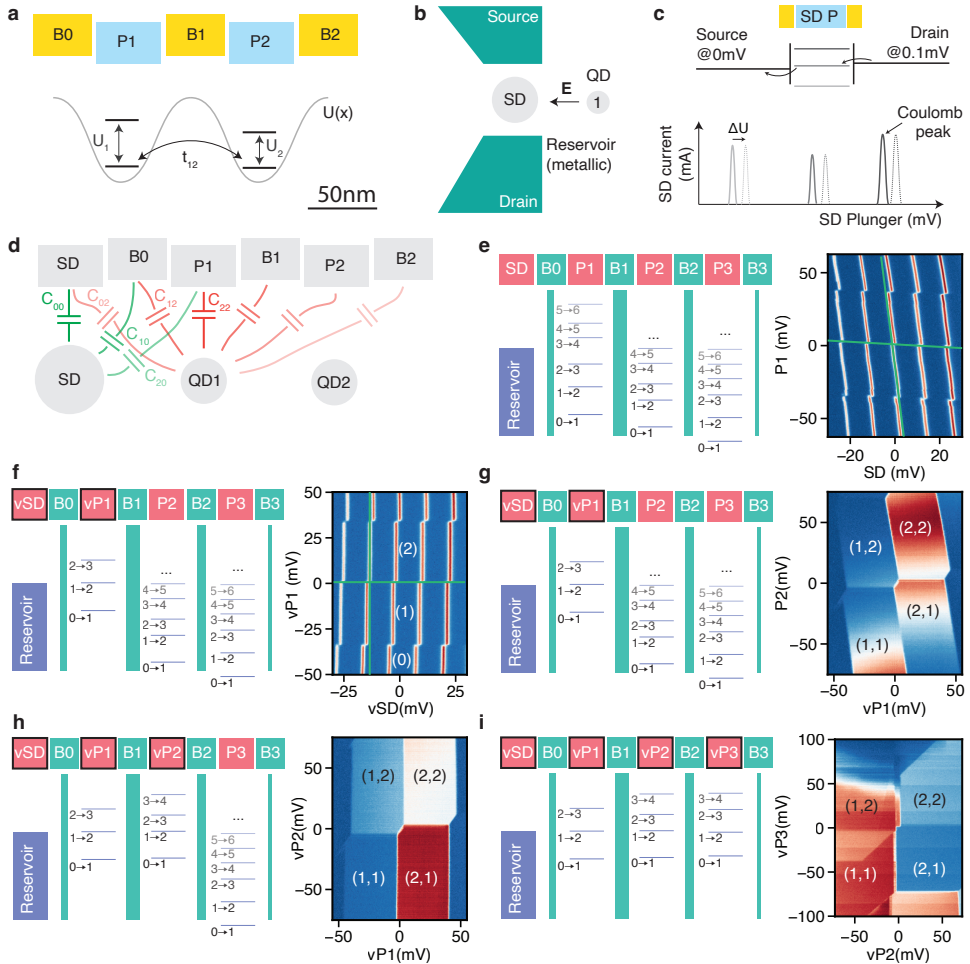


Figure 2.2: Tuning of quantum dots | a, Diagram showing the potential landscape $U(x)$ of two quantum dots and the gates controlling the potential landscape. For each quantum dot, the addition energy is shown (U_1 , U_2). The tunnel coupling between the dots is given by t_{12} . **b,** Schematic of a Sensing dot. The grey areas are weakly accumulated regions in the 2DEG (quantum dots) and the green areas are strongly accumulated regions where one acts as the source and one as the drain. **E** indicates the electric field originating from the quantum dot (QD). **c,** The top panel shows the quantized energy levels of the sensing dot and the electrochemical potential of the source and drain contact. The potential (μ_{SD}) of the sensing dot can be controlled with the 'SD P' gate. In the bottom diagram the 'SD P' gate is swept and the resulting current is plotted. The dotted line shows the response of the sensing dot when an additional electron is loaded in a nearby quantum dot (panel b). **d,** Diagram showing the capacitances between the gates and the quantum dots (not all combinations are shown, to avoid overcrowding). **e-i,** Tune up procedure for an array of 3 quantum dots (see main text). Every panel has on the left a schematic showing the electron transitions of the quantum dots (e.g. from 0 to 1 electron ($0 \rightarrow 1$)). At the right side of each panel, a charge stability diagram is shown with the measurement that corresponds to each tuning step.

2.2. FROM QUANTUM DOT TO QUBIT

The previous section explained how to confine a row of electrons and control properties related to charge. In this section we describe how we turn a single electron into a qubit, more specifically a Loss-DiVincenzo (LD) qubit¹³ [18]. In this section we will explain what a spin is, what is needed to manipulate a single spin, how two spins can interact and how spin initialization and readout can be performed.

What is spin? Spin is defined as the intrinsic angular momentum of a particle. In our case, we use electrons which have a total spin of $S = \frac{1}{2}$. An electron spin has two possible eigenstates, either spin-down: $|\downarrow\rangle$ ($m_z = -\frac{1}{2}$), or spin-up: $|\uparrow\rangle$ ($m_z = \frac{1}{2}$). These two quantum states respectively form the $|0\rangle$ and $|1\rangle$ states of our qubit. The Hamiltonian for a single spin in a magnetic field is given by:

$$\hat{H} = \frac{g\mu_b}{2} \mathbf{B} \cdot \boldsymbol{\sigma} \quad (2.10)$$

Where g is the g -factor of the electron ($g \approx 2$ in silicon), μ_b is Bohr magneton, \mathbf{B} is the applied magnetic field and $\boldsymbol{\sigma}$ are the Pauli matrices, $(\sigma_x, \sigma_y, \sigma_z)^T$. We assume the field is applied in the Z direction. The spin state can be controlled by applying an AC magnetic field, whose frequency corresponds exactly to the energy difference between the spin-up and down state ($f = \frac{g\mu_b|B|}{h}$). The spin transition can only be driven when the driving field is orthogonal (Fig. 2.3a) to the quantization axis of the spin. The Hamiltonian for the driven system is given by:

$$\hat{H} = \frac{g\mu_b}{2} (B_z \sigma_z + B_x \sin(2\pi f t + \phi)) \quad (2.11)$$

Where B_x is the amplitude of driving field in the x direction and ϕ is the phase of the oscillating signal. The phase of signal determines the axis of rotation in the x - y plane, which for example differentiates an X_{90} from a Y_{90} pulse (90 degree rotation around the x or y axis).

Assuming an initial spin-down state, the dynamics of the spin is be given by (see [35] for a full derivation):

$$P_{|\uparrow\rangle - |\downarrow\rangle} = \frac{1}{2} \left(1 - \frac{\Omega^2}{\Omega^2 + \Delta^2} \cos(2\pi\sqrt{\Omega^2 + \Delta^2} t) \right) \quad (2.12)$$

Where Ω ($= \frac{g\mu_B B_x}{h}$) is the Rabi frequency (speed of the spin flips) and Δ the difference between the driving frequency (f_d) and the qubit frequency (f). An example showing a qubit driven on and near resonance is shown in Fig. 2.3b.

The gate model is one of the most popular models [27] that can be used to perform quantum calculations¹⁴. In this model, many small unitary operations (operations on a few qubits) are used to build a larger quantum operation. The most important circuit elements in this model are: single qubit gates, two-qubit gates and measurements. The X_{90} , Y_{90} , X_{180} , Y_{180} , $T (= Z_{45})$, Z_{90} , Z_{180} and the H gate¹⁵ are common single qubit gates.

¹³There also exist other type of spin qubits, where electrons in multiple quantum dots make up one spin qubit (review in [3])

¹⁴An example of an other model is adiabatic quantum computation[8].

¹⁵The Hadamard gate is a 180 degree rotation around the axis in between the X and Z axis

The X_{90} specifies rotation of 90 degrees around the x -axis. For the two-qubit gates, the controlled phase gate (CPhase gate), controlled NOT gate (CNOT gate), SWAP gate and Toffoli gate are quite common. All these gates (except the SWAP gate) can be used to generate entanglement between a pair of qubits. In the coming sections we will describe how these gates are implemented for silicon spin qubits.

Single qubit gates are implemented by applying an oscillating signal which drives the spin transition. Two methods are commonly used to manipulate a single spin:

- **ESR** (electron spin resonance) is a method where one applies an oscillating magnetic field to drive the qubit. The field is generated by placing a microwave antenna on chip, close to the quantum dots, through which an alternating current is sent as shown in Fig. 2.3c. Design considerations of such an antenna can be found in [6]. A central challenge when using striplines is to maintain addressability¹⁶ of the qubits. In addition, an on chip stripline generates only a local magnetic field and is not suitable for large 2D spin qubit arrays. Other methodologies are being pursued, for example by using a microwave (MW) antenna, that provides a global field that can drive all the qubits on the chip[36]. The DC stark effect can be used to modulate the qubits in/out of resonance and perform qubit operations [10].
- **EDSR** (electric-dipole spin resonance) uses an electric field to indirectly drive the qubit. One can either use the intrinsic spin orbit coupling (SOC) [14] (low for electrons in silicon) or create an artificial SO field by creating a magnetic field gradient[31]. In both cases an electric field is used that changes the position/shape of the wavefunction, which results into an effective change of B_x .

The field is applied by applying a microwave excitation via a gate near the quantum dot(s) (e.g. one of the screening gates as shown in chapter 5). The magnetic field gradient is created using micromagnets as illustrated in Fig. 2.3d. In addition to providing a mechanism for driving the qubits, the micromagnets can also be shaped such that the qubits are addressable (e.g. a different resonance frequency for every qubit, see chapter 5). Note that creating this artificial SOC field also provides a way for charge noise to couple to the qubits, which can affect the coherence times.

It has been shown that the single-qubit gates can be created using both methods [38, 15]. A single qubit gate is generated by applying a short burst of microwave power to the sample (gate). After this burst, the next gate can be performed. The rotation angle of a single qubit gate can be controlled by changing the amplitude or the duration of a MW burst. The rotation axis is controlled by the phase of the microwave signal. All angles in the x and y plane are easily accessible in our experiments. When possible, Hadamard gates are replaced by Y_{90} gates, as the rotation angle of a Hadamard gate is hard to create using a single pulse.

During the execution of these gate, errors can appear. The source of these errors is either coherent or incoherent. The coherent errors can be caused by calibration errors,

¹⁶There will be some natural addressability due to g-factor differences between the qubits. These differences can be tuned using the DC Stark effect (e.g. by changing the strength of the confinement) [38].

but could also be due to cross talk between the qubits (next section). Incoherent errors usually originate from noise that alters the Hamiltonian every time a gate is executed. For example, the nuclear spin bath causes changes in the local magnetic environment whenever one of the nuclear spins in the silicon substrate changes orientation.

Qubit Crosstalk: When driving qubits using ESR/EDSR, cross-talk can arise. To gain intuition, we will consider a scenario where one qubit is driven, while the other qubit is idling. The following list describes errors that could occur on the idling qubit:

- A shift in the resonance frequency of a qubit can occur when it is driven near its resonance frequency, as the off-resonant microwaves dress the qubit. This shift is called an AC Stark shift.

The shift in frequency causes a phase error (Z error) on the qubit which can be corrected by applying a virtual Z gate. A virtual Z gate is implemented by adding a phase ϕ to every subsequent single qubit gate performed on the idling qubit.

- Off resonant driving causes Rabi oscillations at a reduced amplitude. The visibility of the off-resonant oscillations corresponds to $\frac{\Omega^2}{\Omega^2 + \Delta^2}$ at a Rabi frequency of $\Omega_{off} = \sqrt{\Omega^2 + \Delta^2}$. As for the AC Stark shift, this effect is most dominant $\frac{\Delta}{\Omega} < 10$. When operating in the regime $\frac{\Delta}{\Omega} < 10$, the synchronization condition [13] can be applied to nullify the effect of the off resonant drive. This can be done by finding the Rabi frequency at which the idling qubit performs a 2π rotation during the operation on the other qubit (see chapter 5). Other methodologies for combating cross-talk also exist, e.g. using windowing functions or the DRAG formalism [24].
- Unknown sources. In the experiments outlined in chapter 3 and 5, frequency shifts were observed which depended on the amount of power applied to the sample. This classical form of cross-talk is most likely due to the heating of the device. The mechanism behind this effect is currently under investigation.

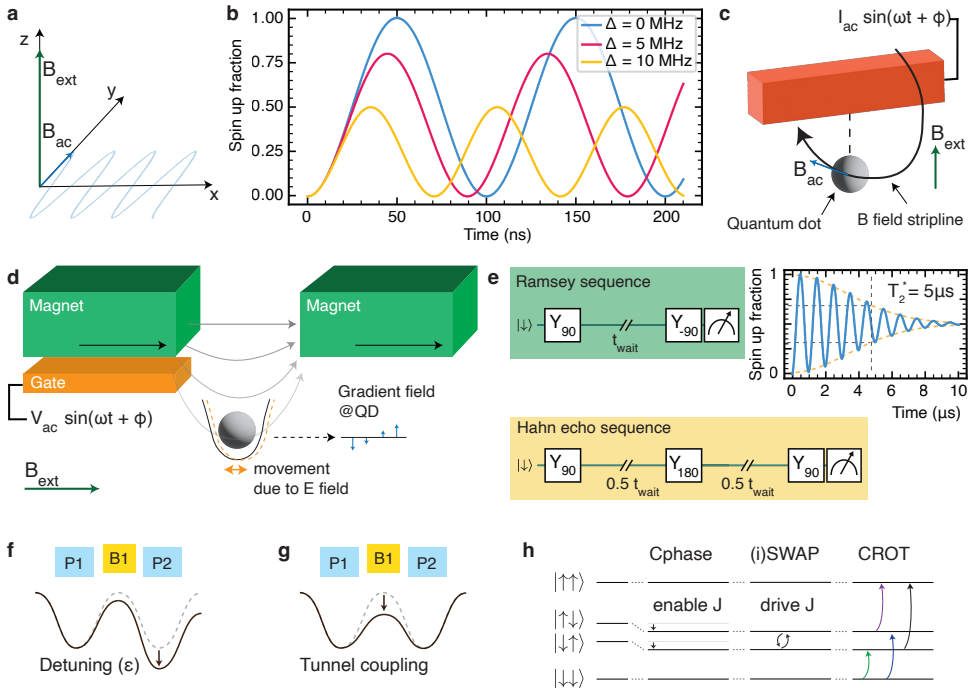


Figure 2.3: **Single and two-qubit gates on quantum dots** | **a**, The orientation of the vectors needed to drive a qubit. The green vector shows the direction of the externally applied field (quantization axis). The blue vector shows the applied oscillating magnet field B_{ac} , orthogonal to the external field. **b**, Rabi oscillations ($\Omega = 10\text{MHz}$) for different frequency detunings Δ . **c**, ESR driving mechanism. The driving field (B_{ac}) is generated by applying an AC current to the stripline (red wire). The external field is applied orthogonal to the AC field. **d**, EDSR driving mechanism. The magnetic field lines originating from the magnets are shown in gray. The z component of the gradient field along the qubit movement axis is shown in blue. The AC signal provided to the gate moves the wavefunction forward and back in the field gradient. The external field is oriented in the x direction (parallel to the magnetization of the magnets). **e**, Ramsey and Hahn echo sequence. The graph shows an example measurement of a Ramsey sequence. Oscillations are induced because the qubit and driving frequency are different. The decay of the signal is given by, $\frac{1}{2} \left(1 - \cos(2\pi\delta t) \exp\left(-\left(\frac{t}{T_2^*}\right)^2\right)\right)$, where δ is the frequency difference between the driving and idling frequency. **f**, Exchange control by detuning. The exchange J is increased by detuning the chemical potential of the second dot. The difference between the chemical potentials is called $\epsilon = \mu_2 - \mu_1$. **g**, Operation around the symmetry point. The exchange interaction is modified using the tunnel coupling between both quantum dots. **h**, Energy level diagram of two electron spins with different Zeeman energies (B_1, B_2). The exchange interaction causes a decrease in energy of the $|\uparrow\downarrow\rangle$ and $|\downarrow\uparrow\rangle$ states. The CPhase gate accumulates a conditional phase created by the two-qubit interaction. The (i)SWAP gate is performed by driving the transition between the $|\uparrow\downarrow\rangle$ and $|\downarrow\uparrow\rangle$ states (by oscillating J). A CROT is implemented by driving one of the 4 transitions shown in the image using a narrow-band drive signal.

Coherence of qubits. The coherence time of a qubit is an important property as it can fundamentally limit the fidelity of single and two-qubit gates. The coherence time describes how long quantum information can be retained in a qubit system. Coherence times are classified in two classes, T_1 and T_2 .

The T_1 time describes the timescale for a qubit to relax to its ground state (energy dissipation).

pation). For electron spin qubits in silicon, this number can approach seconds[46]. The T_1 time depends on various factors, e.g. the electron temperature[30], the valley splitting and magnetic field [30, 2]. The spin relaxation is enhanced when the spin is hybridized with the orbital or valley degree.

The T_2 time describes the timescale for a qubit to dephase (energy conserving processes). The dephasing is caused by fluctuations in the energy of the qubit (f_{res}). These fluctuations can originate from the nuclear spin bath and the coupling of charge noise to the qubit via the (artificial) spin orbit interaction. The coupling to nuclear spins can be minimized by isotopically purifying the substrate (e.g. ^{28}Si wafers). In addition, the dephasing time can also be influenced by elements in the experimental set up (e.g. stability of the magnetic field, 50Hz noise, etc.).

It is hard to give a single metric for the dephasing time as it depends on the spectral density $S(f)$, see chapter 6) of the noise. Common metrics are given below:

- T_2^* , is the dephasing time measured using a Ramsey sequence as illustrated in Fig. 2.3e. This sequence integrates all the noise given by the spectral noise density $S(f)$ for the total experimental time (see chapter 6, section 6.4.1). T_2^* indicates the coherence time of the qubit while idling. For spin qubits in purified silicon this time is typically around $2 - 30\mu\text{s}$ [15, 38, 43].
- T_2^h , is the Hahn time or spin echo time. This dephasing time is measured by executing a Ramsey experiment with a single X_{180} pulse in the middle of the experiment. This additional gate decouples the qubit from the low frequency noise. This extra gate creates in essence a filter function for $S(f)$, extending the coherence. It can be useful to apply decoupling pulses to idling qubits to preserve the quantum information for a longer time. Typical numbers for Hahn echo times are in the order of $10 - 200\mu\text{s}$ [15, 38, 43].

Several other decoupling sequences exist, which each cancel out different parts of the noise spectral density. These sequences can be used to characterize the $S(f)$ function [43, 4].

When comparing coherence times of different devices and platforms, it is always important to also factor in the speed at which the quantum operations are performed, as this will be one of the determinants how well one can perform a quantum operation.

Two-qubit gates are implemented using the exchange interaction. The interaction is defined as¹⁷:

$$\hat{H} = \frac{1}{4} J (\sigma_x \sigma_x + \sigma_y \sigma_y + \sigma_z \sigma_z) = \frac{J}{2} \begin{pmatrix} 0 & 0 & 0 & 0 \\ 0 & -1 & 1 & 0 \\ 0 & 1 & -1 & 0 \\ 0 & 0 & 0 & 0 \end{pmatrix} \quad (2.13)$$

where J is the strength of the exchange interaction. This interaction can be derived from the Fermi-Hubbard model as shown in [21]. The strength (J) can be controlled in two ways, (1) by changing the detuning (ϵ) between the quantum dots or (2) by changing the tunnel coupling as shown in Fig. 2.3 f and g. It is preferred to control the exchange coupling at the symmetry point ($\epsilon = 0$), by only using the tunnel-coupling as it is more resilient to noise[19]. The exchange J has an exponential dependency on the applied voltage on the barrier gate (see chapter 5).

When working with two-qubit gates, it is helpful to build an intuition of the eigenstates in different conditions. Two common experimental conditions are outlined below:

- Both qubits are strongly tunnel-coupled, and have identical qubit frequencies ($J \gg \Delta f$ ¹⁸). In this case the eigenbasis is dominated by the exchange interaction and the basis of the qubits is given by: $|\downarrow\downarrow\rangle, \frac{|\uparrow\downarrow\rangle - |\downarrow\uparrow\rangle}{\sqrt{2}}, \frac{|\uparrow\downarrow\rangle + |\downarrow\uparrow\rangle}{\sqrt{2}}, |\uparrow\uparrow\rangle$, which can also be written as: $|T_-\rangle, |S\rangle, |T_0\rangle, |T_+\rangle$. This is called the Singlet (S)/Triplet (T) basis.
- In the case that ($\Delta f \gg J$), the eigenbasis is given by: $|\downarrow\downarrow\rangle, |\uparrow\downarrow\rangle, |\downarrow\uparrow\rangle, |\uparrow\uparrow\rangle$.

In most cases LD qubits are operated with a frequency difference (Δf) of 30-200MHz between adjacent qubits and an exchange in the range of 10kHz (off) to 20MHz (on).

The **CPhase** gate is a two-qubit gate that can be implemented with a single pulse in LD spin qubits. The gate is performed by turning on the exchange interaction and letting the Hamiltonian evolve for a time $t_{gate} = \frac{1}{2J}$. At first sight it might seem enough to just make a block pulses, but a few things need to be taken into account:

- The rise time of the pulse. When $J_{on} > \frac{\Delta f}{10}$, the eigenbasis will start tilting towards the singlet/triplet basis, i.e. causing SWAP like operations in conjunction with the CPhase gate. The SWAP like evolution can be prevented by ensuring that the system evolves **adiabatically**. More information on the creation of these pulses can be found in chapter 5.
- After the adiabatic pulse is executed, single qubit phase corrections need to be added to both qubits. These corrections are caused by:
 1. The $\sigma_z \sigma_z$ part of the exchange interaction. The following phases need to be added to turn the $\sigma_z \sigma_z$ evolution into a CPhase (neglecting global phases),

$$U_{CPhase} = e^{-i2\pi \frac{\sigma_z \sigma_z}{4} J t_{gate}} \cdot I \otimes Z_{-90} \cdot Z_{-90} \otimes I.$$
 2. The dependency of the resonance frequency of the qubits on the exchange J . The resonance frequency is given by, $f_1 = f_{avg} - \sqrt{J^2 + \Delta f^2}$ and $f_2 = f_{avg} +$

¹⁷To keep notation short, tensors are removed in the equations, e.g. $\sigma_x \otimes \sigma_x$ is written as, $\sigma_x \sigma_x$

¹⁸ Δf is defined as the frequency difference of the qubits. J is also expressed in units of [Hz].

$\sqrt{J^2 + \Delta f^2}$. f_{avg} is the average frequency of both qubits. An additional single qubit phase needs to be added to both qubits to compensate for this effect.

3. A change in the location/confinement of the quantum dots during the exchange pulse. This causes small frequency shifts due to the spin orbit interaction. When operating a device with micromagnets, larger frequency shifts can be observed (few MHz's) as shown in chapter 3 and 5. This effect also needs to be corrected using a single qubit phase on both qubits.

When properly accounting for these coherent error sources, high fidelity two-qubit gates can be obtained as shown in [40, 28, 22]. The CPhase gate can easily be converted into a CNOT gate, by applying a Y_{90} pulse before and a Y_{-90} after the CPhase gate.

An alternative two-qubit gate that has been used in this work (mainly to facilitate read-out), is the controlled rotation gate (CROT). The gate is constructed by running two operations in parallel, (1) evolve a CPhase gate for a time chosen such that $\int_0^{t_{gate}} J(t) dt = 1$ and (2) simultaneously apply a microwave drive. When the exchange is on, the resonance frequency of one qubit depends on the state of the other qubit, e.g. the frequency difference between the $|\downarrow, \downarrow\rangle \leftrightarrow |\uparrow, \downarrow\rangle$, $|\downarrow, \uparrow\rangle \leftrightarrow |\uparrow, \uparrow\rangle$ transitions is J as illustrated in Fig. 2.3h. A CNOT gate can be synthesized by driving a X_{180} gate at the $|\downarrow, \downarrow\rangle \leftrightarrow |\uparrow, \downarrow\rangle$ transition and applying a single-qubit phase correction to each qubit (similar as performed for the CPhase gate)

It is also possible to implement a (i)SWAP gate by driving the exchange interaction¹⁹ [34]. The construction of two-qubit gates in the case when $J_{on} \gg \Delta f$ will not be discussed here, a review can be found in [3].

Readout and initialization are achieved by performing a spin-to-charge conversion, which is either performed using the Elzerman[7] or the Pauli spin blockade [29] method. In the following sections both methods are explained (and applied in chapter 3 and 5). Aside from using these methods we will see that it is also possible to initialize qubits using relaxation hotspots, and that the measurement fidelity can be improved using Quantum Non Demolition (QND) measurements[41, 25].

The Elzerman method performs qubit initialization and readout by comparing the energy of the spin state (down, $\mu_{QD,|\downarrow\rangle}$ and up, $\mu_{QD,|\uparrow\rangle}$) with the chemical potential of the reservoir (μ_{res}). A schematic illustrating the initialization process is shown in Fig. 2.4a. The spin is initialized by (1) emptying the quantum dot and (2) aligning the chemical potential of the quantum dot with the reservoir such that $\mu_{QD,|\downarrow\rangle} < \mu_{res} < \mu_{QD,|\uparrow\rangle}$. The qubit is initialized in spin-down, as only a spin-down electron can tunnel in from the reservoir.

During qubit manipulation, the chemical potential is lowered ($\mu_{QD,|\downarrow\rangle} < \mu_{QD,|\uparrow\rangle} < \mu_{res}$) such that the electron cannot escape from the quantum dot when the spin flips.

¹⁹The recipe is similar to the CPhase gate, except that the exchange interaction should be made to oscillate at the frequency difference of the $|\downarrow\uparrow\rangle$ and $|\uparrow\downarrow\rangle$ state. This can easily be seen by adding the Zeeman terms to the Hamiltonian in equation 2.13.

The readout is performed by pulsing back to the initialization position. The electron collapses either in the spin-down or up state (see Fig. 2.4a) :

- Spin-down : nothing happens, the system is in its ground state.
- Spin-up : the system is in a spin excited state and transitions to the ground state by (1) the tunneling of the spin-up electron to the reservoir and (2) loading of a spin-down electron in the quantum dot (the ground state).

These tunneling events allow a spin-to-charge conversion as the change in the charge occupation can be detected using a sensing dot as shown in Fig. 2.4a.

The fidelity of this readout method depends on:

- The electron temperature of the reservoir with respect to the Zeeman energy of the qubit. An increase in electron temperature broadens the reservoir (Fermi Dirac distribution) causing an increase in 'false' tunneling events. To minimize this error, qubits can be operated at relatively 'high' energies, e.g. 20GHz ($82\mu eV$). This energy scale is limited by the availability of reasonably priced microwave instruments/components at higher frequencies.
- The tunnel rate ($\Gamma_{in}, \Gamma_{out}$) has to be chosen carefully, as performing the readout at a slow rate (Hz/kHz) can cause the qubit to relax to its ground state (T_1 effect). Fast tunnel rates (MHz/GHz) can cause limitations as the tunnel events in the readout signal might be hard to resolve due to a limited signal to noise ratio or limited measurement bandwidth (typ. 500kHz-1MHz).

Pauli Spin blockade is based on the Pauli Exclusion principle, i.e. two fermions cannot have the same quantum number. A spin blockade experiment is carried out by pulsing from the (1,1) region into the (2,0) region as shown in Fig. 2.4b. As two electrons with the same quantum state cannot be in the same location, the spins can only be transferred into the (2,0) state if they are in a singlet state²⁰.

The energy levels involved in the readout are shown in Fig. 2.4c. When pulsing into the readout window, the $|\uparrow, \downarrow\rangle$ state is transferred into the $|S, 0\rangle$ state, while the other states stay into the (1,1) charge occupation. In short, this spin to charge conversion allows to differentiate between the $|\uparrow, \downarrow\rangle$ and $(|\downarrow, \uparrow\rangle; |\downarrow, \downarrow\rangle; |\uparrow, \uparrow\rangle)$ states and is called **Singlet/Triplet** readout²¹.

When Δf is large (> few MHz), there is a strong relaxation process [33] which causes the $|\uparrow, \downarrow\rangle$ to relax to the $|S, 0\rangle$ state. We can now differentiate between even ($|\downarrow, \downarrow\rangle; |\uparrow, \uparrow\rangle$) and uneven states ($|\downarrow, \uparrow\rangle; |\uparrow, \downarrow\rangle$), as such, this readout is called **parity** readout.

The fidelity of the spin blockade readout depends on several factors, and some of the most important ones are listed below, with further more details in chapter 5:

²⁰When pulsing deeper in to the (2,0) region, all spin combinations are able to tunnel in, as the electron can be loaded in an excited orbital/valley state (see Fig. 2.4c).

²¹as it is historically used to readout Singlet Triplet qubits.

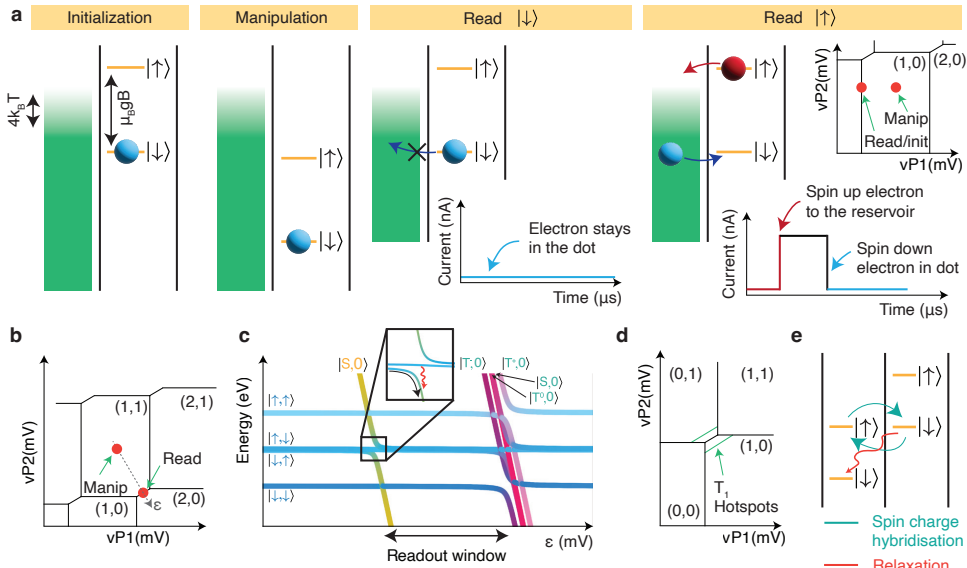


Figure 2.4: Initialization and readout in quantum dots | a, Experimental sequence for an Elzerman readout experiment. The green bars are an indicator for the density of electrons of the reservoir. On the right of each bar, the chemical potential of the $|\downarrow\rangle$ ($\mu_{QD,|\downarrow\rangle}$) and $|\uparrow\rangle$ ($\mu_{QD,|\uparrow\rangle}$) state is shown. Each panel shows the alignment of the chemical potential during a specific part of the experiment. The last two panels show the state of the system just after the qubit collapsed into the down or up state. The current measurements show the difference in the expected readout signal for a spin-down/up electron. The charge stability diagram in the rightmost panel indicates the voltages used for the initialization, manipulation and readout. **b,** Charge stability diagram showing the manipulation and readout points used for Pauli spin blockade readout. The detuning (ϵ) axis is shown by the dashed gray line. **c,** Energy level diagram at the (1,1) - (2,0) anti-crossing, where spin blockade readout occurs. The inset shows a detailed view of the first anticrossing. The black arrow indicates the adiabatic passage from the $|\downarrow,\uparrow\rangle$ state to the $|S,0\rangle$ state. The red arrow shows the relaxation pathway that enables parity readout. The readout window indicates the detuning range used to perform readout. The size of this range is equivalent to the Singlet/Triplet energy ($\approx \epsilon_v$). **d,** Charge stability diagram indicating the location of the T_1 hotspots, which can be used to initialize a qubit. **e,** Schematic explaining the mechanism of the T_1 hotspot. The green arrow indicates spin-orbital hybridization, caused by the tunnel coupling between both electrons. The red arrow is used to indicate the relaxation path to the ground state.

- The adiabatic passage to the $|S,0\rangle$ state; the spin needs to change basis from $|\downarrow,\uparrow\rangle$ to the $|S,0\rangle$ state. We need to be adiabatic with respect to spin and charge, which can be done by optimizing the tunnel coupling (t_{ij}) and the ramp rate towards the readout location. In silicon spin qubits, the couplings of the $|S,0\rangle$ to the $(|\downarrow,\downarrow\rangle; |\uparrow,\uparrow\rangle)$ states is relatively low and can often be neglected²².
- Assuming a long T_1 time at the readout location, an arbitrarily high signal to noise ratio (SNR) can be obtained by averaging longer. When the readout is limited by decoherence, it is possible to increase the relaxation time by decreasing the barrier voltages at the readout stage (lock the electron positions). When a reservoir is available, it is also possible to apply a latched version of spin blockade readout which can increase both the relaxation time and the SNR [12].

A relaxation **Hotspot** can be used to quickly relax a qubit into its ground state ($|\downarrow\rangle$). This is accomplished by waiting at a 'hotspot' : a point in the charge stability diagram where the T_1 time is short (e.g. Fig. 2.4d). The T_1 time can reduce significantly when the spin is hybridized with orbital or valley states. An example is shown in Fig. 2.4e, where one electron is shared between two quantum dots (left : $|L\rangle$ and right : $|R\rangle$). When pulsing from the left quantum dot toward the hotspot, the $|L,\uparrow\rangle$ and $|R,\downarrow\rangle$ state hybridizes²³ into $\frac{1}{\sqrt{2}}(|L,\uparrow\rangle \pm |R,\downarrow\rangle)$ as shown in Fig. 2.4e. The $|R,\downarrow\rangle$ state relaxes quickly into $|L,\downarrow\rangle$ state, as no spin flip is required. Experimental details are available in chapter 3.

A **quantum nondemolition (QND) measurement** is in this case not a fundamental measurement type like Elzerman readout or Pauli spin blockade, rather it is a protocol that can be used to perform a non-destructive readout and/or to enhance the readout fidelity [41, 25]. For a single QND measurement, one would start with a system in the state $|\psi\rangle = |\downarrow\rangle_A \otimes (\alpha|\downarrow\rangle_M + \beta|\uparrow\rangle_M)$, where A is the ancilla qubit and M, the qubit under measurement. Next, a CNOT gate is executed which correlates the state of qubit M with qubit A ($|\psi\rangle = \alpha|\downarrow,\downarrow\rangle + \beta|\uparrow,\uparrow\rangle$). When the ancilla qubit is measured, qubit M will collapse into the same state as the ancilla qubit. Qubit M can still be used for calculations as this measurement is not destructive (unlike with Elzerman/parity readout).

The readout fidelity of qubit M can be increased by performing several sequential QND measurements on qubit M and performing a majority vote at the end of measurements. For each cycle the ancilla qubit is measured and reinitialized.

²²This is not the case for Ge qubits, where special care needs to be taken to prevent this transition from happening [14].

²³Assuming there is a tunnel coupling between these states.

BIBLIOGRAPHY

- [1] *Band structure and carrier concentration of silicon (SI)*. URL: <http://www.ioffe.ru/SVA/NSM/Semicond/Si/bandstr.html>.
- [2] F. Borjans, D. Zajac, T. Hazard, and J. Petta. “Single-spin relaxation in a synthetic spin-orbit field”. *Physical Review Applied* 11.4 (2019), p. 044063.
- [3] G. Burkard, T. D. Ladd, J. M. Nichol, A. Pan, and J. R. Petta. “Semiconductor Spin Qubits”. *arXiv preprint arXiv:2112.08863* (2021).
- [4] E. J. Connors, J. Nelson, L. F. Edge, and J. M. Nichol. “Charge-noise spectroscopy of Si/SiGe quantum dots via dynamically-decoupled exchange oscillations”. *Nature Communications* 13.1 (2022), pp. 1–9.
- [5] D. Degli Esposti, B. Paquelet Wuetz, V. Fezzi, M. Lodari, A. Sammak, and G. Scappucci. “Wafer-scale low-disorder 2DEG in 28Si/SiGe without an epitaxial Si cap”. *Applied Physics Letters* 120.18 (2022), p. 184003.
- [6] J. P. Dehollain, J. Pla, E. Siew, K. Tan, A. Dzurak, and A. Morello. “Nanoscale broadband transmission lines for spin qubit control”. *Nanotechnology* 24.1 (2012), p. 015202.
- [7] J. M. Elzerman, R. Hanson, L. Willems van Beveren, B. Witkamp, L. Vandersypen, and L. P. Kouwenhoven. “Single-shot read-out of an individual electron spin in a quantum dot”. *nature* 430.6998 (2004), pp. 431–435.
- [8] E. Farhi, J. Goldstone, S. Gutmann, and M. Sipser. “Quantum computation by adiabatic evolution”. *arXiv preprint quant-ph/0001106* (2000).
- [9] M. Friesen, S. Chutia, C. Tahan, and S. N. Coppersmith. “Valley splitting theory of Si Ge/ Si/ Si Ge quantum wells”. *Physical Review B* 75.11 (2007), p. 115318.
- [10] I. Hansen, A. E. Seedhouse, A. Saraiva, A. Laucht, A. S. Dzurak, and C. H. Yang. “The SMART protocol–Pulse engineering of a global field for robust and universal quantum computation”. *arXiv preprint arXiv:2108.00776* (2021).
- [11] R. Hanson, L. P. Kouwenhoven, J. R. Petta, S. Tarucha, and L. M. Vandersypen. “Spins in few-electron quantum dots”. *Reviews of modern physics* 79.4 (2007), p. 1217.
- [12] P. Harvey-Collard *et al.* “High-fidelity single-shot readout for a spin qubit via an enhanced latching mechanism”. *Physical Review X* 8.2 (2018), p. 021046.
- [13] I. Heinz and G. Burkard. “Crosstalk analysis for single-qubit and two-qubit gates in spin qubit arrays”. *Physical Review B* 104.4 (2021), p. 045420.
- [14] N. W. Hendrickx, W. I. Lawrie, M. Russ, F. van Riggelen, S. L. de Snoo, R. N. Schouten, A. Sammak, G. Scappucci, and M. Veldhorst. “A four-qubit germanium quantum processor”. *Nature* 591.7851 (2021), pp. 580–585.

- [15] E. Kawakami *et al.* “Electrical control of a long-lived spin qubit in a Si/SiGe quantum dot”. *Nature nanotechnology* 9.9 (2014), pp. 666–670.
- [16] J. Knörzer, C. J. van Diepen, T.-K. Hsiao, G. Giedke, U. Mukhopadhyay, C. Reichl, W. Wegscheider, J. I. Cirac, and L. M. Vandersypen. “Long-range electron-electron interactions in quantum dot systems and applications in quantum chemistry”. *arXiv preprint arXiv:2202.06756* (2022).
- [17] W. I. L. Lawrie *et al.* “Quantum dot arrays in silicon and germanium”. *Applied Physics Letters* 116.8 (2020), p. 080501.
- [18] D. Loss and D. P. DiVincenzo. “Quantum computation with quantum dots”. *Physical Review A* 57.1 (1998), p. 120.
- [19] F. Martins, F. K. Malinowski, P. D. Nissen, E. Barnes, S. Fallahi, G. C. Gardner, M. J. Manfra, C. M. Marcus, and F. Kuemmeth. “Noise suppression using symmetric exchange gates in spin qubits”. *Physical review letters* 116.11 (2016), p. 116801.
- [20] T. McJunkin *et al.* “Valley splittings in Si/SiGe quantum dots with a germanium spike in the silicon well”. *Physical Review B* 104.8 (2021), p. 085406.
- [21] T. Meunier, V. E. Calado, and L. M. K. Vandersypen. “Efficient controlled-phase gate for single-spin qubits in quantum dots”. *Physical Review B* 83.12 (2011), p. 121403.
- [22] A. R. Mills, C. Guinn, M. Gullans, A. Sigillito, M. Feldman, E. Nielsen, and J. Petta. “Two-qubit silicon quantum processor with operation fidelity exceeding 99%”. *arXiv preprint arXiv:2111.11937* (2021).
- [23] A. R. Mills, D. Zajac, M. Gullans, F. Schupp, T. Hazard, and J. Petta. “Shuttling a single charge across a one-dimensional array of silicon quantum dots”. *Nature communications* 10.1 (2019), pp. 1–6.
- [24] F. Motzoi, J. M. Gambetta, P. Rebentrost, and F. K. Wilhelm. “Simple pulses for elimination of leakage in weakly nonlinear qubits”. *Physical review letters* 103.11 (2009), p. 110501.
- [25] T. Nakajima *et al.* “Quantum non-demolition measurement of an electron spin qubit”. *Nature nanotechnology* 14.6 (2019), pp. 555–560.
- [26] S. F. Neyens *et al.* “The critical role of substrate disorder in valley splitting in Si quantum wells”. *Applied Physics Letters* 112.24 (2018), p. 243107.
- [27] M. A. Nielsen and I. Chuang. *Quantum computation and quantum information*. 2002.
- [28] A. Noiri, K. Takeda, T. Nakajima, T. Kobayashi, A. Sammak, G. Scappucci, and S. Tarucha. “Fast universal quantum gate above the fault-tolerance threshold in silicon”. *Nature* 601.7893 (2022), pp. 338–342.
- [29] K. Ono, D. Austing, Y. Tokura, and S. Tarucha. “Current rectification by Pauli exclusion in a weakly coupled double quantum dot system”. *Science* 297.5585 (2002), pp. 1313–1317.
- [30] L. Petit *et al.* “Spin lifetime and charge noise in hot silicon quantum dot qubits”. *Physical review letters* 121.7 (2018), p. 076801.

- [31] M. Pioro-Ladrière, T. Obata, Y. Tokura, Y.-S. Shin, T. Kubo, K. Yoshida, T. Taniyama, and S. Tarucha. “Electrically driven single-electron spin resonance in a slanting Zeeman field”. *Nature Physics* 4.10 (2008), pp. 776–779.
- [32] J. J. Sakurai and E. D. Commins. *Modern quantum mechanics, revised edition*. 1995.
- [33] A. E. Seedhouse *et al.* “Pauli blockade in silicon quantum dots with spin-orbit control”. *PRX Quantum* 2.1 (2021), p. 010303.
- [34] A. J. Sigillito, M. Gullans, L. Edge, M. Borselli, and J. Petta. “Coherent transfer of quantum information in a silicon double quantum dot using resonant SWAP gates”. *npj Quantum Information* 5.1 (2019), pp. 1–7.
- [35] D. A. Steck. “Quantum and atom optics” (2007).
- [36] E. Vahapoglu *et al.* “Coherent control of electron spin qubits in silicon using a global field”. *npj Quantum Information* 8.1 (2022), pp. 1–6.
- [37] C. J. Van Diepen, P. T. Eendebak, B. T. Buijtendorp, U. Mukhopadhyay, T. Fujita, C. Reichl, W. Wegscheider, and L. M. Vandersypen. “Automated tuning of inter-dot tunnel coupling in double quantum dots”. *Applied Physics Letters* 113.3 (2018), p. 033101.
- [38] M. Veldhorst *et al.* “An addressable quantum dot qubit with fault-tolerant control-fidelity”. *Nature nanotechnology* 9.12 (2014), pp. 981–985.
- [39] C. Volk *et al.* “Loading a quantum-dot based “Qubyte” register”. *npj Quantum Information* 5.1 (2019), pp. 1–8.
- [40] X. Xue, M. Russ, N. Samkharadze, B. Undseth, A. Sammak, G. Scappucci, and L. M. Vandersypen. “Quantum logic with spin qubits crossing the surface code threshold”. *Nature* 601.7893 (2022), pp. 343–347.
- [41] X. Xue *et al.* “Repetitive quantum nondemolition measurement and soft decoding of a silicon spin qubit”. *Physical Review X* 10.2 (2020), p. 021006.
- [42] S. Yang, X. Wang, and S. D. Sarma. “Generic Hubbard model description of semiconductor quantum-dot spin qubits”. *Physical Review B* 83.16 (2011), p. 161301.
- [43] J. Yoneda *et al.* “A quantum-dot spin qubit with coherence limited by charge noise and fidelity higher than 99.9%”. *Nature nanotechnology* 13.2 (2018), pp. 102–106.
- [44] D. M. Zajac, T. Hazard, X. Mi, E. Nielsen, and J. R. Petta. “Scalable gate architecture for a one-dimensional array of semiconductor spin qubits”. *Physical Review Applied* 6.5 (2016), p. 054013.
- [45] F. A. Zwanenburg, A. S. Dzurak, A. Morello, M. Y. Simmons, L. C. Hollenberg, G. Klimeck, S. Rogge, S. N. Coppersmith, and M. A. Eriksson. “Silicon quantum electronics”. *Reviews of modern physics* 85.3 (2013), p. 961.
- [46] A. M. J. Zwerver *et al.* “Qubits made by advanced semiconductor manufacturing”. *arXiv preprint arXiv:2101.12650* (2021).

3

A PROGRAMMABLE TWO-QUBIT QUANTUM PROCESSOR IN SILICON

Now that it is possible to achieve measurement and control fidelities for individual quantum bits (qubits) above the threshold for fault tolerance, attention is moving towards the difficult task of scaling up the number of physical qubits to the large numbers that are needed for fault-tolerant quantum computing [1, 4]. In this context, quantum-dot-based spin qubits could have substantial advantages over other types of qubit owing to their potential for all-electrical operation and ability to be integrated at high density onto an industrial platform [19, 21, 32]. Initialization, readout and single- and two-qubit gates have been demonstrated in various quantum-dot-based qubit representations [29, 17, 35, 22]. However, as seen with small-scale demonstrations of quantum computers using other types of qubit [34, 7, 12, 28], combining these elements leads to challenges related to qubit crosstalk, state leakage, calibration and control hardware. Here we overcome these challenges by using carefully designed control techniques to demonstrate a programmable two-qubit quantum processor in a silicon device that can perform the Deutsch–Jozsa algorithm and the Grover search algorithm—canonical examples of quantum algorithms that outperform their classical analogues. We characterize the entanglement in our processor by using quantum-state tomography of Bell states, measuring state fidelities of 85–89 percent and concurrences of 73–82 percent. These results pave the way for larger-scale quantum computers that use spins confined to quantum dots.

This work was originally published as :

T. F. Watson, S. G. J. Philips, E. Kawakami, D. R. Ward, P. Scarlino, M. Veldhorst, D. E. Savage, M. G. Lagally, Mark Friesen, S. N. Coppersmith, M. A. Eriksson and L. M. K. Vandersypen, A programmable two-qubit quantum processor in silicon. *Nature* 555, 633–637 (2018).

3.1. INTRODUCTION

Solid-state approaches to quantum computing are challenging to realise due to unwanted interactions between the qubit and the host material. For quantum dot based qubits, charge and nuclear spin noise are the dominant sources of decoherence and gate errors. While some of these effects can be cancelled out by using dynamical decoupling [2] or decoherence-free subspaces [25, 22], there has also been significant progress in reducing these noise sources through growing better oxides and heterostructures [40] and moving to silicon (Si) due to its naturally low abundance of nuclear spin isotopes which can be removed through isotopic purification [31]. These material developments have dramatically extended qubit coherence times enabling single-qubit gate fidelities above 99% [36, 24, 16, 38] and recently resulted in the demonstration of a controlled phase (CZ) gate between two single electron spin qubits in a silicon metal-oxide-semiconductor (Si-MOS) device [35]. Here, we show that with two single electron spin qubits in a natural silicon/silicon-germanium (Si/SiGe) double quantum dot (DQD), we can combine initialisation, readout, single- and two-qubit gates to form a programmable quantum processor in silicon that can perform simple quantum algorithms.

3.2. SINGLE AND TWO-QUBIT GATE IMPLEMENTATION

A schematic of the two-qubit quantum processor is shown in Fig. 3.1(a). The device is similar to that described in [15] except for an additional micromagnet. A two-dimensional electron gas (2DEG) is formed in the natural Si quantum well of a SiGe heterostructure using two accumulation gates. The DQD is defined in the 2DEG by applying negative voltages to the depletion gates with the estimated position of the first (D1) and second (D2) quantum dot shown by the purple and orange circle, respectively. The two qubits, Q1 and Q2, are defined by applying a finite magnetic field of $B_{ext} = 617$ mT and using the Zeeman-split spin-down $|0\rangle$ and spin-up $|1\rangle$ states of single electrons respectively confined in D1 and D2. The initialisation and readout of Q2 is performed by spin-selective tunnelling to a reservoir [8] while Q1 is initialised at a spin relaxation hotspot [30] and measured via Q2 using a controlled rotation (CROT). The complete measurement sequence and setup are described in Fig. 3.4, 3.5 where we achieve initialisation and readout fidelities of $F_{I1} > 99\%$, $F_{I2} > 99\%$, $F_{m1} = 73\%$, and $F_{m2} = 81\%$ (see methods).

The coherent individual control of both qubits is achieved by patterning three cobalt micromagnets on top of the device (see Fig. 3.1(a)). These micromagnets provide a magnetic field gradient with a component that is perpendicular to the external magnetic field for electric dipole spin resonance (EDSR) [26]. Furthermore, the field gradient across the two dots results in qubit frequencies that are well separated ($f_{Q1} = 18.4$ GHz, $f_{Q2} = 19.7$ GHz), allowing the qubits to be addressed independently. For both qubits, we achieve Rabi frequencies of $f_R = \omega_R/2\pi = 2$ MHz and perform single qubit X and Y gates by using vector modulation of the microwave (MW) drive signals. Here, we define an X (Y) gate to be a $\pi/2$ rotation around \hat{x} (\hat{y}) and henceforth define a π rotation to be X^2 (Y^2). We measure the qubit properties of Q1 (Q2) in the (1,1) regime (where (m, n) denotes a configuration with m electrons in D1 and n electrons in D2) to be $T_1 > 50$ ms (3.7 ± 0.5 ms), $T_2^* = 1.0 \pm 0.1$ μ s (0.6 ± 0.1 μ s), $T_{2Hahn} = 19 \pm 3$ μ s (7 ± 1 μ s) (see Fig. 3.6).

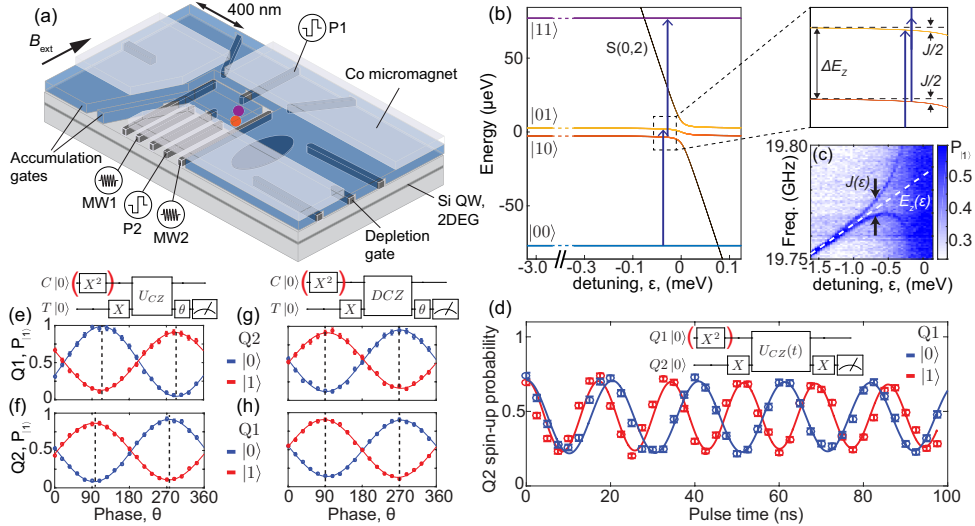


Figure 3.1: Two-qubit quantum processor in silicon. (a) Schematic of a Si/SiGe double quantum dot device showing the estimated position of quantum dots D1 (purple circle) and D2 (orange circle) used to confine two electron spin qubits Q1 and Q2, respectively. Both quantum dots were formed on the right side of the device to achieve an interdot tunnel coupling suitable for two-qubit gates. The position of the dots was realised through the tuning of the numerous electrostatic gates but was most likely helped by disorder in the Si/SiGe heterostructure. The ellipse shows the position of the QD sensor used for spin readout. Microwave signals MW1 and MW2 are used to perform EDSR on Q1 and Q2, respectively, while voltage pulses are applied to plunger gates P1 and P2 for qubit manipulation and readout. (b) Energy level diagram of two electron spins in a double quantum dot as a function of the detuning energy, ϵ , between the $|11\rangle$ and $|02\rangle$ charge states. (c) Microwave spectroscopy of Q2 versus detuning energy after initialisation of Q1 to $(|0\rangle + |1\rangle)/\sqrt{2}$. The detuning voltage was converted to energy using a lever arm of $\alpha = 0.09e$ (see Fig. 3.8). The map shows that Q2 has two different resonant frequencies (blue arrows in (b)) depending on the spin state of Q1, which are separated by the exchange energy, J . (d) The spin-up probability of Q2 as a function of the detuning pulse duration in a Ramsey sequence with the control Q1 initialised to spin-down (blue curve) and spin-up (red curve). (e-f) Calibration of the \hat{z} rotations on Q1 and Q2 needed to form the CZ_{ij} gates are performed by using a Ramsey sequence and varying the phase of the last $\pi/2$ pulse. Here the spin-up probability has been normalised to remove initialisation and readout errors and the exchange energy is $J/h = 10$ MHz. (g,h) A decoupled version of the CZ gate removes the unconditional \hat{z} rotations due to the detuning dependence on $E_Z(\epsilon)$. Consequently, the required \hat{z} rotations to form the CZ_{ij} gates (dashed black lines) are always at 90° and 270° , simplifying calibration. All error bars are 1σ from the mean calculated from a Monte Carlo estimation (see methods).

Using single qubit randomised benchmarking [18, 16] we find an average Clifford gate fidelity of 98.8% for Q1 and 98.0% for Q2 (see Fig. 3.7) which are close to the fault tolerant error threshold for surface codes [9].

3

Universal quantum computing requires the implementation of both single- and two-qubit gates. In this quantum processor we implement a two-qubit controlled-phase (CZ) gate [23, 35]. This gate can be understood by considering the energy level diagram for two electron spins in a double quantum dot, shown in Fig. 3.1(b), in the regime where the Zeeman energy difference is comparable to the interdot tunnel coupling, $\delta E_Z \sim t_c$. The energies of the two-spin states ($|00\rangle$, $|01\rangle$, $|10\rangle$, $|11\rangle$) in the (1,1) charge regime and the singlet ground state in the (0,2) charge regime are plotted as a function of the detuning, ϵ . Here, detuning describes the energy difference between the (1,1) and (0,2) charge states of the DQD, controlled with the voltage applied to gate P1 (see Fig. 3.5). The anti-crossing between the S(0,2) and the antiparallel $|01\rangle$ and $|10\rangle$ states causes the energy of the antiparallel states to decrease by $J(\epsilon)/2$ as the detuning is decreased (see Fig. 3.1(b)), where $J(\epsilon)$ is the exchange coupling between the two electron spins.

The energy structure of the two-electron system can be probed by performing MW spectroscopy as a function of detuning as shown in Fig. 3.1(c). At negative detuning, the resonance frequency (Zeeman energy) increases linearly (dashed line) due to the electron wavefunction moving in the magnetic field gradient. At more positive detuning closer to the (0,2) regime, the exchange energy is significant compared to the linewidth of the resonance $J/h > \omega_R$, resulting in two clear resonances. Applying a π pulse at one of these frequencies results in a CROT gate which is used to perform the projective measurement of Q1 via the readout of Q2 (see Fig. 3.9).

The CZ gate is implemented by applying a detuning pulse for a fixed amount of time, t , which shifts the energy of the antiparallel states. Throughout the pulse, we stay in the regime where $J(\epsilon) \ll \Delta E_z$, so the energy eigenstates of the system are still the two-spin product states and the two-qubit interaction can be approximated by an Ising Hamiltonian, leading to the following unitary operation,

$$U_{CZ}(t) = Z_1(\theta_1) Z_2(\theta_2) \begin{pmatrix} 1 & 0 & 0 & 0 \\ 0 & e^{iJ(\epsilon)t/2\hbar} & 0 & 0 \\ 0 & 0 & e^{iJ(\epsilon)t/2\hbar} & 0 \\ 0 & 0 & 0 & 1 \end{pmatrix}, \quad (3.1)$$

where the basis states are $|00\rangle$, $|01\rangle$, $|10\rangle$, and, $|11\rangle$, and $Z_1(\theta_1)$ and $Z_2(\theta_2)$ are rotations around \hat{z} caused by the change in the Zeeman energy of the qubits due to the magnetic field gradient. The CZ gate is advantageous over the CROT as it is faster and less time is spent at low detuning, where the qubits are more sensitive to charge noise. In addition, we observed that performing the CROT with EDSR can lead to state leakage into the S(0,2) state, seen in Fig. 3.1(c) by the increase in background dark counts near $\epsilon = 0$. The CZ gate is demonstrated in Fig. 3.1(d); the duration of a CZ voltage pulse between two X gates on Q2 in a Ramsey experiment is varied, showing that the frequency of the \hat{z} rotation on Q2 is conditional on the spin state of Q1. The processor's primitive two-

qubit gates, $CZ_{ij}|m,n\rangle = (-1)^{\delta(i,m)\delta(j,n)}|m,n\rangle$ for $i, j, m, n \in \{0, 1\}$, are constructed by applying the CZ gate for a time $t = \pi\hbar/J$ followed by \hat{z} rotations on Q1 and Q2, $CZ_{ij} = Z_1((-1)^j\pi/2 - \theta_1)Z_2((-1)^i\pi/2 - \theta_2)U_{CZ}(\pi\hbar/J)$. Rather than physically performing the \hat{z} rotations, we use a software reference frame change where we incorporate the rotation angle θ_1 and θ_2 into the phase of any subsequent MW pulses [34].

3.3. UNIVERSAL CONTROL

Combining single- and two-qubit gates together with initialisation and readout, we demonstrate a programmable processor — where we can program arbitrary sequences for the two-qubit chip to execute within the coherence times of the qubits. To achieve this, a number of challenges needed to be overcome. The device had to be further tuned so that during single-qubit gates the exchange coupling was low, $J_{off}/h = 0.27$ MHz (see Fig. 3.10), compared to our single-qubit gate times (~ 2 MHz) and two-qubit gate times ($\sim 6 - 10$ MHz). Tuning was also required to raise the energy of low-lying valley-excited states to prevent them from being populated during initialisation [15]. Furthermore, we observed that applying MW pulses on Q1 shifts the resonance frequency of Q2 by ~ 2 MHz. We rule out the AC Stark shift, effects from coupling between the spins, and heating effects as possible explanations but find the quantum dot properties affect the frequency shift (see 3.6.1). While the origin of the shift is unknown, we keep the resonance frequency of Q2 fixed during single-qubit gates by applying an off-resonant pulse (30 MHz) to Q1 if Q1 is idle.

Before running sequences on the quantum processor, all gates need to be properly calibrated. The single-qubit X and Y gates were calibrated using both a Ramsey sequence and the AlIXY calibration sequence to determine the qubit resonance frequency and the power needed to perform a $\pi/2$ gate (see 3.6.2). To calibrate the CZ_{ij} gates we performed the Ramsey sequence in Fig. 3.1(e) and varied the phase of the last $\pi/2$ gate. Fig. 3.1(e) shows the results of this measurement where Q1 is the target qubit and the control qubit Q2 is either prepared in $|0\rangle$ (blue curve) or $|1\rangle$ (red curve). The duration of the CZ gate is calibrated so that the blue and red curve are 180° out of phase. These measurements also determine the \hat{z} rotation on Q1 needed to form CZ_{ij} , which corresponds to the phase of the last $\pi/2$ gate which either maximises or minimises the Q2 spin-up probability (dashed lines in Fig. 3.1(e)). The \hat{z} rotation needed for Q2 is calibrated by performing a similar measurement, where the roles of Q1 and Q2 are switched (Fig. 3.1(f)).

The \hat{z} rotations in Eq. 1 can be eliminated by using a decoupled CZ gate $DCZ = U_{CZ}(\pi\hbar/2J)X_1^2X_2^2U_{CZ}(\pi\hbar/2J)$ which incorporates refocusing pulses and can be used to perform $DCZ_{ij} = X_1^2X_2^2CZ_{ij} = Z_1((-1)^j\pi/2)Z_2((-1)^i\pi/2)DCZ$. This is demonstrated in the Ramsey experiment in Fig. 3.1(g,h), where the minimum and maximum spin-up probabilities occur at a phase of either 90° or 270° . In addition to removing the need to calibrate the required \hat{z} rotations, this gate is advantageous as it cancels out the effect of low frequency noise that couples to the spins via $\sigma_Z \otimes I$ and $I \otimes \sigma_Z$ terms during the gate.

After proper calibration, we can characterise entanglement in our quantum processor by preparing Bell states and reconstructing the two-qubit density matrix using quantum state tomography. The quantum circuit for the experiment is shown in Fig. 3.2(a).

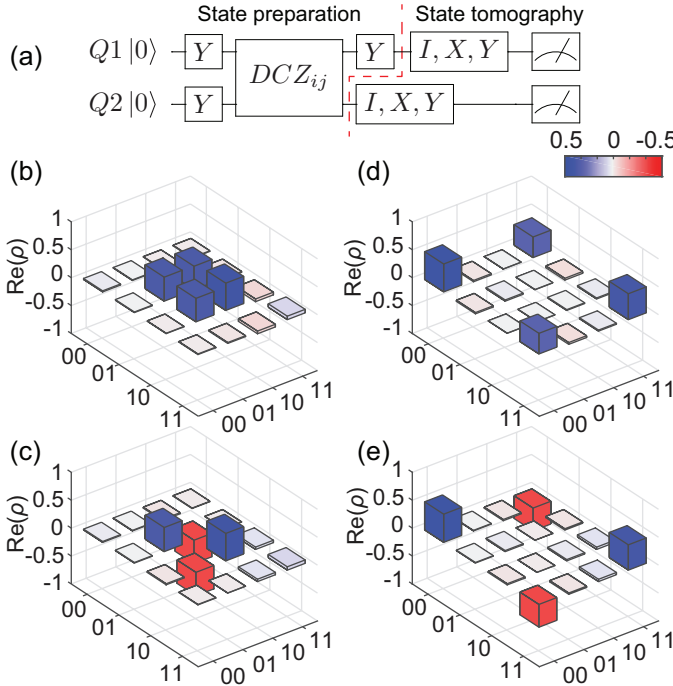


Figure 3.2: Preparation of the Bell states and two-qubit entanglement in silicon. (a) The quantum circuit used to prepare the Bell states and perform quantum state tomography. (b-e) The real component of the reconstructed density matrices using a maximum likelihood estimation for the four Bell states (b) $\Psi^+ = (|01\rangle + |10\rangle)/\sqrt{2}$, (c) $\Psi^- = (|01\rangle - |10\rangle)/\sqrt{2}$, (d) $\Phi^+ = (|00\rangle + |11\rangle)/\sqrt{2}$, (e) $\Phi^- = (|00\rangle - |11\rangle)/\sqrt{2}$. The imaginary components of the density matrices are < 0.08 for all elements (see 3.6.3). We measure state fidelities of $F_{\Psi^+} = 0.88 \pm 0.02$, $F_{\Psi^-} = 0.88 \pm 0.02$, $F_{\Phi^+} = 0.85 \pm 0.02$, $F_{\Phi^-} = 0.89 \pm 0.02$ and concurrences of $c_{\Psi^+} = 0.80 \pm 0.03$, $c_{\Psi^-} = 0.82 \pm 0.03$, $c_{\Phi^+} = 0.73 \pm 0.03$, $c_{\Phi^-} = 0.79 \pm 0.03$. All errors are 1σ from the mean.

The Bell states are prepared using a combination of single-qubit gates and the decoupled two-qubit DCZ_{ij} gates. The density matrix is reconstructed by measuring two-spin probabilities for the 9 combinations of 3 different measurement bases (x,y,z) with 10,000 repetitions (see methods). In our readout scheme the states are projected into the z-basis while measurements in the other bases are achieved by performing X and Y pre-rotations. Due to the time needed to perform these measurements (~ 2 hrs) the frequency of the qubits was calibrated after every 100 repetitions. The real components of the reconstructed density matrices of the four Bell states ($1/\sqrt{2}(|00\rangle \pm |11\rangle)$, $1/\sqrt{2}(|01\rangle \pm |10\rangle)$) are shown in Fig. 3.2(b-e). The state fidelities, $F = \langle \psi | \rho | \psi \rangle$, between these density matrices and the target Bell states range between 85-89% and the concurrences range between 73-82%, demonstrating entanglement. A parallel experiment reported a 78% Bell state fidelity [39].

To test the programmability of the two-qubit quantum processor we perform the Deutsch-Josza [5] and the Grover search [11] quantum algorithms. The Deutsch-Josza algorithm determines whether a function is constant ($f_1(0) = f_1(1) = 0$ or $f_2(0) = f_2(1) = 1$) or bal-

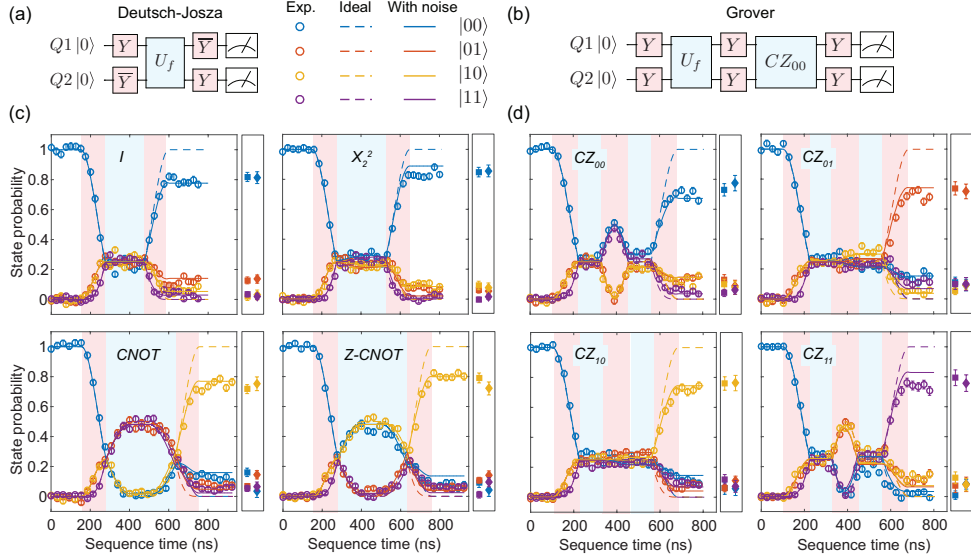


Figure 3.3: Two-qubit quantum algorithms in silicon. (a,b) The quantum circuits for the (a) Deutsch-Josza algorithm and (b) Grover search algorithm for two qubits. (c,d) Two-spin probabilities as a function of time throughout the sequence during the (c) Deutsch-Josza algorithm and the (d) Grover search algorithm for each of four possible functions. Each point corresponds to 4000 repetitions and has been normalised to remove readout errors. The dash lines are the simulated ideal cases while the solid lines are the simulated results where decoherence is introduced by including quasistatic nuclear spin noise and charge noise ($\sigma_c = 11 \mu\text{eV}$). For both algorithms, the square data points show the final results of the algorithms where all four functions are evaluated in the same measurement run with identical calibration. The diamonds show the result of both algorithms when using the decoupled CZ gate showing similar performance. For the Deutsch-Josza algorithm the identity is implemented as either a 200 ns wait (circle and square data points) or as $I = X_1^4 X_2^4$ (diamond data points). All error bars are 1σ from the mean.

anced ($f_3(0) = 0$, $f_3(1) = 1$ or $f_4(0) = 1$, $f_4(1) = 0$). These four functions are mapped onto the following unitary operators, $U_{f1} = I$, $U_{f2} = X_2^2$, $U_{f3} = \text{CNOT} = Y_2 CZ_{11} \bar{Y}_2$, $U_{f4} = Z\text{-CNOT} = \bar{Y}_2 CZ_{00} Y_2$ where the overline denotes a negative rotation. For both the controlled NOT (CNOT) and the zero-controlled NOT (Z-CNOT) the target qubit is Q2. At the end of the sequence the input qubit (Q1) will be either $|0\rangle$ or $|1\rangle$ for the constant and balanced functions, respectively. Grover's search algorithm provides an optimal method for finding the unique input value x_0 of a function $f(x)$ that gives $f(x_0) = 1$ where $f(x) = 0$ for all other values of x . In the two-qubit version of this algorithm there are four input values, $x \in \{00, 01, 10, 11\}$, resulting in four possible functions, $f_{ij}(x)$ where $i, j \in \{0, 1\}$. These functions are mapped onto the unitary operators, $CZ_{ij}|x\rangle = (-1)^{f_{ij}(x)}|x\rangle$, which mark the input state with a negative phase if $f_{ij}(x) = 1$. The algorithm finds the state that has been marked and outputs it at the end of the sequence.

Fig. 3.3 shows the measured two-spin probabilities as a function of time during the algorithms for each function. The experimental results (circles) are in good agreement with the simulated ideal cases (dashed lines). Although a number of repetitions are needed due to gate and readout errors, the algorithms are successful at determining the bal-

anced and constant functions and finding the marked state in the oracle functions. The square data points are taken shortly after calibration and are in line with the circle data points, indicating that calibrations remain stable throughout the hour of data collection for the main panels. The diamond data points show the outcome of the algorithms using the decoupled CZ gate. In most cases, the diamond data points also give similar values to the circles, which means that the decoupled CZ gate does not improve the final result. This suggests that low-frequency single-qubit noise during the CZ gate is not dominant. The substantial difference between Hahn echo and Ramsey decay times still points at significant low-frequency noise. Single-qubit low-frequency noise, whether from nuclear spins or charge noise, reduces single-qubit coherence in particular during wait and idle times in the algorithms. Additionally charge noise affects the coupling strength J during the CZ gates. Numerical simulations (solid lines in Fig. 3.3(c,d) and Fig. 3.13) show that quasi-static nuclear spin noise and charge noise can reproduce most features seen in the two-qubit algorithm data (see Methods). Smaller error contributions include residual coupling during single-qubit operations and miscalibrations.

3.4. CONCLUSION

Significant improvements could be made in the performance of the processor by using isotopically purified ^{28}Si [24, 36, 38], which would increase the qubit coherence times. Furthermore, recent experiments have shown that symmetrically operating an exchange gate by pulsing the tunnel coupling rather than detuning leads to a gate which is less sensitive to charge noise, significantly improving fidelities [27, 20]. With these modest improvements combined with more reproducible and scalable device structures, quantum computers with multiple qubits and fidelities above the fault tolerant threshold should be realisable.

3.5. METHODS

Estimation of initialisation and readout errors for Q1 and Q2.

The initialisation and readout procedures for Q1 and Q2 are described in the Fig. 3.5. The initialisation and readout fidelities of Q2 were extracted by performing the following three experiments and measuring the resulting spin-up probabilities (P_1, P_2, P_3): (i) Initialise Q2 and wait $7T_1$. (ii) Initialise Q2. (iii) Initialise and perform a π rotation on Q2. These three spin-up probabilities are related to the initialisation fidelity (γ_2) and the spin-up and spin-down readout fidelities ($F_{|0\rangle,2}, F_{|1\rangle,2}$) by,

$$P_1 = 1 - F_{|0\rangle,2}, \quad (3.2)$$

$$P_2 = F_{|1\rangle,2}(1 - \gamma_2) + (1 - F_{|0\rangle,2})\gamma_2, \quad (3.3)$$

$$P_3/P_{\pi 2} = F_{|1\rangle,2}(\gamma_2) + (1 - F_{|0\rangle,2})(1 - \gamma_2), \quad (3.4)$$

where $P_{\pi 2}$ is the expected probability to be in the up state after the application of the π pulse for Q2, which is determined as described below. In Eq. 3.4 we assume that waiting $7T_1$ leads to 100% initialisation and the measured spin-up counts are due to

the readout infidelity. By solving these three equations we can extract the initialisation and readout fidelities. For Q1, we performed initialisation by pulsing to a spin relaxation hotspot (see Fig. 3.8) for $500T_1$ and therefore we assume the initialisation fidelity is $\sim 100\%$. Consequently, the readout fidelities of Q1 were extracted by only performing experiments (ii) and (iii) above. The readout and initialisation fidelities for Q1 (Q2) during the state tomography experiments were estimated to be $\gamma_1 > 99\%$ ($\gamma_2 > 99\%$), $F_{|0\rangle,1} = 92\%$ ($F_{|0\rangle,2} = 86\%$), and $F_{|1\rangle,1} = 54\%$ ($F_{|1\rangle,2} = 76\%$) where we used $P_{\pi 1} = 98\%$ ($P_{\pi 2} = 97\%$) based on simulations which include the dephasing time of the qubits (see below). The average measurement fidelity, $F_m = (F_{|0\rangle} + F_{|1\rangle})/2$, for Q1(Q2) is 73% (81%). These fidelities are mostly limited by the finite electron temperature $T_e \approx 130$ mK and the fast spin relaxation time of Q2 ($T_1 = 3.7$ ms), which is most likely caused by a spin relaxation hotspot due to a similar valley splitting and Zeeman energy [37].

Removing readout errors from the measured two-spin probabilities.

In the experiment the measured two-spin probabilities $P^M = (P_{|00\rangle}^M, P_{|01\rangle}^M, P_{|10\rangle}^M, P_{|11\rangle}^M)^T$ include errors due to the limited readout fidelity $F_{|0\rangle,i}$ and $F_{|1\rangle,i}$, of a spin down $|0\rangle$ and spin up $|1\rangle$ electron for qubit i . To remove these readout errors to get the actual two-spin probabilities, $P = (P_{|00\rangle}, P_{|01\rangle}, P_{|10\rangle}, P_{|11\rangle})^T$, we use the following relationship,

$$P^M = (\hat{F}_1 \otimes \hat{F}_2) P \quad (3.5)$$

where,

$$\hat{F}_i = \begin{pmatrix} F_{|0\rangle,i} & 1 - F_{|1\rangle,i} \\ 1 - F_{|0\rangle,i} & F_{|1\rangle,i} \end{pmatrix}. \quad (3.6)$$

State tomography

The density matrix of a two-qubit state can be expressed as $\rho = \sum_{i=1}^{16} c_i M_i$ where M_i are 16 linearly independent measurement operators. The coefficients c_i were calculated from the expectation values, m_i , of the measurement operators using a maximum likelihood estimation [14, 7]. The expectation values were calculated by performing 16 combinations of I, X, Y, X^2 prerotations on Q1 and Q2 and measuring the two-spin probabilities over 10,000 repetitions per measurement. The two-spin probabilities were converted to actual two-spin probabilities by removing readout errors using Eq. 3.6. For the calculation of the density matrices in Fig. 3.2 we only used the data from the I, X, Y prerotations with the assumption that I will give a more accurate estimation of the expectation values than X^2 due to gate infidelities. If we include the X^2 we achieve state fidelities between 80–84% and concurrences between 67–71% (see 3.6.3). In the analysis we assume the prerotations are perfect which is a reasonable approximation due to the high single-qubit Clifford gate fidelities $> 98\%$ compared to the measured state fidelities 85 – 89%. The state tomography experiment was performed in parallel with both the fidelity experiments described above and a Ramsey experiment used to actively calibrate the frequency.

Error analysis.

Error analysis was performed throughout the manuscript using a Monte Carlo method by assuming a multinomial distribution for the measured two-spin probabilities and a binomial distribution for the probabilities (P_1 , P_2 , P_3) used to calculate the fidelities. Values from these distributions were randomly sampled and the procedures from above were followed. This was repeated 250 times to build up a final distributions which we use to determine the mean values and the standard deviation.

3

Simulation of two electron spins in a double quantum dot.

In the simulation, we consider two electrons in two tunnel-coupled quantum dots where an external magnetic field B_0 is applied to both dots. In addition to this field, the two dots have different Zeeman energies due to the magnetic field gradient across the double quantum dot generated by micromagnets. The Zeeman energy of Q1 (Q2) will be denoted as B_1 (B_2). The double dot system is modelled with the following Hamiltonian [3],

$$\hat{H} = \begin{pmatrix} -\beta & 0 & 0 & 0 & 0 & 0 \\ 0 & -\Delta\nu & 0 & 0 & t & t \\ 0 & 0 & \Delta\nu & 0 & -t & -t \\ 0 & 0 & 0 & \beta & 0 & 0 \\ 0 & t & -t & 0 & U_1 + \epsilon & 0 \\ 0 & t & -t & 0 & 0 & U_2 - \epsilon \end{pmatrix}, \quad (3.7)$$

with the following states as the eigenbasis ($|00\rangle$, $|01\rangle$, $|10\rangle$, $|11\rangle$, $S(2,0)$, $S(0,2)$). In this Hamiltonian, $\beta = \frac{B_1+B_2}{2}$, $\Delta\nu = \frac{B_1-B_2}{2}$, $\sqrt{2}t$ is the tunnel coupling between the (1,1) and (0,2)/(2,0) singlet states, and U_i is the on-site charging energy of the i^{th} quantum dot. In order to study the phases of the qubits during control pulses, the Hamiltonian is transformed into a rotating frame using,

$$\tilde{H} = VHV^\dagger + i\hbar(\partial_t V)V^\dagger, \quad (3.8)$$

where $V = e^{-i(B_1(\hat{\sigma}_z \otimes \hat{I}) + B_2(\hat{I} \otimes \hat{\sigma}_z))t}$ is the matrix that describes the unitary transformation where $\hbar = 1$. The transformed Hamiltonian is,

$$\tilde{H} = \begin{pmatrix} 0 & 0 & 0 & 0 & 0 & 0 \\ 0 & 0 & 0 & 0 & te^{i\Delta\nu t} & te^{i\Delta\nu t} \\ 0 & 0 & 0 & 0 & -te^{-i\Delta\nu t} & -te^{-i\Delta\nu t} \\ 0 & 0 & 0 & 0 & 0 & 0 \\ 0 & te^{-i\Delta\nu t} & -te^{i\Delta\nu t} & 0 & U_1 + \epsilon & 0 \\ 0 & te^{-i\Delta\nu t} & -te^{i\Delta\nu t} & 0 & 0 & U_2 - \epsilon \end{pmatrix}. \quad (3.9)$$

To model the single qubit gates during EDSR, we used the following Hamiltonian,

$$\hat{H}_{mw} = \sum_k B_{mw,k} \cos(\omega_k t + \phi_k) [\hat{\sigma}_x \otimes \hat{I} + \hat{I} \otimes \hat{\sigma}_x], \quad (3.10)$$

which assumes the same drive amplitude on each of the qubits. Here, k represents the k^{th} signal with an angular frequency ω_k , phase ϕ_k , and driving amplitude $B_{mw,k}$. This Hamiltonian is transformed into the rotating frame using equation 3.8 and the rotating wave approximation (RWA) can be made to remove the fast driving elements as the Rabi frequency is much smaller than the Larmor precession. This gives the following Hamiltonian,

$$\tilde{H}_{mw} = \sum_k \begin{pmatrix} 0 & \Omega_k e^{i\Delta\omega_1 t} & \Omega_k e^{i\Delta\omega_2 t} & 0 & 0 & 0 \\ \Omega_k^* e^{-i\Delta\omega_1 t} & 0 & 0 & \Omega_k e^{i\Delta\omega_2 t} & 0 & 0 \\ \Omega_k^* e^{-i\Delta\omega_2 t} & 0 & 0 & \Omega_k e^{i\Delta\omega_1 t} & 0 & 0 \\ 0 & \Omega_k^* e^{-i\Delta\omega_2 t} & \Omega_k^* e^{-i\Delta\omega_1 t} & 0 & 0 & 0 \\ 0 & 0 & 0 & 0 & 0 & 0 \\ 0 & 0 & 0 & 0 & 0 & 0 \end{pmatrix}, \quad (3.11)$$

where Ω_k is defined as $B_{MW,k}e^{i\phi_k}$, Ω_k^* is the complex conjugate of Ω , and $\Delta\omega_k$ is defined as $\omega_k - \omega_{qubit_i}$.

The dynamics of the two qubit system can be described by the Schrödinger-von Neumann equation,

$$\rho_{t+\Delta t} = e^{\frac{-i\tilde{H}t}{\hbar}} \rho_t e^{\frac{i\tilde{H}t}{\hbar}}, \quad (3.12)$$

which was solved numerically using the Armadillo linear algebra library in C++ where the matrix exponentials were solved using scaling methods ($e^A = \prod^s e^{\frac{A}{2^s}}$) and a Taylor expansion. In the experiments, we apply microwave pulses with square envelopes that have a finite rise time due to the limited bandwidth of the I/Q channels of the MW vector source. For simplicity, we approximate these MW pulses with a perfect square envelope. On the other hand, the detuning pulses were modelled with a finite rise/fall time using a Fermi-Dirac function in order to take (a)diabatic effects into account. The finite rise time was set to 2 ns based on the cut-off frequency of low-pass filter attached to the lines used to pulse the detuning pulses.

Modelling noise in the simulation.

In the model we include three different noise sources. The first two noise sources are from fluctuating nuclear spins in the natural silicon quantum well which generate quasi-static magnetic noise which couples to the qubits via the $Z \otimes I$ and $I \otimes Z$ terms in the Hamiltonian. These fluctuations are treated as two independent noise sources as D1 and D2 are in different locations in the quantum well and will sample the field from different nuclear spins. The third noise source is charge noise which can couple to the qubits via the magnetic field gradient from the micromagnets which we model as magnetic noise on the $Z \otimes I$ and $I \otimes Z$ terms in the Hamiltonian. In addition, charge noise also couples to the spins via the exchange coupling which leads to noise on the $Z \otimes Z$ term in the Hamiltonian.

In our simulations, we treat these noise sources as quasistatic where the noise is static within each cycle and only changes between measurement cycles. This approximation is reasonable because the noise in the system is pink, with low frequencies in the power

spectrum more pronounced [16]. The static noise due to each noise source was modelled by sampling a random value from a Gaussian distribution with a standard deviation, σ , corresponding to the contribution to dephasing of that noise process. After sampling the static noise, the time evolution of the qubits during a gate sequence was calculated. This time evolution was averaged over many repetitions to give the final result where for each repetition new values for the static noise were sampled. In total, for each simulation we performed 5000 repetitions to ensure convergence.

3

In the experiment, single-qubit gates are performed at higher detuning near the center of the (1,1) $\epsilon = -3$ meV where the exchange is low, $J_{off} = 270$ kHz, and a two qubit CZ gate is performed by pulsing to low detuning $\epsilon = -0.7$ meV where the exchange is high, $J_{on} = 6$ MHz. To estimate the relative effect of charge noise on the $Z \otimes I$, $I \otimes Z$, and $Z \otimes Z$ terms at these two detuning points, we use the spectroscopy data of the qubits as a function of detuning energy shown in Fig. 3.11. The four observed resonances correspond to the four transitions shown in Fig. 3.11(c) between the $|00\rangle, |01\rangle, |10\rangle, |11\rangle$ eigenstates. From the fits of this data we can estimate the derivative of the transition energy from state $|i\rangle$ to $|j\rangle$ at a particular detuning, $\frac{dE_{|i\rangle \rightarrow |j\rangle}}{d\epsilon}|_\epsilon$, which is directly proportional to the magnitude of fluctuations in the transition energy under the influence of charge noise. Fixing the energy of the $|00\rangle$ state, from these derivatives we can calculate the relative noise levels on the other energy eigenstates,

$$B(\epsilon) = \begin{pmatrix} 0 \\ \frac{\partial E_{|00\rangle \rightarrow |01\rangle}}{\partial \epsilon}|_\epsilon \\ \frac{\partial E_{|00\rangle \rightarrow |10\rangle}}{\partial \epsilon}|_\epsilon \\ \frac{\partial E_{|00\rangle \rightarrow |01\rangle}}{\partial \epsilon}|_\epsilon + \frac{\partial E_{|01\rangle \rightarrow |11\rangle}}{\partial \epsilon}|_\epsilon \end{pmatrix} \quad (3.13)$$

In the regime where $J \ll \Delta\nu$, the Hamiltonian of the system can be approximated as $H = -B_1(Z \otimes I) - B_2(I \otimes Z) + J(Z \otimes Z) - J/4(I \otimes I)$. The relative noise on B_1 , B_2 , and J can be found by decomposing the four noise levels in Eq. 3.13 in terms of the basis $(-Z \otimes I, -I \otimes Z, Z \otimes Z, -I \otimes I/4)$ by calculating $A^{-1} * B(\epsilon)$ where,

$$A = \begin{pmatrix} -1/2 & -1/2 & 1/4 & -1/4 \\ -1/2 & 1/2 & -1/4 & -1/4 \\ 1/2 & -1/2 & -1/4 & -1/4 \\ 1/2 & 1/2 & 1/4 & -1/4 \end{pmatrix} \quad (3.14)$$

We estimate the relative composition of the noise for (B_1 , B_2 , J) at $\epsilon = -3$ meV to be (0.12, 0.24, 0) and at $\epsilon = -0.7$ meV ($J = 6$ MHz) to be (0.61, 0.23, 0.26). Note that this is a crude approximation since we only take into account voltage noise along the detuning axis, whereas in reality charge noise acts also along other axes. Not included in the simulation are calibration errors. Based on the the AllXY and Ramsey calibration experiments (see 3.6.2), few % miscalibrations are possible.

Estimating charge noise from the decay of the decoupled CZ oscillations.

Dephasing due to charge noise coupling into the double dot system via the exchange energy is measured by varying the duration of the decoupled CZ gate between two $\pi/2$

pulses on Q1 as shown in Fig. 3.12 for $J = 6 \text{ MHz}$. The decoupled CZ gate removes the effect of quasi-static noise on the $Z \otimes I$ and $I \otimes Z$ terms in the Hamiltonian and the decay of the oscillations $T_2 = 1640 \text{ ns}$ is assumed to be due to noise on the $Z \otimes Z$ term. The data is fitted using either a Gaussian (black line) or exponential decay (red line). The exponential decay seems to fit best to the data which suggests that either higher frequency noise plays a role [6] or the origin of the noise is from a few two-level fluctuators [13]. Since the decoupling CZ decay is slower than the not-decoupled CZ decay, there is also a significant quasi-static noise contribution. For simplicity, we only include the quasi-static contribution in our noise model. For Gaussian quasi-static noise with a standard deviation σ_ϵ , the decay time is,

$$1/T_2 = \frac{1}{2} \frac{\partial J}{\partial \epsilon}|_\epsilon \frac{\sigma_\epsilon}{\sqrt{2\hbar}} \quad (3.15)$$

The factor of $\frac{1}{2}$ is needed as it is the noise on $J/2$ which contributes to the decay. This is because the target qubit precesses with frequency of $J/2$ (ignoring the $I \otimes Z$ and $Z \otimes I$ terms) when the control qubit is in an eigenstate. From the dephasing time and $\frac{\partial J}{\partial \epsilon}|_\epsilon = 1.0 \times 10^{-4}$ extracted from Fig. 3.11(a-b) we can estimate the charge noise on detuning to be $11 \mu\text{eV}$. The data in Fig. 3.12 used to extract this value of charge noise was taken over ~ 40 minutes with no active calibration on the detuning pulse. The time needed for each single-shot measurement was $\sim 10 \text{ ms}$.

Simulations of the two qubit algorithms.

To describe the double dot system used in the experiment, we used the following parameters in the Hamiltonian. The qubit frequencies were chosen to be $B_1 = 18.4 \text{ GHz}$, $B_2 = 19.7 \text{ GHz}$, and the on-site charging energies to be $U_1 = U_2 = 3.5 \text{ meV}$, comparable to the experimental values. The tunnel coupling was chosen to be $t = 210 \text{ MHz}$ so that the residual exchange energy J_{off} was equal to 300 kHz , giving a similar J_{off} as measured in the experiment. The two-qubit gates are implemented by choosing a value of ϵ where $J = 6 \text{ MHz}$, when diagonalizing the Hamiltonian \hat{H} .

The results of the simulations for the Deutsch-Josza algorithm and the Grover algorithm using both the CZ gate and the decoupled CZ gate are shown in Fig. 3.3 and Fig. 3.13. The amplitudes for the three noise sources used in the simulations were identical for all 16 panels. The value of charge noise used was $11 \mu\text{eV}$ (see above) while the nuclear spin noise for Q1 and Q2 was chosen to give the single qubit decoherence times $T_2^* = 1000 \text{ ns}$ and $T_2^* = 600 \text{ ns}$ measured in the Ramsey experiment in the Fig. 3.6. This gave a dephasing time of Q1 (Q2) due to nuclear spin of $T_{2nuc}^* = 1200 \text{ ns}$ (800 ns). The simulations reproduce many of the features found in the experimental data for the algorithms.

By simulating the algorithms, we learn that the residual exchange coupling J_{off} during single-qubit gates has little effect (< 2%) on the result of the algorithms. Furthermore, we find that without noise on the single-qubit terms, it is difficult to get a consistent agreement with the data. Additional noise on the coupling strength improves the agreement. Different from the cases of the Deutsch-Jozsa algorithm and the conventional Grover algorithm, the simulation for the decoupled version of Grover's algorithm predicts a better outcome than the experiment. This case uses the longest sequence of operations,

leaving most room for discrepancies between model and experiment to build up. Those could have a number of origins: (i) the implementation of the static noise model is not accurate enough, (ii) non-static noise plays a role, (iii) the calibration errors in the gates that were left out of the simulation, and (iv) variations in the qubit parameters and noise levels between experiments. Finally, we note that initialisation and readout errors are not taken into account in the simulations. Since initialisation errors are negligible and the data shown was renormalised to remove the effect of readout errors, the simulated and experimental results can be compared directly.

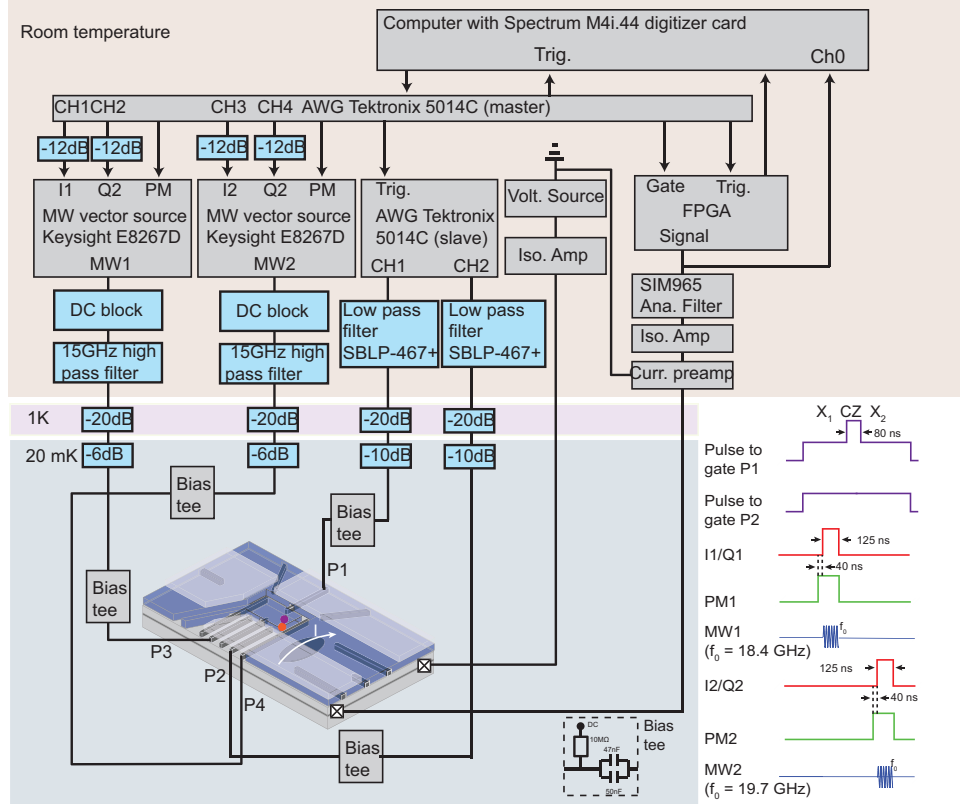


Figure 3.4: Schematic of the measurement setup. The sample was bonded to a printed circuit board (PCB) mounted onto the mixing chamber of a dilution refrigerator. All measurements were performed at the base temperature of the fridge, $T_{base} \sim 20$ mK. DC voltages are applied to all the gate electrodes using room temperature (RT) DACs via filtered lines (not shown). Voltage pulses are applied to plunger gates P1 and P2 using a Tektronix 5014C arbitrary waveform generator (AWG) with 1 GHz clock rate. The signals from the AWG's pass through a RT low-pass filter and attenuators at different stages of the fridge and are added to the DC signals via bias tees mounted on the PCB. Two Keysight E8267D vector microwave sources, MW1 and MW2, are used to apply microwaves (18 – 20 GHz) to perform EDSR on Q1 and Q2, respectively. The signals pass through RT DC blocks, homemade 15 GHz high-pass filters, and attenuators at different stages of the fridge and are added to the DC signals via bias tees mounted on the PCB. The output of the MW source (phase, frequency, amplitude, duration) is controlled with I/Q vector modulation. The I/Q signals are generated with another Tektronix 5014C which is the master device for the entire setup and provides trigger signals for the other devices. In addition to the vector modulation we employ pulse modulation to give an on/off microwave power output ratio of 120 dB. While I/Q modulation can be used to output multiple frequencies, the bandwidth of the AWG was not enough to control both qubits with one microwave source due to their large separation in frequency (1.3 GHz). The sensor current, I , is converted to a voltage signal with a homebuilt preamplifier and an isolation amplifier is used to separate the signal ground with the measurement equipment ground to reduce interference. Following this, a 20 kHz Bessel low-pass filter is applied to the signal using a SIM965 analog filter. An FPGA analyses the voltage signal during the readout and assigns the trace to be spin-up if the voltage falls below a certain threshold. The voltage signal can also be measured with a digitizer card in the computer. The shape of the pulses generated by the AWGs and MW sources during qubit manipulation with the typical timescales is shown in the lower left. Square pulses were used to perform the CZ gate and as the input for the I/Q modulation to generate MW pulses. The pulse modulation was turned on 40 ns before turning on the I/Q signal due to the time needed for the modulation to switch on.

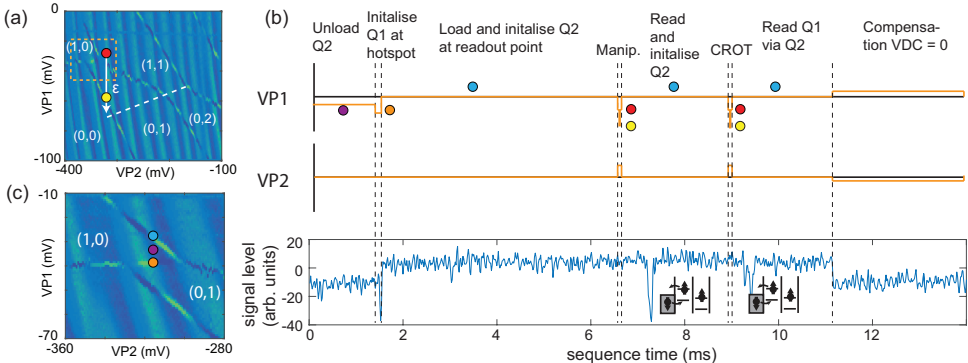


Figure 3.5: Measurement protocol for two electron spins. (a) Stability diagram of the double quantum dot showing the positions in gate space used to perform single qubit gates (red circle) and the two-qubit gates (yellow circle). The white dashed line is the (1,1)-(0,2) inter-dot transition line. The white arrow indicates the detuning axis, ϵ , used in the experiments. Although the detuning pulse for the two-qubit gate crosses the charge addition lines of D1 and D2, the quantum dots remain in the (1,1) charge state as the pulse time is much shorter than the electron tunnel times to the reservoirs. (b) Plot of the voltage pulses applied to plunger gates P1 and P2 and the response of the quantum dot charge sensor over one measurement cycle. Firstly, D2 is unloaded by pulsing into the (1,0) charge region for 1.5 ms (purple circle). The electron on D1 is initialised to spin-down by pulsing to a spin relaxation hotspot at the (1,0) and (0,1) charge degeneracy (orange circle) for 50 μ s (see Fig. 3.8). D2 is loaded with a spin-down electron by pulsing to the readout position for 4 ms (blue circle). During manipulation, the voltages on the plunger gates are pulsed to the red circle for single-qubit gates and to the yellow circle for two qubit gates where the exchange is ~ 6 MHz. After manipulation, the spin of the electron on D2 is measured by pulsing to the readout position (blue circle) for 0.7 ms where the Fermi level of the reservoir is between the spin-up and spin-down electrochemical potentials of D2. If the electron is spin-up it can tunnel out followed by a spin-down electron tunnelling back in. These two tunnel events are detected by the QD sensor as a single blip in the current signal. An additional 1.3 ms is spent at the readout position so that D2 is initialised to spin-down with high fidelity. Following this, Q1 is measured by first performing a CROT at the yellow circle so that $\alpha|00\rangle + \beta|10\rangle \xrightarrow{\text{CROT12}} \alpha|00\rangle + \beta|11\rangle$. A projective measurement of Q1 is then performed by measuring Q2 at the readout position for 0.7 ms (blue circle). Finally, we add a compensation pulse to VP1 and VP2 so that over the measurement cycle $V_{DC} = 0$ to mitigate charging effects in the bias tees. (b) Close-up of the stability diagram in (a) showing the positions in gate-space used for initialisation and readout.

3.6. SUPPLEMENTARY INFORMATION

3.6.1. FREQUENCY SHIFTS ON Q2 DUE TO OFF-RESONANT FREQUENCY PULSES

As discussed in the main manuscript, we observe a large frequency shift on Q2 while applying off-resonant microwaves (MW). Similar effects have been observed for electron spins bound to single donor atoms [10] but with a significantly smaller frequency shift and with transient behaviour occurring over $\sim 100\mu$ s. In our experiment the microwave source MW1 (MW2) applies MWs to gate P3 (P4) to manipulate Q1 (Q2) as shown in Fig. 3.4. Fig. 3.14(a) shows the resonant frequency of Q2 shifting by 2 MHz while off-resonant MWs of 18.5 GHz are applied with MW1 via P3. One possible mechanism to explain this effect is the AC stark shift, where off-resonance MW's will shift the qubit's resonance frequency (ω_L) by $\sim \omega_R^2/2(\omega_1 - \omega_L)$ away from the drive frequency, ω_1 [33]. However, this is a negligible effect and the observed frequency shift is towards the off-resonant MW frequency ruling out the AC-stark shift as a possible cause. We also per-

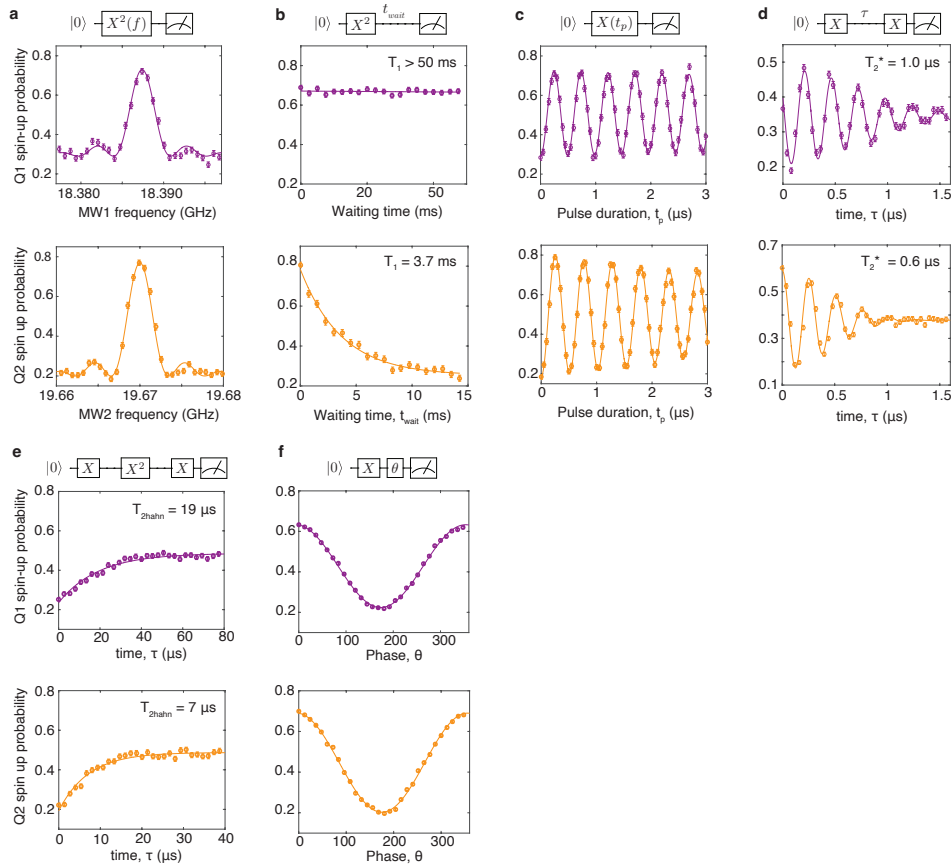


Figure 3.6: Single qubit properties and two-axis control. The purple (top) and orange (bottom) data correspond to measurements performed on Q1 and Q2, respectively, in the (1,1) regime (red circle in Figure 3.5). (a) Spin-up fraction as a function of the MW frequency of an applied π pulse showing a resonant frequency of 18.424 GHz (19.717 GHz) for Q1 (Q2). (b) The spin relaxation time is measured by preparing the qubit to spin-up and varying the wait time before readout. From the exponential decay in the spin-up probability we measure $T_1 > 50$ ms ($T_1 = 3.7 \pm 0.5$ ms) for Q1 (Q2). (c) Spin-up probability as a function of MW duration showing Rabi oscillations of 2.5 MHz for Q1 and Q2. (d) The dephasing time is measured by applying a Ramsey pulse sequence and varying the free evolution time, τ . Oscillations were added artificially to help fit of the decay by making the phase of the last microwave pulse dependent on the free evolution time, $\phi = \sin(\omega\tau)$ where $\omega = 4$ MHz. By fitting the data with a Gaussian decay, $P_{|1\rangle} \propto \exp[-(\tau/T_2^*)^2] \sin(\omega\tau)$, we extract $T_2^* = 1.0 \pm 0.1 \mu$ s ($T_2^* = 0.6 \pm 0.1 \mu$ s) for Q1 (Q2). In the measurement for Q1 the first $\pi/2$ MW pulse is a Y gate. The Ramsey measurement was performed over ~ 20 mins with the frequency calibrated every ~ 1 min. (e) The coherence time of Q1 (Q2) can be extended to $T_{2\text{Hahn}} = 19 \pm 3 \mu$ s ($7 \pm 1 \mu$ s) by a Hahn echo sequence. The coherence time is extracted from an exponential fit to the spin-up probability as a function of the free evolution time in the Hahn echo sequence. (f) Full two axis control is demonstrated by applying two $\pi/2$ pulses and varying the phase of the last $\pi/2$ pulse.

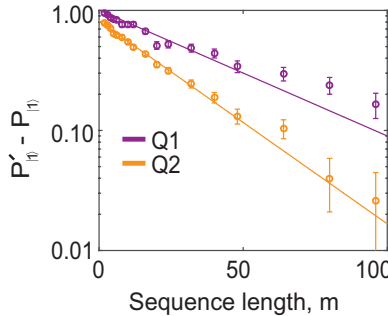
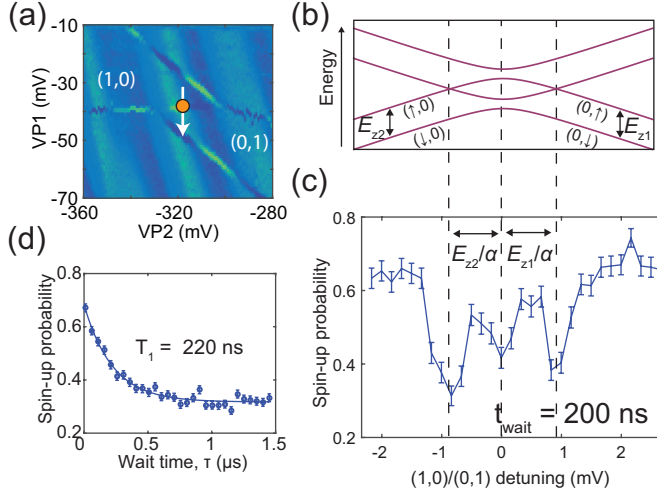


Figure 3.7: Randomised benchmarking of single-qubit gates. Randomised benchmarking of the single qubit gates for each qubit is performed by applying a randomised sequence of a varying number of Clifford gates, m , to either the $|1\rangle$ or $|0\rangle$ state and measuring the final spin-up probability $P'_{|1\rangle}$ or $P_{|1\rangle}$, respectively. All gates in the Clifford group are decomposed into gates from the set $\{I, \pm X, \pm X^2, \pm Y, \pm Y^2\}$. The purple (orange) data points show the difference in the spin-up probabilities $P'_{|1\rangle} - P_{|1\rangle}$ for Q1 (Q2) as a function of sequence length. For each sequence length, m , we average over 32 different randomised sequences. From an exponential fit (solid lines) of the data, $P'_{|1\rangle} - P_{|1\rangle} = ap^m$, we estimate an average Clifford gate fidelity $F_C = 1 - (1-p)/2$ of 98.8% and 98.0% for Q1 and Q2, respectively. The last three data points from both data sets were omitted from the fits as they begin to deviate from a single exponential[16]. All errors are 1σ from the mean.

formed the same experiment in the (0,1) charge regime where we observed similar behaviour (Fig. 3.14(b)) eliminating effects due to the coupling between the two electron spins. Fig. 3.14(c) shows that the resonant frequency also shifts if instead we apply off-resonant MWs using MW2 via P4 demonstrating that this effect does not depend on the gate electrode/coaxial line used to apply the MW's. Interestingly, we do not see the effect on the other qubit as shown in Fig. 3.14(d) where we apply off-resonant microwaves at 18.5 GHz at nearly the maximum output power ($P = 22$ dBm) of the MW2 source suggesting that the effect is due to some property of the quantum dot. The frequency shift is also measured in a Ramsey sequence where during the $\pi/2$ pulse both MW sources are on and during the wait time both MW sources are off. This indicates the frequency shift occurs faster than the Ramsey wait time (<100 ns) ruling out local heating effects which would require time to dissipate. Finally, we observe that the frequency shift is strongly dependent on the power of the off-resonance MW's as shown in Fig. 3.15.

The dependence on the quantum dot properties and power would be compatible with the rectification of the AC signal as an explanation. An asymmetric quantum dot potential will lead to a DC displacement in response to an AC excitation on the gate. We tried to estimate this by measuring the resonance frequency of Q2 as a function of the voltage applied on plunger P3 around the position in gate-space where we perform the single-qubit gates. Over the estimated range of the AC signal, $V_{RMS} \sim 5$ mV for an output power of $P = 16$ dBm and measured attenuation of the coaxial line (~ 43 dB at 20 GHz), we observe a change in frequency of ~ 1 MHz and no measurable non-linearity in the resonance frequency. While this suggests rectification effects are small, it is difficult to get an accurate estimation on the AC signal at the sample and further work is required to rule out this possibility.



3

Figure 3.8: Spin relaxation hotspots used for high fidelity initialisation. (a) Close-up stability diagram of the $(1,0)$ to $(0,1)$ charge transition. The white arrow defines the detuning axis between D1 and D2 controlled with P1. (b) Schematic of the energy level diagram as a function of detuning for one electron spin in a double quantum dot. (c) Spin relaxation hotspots are measured by first preparing the electron on D1 to spin-up using EDSR, applying a voltage pulse along the detuning axis (white arrow in (a)) for a wait time of 200 ns, and performing readout of the electron spin. We observe three dips in the spin-up probability corresponding to spin relaxation hot spots. The first and third hotspot are due to anticrossings between the $(0,\downarrow)$ and $(\uparrow,0)$ states and the $(\downarrow,0)$ and $(0,\uparrow)$ states [30]. The second hotspot occurs at zero detuning. The voltage separation between the first and third hot spot corresponds to the sum of the Zeeman energy of D1 and D2 divided by the gate lever arm α along the detuning axis. Knowing precisely the Zeeman energies from EDSR spectroscopy we can accurately extract the gate lever arm to be $\alpha = 0.09e$. (d) The spin relaxation time at zero detuning (orange circle in (a)) is found to be $T_1 = 220$ ns by measuring the exponential decay of the spin-up probability as a function of wait time, τ , at zero detuning.

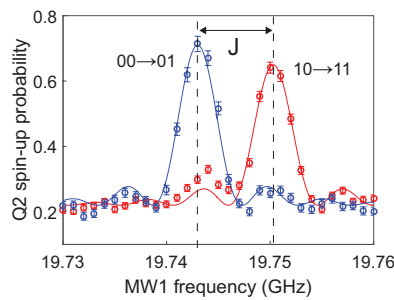


Figure 3.9: Two-qubit controlled rotation (CROT) gate. (a) Microwave spectroscopy of Q2 close to zero detuning between the $(1,1)$ and $(0,2)$ state (yellow dot in Fig. 3.5(a)) where the exchange coupling is on. The blue and red curve show the resonance of Q2 after preparing Q1 into spin-down or up, respectively. The resonance frequency of Q2 shifts by the exchange coupling and by applying a π pulse at one of these frequencies we can perform a CROT, which is equivalent to a CNOT up to a \hat{z} rotation. As discussed in the main text, this CROT gate is used to perform the projective measurement of Q1.

3

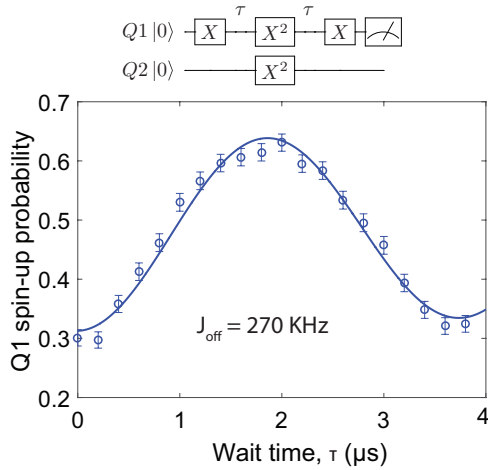


Figure 3.10: Measurement of J_{off} using a decoupling sequence. The exchange coupling J_{off} during single-qubit gates is measured using a two-qubit Hahn echo sequence which cancels out any unconditional \hat{z} rotations during the free evolution time τ . Fitting the spin-up probability as a function of free evolution time τ using the functional form $\sin(2\pi J_{\text{off}}\tau)$, we extract $J_{\text{off}} = 270 \text{ kHz}$.

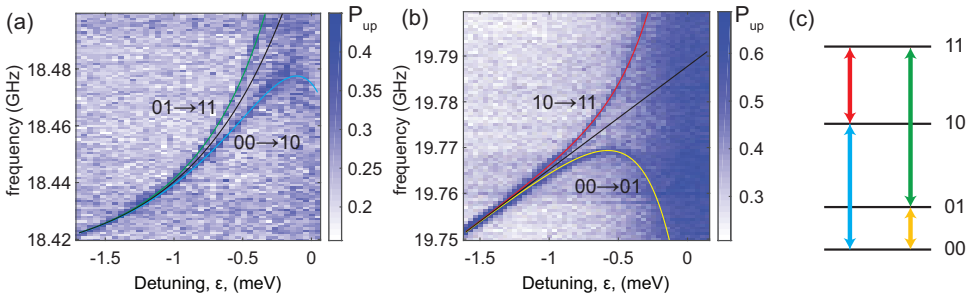


Figure 3.11: Microwave spectroscopy of Q1 and Q2. (a,b) Spectroscopy of (a) Q1 and (b) Q2 versus detuning energy, ϵ , after initialising the other qubit to $(|0\rangle + |1\rangle)/\sqrt{2}$. Towards $\epsilon = 0$ there are two resonances for Q1 (Q2) which are separated by the exchange energy, $J(\epsilon)/\hbar$. As discussed in the manuscript, the Zeeman energy $E_Z(\epsilon)$ of Q1 and Q2 also depends on detuning as changes to the applied voltages will shift the position of the electron in the magnetic field gradient. The four resonance frequencies are fitted (green, blue, red and yellow lines) with $f_{jk} = E_{Zj}(\epsilon) + (-1)^{k+1} J(\epsilon)$ where j denotes the qubit and k denotes the state of the other qubit. The data is fit well using $J(\epsilon) \propto e^{C_1 \epsilon}$, $E_{Z1}(\epsilon) \propto e^{C_2 \epsilon}$, and $E_{Z2}(\epsilon) \propto \epsilon$. The fitted Zeeman energies of Q1 and Q2 are shown by the black lines. We observe that the Zeeman energy of Q1 has an exponential dependence towards the (0,2) charge regime ($\epsilon = 0$) which can be explained by the electron delocalising from D1 towards D2 which has a significantly higher Zeeman energy. (c) Schematic showing the color coded transitions that correspond to the resonances in (a,b).

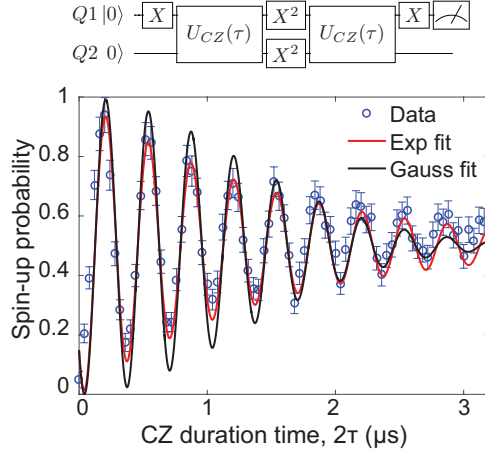


Figure 3.12: Decay of the decoupled CZ oscillations. The normalised spin up probability of Q1 as a function of the total duration time, 2τ , of the two CZ gates in the decoupled CZ sequence. The data is fitted using a sinusoid, $P_{|1\rangle} = 0.5 \sin 2\pi f\tau + 0.5$, with either a Gaussian (black line), $e^{-(2\tau/T_2)^2}$, or exponential (red line), $e^{-2\tau/T_2}$, decay. From these fits we find a decay time of $T_2 = 1.6 \mu\text{s}$.

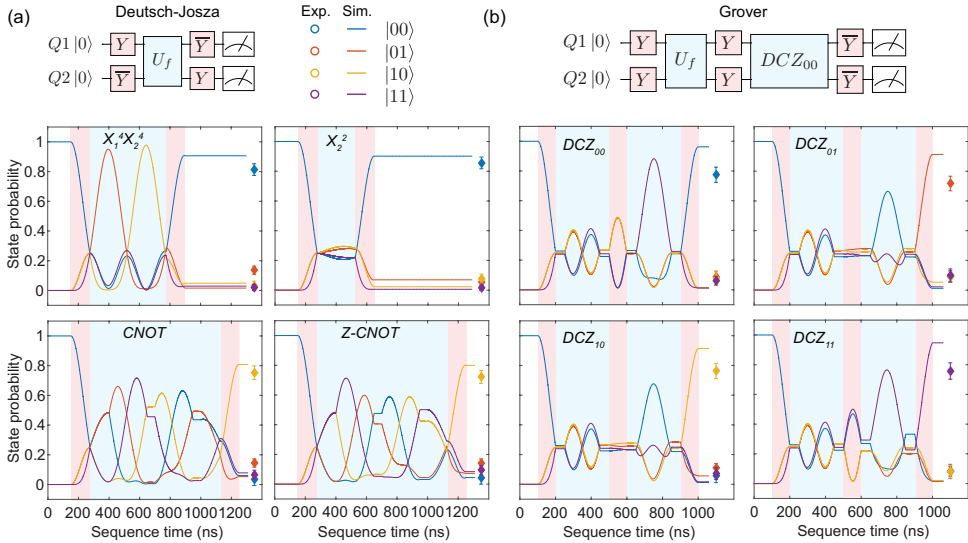
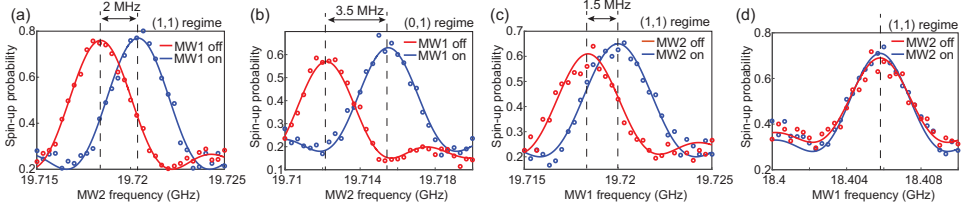


Figure 3.13: Simulation of the Deutsch-Josza and Grover algorithms using the decoupled CZ gate. Two-spin probabilities as a function of the sequence time during the (a) Deutsch-Josza algorithm and the (b) Grover search algorithm for each function using the decoupled version of the two-qubit CZ gate. The solid lines show the outcome of the simulations which include decoherence due to quasi-static charge noise and nuclear spin noise.



3
Figure 3.14: **Frequency shift on Q2 due to off-resonant microwave signals.** (a) Spectroscopy of Q2 with MW2 while MW1 is either off (blue data) or applying off-resonant MWs (red) to plunger gate P3 with a frequency $f = 18.5$ GHz and power $P = 16$ dBm. (b) The same experiment is performed in the (0,1) charge regime where there is only one electron in the double quantum dot. (c) Spectroscopy of Q2 with MW1 while MW2 is off (blue data) or applying off-resonant MWs (red) to plunger gate P4 with a frequency $f = 18.5$ GHz and power $P = 10$ dBm. (d) Spectroscopy of Q1 with MW1 while MW2 is off (blue data) or applying off-resonant MWs (red) to plunger gate P4 with a frequency $f = 18.5$ GHz and power $P = 22$ dBm.

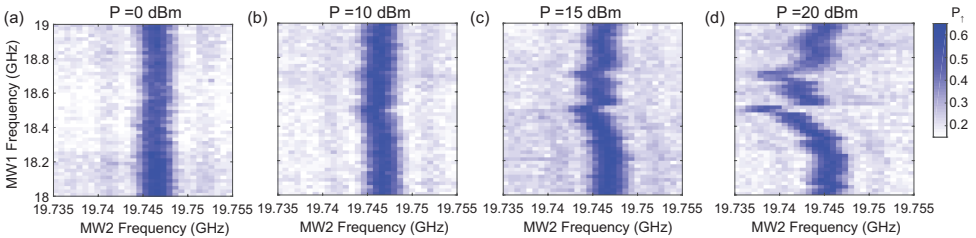


Figure 3.15: **Power dependence of the Q2 frequency shift.** Spectroscopy maps showing the resonance frequency of Q2 measured with MW2 as a function of the off-resonant MW frequency applied using MW1. These maps are measured at MW1 powers (a) 0 dBm, (b) 10 dBm, (c) 15 dBm, and (d) 20 dBm. The larger shifts in the resonance frequency most likely occur at transmission resonances where the power applied on the device is larger.

3.6.2. CALIBRATION OF SINGLE-QUBIT GATES

To perform accurate single-qubit gates on Q1 and Q2 we need to calibrate the following parameters of our MW pulses, (i) the frequency needed to be on resonance with Q1 and Q2, (ii) the power needed to perform a $\pi/2$ pulse on Q1 and Q2, (iii) the power needed for the 30 MHz off-resonance pulse during Q1 idle times to compensate for the Q2 frequency shift described above. The resonance frequency of Q1 (Q2) was measured using the Ramsey sequence shown in Fig. 3.16(a) and corresponds to the MW frequency that gives the maximum spin-up probability for Q1 (Q2). During the 300 ns wait time we apply the off-resonant MW pulse to Q1 to keep the resonance frequency of Q2 constant throughout the sequence. The power of the applied MW pulses was calibrated using the AllXY calibration sequence. In this sequence, two single-qubit gates, A and B where $A, B \in \{I, X, X^2, Y, Y^2\}$, are applied sequentially to the qubit as shown in Fig. 3.16(b). All possible combinations of A and B are applied and the final spin-up probabilities are measured. If the gates are ideal then the different combinations give the expected final probability of either 0, 0.5, or 1. MW power and frequency errors during the single-qubit gates result in characteristic deviations from these probabilities and can be corrected. In addition, if there is an error in the applied power of the off-resonant MW pulse during

the Ramsey calibration so that the resonance frequency of Q2 is not the same during the wait time and the X gates, this will show up as a frequency error in the AllXY sequence and can also be easily corrected. Fig. 3.16(c) shows an example of the result of the Ramsey and AllXY sequences after all the parameters have been calibrated.

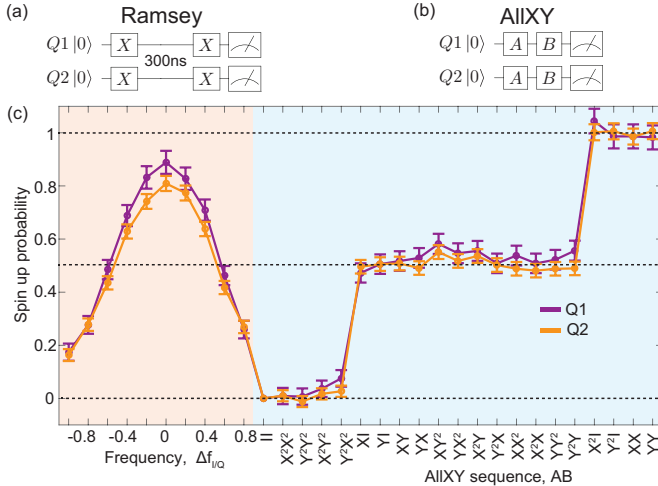


Figure 3.16: Calibration of the single-qubits gates. (a) Ramsey and (b) AllXY sequences used to calibrate the single-qubit gates for Q1 and Q2. (c) The measured spin-up probability of Q1 (purple data points) and Q2 (orange data points) during the Ramsey and AllXY experiments after the single-qubit gates have been calibrated. Here, errors due to readout have been removed from the spin-up probabilities. In the Ramsey experiment the MW frequency is swept around the local oscillator frequency of the MW source using I/Q modulation. In the AllXY experiment the x-axis corresponds to the 21 different combinations of the A and B single-qubit gates.

3.6.3. STATE TOMOGRAPHY OF BELL STATES

The density matrix of a two-qubit state can be expressed as $\rho = \sum_{i=1}^{16} c_i M_i$ where M_i are 16 linearly independent measurement operators. The coefficients c_i were calculated from the expectation values of the measurement operators either through linear inversion or a maximum likelihood estimation where the later ensures a physical density matrix that is Hermitian and positive semi-definite [14]. Fig. 3.17 shows a comparison of the density matrices for the state $\Psi^- = (|01\rangle - |10\rangle)/\sqrt{2}$ calculated using either linear inversion and MLE. The results are nearly identical indicating the estimated expectation values from the MLE are close to the measured expectation values in the experiment. For all measured states, the elements of the density matrix calculated with either linear inversion and MLE differ on average by ~ 0.005 . The calculated density matrices for the four Bell

states using MLE are:

$$\Psi^+ = \begin{pmatrix} 0.019 + 0i & 0.010 - 0.018i & -0.006 - 0.030i & -0.009 + 0.016i \\ 0.010 + 0.018i & 0.425 + 0i & 0.422 - 0.026i & -0.014 + 0.078i \\ -0.006 + 0.030i & 0.422 + 0.026i & 0.493 + 0i & -0.050 + 0.058i \\ -0.009 - 0.016i & -0.014 - 0.078i & -0.050 - 0.058i & 0.063 + 0i \end{pmatrix}, \quad (3.16)$$

$$\Psi^- = \begin{pmatrix} 0.016 + 0i & 0.009 + 0.052i & -0.016 - 0.035i & -0.008 + 0.005i \\ 0.009 - 0.052i & 0.429 + 0i & -0.420 - 0.007i & 0 + 0.050i \\ -0.016 + 0.035i & -0.420 + 0.007i & 0.495 + 0i & 0.040 - 0.062i \\ -0.008 - 0.005i & 0 - 0.050i & 0.040 + 0.062i & 0.060 + 0i \end{pmatrix}, \quad (3.17)$$

$$\Phi^+ = \begin{pmatrix} 0.501 + 0i & -0.024 + 0.023i & 0.002 + 0.021i & 0.370 + 0.013i \\ -0.024 - 0.023i & 0.019 + 0i & 0.003 - 0.003i & -0.03 - 0.028i \\ -0.002 - 0.021i & 0.003 + 0.003i & 0.013 + 0i & 0.017 + 0.019i \\ 0.370 - 0.013i & -0.031 + 0.028i & 0.017 - 0.019i & 0.467 + 0i \end{pmatrix}, \quad (3.18)$$

$$\Phi^- = \begin{pmatrix} 0.505 + 0i & 0.010 - 0.047i & -0.019 + 0.015i & -0.407 + 0.001i \\ 0.010 + 0.047i & 0.019 + 0i & -0.002 + 0.010i & -0.024 - 0.025i \\ -0.019 - 0.015i & -0.002 - 0.010i & 0.024 + 0i & 0.040 + 0.039i \\ -0.407 - 0.001i & -0.024 + 0.025i & 0.040 - 0.039i & 0.452 + 0i \end{pmatrix}, \quad (3.19)$$

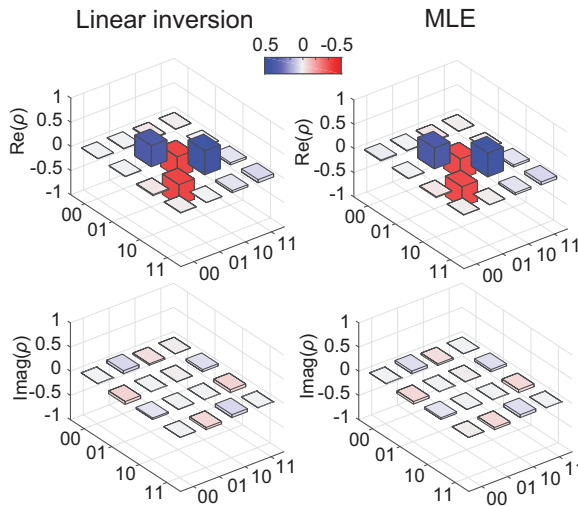


Figure 3.17: Comparison between the maximum likelihood estimation and linear inversion for the Bell state $\Psi^- = \frac{1}{\sqrt{2}}(|01\rangle - |10\rangle)$.

In quantum state tomography, the density matrix can be reconstructed by measuring the two-spin probabilities after applying 9 combinations of the prerotations I, X, Y . In the actual experiment, we also included the prerotation X^2 to help detect systematic errors leading to 16 combinations in total. Fig. 3.18 shows the real component of the estimated density matrices for the four Bell states and $\psi = (|10\rangle + |11\rangle)/\sqrt{2}$. These were calculated using either all prerotations or a subset of these prerotations, I, X, Y or X, Y, X^2 . Using either X, Y, X^2 or I, X, Y, X^2 gives similar results where the state fidelities and concurrences are 2 – 9% and 4 – 11% less than those calculated with I, X, Y . For the final

estimate of the density matrices we use only the prerotations I, X, Y as I should give a better estimate for the expectation values than X^2 due to decoherence and small calibration errors in our system. We did not account for decoherence and other errors in the prerotation pulses, which likely causes us to underestimate the overlaps with the ideal Bell states. Future work will include incorporating the prerotation errors into the state tomography analysis.

3

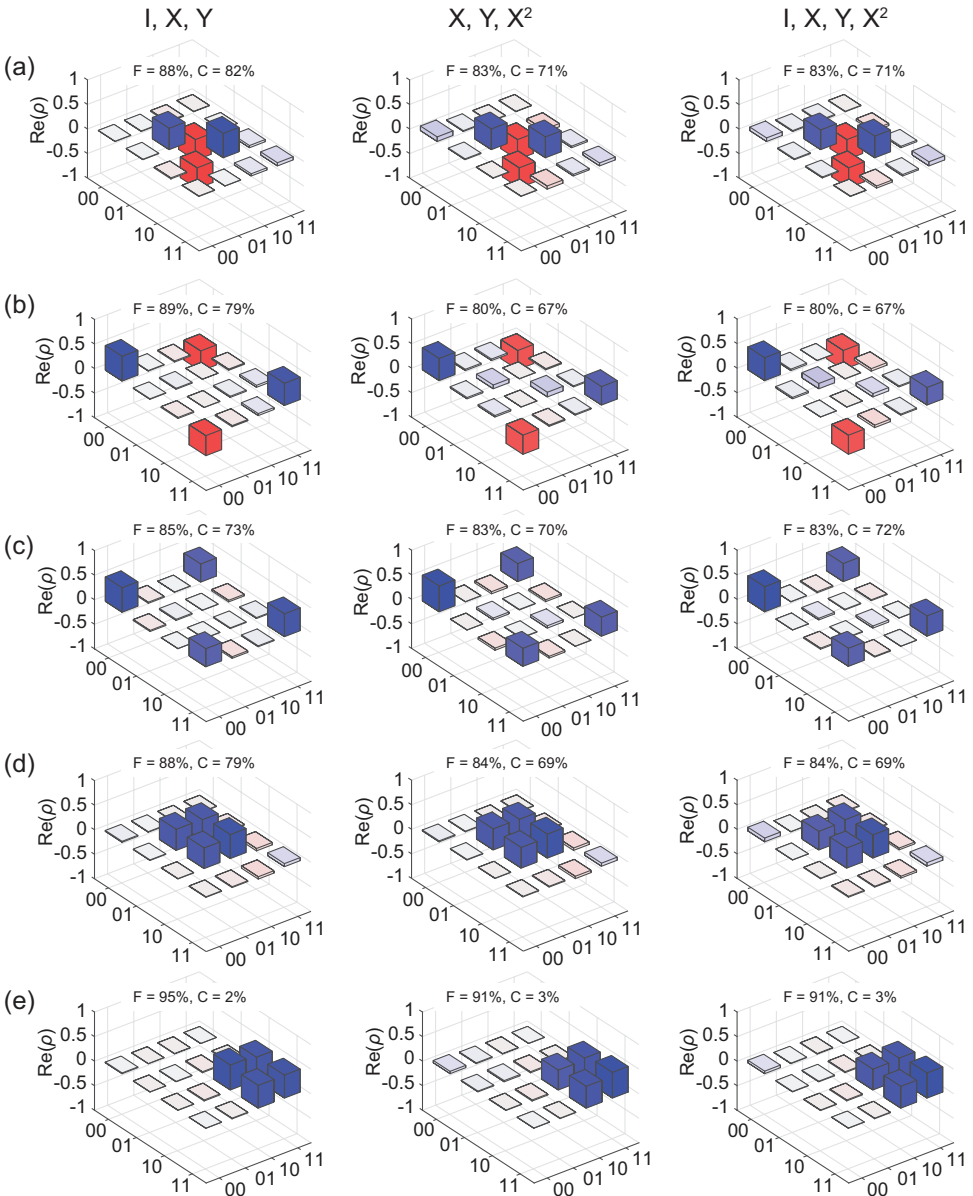


Figure 3.18: Comparison between density matrices constructed using different prerotations. The real component of the reconstructed density matrices using a maximum likelihood estimation for the four Bell states (a) $\Psi^+ = (|01\rangle + |10\rangle)/\sqrt{2}$, (b) $\Psi^- = (|01\rangle - |10\rangle)/\sqrt{2}$, (c) $\Phi^+ = (|00\rangle + |11\rangle)/\sqrt{2}$, (d) $\Phi^- = (|00\rangle - |11\rangle)/\sqrt{2}$, and (e) $\Psi = (|10\rangle + |11\rangle)/\sqrt{2}$. Here, the columns label whether the I, X, Y or X, Y, X^2 or I, X, Y, X^2 prerotations were used to calculate the expectation values in the estimation of the density matrices.

BIBLIOGRAPHY

- [1] R. Barends *et al.* “Superconducting quantum circuits at the surface code threshold for fault tolerance”. *Nature* 508.7497 (Apr. 2014), pp. 500–503. ISSN: 0028-0836.
- [2] H. Bluhm, S. Foletti, I. Neder, M. Rudner, D. Mahalu, V. Umansky, and A. Yacoby. “Dephasing time of GaAs electron-spin qubits coupled to a nuclear bath exceeding $200\mu\text{s}$ ”. *Nat. Phys.* 7.2 (Feb. 2011), pp. 109–113. ISSN: 1745-2473.
- [3] S. Das Sarma, X. Wang, and S. Yang. “Hubbard model description of silicon spin qubits: Charge stability diagram and tunnel coupling in Si double quantum dots”. *Phys. Rev. B* 83 (23 June 2011), p. 235314.
- [4] S. Debnath, N. M. Linke, C. Figgatt, K. A. Landsman, K. Wright, and C. Monroe. “Demonstration of a small programmable quantum computer with atomic qubits”. *Nature* 536.7614 (Aug. 2016), pp. 63–66. ISSN: 0028-0836.
- [5] D. Deutsch and R. Jozsa. “Rapid Solution of Problems by Quantum Computation”. *Proceedings of the Royal Society of London A: Mathematical, Physical and Engineering Sciences* 439.1907 (1992), pp. 553–558. ISSN: 0962-8444.
- [6] O. E. Dial, M. D. Shulman, S. P. Harvey, H. Bluhm, V. Umansky, and A. Yacoby. “Charge Noise Spectroscopy Using Coherent Exchange Oscillations in a Singlet-Triplet Qubit”. *Phys. Rev. Lett.* 110 (14 Apr. 2013), p. 146804.
- [7] L. DiCarlo *et al.* “Demonstration of two-qubit algorithms with a superconducting quantum processor”. *Nature* 460.7252 (July 2009), pp. 240–244. ISSN: 0028-0836.
- [8] J. M. Elzerman, R. Hanson, L. H. Willems van Beveren, B. Witkamp, L. M. K. Vandersypen, and L. P. Kouwenhoven. “Single-shot read-out of an individual electron spin in a quantum dot”. *Nature* 430.6998 (July 2004), pp. 431–435. ISSN: 0028-0836.
- [9] A. G. Fowler, M. Mariantoni, J. M. Martinis, and A. N. Cleland. “Surface codes: Towards practical large-scale quantum computation”. *Phys. Rev. A* 86 (3 Sept. 2012), p. 032324.
- [10] S. Freer *et al.* “A single-atom quantum memory in silicon”. *Quantum Science and Technology* 2.1 (2017), p. 015009.
- [11] L. K. Grover. “Quantum Mechanics Helps in Searching for a Needle in a Haystack”. *Phys. Rev. Lett.* 79 (2 July 1997), pp. 325–328.
- [12] S. Gulde, M. Riebe, G. P. T. Lancaster, C. Becher, J. Eschner, H. Haffner, F. Schmidt-Kaler, I. L. Chuang, and R. Blatt. “Implementation of the Deutsch-Jozsa algorithm on an ion-trap quantum computer”. *Nature* 421.6918 (Jan. 2003), pp. 48–50. ISSN: 0028-0836.
- [13] G. Ithier *et al.* “Decoherence in a superconducting quantum bit circuit”. *Phys. Rev. B* 72 (13 Oct. 2005), p. 134519.

- 3
- [14] D. F. V. James, P. G. Kwiat, W. J. Munro, and A. G. White. "Measurement of qubits". *Phys. Rev. A* 64 (5 Oct. 2001), p. 052312.
 - [15] E. Kawakami *et al.* "Electrical control of a long-lived spin qubit in a Si/SiGe quantum dot". *Nat. Nanotechnol.* 9.9 (Sept. 2014), pp. 666–670. ISSN: 1748-3387.
 - [16] E. Kawakami *et al.* "Gate fidelity and coherence of an electron spin in an Si/SiGe quantum dot with micromagnet". *Proc. Natl. Acad. Sci.* 113.42 (2016), pp. 11738–11743.
 - [17] D. Kim *et al.* "Quantum control and process tomography of a semiconductor quantum dot hybrid qubit". *Nature* 511.7507 (July 2014), pp. 70–74. ISSN: 0028-0836.
 - [18] E. Knill *et al.* "Randomized benchmarking of quantum gates". *Phys. Rev. A* 77 (1 Jan. 2008), p. 012307.
 - [19] D. Loss and D. P. DiVincenzo. "Quantum computation with quantum dots". *Phys. Rev. A* 57.1 (Jan. 1998), pp. 120–126.
 - [20] F. Martins, F. K. Malinowski, P. D. Nissen, E. Barnes, S. Fallahi, G. C. Gardner, M. J. Manfra, C. M. Marcus, and F. Kuemmeth. "Noise Suppression Using Symmetric Exchange Gates in Spin Qubits". *Phys. Rev. Lett.* 116 (11 Mar. 2016), p. 116801.
 - [21] R. Maurand *et al.* "A CMOS silicon spin qubit". *Nat. Commun.* 7 (Nov. 2016), pp. 13575–.
 - [22] J. Medford *et al.* "Self-consistent measurement and state tomography of an exchange-only spin qubit". *Nat. Nanotechnol.* 8.9 (Sept. 2013), pp. 654–659. ISSN: 1748-3387.
 - [23] T. Meunier, V. E. Calado, and L. M. K. Vandersypen. "Efficient controlled-phase gate for single-spin qubits in quantum dots". *Phys. Rev. B* 83 (12 Mar. 2011), p. 121403.
 - [24] J. T. Muhonen *et al.* "Storing quantum information for 30 seconds in a nanoelectronic device". *Nat. Nanotechnol.* 9.12 (Dec. 2014), pp. 986–991. ISSN: 1748-3387.
 - [25] J. R. Petta, A. C. Johnson, J. M. Taylor, E. A. Laird, A. Yacoby, M. D. Lukin, C. M. Marcus, M. P. Hanson, and A. C. Gossard. "Coherent manipulation of coupled electron spins in semiconductor quantum dots". *Science* 309.5744 (2005), pp. 2180–2184.
 - [26] M. Pioro-Ladrière, T. Obata, Y. Tokura, Y.-S. Shin, T. Kubo, K. Yoshida, T. Taniyama, and S. Tarucha. "Electrically driven single-electron spin resonance in a slanting Zeeman field". *Nature Physics* 4.10 (2008), pp. 776–779.
 - [27] M. D. Reed *et al.* "Reduced Sensitivity to Charge Noise in Semiconductor Spin Qubits via Symmetric Operation". *Phys. Rev. Lett.* 116 (11 Mar. 2016), p. 110402.
 - [28] T. van der Sar *et al.* "Decoherence-protected quantum gates for a hybrid solid-state spin register". *Nature* 484.7392 (Apr. 2012), pp. 82–86. ISSN: 0028-0836.
 - [29] M. D. Shulman, O. E. Dial, S. P. Harvey, H. Bluhm, V. Umansky, and A. Yacoby. "Demonstration of Entanglement of Electrostatically Coupled Singlet-Triplet Qubits". *Science* 336.6078 (2012), pp. 202–205.
 - [30] V. Srinivasa, K. C. Nowack, M. Shafiei, L. M. K. Vandersypen, and J. M. Taylor. "Simultaneous Spin-Charge Relaxation in Double Quantum Dots". *Phys. Rev. Lett.* 110 (19 May 2013), p. 196803.

- [31] A. M. Tyryshkin *et al.* “Electron spin coherence exceeding seconds in high-purity silicon”. *Nat. Mater.* 11.2 (Feb. 2012), pp. 143–147. ISSN: 1476-1122.
- [32] L. M. K. Vandersypen, H. Bluhm, J. S. Clarke, A. S. Dzurak, R. Ishihara, A. Morello, D. J. Reilly, L. R. Schreiber, and M. Veldhorst. “Interfacing spin qubits in quantum dots and donors—hot, dense, and coherent”. *npj Quantum Information* 3.1 (2017), p. 34. ISSN: 2056-6387.
- [33] L. M. K. Vandersypen and I. L. Chuang. “NMR techniques for quantum control and computation”. *Rev. Mod. Phys.* 76 (4 Jan. 2005), pp. 1037–1069.
- [34] L. M. K. Vandersypen, M. Steffen, G. Breyta, C. S. Yannoni, M. H. Sherwood, and I. L. Chuang. “Experimental realization of Shor’s quantum factoring algorithm using nuclear magnetic resonance”. *Nature* 414.6866 (Dec. 2001), pp. 883–887. ISSN: 0028-0836.
- [35] M. Veldhorst *et al.* “A two-qubit logic gate in silicon”. *Nature* 526.7573 (Oct. 2015), pp. 410–414. ISSN: 0028-0836.
- [36] M. Veldhorst *et al.* “An addressable quantum dot qubit with fault-tolerant control-fidelity”. *Nat Nano* 9.12 (Dec. 2014), pp. 981–985. ISSN: 1748-3387.
- [37] C. Yang *et al.* “Spin-valley lifetimes in a silicon quantum dot with tunable valley splitting”. *Nature communications* 4.1 (2013), pp. 1–8.
- [38] J. Yoneda *et al.* “A quantum-dot spin qubit with coherence limited by charge noise and fidelity higher than 99.9%”. *Nature Nanotechnology* (2017). ISSN: 1748-3395. URL: <https://doi.org/10.1038/s41565-017-0014-x>.
- [39] D. M. Zajac, A. J. Sigillito, M. Russ, F. Borjans, J. M. Taylor, G. Burkard, and J. R. Petta. “Resonantly driven CNOT gate for electron spins”. *Science* (2017). ISSN: 0036-8075. DOI: [10.1126/science.aao5965](https://doi.org/10.1126/science.aao5965).
- [40] F. A. Zwanenburg, A. S. Dzurak, A. Morello, M. Y. Simmons, L. C. L. Hollenberg, G. Klimeck, S. Rogge, S. N. Coppersmith, and M. A. Eriksson. “Silicon quantum electronics”. *Rev. Mod. Phys.* 85 (3 July 2013), pp. 961–1019.

4

RADIO FREQUENCY REFLECTOMETRY IN SILICON-BASED QUANTUM DOTS

RF reflectometry offers a fast and sensitive method for charge sensing and spin read-out in gated quantum dots. We focus in this work on the implementation of RF read-out in accumulation-mode gate-defined quantum dots, where the large parasitic capacitance poses a challenge. We describe and test two methods for mitigating the effect of the parasitic capacitance, one by on-chip modifications and a second by off-chip changes. We demonstrate that these methods enable high-performance charge readout in Si/SiGe quantum dots, achieving a fidelity of 99.9% for a measurement time of 1 μ s.

This work was originally published as :

Y.-Y. Liu*, S.G.J Philips*, L.A. Orona, N. Samkharadze, T. McJunkin and E.R. MacQuarrie and M.A. Eriksson, L.M.K. Vandersypen and A. Yacoby, Radio-Frequency Reflectometry in Silicon-Based Quantum Dots. Phys. Rev. Appl. 16 (1), 014057-014064 (2021).

4.1. INTRODUCTION

Quantum computing promises significant speedup of computational tasks that are practically impossible to solve on conventional computers [17, 3, 1, 16]. Of the physical platforms available, spin-based quantum bits (qubits) in semiconductors are particularly promising [9, 21]. Single-qubit gates with fidelities above 99.9% [18] and two qubit gate fidelities up to 98% [6, 23] have been demonstrated. Spin qubits in silicon are considered a strong candidate for realizing a large-scale quantum processor due to the small qubit dimensions, localized nature of the control, CMOS compatibility, long coherence times [25] and possibility of operating beyond 1 Kelvin [11, 24].

Charge sensing is an important technique for measuring spin qubits as their long-lived spin states can be converted into detectable charge states [5, 2]. To detect a charge state, a sensing dot (SD) is placed in close proximity ($d < \sim 300$ nm) to the qubit as shown in Figure 4.1(a). The sensing dot's resistance is strongly dependent on the charge state. However, measuring this resistance in DC with a amplifier at room temperature requires an integration time on the order of $30\ \mu\text{s} - 1\ \text{ms}$ due to the presence of noise and the RC time constant from the line capacitance and the amplifier input impedance [5, 11]. This slow readout forms a bottleneck when performing spin qubit experiments, since initialization and manipulation can be performed on the nanosecond or microsecond scale [12, 8, 7].

Radio Frequency (RF) reflectometry [15] has been successfully applied to depletion-mode GaAs quantum dots and has enabled single shot readout with only several microseconds of integration time [13]. However, in accumulation-mode devices, the large parasitic capacitance of the accumulation gates to the two dimensional electron gas (2DEG) below provides a low-impedance leakage pathway to ground for the RF signal, complicating RF reflectometry measurements. Previous works have addressed this problem by the use of circuit board elements [22] and careful gate design [4, 10].

In this work, we further develop the theoretical model of the leakage pathway introduced by this parasitic capacitance and apply it to two methods of circumventing the impact of the parasitic capacitance. We first apply this model in the "ohmic-style" implementation, similar to GaAs, where the signal is sent through an ohmic contact. For this approach, we mitigate the effects of the capacitance by optimizing the on-board elements and device design. Second, we present the "split-gate style", where the RF signal is carried by a gate which is capacitively coupled to the 2DEG [22]. By an adaptation of the sample design, the leakage pathway to the ohmic contact is blocked by a highly resistive channel.

4.2. RF REFLECTOMETRY

When performing RF-readout, a fixed frequency signal is applied to a sensing dot (Figure 4.1(c)). The reflectance of the applied signal is measured. It can be expressed as

$$\Gamma = (Z_L - Z_0)/(Z_L + Z_0), \quad (4.1)$$

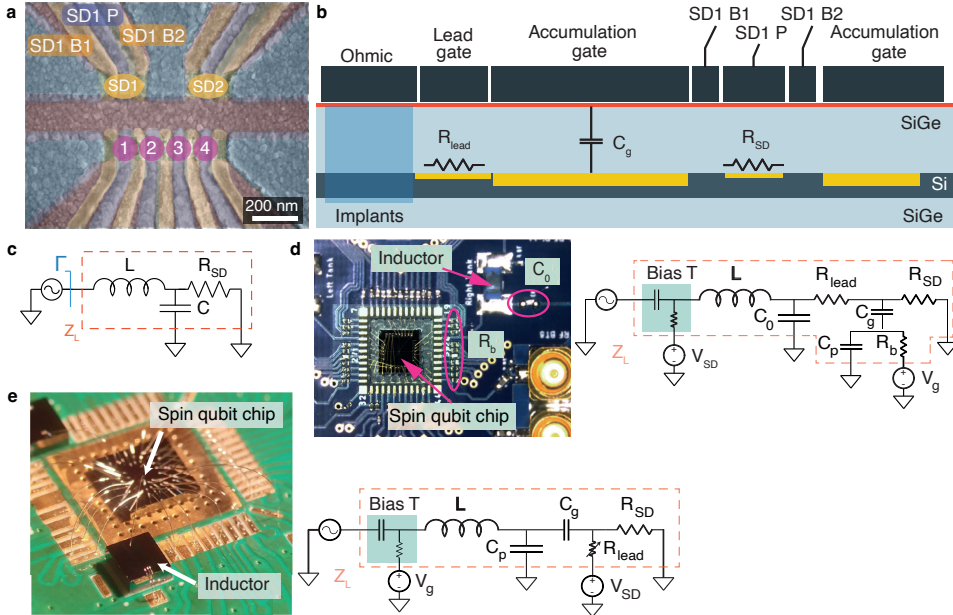


Figure 4.1: (a) false-colored SEM image of a Si/SiGe device, similar to the one used in this work. (b) Schematic cross-section of the sample showing the Si/SiGe quantum well and the gate stack on top. Yellow regions indicate a finite electron density in the quantum well. The three gates SD1 are used as plunger and barrier gates of the sensing dot, with resistance R_{SD} . The accumulation gate induces a 2DEG connecting the quantum dot to the ohmic contact, via a smaller area controlled by the lead gate. We use the lead gate to set the resistance R_{lead} . The path between the bond wire to the ohmic contact and the quantum dot also contains a contact resistance and the resistance of the 2DEG below the accumulation gate, which we both absorb into R_{lead} for simplicity. The capacitance between the 2DEG and the gates is dominated by C_g . (c) Circuit diagram showing an LCR circuit containing R_{SD} . (d) Optical image (left) and circuit diagram (right) of the wire-bonded sample on the PCB used for the Ohmic approach. The RF signal is applied to the ohmic contact. C_0 is a capacitor on the PCB. R_b are resistors on the PCB to prevent leakage of the RF signal into the DC lines (e.g. the accumulation gate electrode). The bias tee ($R = 5 \text{ k}\Omega$, $C = 100 \text{ nF}$) is implemented on the PCB to combine DC (V_{SD}) and RF signals. C_p is the parasitic capacitance of the bond wire and accumulation gate to the ground plane of the PCB. (e) Optical image (left) and circuit diagram (right) of a wire-bonded sample and inductors on the PCB used for the split-gate approach. The RF signal is applied to the accumulation gate.

where Z_L here represents the load impedance of the entire circuit (including matching networks and bias tees, as applicable) and Z_0 is the input impedance, equal to the output impedance of the RF source ($Z_0 = 50 \Omega$). A maximal power transfer occurs when $\Gamma = 0$, which is called the matching condition ($Z_0 \approx Z_L$). Given the resistive load from the sensing dot, R_{SD} , we can reach a matching condition by adding a matching network consisting of an inductor and a capacitor, as in Figure 4.1(c) [13]. The impedance of this LCR circuit is given by:

$$Z_L = i2\pi fL + \frac{1}{\frac{1}{R_{SD}} + i2\pi fC}. \quad (4.2)$$

For this simple LCR network, matching occurs when $f_{res} = 1/(2\pi\sqrt{LC_0})$ and $R_{SD} = L/C_0 Z_0$. In general, we denote throughout the frequency and sensing dot resistance for the matching condition as f_M and R_M . Ideally, matching occurs where R_M is reached at the flank of the sensing dot Coulomb blockade peak, where the sensing dot resistance is most sensitive to the qubit dot's charge occupation, typically in the range of $50 - 500 \text{ k}\Omega$.

4

In Si/SiGe quantum dots, the large parasitic capacitance from the 2DEG to the accumulation gate (C_g in Figure 4.1(b)), makes it hard to find a practical matching condition. The large C_g ($\sim 1 \text{ pF}$) can be compensated by increasing the inductance of the inductor, but this causes the resonance frequency to drop to a regime where most cryogenic amplifiers do not perform well (below 50-100 MHz). We solve these problems by slightly altering the circuit. We consider two approaches which we explain in more detail below:

- The ohmic approach – the RF signal is sent through the ohmic contact. The effect of C_g is mitigated by optimizing the circuit board and sample design (Figure 4.1(d)).
- The split-gate approach – the accumulation gate is split into two parts. The RF signal is carried to the SD using the large C_g between the accumulation gate and the 2DEG below (Figures 4.1(b) and 4.1(e)). The lead gate (R_{lead}) is used to create a high-impedance path to the ohmic.

These two approaches are tested on quadruple quantum dot devices on a Si/SiGe heterostructure. Figure 4.1(a) shows a SEM image of a typical device. Four quantum dots are formed with the lower set of gates of the device and two sensors are formed with the upper set of gates. Large accumulation gates control the electron density from the quantum dots to the ohmic contacts, approximately $50 \mu\text{m}$ away.

4.3. THE OHMIC APPROACH

The ohmic approach is shown in Figure 4.1(d) and introduces the RF signal to the lead of the SD through the ohmic contact. The large C_g and R_{lead} prohibit application of the simple RLC model to accumulation-mode SiGe devices. The gates are connected to ground by two channels: the line resistance R_b to the input lines for the gate voltages V_g which serves as RF ground, and the parasitic capacitance C_p to ground from all the metal on the sample side of R_b (gate, bond wire, bond pad, PCB trace). We will begin by exploring how the tank circuit parameters (R_b , C_p , C_0 and L) and the device parameters (R_{lead} and C_g) affect the matching conditions (f_M and R_M). This understanding will then be applied to demonstrate several key strategies that allow for ohmic-style RF reflectometry

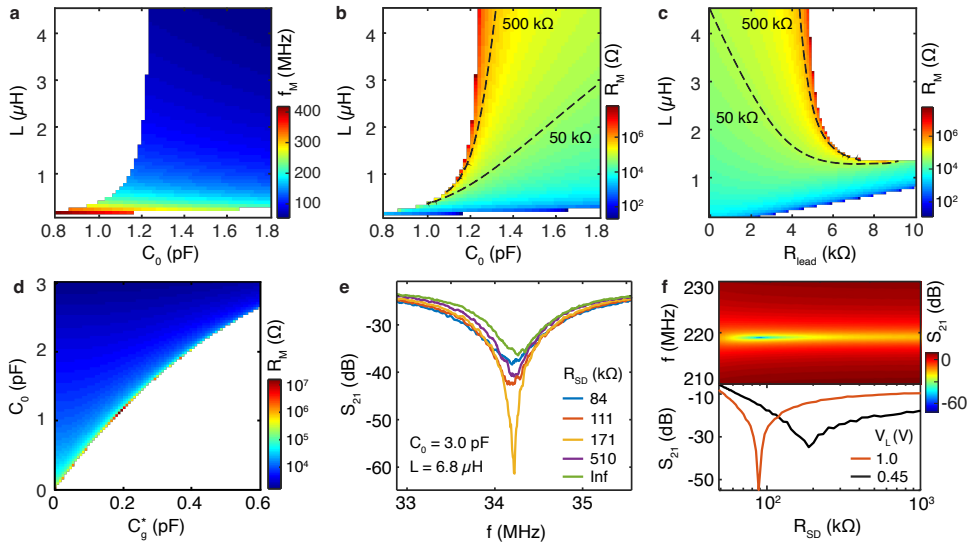


Figure 4.2: (a) and (b) Simulations of f_M and R_M as a function of C_0 and L with fixed parameters of $C_g^* = 0.2$ pF and $R_{\text{lead}} = 3$ k Ω . White regions are where no matching can be achieved. (c) Simulation of R_M as a function of R_{lead} and L with fixed $C_g^* = 0.2$ pF and $C_0 = 1.6$ pF. (d) Simulation of R_M as a function of C_0 and C_g^* with $L = 1$ μ H, and $R_{\text{lead}} = 3$ k Ω . (e) Experimental demonstration of best matching with $f_M = 34$ MHz and $R_M = 170$ k Ω . (f) Upper panel: S_{21} measured as a function of R_{SD} and f for an optimized device and circuit board. Lower panel: S_{21} at f_M (red and black) as a function of R_{SD} when $V_L=1$ V, 0.45 V respectively.

in Si/SiGe accumulation-mode devices. The goal is to achieve R_M and f_M values that are experimentally achievable and to ensure the majority of the power is dissipated in R_{SD} resulting in a usable signal-to-noise ratio (SNR). For that we aim at a $R_M \sim 50 - 500$ k Ω and $f_M \sim 100 - 300$ MHz.

Prevent shunting to ground through C_g .[22] The RF signal in the lead 2DEG has a low impedance path to the accumulation gates through C_g . In order to block this pathway, we have designed the printed circuit board (PCB) to have surface mount resistors to increase R_b between the sample bond pads and input lines for gate voltages, V_g . C_p is in parallel to R_b and limits the ability to decrease the impact of C_g by just increasing R_b . We place the blocking resistors close to the bond pads to minimize the amount of metal on the sample side and thereby reduce C_p . In the end we find a minimum $C_p = 0.2$ pF. At $f > 10$ MHz this would be a leakage path with a resistance smaller than 80 k Ω . The role of C_g , R_b and C_p together can be represented by one effective gate capacitor $C_g^* = C_p C_g / (C_p + C_g) = 0.2$ pF for any $R_b > 100$ k Ω at our target frequency range, because C_p is the more dominant leak channel compared to R_b .

Solution of Lumped Element Model. The simple LCR model always has a physically meaningful solution of f_M and R_M for the impedance matching condition. However, device simulations and experiments demonstrate that large values of R_{lead} and C_g^* can prevent there being a R_M and f_M and therefore the ability to use the tank circuit for charge detection. In Figure 4.2 we explore the dependence of the matching conditions

on C_0 , L , C_g^* and R_{lead} . Simulations are performed by solving for R_{SD} and f such that the circuit impedance Z matches $Z_0 = 50\Omega$, giving R_M and f_M respectively. The constraints that f_M is real and that R_M is real and positive result in there being conditions where no matching can be achieved, which are shown as white regions in Figure 4.2(a-d).

Control matching with C_0 and L . When a sample is fabricated, C_g and R_{lead} are roughly fixed, meaning that the only way to change R_M and f_M is through the tank circuit parameters L and C_0 . We present solutions of f_M in Figure 4.2(a) and R_M in Figure 4.2(b) as a function of L and C_0 with $C_g^* = 0.2 \text{ pF}$ and $R_{\text{lead}} = 3 \text{ k}\Omega$. We note that far from the non-matching regions, the behavior is approximately that of the standard LCR model. Under these conditions, $C_0 \gg C_g$ which means that C_0 dominates the capacitance of the loaded tank circuit. When C_0 is comparable to or smaller than C_g^* , R_M diverges.

4

In order to tune C_0 and L , our PCB has been designed with solder pads for a surface mount inductor, L , and a surface mount capacitor to control C_0 . The board parasitic capacitance also provides a significant contribution ($\sim 1 \text{ pF}$) to C_0 and sets a lower bound for possible values of C_0 . The ground plane near the tank circuit should be minimized to reduce this board parasitic capacitance, ensuring the tunability of the tank circuit by C_0 and L . Following the prediction of the model, we tested lumped elements with $L = 6.8 \mu\text{H}$ and $C_0 = 3.0 \text{ pF}$ for a device with estimated $R_{\text{lead}} = 4 \text{ k}\Omega$ and $C_g = 0.5 \text{ pF}$ ($C_g^* = 0.2 \text{ pF}$). The result in Figure 4.2(e) demonstrates impedance matching behavior with a usable R_M . However, it comes at a cost of a very low and unusable f_M . Practically, we need C_0 to be as low as allowed by C_g^* to guarantee a f_M that is above 100 MHz. For this reason, it is important to reduce C_g and thus C_g^* .

Balancing C_g and R_{lead} in sample design. The dependence of the matching conditions is strongly dependent on R_{lead} , as shown in Figure 4.2(c). At $R_{\text{lead}} = 0$, the model is reduced to the standard LCR model with an effective $C_0^* = C_0 + C_g$. The range of L that can achieve matching is drastically reduced as R_{lead} increases, since more rf power would be dissipated by R_{lead} before R_{SD} . Reducing R_{lead} is therefore key to achieving RF reflectometry. To capture the impact of C_g , we present a simulation of the dependence of R_M on C_g^* and C_0 in Figure 4.2(d). We again observe that matching is only achieved when C_0 is large enough compared to C_g .

The sample design impacts both C_g and R_{lead} , both of which we want to minimize, through the length l and width w of the accumulation gate. Knowing that $C_g \propto l w$ and $R_{\text{lead}} \propto l/w$ reveals that decreasing l is ideal for both parameters while decreasing w to improve C_g comes at the cost of increasing R_{lead} and vice versa. We have found that $w = 5 \mu\text{m}$ is sufficient to achieve consistent accumulation for usable R_{lead} without increasing C_g drastically. In the future we would place ohmics as close to the SD as possible to limit l as in [4]. The optimized result is demonstrated in Figure 4.2(f), where we plot the reflected power S_{21} in the upper panel as a function of f and R_{SD} . We apply $V_L = 1 \text{ V}$ on the lead gate to fully turn it on and thus minimize R_{lead} . With this we achieved both a usable $R_M \sim 100 \text{ k}\Omega$ and $f_M = 220 \text{ MHz}$.

Tuning R_{lead} . To experimentally confirm the dependence of R_M on R_{lead} , we make use of the lead gate. When V_L is small, the lead gate is partially turned on and thus leads to a larger R_{lead} . The lower panel in Figure 4.2(f) shows S_{21} at f_M as a function of R_{SD} when $V_L = 1 \text{ V}$ and 0.45 V . The best matching is achieved with $67 \text{ k}\Omega$ for the minimized

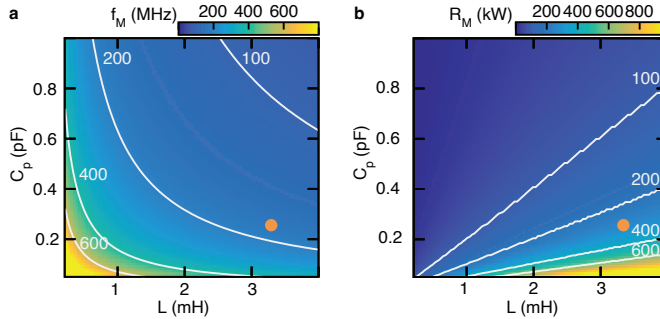


Figure 4.3: Simulation results for (a) f_M and (b) R_M as a function of C_p and L for the split accumulation gate circuit when $R_{lead} = 10 \text{ M}\Omega$ and $C_g = 280 \text{ fF}$. The orange dot indicates the parameters for the device and circuit used in experiment.

4

R_{lead} , and $200 \text{ k}\Omega$ for a larger R_{lead} , which agrees with the simulation in Figure 4.2(c). This tunability also allows the use of fixed C_0 and L for general devices as the matching condition of the device can be tuned in situ. This tunability, however, is not ideal since the larger R_{lead} gets more energy is lost before the sensor dot, resulting in a reduced signal to noise ratio.

4.4. SPLIT-GATE APPROACH

In this approach, the RF signal is sent to the sensing dot via the accumulation gate instead of via the ohmic contact (Figure 4.1(b)) [22]. The capacitance C_g between the accumulation gate and 2DEG allows the RF signal to couple in to the 2DEG, as shown in Figure 4.1(e). The lead gate is used to generate a high-impedance channel to the ohmic contact, preventing leakage of the RF signal.

We aim for similar design specifications for this method as for the ohmic method: a matching resistance (R_M) ranging from $200 \text{ k}\Omega$ to $600 \text{ k}\Omega$ and a matching frequency (f_M) larger than 100 MHz . We simulated f_M and R_M for different circuit configurations. We estimated C_g to be 280 fF from the sample design and $R_{lead} = 10 \text{ M}\Omega$. We varied the parasitic capacitance C_p (from the bond wires and the accumulation gate to the ground plane of the PCB) and the inductance L , as these are parameters controllable by the device design and inductor choice. From the simulation results in Figure 4.3, we find a large parameter space that achieves the desired matching condition for practical values of L up to about $5 \mu\text{H}$ as long as $C_p < 0.3 \text{ pF}$. In this case, the circuit reduces to the standard LCR model [19] given that the reactance of C_g , $\chi_g = \frac{1}{2\pi f C_g} \ll R_{SD}$ and $R_{lead} \gg R_{SD}$ (see Fig. 4.1(e)). We also simulated the expected measurement bandwidth at the matching condition of this circuit. We only see a weak dependence of the bandwidth on L and C_p . The bandwidth of the circuit ranges from 0.5 to 1 MHz .

For the devices used to demonstrate the split accumulation gate approach, we estimated by simulation the total parasitic capacitance to be around $C_p \sim 250 \text{ fF}$. The parasitic capacitance was kept low using a compact gate layout and high-kinetic-inductance resonators as inductors [14]. We aim for an inductor value of $L \sim 3.4 \mu\text{H}$, which is expected

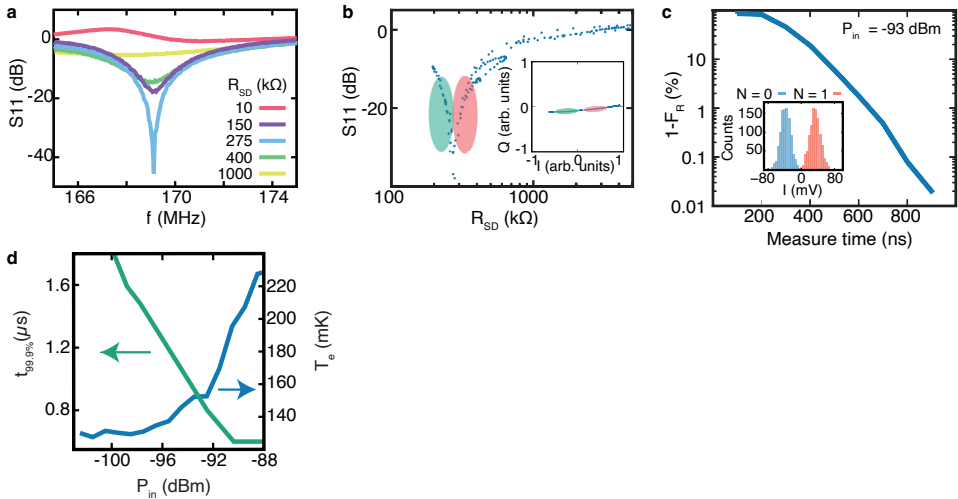


Figure 4.4: Characteristics obtained with the split accumulation gate approach. (a) Measured reflection coefficient as a function of f for several values of R_{SD} . (b) Reflection coefficient S_{11} at f_M as a function of R_{SD} . $R_M = 275$ k Ω . The sensitive regions are marked in red and green respectively. The inset plots the theoretical response in the IQ plane. (c) Infidelity of charge detection versus measurement time for an interdot transition. The inset: an example histogram for calculating the fidelity. (d) $t_{99.9\%}$ and T_e as a function of P_{in} .

to lead to a resonance frequency of ~ 180 MHz and a matching resistance of 300 k Ω for the sensing dot. When operating the device, leakage to the ohmic contact was cut off by tuning R_{Lead} above 10 M Ω .

Figure 4.4(a) shows the response of the resonator versus frequency for several values of R_{SD} . We see that f_M is slightly below 170 MHz. In Figure 4.4(b), we find $R_M = 275$ k Ω . The circuit bandwidth can be extracted from the full-width-half-max (FWHM) of the resonance line. For R_{SD} equal to R_M , the bandwidth is 0.8 MHz which means that we can measure signals up to time scales as short as ~ 600 ns, provided the signal-to-noise ratio is sufficiently high. Two sensitive regions where the reflected signal depends strongly on R_{SD} are visible in Figure 4.4(b), as indicated by the red and green shaded areas. The inset shows the expected response of the circuit in the IQ plane around R_M . The red and green regions can be differentiated by a phase π in the measured signal. In practice, the coax line between the sample and the measurement circuit adds an unknown phase. In order to maximize the signal-to-noise ratio (SNR), we record both I and Q and convert the result to a scalar.

In practice, we found that the resistance range for R_{SD} that gives the largest charge sensing signal, was roughly 0.4-1.0 M Ω , just above $R_M = 275$ k Ω . This implies we could improve the SNR by a factor of 2 by matching within this range (e.g. 600 k Ω). This could be done by reducing C_p from 250 fF to 150 fF (smaller gate footprint) or by increasing the inductance L (see figure 4.3).

To characterize the readout performance experimentally, we measured the charge readout fidelity (F_R). This fidelity is defined as the probability to correctly determine whether

a quantum dot is occupied with no ($N=0$) or one ($N=1$) electron. To estimate F_R , we send a train of 10,000 square pulses to the target quantum dot. The dot-reservoir tunnel time is several orders of magnitude shorter than the periods used in the experiment, which means the quantum dot charge state tracks the square pulse. We sample the IQ signal for each half period of the square pulse and plot the distribution for both half periods as shown in the inset of Figure 4.4(c). The overlap of both signals is the reported infidelity ($1-F_R$). For these measurements, we used a digital filter (FIR type) with a passband between 100 kHz and 2.5 MHz. The lower frequency of the passband was determined by the slowest signal we wanted to detect ($5\ \mu s$ in this case). The upper frequency was taken larger than the bandwidth of the matching circuit not to limit the measurement speed.

Figure 4.4(c) plots the readout infidelity $1 - F_R$ versus the measurement time when we apply an input signal power (P_{in}) of -93 dBm to the readout circuit (estimated from the output power at the source and the specified losses of the transmission line). We find a minimum measurement time of $t_{99.9\%} = 780$ ns in order to achieve $F_R > 99.9\%$. We see that $t_{99.9\%}$ strongly depends on the input power of the RF-readout circuit (Figure 4.4(d)). The SNR is improved by larger P_{in} until the bandwidth limit of the circuit is reached (0.8 MHz). On the other hand, larger P_{in} also affects the effective electron temperature of the quantum dots. To characterize the trade off, we measured T_e by measuring the polarization line of an interdot transition [20] and plot the result as a function of P_{in} in Figure 4.4(d). We note that T_e starts to increase dramatically once $P_{in} > -93$ dBm. We recommend to only supply power to the RF readout circuit when readout is being done, to prevent the readout from affecting qubit operations.

4.5. CONCLUSION

In this work we demonstrated two methods that can be used to achieve a reasonable matching condition for RF reflectometry measurements in accumulation mode devices. For the ohmic method, we demonstrate that a series resistance can be used to reduce leakage through the parasitic capacitance. Additionally, a careful sample design is necessary in order to obtain both a workable frequency and matching resistance. With further design changes, such as moving the ohmic contact closer to the quantum dot and drastically reducing the accumulation gate capacitance, the ohmic method can perform as well as the split accumulation gate method [4, 10]. For the split accumulation gate method, the RF source is directed to the accumulation gate of the sensing dot, and the addition of the lead gate allows to efficiently cut off the leakage path to the ohmic contact. The charge state of a qubit dot can be read out within $1\ \mu s$ with a $>99.9\%$ fidelity, which matches state-of-the-art readout performance. The split accumulation gate method is useful when it is difficult to achieve a very low C_g and/or to keep R_{2DEG} sufficiently low.

BIBLIOGRAPHY

- [1] A. Aspuru-Guzik, A. D. Dutoi, P. J. Love, and M. Head-Gordon. “Simulated quantum computation of molecular energies”. *Science* 309.5741 (2005), pp. 1704–1707.
- [2] C. Barthel, D. Reilly, C. M. Marcus, M. Hanson, and A. Gossard. “Rapid single-shot measurement of a singlet-triplet qubit”. *Physical Review Letters* 103.16 (2009), p. 160503.
- [3] G. Carleo and M. Troyer. “Solving the quantum many-body problem with artificial neural networks”. *Science* 355.6325 (2017), pp. 602–606.
- [4] E. J. Connors, J. Nelson, and J. M. Nichol. “Rapid High-Fidelity Spin-State Readout in Si/Si-Ge Quantum Dots via rf Reflectometry”. *Phys. Rev. Applied* 13 (2 2020), p. 024019. DOI: [10.1103/PhysRevApplied.13.024019](https://doi.org/10.1103/PhysRevApplied.13.024019).
- [5] J. M. Elzerman, R. Hanson, L. Willems van Beveren, B. Witkamp, L. Vandersypen, and L. P. Kouwenhoven. “Single-shot read-out of an individual electron spin in a quantum dot”. *nature* 430.6998 (2004), pp. 431–435.
- [6] W. Huang *et al.* “Fidelity benchmarks for two-qubit gates in silicon”. *Nature* 569.7757 (2019), pp. 532–536. ISSN: 1476-4687. URL: <https://doi.org/10.1038/s41586-019-1197-0>.
- [7] D. Kim, D. R. Ward, C. B. Simmons, D. E. Savage, M. G. Lagally, M. Friesen, S. N. Coppersmith, and M. A. Eriksson. “High-fidelity resonant gating of a silicon-based quantum dot hybrid qubit”. *Npj Quantum Information* 1.1 (2015), p. 15004.
- [8] F. H. Koppens, C. Buizert, K.-J. Tielrooij, I. T. Vink, K. C. Nowack, T. Meunier, L. Kouwenhoven, and L. Vandersypen. “Driven coherent oscillations of a single electron spin in a quantum dot”. *Nature* 442.7104 (2006), pp. 766–771.
- [9] J. J. Morton and B. W. Lovett. “Hybrid Solid-State Qubits: The Powerful Role of Electron Spins”. *Annual Review of Condensed Matter Physics* 2.1 (2011), pp. 189–212.
- [10] A. Noiri, K. Takeda, J. Yoneda, T. Nakajima, T. Kodera, and S. Tarucha. “Radio-Frequency-Detected Fast Charge Sensing in Undoped Silicon Quantum Dots”. *Nano Letters* 20.2 (2020), pp. 947–952.
- [11] L. Petit, H. G. J. Eenink, M. Russ, W. I. L. Lawrie, N. W. Hendrickx, S. G. J. Philips, J. S. Clarke, L. M. K. Vandersypen, and M. Veldhorst. “Universal quantum logic in hot silicon qubits”. *Nature* 580.7803 (2020), pp. 355–359. ISSN: 1476-4687. URL: <https://doi.org/10.1038/s41586-020-2170-7>.
- [12] J. R. Petta, A. C. Johnson, J. M. Taylor, E. A. Laird, A. Yacoby, M. D. Lukin, C. M. Marcus, M. P. Hanson, and A. C. Gossard. “Coherent manipulation of coupled electron spins in semiconductor quantum dots”. *Science* 309.5744 (2005), pp. 2180–2184.

- [13] D. Reilly, C. Marcus, M. Hanson, and A. Gossard. "Fast single-charge sensing with a rf quantum point contact". *Applied Physics Letters* 91.16 (2007), p. 162101.
- [14] N. Samkharadze, A. Bruno, P. Scarlino, G. Zheng, D. P. DiVincenzo, L. DiCarlo, and L. M. K. Vandersypen. "High-Kinetic-Inductance Superconducting Nanowire Resonators for Circuit QED in a Magnetic Field". *Phys. Rev. Applied* 5 (4 Apr. 2016), p. 044004. DOI: [10.1103/PhysRevApplied.5.044004](https://doi.org/10.1103/PhysRevApplied.5.044004).
- [15] R. J. Schoelkopf, P. Wahlgren, A. A. Kozhevnikov, P. Delsing, and D. E. Prober. "The Radio-Frequency Single-Electron Transistor (RF-SET): A Fast and Ultrasensitive Electrometer". *Science* 280.5367 (1998), pp. 1238–1242. ISSN: 0036-8075. eprint: <https://science.scienmag.org/content/280/5367/1238.full.pdf>. DOI: [10.1126/science.280.5367.1238](https://doi.org/10.1126/science.280.5367.1238).
- [16] P. W. Shor. "Polynomial-time algorithms for prime factorization and discrete logarithms on a quantum computer". *SIAM review* 41.2 (1999), pp. 303–332.
- [17] R. D. Somma, S. Boixo, H. Barnum, and E. Knill. "Quantum simulations of classical annealing processes". *Physical review letters* 101.13 (2008), p. 130504.
- [18] K. Takeda *et al.* "Optimized electrical control of a Si/SiGe spin qubit in the presence of an induced frequency shift". *npj Quantum Information* 4.1 (2018), pp. 54–. ISSN: 2056-6387. URL: <https://doi.org/10.1038/s41534-018-0105-z>.
- [19] L. Taskinen, R. Starrett, T. Martin, A. Micolich, A. Hamilton, M. Simmons, D. Ritchie, and M. Pepper. "Radio-frequency reflectometry on large gated two-dimensional systems". *Review of Scientific Instruments* 79.12 (2008), p. 123901.
- [20] C. J. Van Diepen, P. T. Eendebak, B. T. Buijtendorp, U. Mukhopadhyay, T. Fujita, C. Reichl, W. Wegscheider, and L. M. Vandersypen. "Automated tuning of inter-dot tunnel coupling in double quantum dots". *Applied Physics Letters* 113.3 (2018), p. 033101.
- [21] L. M. K. Vandersypen, H. Bluhm, J. Clarke, A. Dzurak, R. Ishihara, A. Morello, D. Reilly, L. Schreiber, and M. Veldhorst. "Interfacing spin qubits in quantum dots and donors—hot, dense, and coherent". *npj Quantum Information* 3.1 (2017), pp. 1–10.
- [22] C. Volk, A. Chatterjee, F. Ansaloni, C. M. Marcus, and F. Kuemmeth. "Fast Charge Sensing of Si/SiGe Quantum Dots via a High-Frequency Accumulation Gate". *Nano Lett.* 19.8 (2019), pp. 5628–5633. DOI: <https://doi.org/10.1021/acs.nanolett.9b02149>.
- [23] X. Xue *et al.* "Benchmarking gate fidelities in a Si/SiGe two-qubit device". *Physical Review X* 9.2 (2019), p. 021011.
- [24] C. H. Yang *et al.* "Operation of a silicon quantum processor unit cell above one kelvin". *Nature* 580.7803 (2020), pp. 350–354. ISSN: 1476-4687. URL: <https://doi.org/10.1038/s41586-020-2171-6>.
- [25] F. A. Zwanenburg, A. S. Dzurak, A. Morello, M. Y. Simmons, L. C. Hollenberg, G. Klimeck, S. Rogge, S. N. Coppersmith, and M. A. Eriksson. "Silicon quantum electronics". *Reviews of modern physics* 85.3 (2013), p. 961.

5

UNIVERSAL CONTROL OF A SIX-QUBIT QUANTUM PROCESSOR IN SILICON

Future quantum computers capable of solving relevant problems will require a large number of qubits that can be operated reliably[9]. However, the requirements of having a large qubit count and operating with high-fidelity are typically conflicting. Spins in semiconductor quantum dots show long-term promise[67, 49] but demonstrations so far use between one and four qubits and typically optimize the fidelity of either single- or two-qubit operations, or initialization and readout[52, 60, 57, 34, 32, 46, 29, 20]. Here we increase the number of qubits and simultaneously achieve respectable fidelities for universal operation, state preparation and measurement. We design, fabricate and operate a six-qubit processor with a focus on careful Hamiltonian engineering, on a high level of abstraction to program the quantum circuits and on efficient background calibration, all of which are essential to achieve high fidelities on this extended system. State preparation combines initialization by measurement and real-time feedback with quantum-non-demolition measurements. These advances will allow for testing of increasingly meaningful quantum protocols and constitute a major stepping stone towards large-scale quantum computers.

This work was originally published as :

S. G. J. Philips*, M. T. Mądzik*, S. V. Amitonov, S. L. de Snoo, M. Russ, N. Kalhor, C. Volk, W. I. L. Lawrie, D. Brousse, L. Tryputen, B. Paquelet Wuetz, A. Sammak, M. Veldhorst, G. Scappucci and L. M. K. Vandersypen, Universal control of a six-qubit quantum processor in silicon. Nature 609, 919–924 (2022).

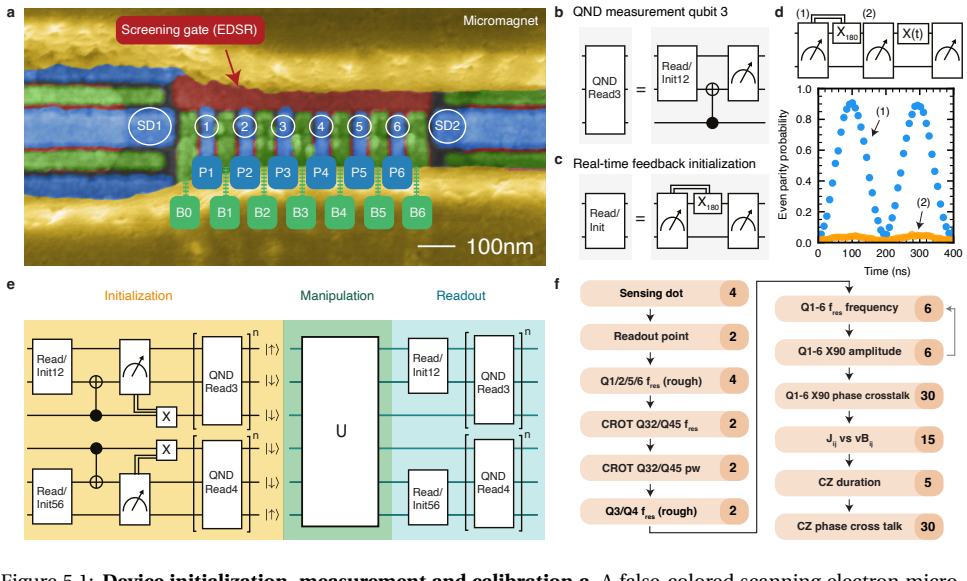


Figure 5.1: Device initialization, measurement and calibration **a**, A false-colored scanning electron microscope image of a device similar to the one used in the experiments. Each color represents a different metallization layer. Plunger (blue) and barrier (green) gates are used to define quantum dots in the channel between the screening gates (red). Two cobalt micromagnets (yellow) are placed on top of the gate stack. **b-c**, Building blocks used for readout and initialization in this experiment. Panel **b** shows the circuit used to perform a single QND measurement of qubit 3, panel **c** shows the circuit used for spin measurement and initialization using a parity measurement. The double line in the diagram indicates that X_{180} rotation is conditional on the measurement outcome. **d**, shows an example of a conditional rotation used to initialize the qubits. The sequence shown is applied repeatedly with short time intervals, with the final state of one cycle being the initial state of the next. (1) shows the even parity probability of the first measurement, (2) shows the even parity probability after the bit flip conditional on the first measurement outcome. **e**, Schematic showing the total scheme used for the initialization and readout of all six qubits (see Fig. 5.7 for an expanded view). **f**, Calibration graph used in the experiments. The numbers on the right show the number of parameters that are calibrated in each step.

5.1. INTRODUCTION

On the path to practical large-scale quantum computation, electron spin qubits in semiconductor quantum dots [50] show promise due to their inherent potential for scaling through their small size [6, 62], long-lived coherence [52] and compatibility with advanced semiconductor manufacturing techniques [68]. Nevertheless, spin qubits currently lag behind in scale when compared to superconducting, trapped ions and photonic platforms, which have demonstrated control of several dozen qubits [3, 14, 66]. By comparison, using semiconductor spin qubits, partial [15] and universal [20] control of up to four qubits was achieved and entanglement of up to three qubits was quantified [46, 29, 45]. In a six-dot linear array, two qubits encoded in the state of three spins each were operated [55] and spin exchange oscillations in a 3x3 array have been reported [33].

Furthermore, the experience with other qubit platforms shows that in scaling up, maintaining the quality of the control requires significant efforts, for instance to deal with the denser motional spectrum in trapped ions [8], to avert cross-talk in superconducting cir-

cuits [65] or to avoid increased losses in photonic circuits [2]. For small semiconductor spin qubit systems, state-of-the-art single-qubit gate fidelities exceed 99.9% [60, 59, 25] and two-qubit gates well above 99% fidelity have been demonstrated recently [57, 34, 32, 29]. Most quantum dot based demonstrations suffer from rather low initialization or readout fidelities, with typical visibilities of no more than 60–75%, with few recent exceptions [32, 5, 55]. Conversely, high-fidelity spin readout has been claimed based on an analysis of the readout error mechanisms, but these claims have not been validated in combination with high-fidelity qubit control [10, 18]. While high-fidelity initialization, readout, single-qubit gates and two-qubit gates have thus been demonstrated individually in small systems, almost invariably one or more of these parameters are significantly compromised while optimizing others. A major challenge and important direction for the field is therefore to achieve high fidelities for all components while at the same time enlarging the qubit count.

Here we study a system of six spin qubits in a linear quantum dot array and test what performance can be achieved using known methods such as multi-layer gate patterns for independent control of the two-qubit exchange interaction [1, 63, 26] and micromagnet gradients for electric-dipole spin resonance and selective qubit addressing [40]. Furthermore, we introduce several novel techniques for semiconductor qubits that, collectively, are critical to improve on the results and facilitate scalability, such as initialization by measurement using real-time feedback [42], qubit initialization and measurement without reservoir access, and efficient calibration routines. Initialization and readout circuits span over the full six-qubit array. We characterize the quality of the control by preparing maximally entangled states of two and three spins across the array.

5.2. DEFINING INITIALIZATION, READOUT, SINGLE AND TWO-QUBIT GATES ON A SIX-QUBIT QUANTUM PROCESSOR

The six-qubit array is defined electrostatically in the ^{28}Si quantum well of a $^{28}\text{Si}/\text{SiGe}$ heterostructure, between two sensing quantum dots, as seen in Figure 5.1a (see Methods). The multi-layer gate pattern allows for excellent control of the charge occupation of each quantum dot, and of the tunnel couplings between neighbouring quantum dots. These parameters are controlled independently through linear combinations of gate voltages, known as virtual gates [53]. The inter-dot pitch is chosen to be 90 nm, which for this 30 nm deep quantum well yields easy access to the regime with one electron in each dot, for short indicated as the (1,1,1,1,1,1) charge occupation. Low valley splittings on Si/SiGe devices have hindered progress in the past [23], but in this device all valley splittings are in the range of 100–300 μeV (See Supplementary materials).

In designing the qubit measurement scheme, we focused on achieving short measurement cycles in combination with high-fidelity readout, as this accelerates testing of all other aspects of the experiment. For measuring the outer qubit pairs, we use Pauli-Spin blockade (PSB) to probe the parity of the two spins (rather than differentiating between singlet and triplet states), exploiting the fact that the T_0 triplet relaxes to the singlet well

before the end of the 10 μs readout window. We tune the outer dot pairs of the array to the (3,1) electron occupation, where the readout window is larger than in the (1,1) regime (see Fig. 5.6). Since the sensing dots are less sensitive to the charge transition between the center dots, the middle qubits are measured by quantum-non-demolition (QND) measurements that map the state of qubit 3(4) on qubit 2(5) via a conditional rotation (CROT) (Fig. 5.1b) [60, 58]. In this way, for every iteration of the experiment, 4 bits of information are retrieved which depend on the state of all 6 physical qubits. Iterative operation permits full readout of the 6-qubit system.

Qubit initialization is based on measurements of the spin state across the array followed by real-time feedback to place all qubits in the target initial state. This scheme has the benefit of not relying on slow thermalization and that no access to electron reservoirs is needed to bring in fresh electrons, which is helpful for scaling to larger arrays. In fact, we had experiment runs of more than one month in which the electrons stayed within the array continuously. For qubits 3 and 4, real-time feedback simply consists of flipping the qubit if the measurement returned $|\uparrow\uparrow\rangle$. Initialization of qubits 1-2 (or 5-6) using parity measurements and real-time feedback is illustrated in Figure 5.1c. First, assuming that the qubits start from a random state, we perform a parity measurement that will cause the state to either collapse to an even ($|\downarrow\downarrow\rangle, |\uparrow\uparrow\rangle$) or odd ($|\uparrow\downarrow\rangle/|\downarrow\uparrow\rangle$) parity (see Methods). After the measurement, a π pulse is applied to qubit 1 in case of even parity, which converts the state to odd parity (feedback latency 660 ns). Subsequently, we perform a second measurement, which converts either of the odd parity states to $|\uparrow\downarrow\rangle$. Specifically, when pulsing towards the readout operating point, both $|\uparrow\downarrow\rangle$ and $|\downarrow\uparrow\rangle$ relax into the singlet state ((4,0) charge occupation). When pulsing adiabatically from the (4,0) back to the (3,1) charge configuration, the singlet is mapped onto the $|\uparrow\downarrow\rangle$ state. If the qubit initialization is successful, the second measurement should return an odd parity (typically $\sim 95\%$ success rate). To further boost the initialization fidelity we use the outcome of the second measurement to post-select successful experiment runs (see Fig. 5.6d). Figure 5.1d shows initialization by measurement of the first two qubits. The first readout outcome (blue) shows Rabi oscillations controlled by a microwave burst of variable duration applied near the end of the previous cycle (see methods for more details). The second readout outcome (green) shows the state after the real-time classical feedback step. The oscillation has largely vanished, indicating successful initialization by measurement and feedback.

The sequence to initialize and measure all qubits is shown in Figure 5.1e (see Fig. 5.7 for the unfolded quantum circuit). We sequentially initialize qubit pair 5-6, then qubit 4, then qubits 1-2, and finally qubit 3, using the steps described above (for compactness, the steps appear as simultaneous in the diagram). In order to further enhance the measurement and initialization fidelities, we repeat the QND measurement three times, alternating the order of qubit 3 and 4 measurements. We post-select runs with three identical QND readout outcomes in both the initialization and measurement steps (except for Fig. 5 below, where readout simply uses majority voting). After performing the full initialization procedure depicted in Fig. 5.1e, the six qubit array is initialized in the state $|\uparrow\downarrow\downarrow\downarrow\downarrow\uparrow\rangle$. In all measurements below, we initialize either two, three or all six qubits,

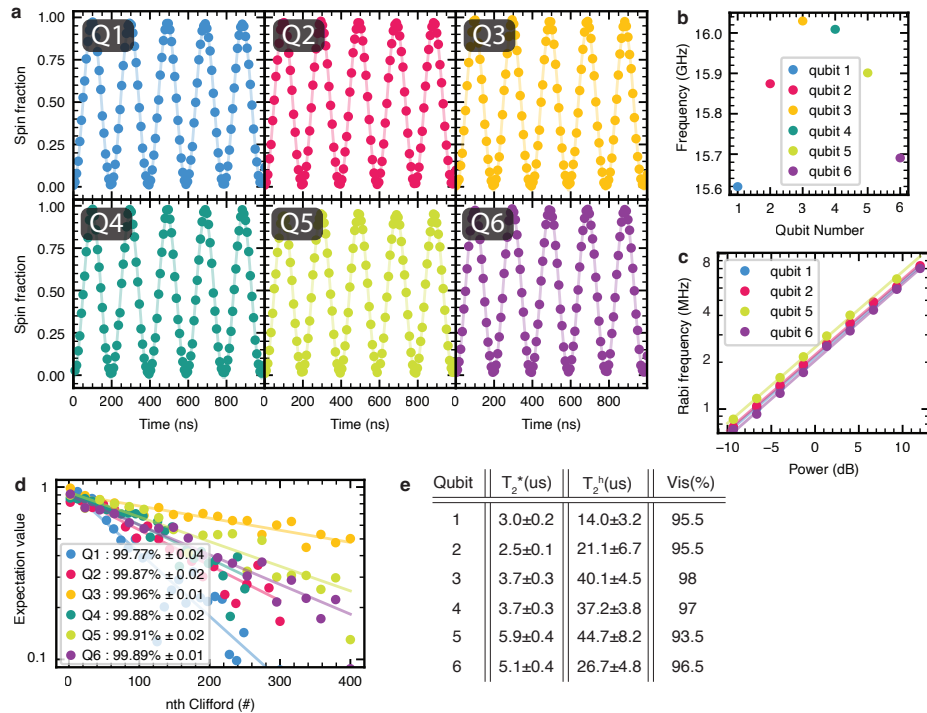


Figure 5.2: Single-qubit gate characterization **a**, Rabi oscillations for every qubit, taken sequentially. The spin fraction refers to the spin-up fraction for qubits 2-5 and to the spin-down fraction for qubits 1 and 6. The drive amplitudes were adjusted in order to obtain uniform Rabi frequencies of 5 MHz. **b**, Qubit frequency for each of the six qubits. **c**, Rabi frequency of each qubit as a function of the applied microwave power. **d**, Randomized benchmarking results for each qubit, using a 5 MHz Rabi frequency. The reported fidelity is the average single-qubit gate fidelity. The error bars (2σ) are calculated using the covariance matrix of the fit. **e**, Table showing the dephasing time T_2^* , Hahn echo decay time and visibilities for each qubit.

depending on the requirement of the specific quantum circuit we intend to run. We leave the unused qubits randomly initialized, as the visibilities decrease when initializing all 6 qubits within a single shot sequence (see Fig. 5.8). When operating on individual qubits, the initialization and measurement procedures yield visibilities of 93.5-98% (see Fig. 5.2e). To put these numbers in perspective, if the readout error for both $|0\rangle$ and $|1\rangle$ were 1% alongside an initialization error of 1%, the visibility would be 96%.

We manipulate the qubits via electric-dipole spin resonance (EDSR) [36]. A micromagnet located above the gate-stack is designed to provide both qubit addressability and a driving field gradient (see Fig. 5.1a and Supplementary Data). We can address each qubit individually and drive coherent Rabi oscillations as depicted in figure 5.2. We observe no visible damping in the first five periods. The data in figure 5.2b shows that the qubit frequencies are not spaced linearly, deviating from our prediction based on numerical simulations of the magnetic field gradients (Figure 1). However, the smallest qubit frequency separation of ≈ 20 MHz is sufficient for selective qubit addressing with

our operating speeds varying between 2 MHz and 5 MHz. The Rabi frequency is linear in the driving amplitude over the typical range of microwave power used in the experiment (Fig. 5.2c). We operate single-qubit gates sequentially, to ensure we stay in this linear regime and to keep the calibration simple. Simultaneous rotations would involve additional characterization and compensation of cross-talk effects, see also Fig. 5.10. We characterize the single-qubit properties of each qubit separately. Figure 5.2d shows results of randomized benchmarking experiments. All average single-qubit gate fidelities are between $99.77\% \pm 0.04$ and $99.96\% \pm 0.01$, which demonstrates that even within this extended qubit array, we retain high-fidelity single-qubit control. The coherence times of each qubit are tabulated in figure 5.2e. We expect spin coherence to be limited by charge noise coupling in by the micromagnet [24].

Two-qubit gates are implemented by pulsing the (virtual) barrier gate between adjacent dots while staying at the symmetry point. Pulsing the barrier gate leads to a ZZ interaction (throughout, X, Y and Z stand for the Pauli operators, I for the identity, and ZZ is shorthand for the tensor product of two Pauli Z operators, etc), given that the effect of the flip-flop terms of the spin exchange interaction is suppressed due to the differences in the qubit splittings [31]. The quantum circuit in Fig. 5.3a measures the time evolution under the ZZ component of the Hamiltonian only, as the single-qubit π pulses in between the two exchange pulses decouple any IZ/ZI terms [54]. The measured signal oscillates at a frequency $J/2$ (Fig. 5.3b-f) as a function of the barrier gate pulse duration, corresponding to Controlled Phase (CPhase) evolution. When pulsing only the barrier gate between the target qubit pair, the desired on/off ratio of J_{ij} (>100) could not be achieved. We solve this, without sacrificing operation at the symmetry point, by using a linear combination of the virtual barrier gates (vB1-vB6). Specifically, the barrier gates around the targeted quantum dot pair are pulsed negatively to push the corresponding electrons closer together and thereby enhance the exchange interaction (see Fig. 5.1). The exponential dependence of J_{ij} on virtual barrier gates is seen in Fig. 5.3h. In Fig. 5.3g we investigate the residual exchange of idle qubit pairs, while one qubit pair is pulsed to its maximal exchange value within the operating range. The results show minimal residual exchange amplitudes in the off-state between the other pairs.

Through suitable timing, we use the CPhase evolution to implement a Controlled-Z (CZ) gate. Fig. 5.3j shows the pulse shape that is used to ensure a high degree of adiabaticity throughout the CZ gate [57]. We use a Tukey window as waveform, with a ramp time of $\tau_{\text{ramp}} = \frac{3}{\sqrt{\delta B^2 + J_{\text{max}}^2}}$ [30]. This pulse shape is defined in units of energy and we convert it into barrier voltages using the measured voltage to exchange energy relation [57].

One of the challenges when operating larger quantum processors is to track and compensate any dynamical changes in qubit parameters to ensure high-fidelity operation, initialization and readout. Another challenge is to keep track of and compensate for cross-talk effects imparted by both single- and two-qubit gates on the phase evolution of each qubit. We perform automated calibrations, as shown in Fig. 5.1f, and correct 108 parameters in total. The detailed description of each calibration routine is included in the methods section and Fig. 5.9. Twice a week, we run the full calibration scheme, which takes about one hour. Every morning, we run the calibration scheme leaving out

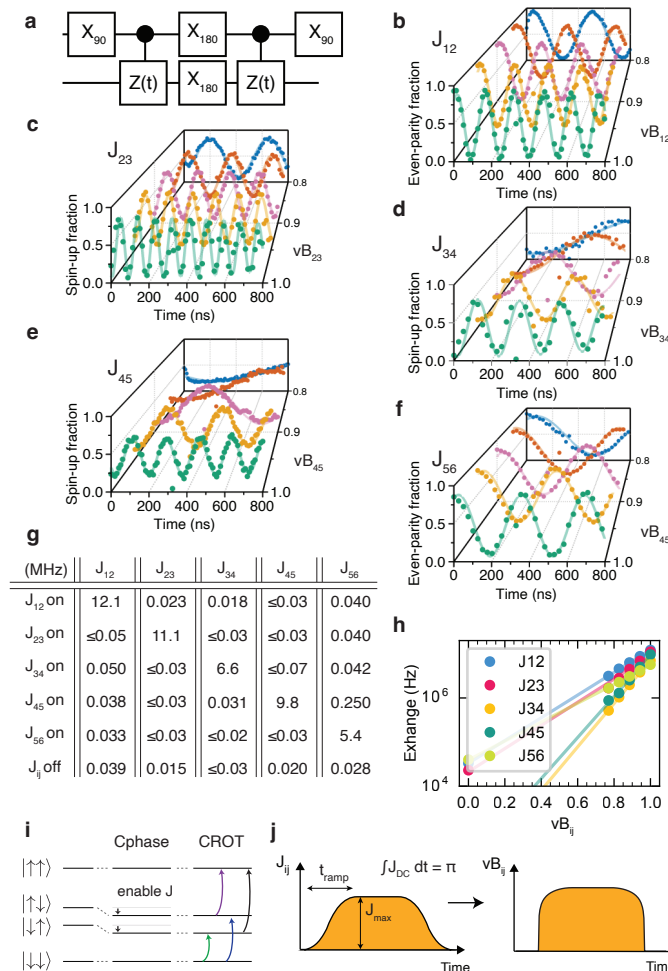


Figure 5.3: **Two-qubit gate characterization** **a**, Quantum circuit used to measure CPhase oscillations between a pair of qubits. **b-f**, Measured spin probabilities as a function of the total evolution time $2t$ for neighbouring qubit pairs for different virtual barrier gate voltages (with 0 and 1 corresponding to the exchange switched off and at its maximum value). **g**, Maximum exchange coupling measured for each qubit pair, and the corresponding residual exchange coupling for the other pairs, achievable within the AWG pulsing range without DC retuning. Bottom row: J_{ij} with all exchange couplings switched off (see Supplementary Data for error bars). **h**, Exchange coupling versus virtual barrier gate voltage for all qubit pairs. **i**, Schematic showing the energy levels in the absence (left) and presence (middle, right) of the effective Ising ZZ interaction under exchange (see main text). Due to the ZZ coupling term, the antiparallel spin states are lowered in energy, and pick up an additional phase as a function of time, resulting in a CPhase evolution. The shifted energy levels also allow for conditional microwave-driven rotations (CROT), which we use during initialization and readout. **j**, Pulse shape of the exchange amplitude throughout a gate voltage pulse used for the CZ gate, and the corresponding pulse shape converted to gate voltage.

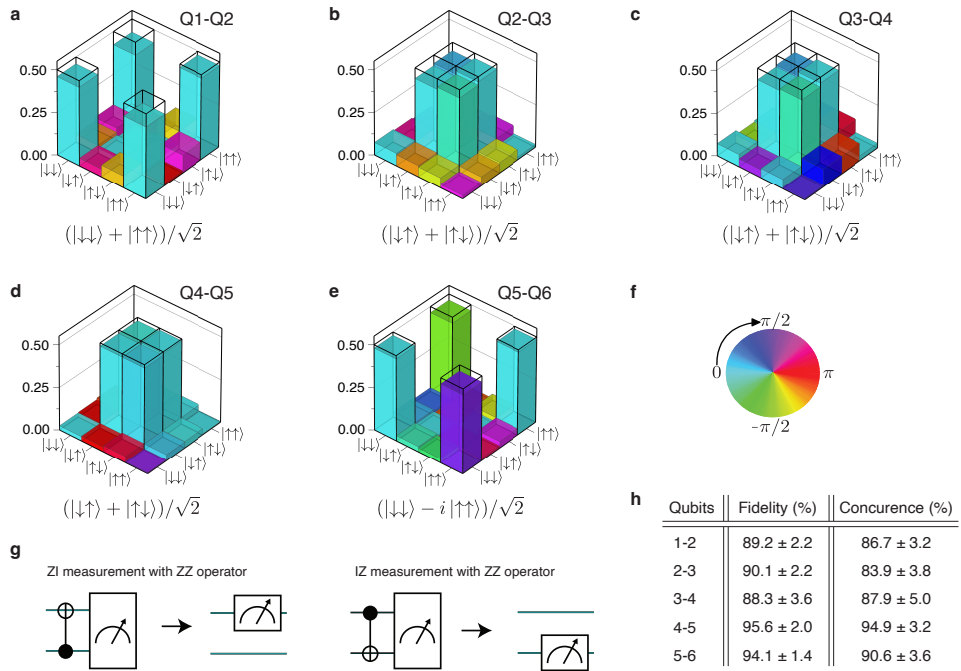


Figure 5.4: Bell state tomography **a-e**, Measured two-qubit density matrices for each pair of neighboring qubits, after removal of state preparation and measurement (SPAM) errors (see Supplementary Data for the uncorrected density matrices). The target Bell states are indicated and outlined with the wireframes. **f**, Color-wheel with phase information for the density matrices presented in panels **a-e**. **g**, Quantum circuits used for converting parity readout (ZZ) into effective single-qubit readout (IZ and ZI). **h**, State fidelities of the measured density matrices with respect to the target Bell states and the concurrences for the measured density matrices. Error bars (2σ) are derived from Monte-Carlo bootstrap resampling [44, 22, 46]. State fidelities without readout error removal, Q12: 88.2%, Q23: 83.8%, Q34: 78.0%, Q45: 91.3%, Q56: 91.3%.

the phase corrections for single-qubit operations and the dependence of J_{ij} on the virtual barrier gates vB_{ij} . Sometimes, specific calibrations, especially qubit frequencies and readout coordinates, are rerun throughout the day, as needed. Supplementary Data figure 3 plots the evolution of the calibrated values for a number of qubit parameters over the course of one month.

5.3. GENERATING ENTANGLED STATES

With single- and two-qubit control established across the six-qubit array, we proceed to create and quantify pairwise entanglement across the quantum dot array as a measure of the quality of the qubit control (Fig. 5.4a-e). These experiments benefited from a high level of abstraction in the measurement software, allowing us to flexibly program a variety of quantum circuits acting on any of the qubits, drawing on the table of 108 calibration parameters that is kept updated in the background and on the detailed waveforms to achieve high-fidelity gates. The parity readout of the outer qubits yields a native ZZ

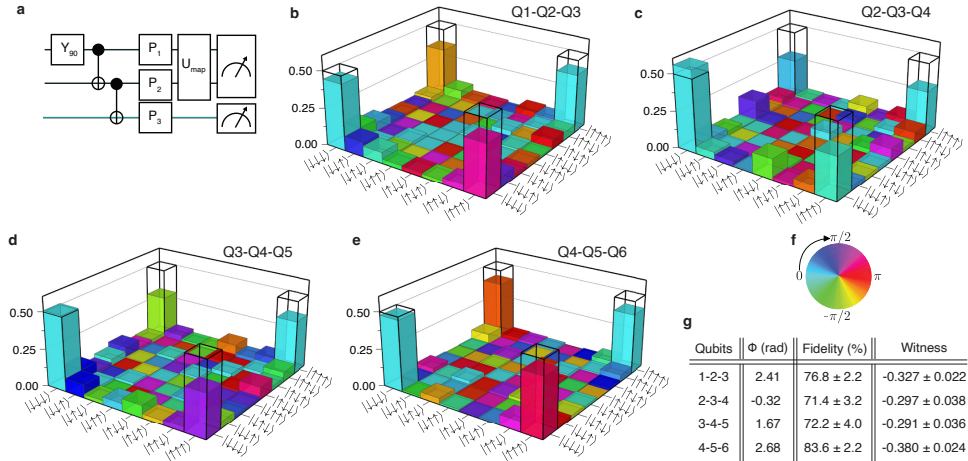


Figure 5.5: Three-qubit Greenberger-Horne-Zeilinger state tomography **a**, Circuit diagram used to prepare the GHZ states. The U_{map} operation is the unitary that is executed in case we measure the IZ or ZI projections on qubits 1/2 and 5/6, similar to the Bell state experiments. **b-e**, Density matrices of the prepared GHZ states using qubit 123, 234, 345 and 456, obtained using quantum state tomography, after removal of SPAM errors (see Supplementary Data for the uncorrected density matrices). The black wireframes correspond to the ideal GHZ state. **f**, Colorwheel with phase information for the density matrices presented in panels **d-e**. **g**, Table showing the state fidelities and entanglement witness values for the different qubit sets. We choose ϕ in $|\psi_{\text{GHZ}}\rangle = (|000\rangle + e^{i\phi}|111\rangle)/\sqrt{2}$, with respect to the highest state fidelity. State fidelities without SPAM removal, Q123: 64.3%, Q234: 52.8%, Q345: 52.7%, Q456: 67.2%

5

measurement operator. We measure single-qubit expectation values by mapping the ZZ operator to a ZI/I_Z operator, as shown in figure 5.4g. This allows full reconstruction of the density matrix. The state fidelity is calculated using $F = \langle \psi | \rho | \psi \rangle$, where ψ is the target state and ρ is the measured density matrix. The target states are maximally entangled Bell states. The obtained density matrices measured across the six-dot array have state fidelity ranging from 88% to 96%, which is considerably higher than the Bell state fidelities of 78% to 89% (all SPAM corrected, see methods) reported on two-qubit quantum dot devices just a few years ago [54, 22, 64].

As a final characterization of the qubit control across the array, we prepare Greenberger-Horne-Zeilinger (GHZ) states, which are the most delicate entangled states of three qubits [16, 41]. Fig. 5.5a shows the quantum circuit we used to prepare the GHZ states. The full circuit, including initialization and measurement, contains up to 14 CROT operations, 2 CZ operations, 42 parity measurements, 16 single-qubit rotations conditional on real-time feedback, and 5 single-qubit X₉₀ rotations (see Fig. 5.7). The measurement operators for quantum state tomography are generated in a similar manner as for the Bell states. In order to reconstruct three-qubit density matrices, we perform measurements in 26 (for qubits 234 and 345) or 44 (for qubit 123 and 456) different basis and repeat each set 2000 times to collect statistics. A full dataset consisting of 52000 (88000) single-shot repetitions takes about 5 minutes to acquire, thanks to the efficient uploading of waveforms to the waveform generator (see Methods) and the short

single-shot cycle times. Figs. 5.5b-e show the measured density matrices for qubits 123, 234, 345 and 456. The obtained state fidelities range from 71% to 84% (see Methods for a brief discussion of dephasing effects from heating). For comparison, the record GHZ state fidelity reported recently for a triple quantum dot spin qubit system is 88% [46]. The same data set from [46] analyzed without readout correction yields 45.8% fidelity, while our results with no readout error removal range from 52.8% to 67.2% (see Supplementary Data). The reduction in state fidelities compared to the two-qubit case (especially when involving qubits 3 and 4) is mainly due to increased SPAM errors. From the same data sets, we calculate entanglement witnesses, which clearly demonstrate three-qubit entanglement (see Supplementary Data).

5.4. CONCLUSION

The demonstration of universal control of six qubits in a $^{28}\text{Si}/\text{SiGe}$ quantum dot array advances the field in multiple ways. While scaling to a record number of qubits for a quantum dot system, we achieve Rabi oscillations for each qubit with visibilities of 93.5-98%, implying high readout and initialization fidelities. Initialization uses a novel scheme relying on qubit measurement and real-time feedback. Readout relies on Pauli spin blockade and quantum-non-demolition measurements. This combination of initialization and readout allows to the device to be operated while retaining the six electrons in the linear quantum dot array, alleviating the need for access to electron reservoirs. All single-qubit gate fidelities are around 99.9% and the high quality of the two-qubit gates can be inferred from the 89-95% fidelity Bell states prepared across the array. The development of a modular software stack, efficient calibration routines and reliable device fabrication have been essential for this experiment. Future work must focus on understanding and mitigating heating effects leading to frequency shifts and reduced dephasing times, as we find this to be the limiting factor in executing complicated quantum circuits on many qubits. The use of simultaneous single-qubit rotations and simultaneous two-qubit CZ gates will keep pulse sequences more compact, at the expense of additional calibrations. This will require accounting for cross-talk effects, which we anticipate will be easiest for the two-qubit gates. We estimate that the concepts used here for control, initialization and readout can be used without substantial modification in arrays that are twice as long, as well as in small two-dimensional arrays (see Supplementary Information). Scaling further will require additional elements such as cross-bar addressing to control dense 2D arrays [51, 27] and on-chip quantum links to connect local quantum registers together [48, 49, 7, 11].

5.5. METHODS

DEVICE FABRICATION

Devices are fabricated on an undoped $^{28}\text{Si}/\text{SiGe}$ heterostructure featuring an 8 nm strained ^{28}Si quantum well, with a residual ^{29}Si concentration of 0.08%, grown on a strain-relaxed $\text{Si}_{0.7}\text{Ge}_{0.3}$ buffer layer. The quantum well is separated from the surface by a 30 nm thick $\text{Si}_{0.7}\text{Ge}_{0.3}$ spacer and a sacrificial 1 nm Si capping layer. The gate stack consists of 3 lay-

ers of Ti:Pd metallic gates (3:17, 3:27, 3:27 nm) isolated from each other by 5 nm Al₂O₃ dielectrics, deposited using atomic layer deposition. A ferromagnetic Ti:Co (5:200 nm) layer on top of the gate stack creates a local magnetic field gradient for qubit addressing and manipulation. The ferromagnetic layer is isolated from the gate layers by 10 nm of Al₂O₃ dielectric. The cobalt layer is not covered with a dielectric. Further details of device fabrication methods can be found in [26].

After fabrication, all the devices are screened at 4 Kelvin. We check for current leakage, accumulation below the gates and device stability (e.g. drifts in current). The best device (if it meets our requirements) is selected and cooled down in a dilution refrigerator. The fraction of devices that pass these 4 K checks varies from 0 to 50% per batch (a batch contains either 12 or 24 devices).

MICROWAVE CROSSTALK AND SYNCHRONIZATION CONDITION

In Fig. 5.2, the single-qubit gates are chosen to be operated at a 5 MHz Rabi frequency and all single-qubit randomized benchmarking (RB) results are taken at this frequency as well. When operating all qubits within the same sequence, we were unable to operate at a 5 MHz Rabi frequency as qubits 2(3) and 5(4) are too close to each other in frequency. We used the synchronization condition [19, 43] to choose Rabi frequencies for the single-qubit gates for which the qubit that suffers cross-talk does not undergo a net rotation while the target qubit is rotated by 90 degrees or multiples thereof (see Fig. 5.10). The Rabi frequencies for the state tomography experiments are as follows (qubit 1-6): 4.6 MHz, 1.9 MHz, 4.2 MHz, 3.6 MHz, 2.4 MHz and 5 MHz.

AUTOMATED CALIBRATION ROUTINES

Calibrations are a crucial part in operating a multi-qubit device. Figure 5.1f lists the necessary calibration types that need to be corrected periodically and the Fig. 5.9 shows an example calibration for each parameter type. Every calibration uses an automated script to extract the optimal value for the measured parameter, which is recorded in a database. In our framework, the operator chooses to accept this value or to re-run the calibration.

Sensing dot – (5 s) – The calibrations routine starts by calibrating the sensing dots (Fig. 5.9a) to the most sensitive operating point for parity mode PSB readout. We scan the (virtual) plunger voltage of the sensing dot for two different charge configurations of the corresponding double dot, corresponding to the singlet and triplet states. One configuration is well in the (3,1) region, the other well in the (4,0) region, in order to be insensitive to small drifts in the gate voltages. The calibration returns the plunger voltage for which the largest difference is obtained in the sensing dot signal between these two cases (Fig. 5.9a). From this difference, we also set the threshold in the demodulated IQ signal of the RF-readout, to allow singlet/triplet differentiation (the IQ signal is converted to a scalar by adjusting the phase of the signal). The threshold is chosen halfway between the signals for the two charge configuration. During qubit manipulation, the sensing dot is kept in Coulomb blockade. It is only pulsed to the readout configuration when executing the readout.

Readout point – (35 s) – The parity mode PSB readout is calibrated by finding the optimal voltage of the plunger gates near the anticrossing for the readout. The readout point is only calibrated along one axis (vP1 or vP5), for simplicity, and since the performance of the PSB readout is similar at any location along the anticrossing. In the calibration shown in Fig. 5.9b, we initialize either a singlet ($| \uparrow \downarrow \rangle$) or a triplet ($| \downarrow \downarrow \rangle$, using a single-qubit gate) state and sweep the plunger gate to find to optimal readout point.

Q1/2/5/6 resonance frequency (rough) – (17 s) – We perform a coarse scan of the resonance frequencies of qubits 1, 2, 5 and 6 (Fig. 5.9c) around the previously saved values. We fit the Rabi formula

$$P_s(t) = \frac{\Omega^2}{\Omega^2 + \Delta^2} \sin^2 \left(\frac{\sqrt{\Omega^2 + \Delta^2}}{2} t \right) \quad (5.1)$$

to the experimental data and extract the resonance frequency.

5

QND READOUT: CROT Q32/Q45 f_{res} – (14 s) –

Subsequently, we calibrate the QND readout for qubits 3 and 4. To perform QND readout, we need to calibrate a CROT gate. We choose to use a controlled rotation two-qubit gate, as it requires little calibration (compared to the CPhase) given that we can ignore phase errors during readout.

We set the exchange to 10-20 MHz via barrier gate pulses and scan the CROT driving frequency (Fig. 5.9d) around the previously saved values. Again, we fit the Rabi formula

$$P_s(t) = \frac{\Omega^2}{\Omega^2 + \Delta^2} \sin^2 \left(\frac{\sqrt{\Omega^2 + \Delta^2}}{2} t \right) \quad (5.2)$$

to extract the optimal resonance frequency.

QND readout: CROT Q32/Q45 pulse width – (25 s) – Next, we tune the optimal microwave burst duration for the CROT gate, by driving Rabi oscillations (Fig. 5.9e) in the presence of the exchange coupling. We fit the decaying sinusoid

$$P_s(t) = \frac{A}{2} \sin(\omega t - \phi_0) e^{-\frac{t}{\tau}} + B \quad (5.3)$$

and extract the pulse width the for CROT gate.

Q3/4 resonance frequency (rough) – (28 s) – With QND readout established, we scan the driving frequency for qubit 3 and 4 in a similar manner as we did for Q1/2/5/6 (Fig 5.9f). The calibration scripts will automatically use QND readout for Q3 and Q4 calibration, in place of PSB readout for Q1, Q2, Q5, Q6.

Q1-6 resonance frequency and amplitude (fine) – (Q1, Q2, Q5, Q6 → frequency 22 s, amplitude 23 s; Q3, Q4 → frequency 32 s, amplitude 34 s) – We calibrate more accurately the qubit frequency and driving amplitude using an error amplification sequence (Fig. 5.9g-h), where we execute an X₉₀ gate 18 times and sweep either the frequency or the amplitude of the microwave burst. We fit the data using the Rabi formula once again

$$P_s(t) = \frac{\Omega^2}{\Omega^2 + \Delta^2} \sin^2 \left(\frac{\sqrt{\Omega^2 + \Delta^2}}{2} t \right) \quad (5.4)$$

to extract the resonance frequency. The amplitude of the microwave burst is controlled via the I/Q input channels of the vector source we used. To calibrate the amplitude for an X₉₀ rotation, we vary the amplitude applied to the I/Q input and fit the result to

$$P_s(x) = \alpha e^{-\frac{(x-\mu)^2}{2\sigma^2}}. \quad (5.5)$$

This functional form is not strictly correct but it does find the optimal amplitude for an X₉₀ rotation. We suspect that the longer amplification sequences gave better results, as they more closely resemble the sequence lengths used for randomized benchmarking (including some 'heating effects').

In these calibrations, we only calibrate the X₉₀ gate. The Y₉₀ gate is implemented similarly to the X₉₀, but phase shifted. Z gates are performed in software by shifting the reference frame. X₁₈₀ and Y₁₈₀ rotations are performed by applying two 90 degree rotations. We do not simultaneously drive two or more qubits.

Q1-6 X₉₀ phase crosstalk – (Q1, Q2, Q5, Q6 → 27 s; Q3, Q4 → 45 s) – Any single-qubit gate causes the Larmor frequency of the other qubits to shift slightly due to the applied microwave drive. We compensate for this by applying a virtual Z rotation to every qubit after a single-qubit gate has been performed. The Ramsey based sequence is used to calibrate the required phase corrections (Fig. 5.9i) and data is fitted with

$$P_s(\phi) = -\frac{A}{2} \cos(\phi - \phi_0) + B \quad (5.6)$$

to extract the necessary phase correction, ϕ_0 . A single X₉₀ pulse on one qubit will impart phase errors on qubits 2 to 6. Thus we need to calibrate separately 30 different phase factors, five for each qubit.

J_{ij} vs vB_{ij} – (Qubit pairs 12, 56 → 146 s; Qubit pairs 23, 45 → 207 s; Qubit pair 34 → 299 s) – Two-qubit gates are implemented by applying a voltage pulse that increases the tunnel coupling between the respective quantum dots. To enable two-qubit gates, we take the following elements into account:

- Exchange strength. We operate the two-qubit gates at exchange strengths J_{on} where the quality factor of the oscillations is maximal. This condition is found for $J_{\text{on}} \approx 5$ MHz.

- Adiabaticity condition. When the Zeeman energy difference (ΔE_z) and the exchange ($J(t)$) are of the same order of magnitude, care has to be taken to maintain adiabaticity throughout the CPhase gate. We do this by applying a Tukey based pulse, where the ramp time is chosen as $\tau_{\text{ramp}} = \frac{3}{\sqrt{\Delta E_z^2 + J_{\text{on}}^2}}$ [30].
- Single-qubit phase shifts. As we apply the exchange pulse, the qubits will physically be slightly displaced. This causes a frequency shift and hence phase accumulation, which needs to be corrected for.

In order to satisfy these conditions, we need to know the relationship between the barrier voltage and the exchange strength. We construct this relation by measuring the exchange strength (see figure 5.3a) for the last 25% of the virtual barrier pulsing range ($J > 1$ MHz regime). We fit the exchange to an exponential and extrapolate this to any exchange value (Fig. 5.9j). This allows us to generate the adiabatic pulse as described in the main text and choose the target exchange value.

5

CZ duration – (Qubit pairs 12, 56 → 29 s; Qubit pairs 23, 45 → 34 s; Qubit pair 34 → 45 s) – The gate voltage pulse to implement a CZ operation uses a Tukey shape in J by inverting the relationship $J(vB_{ij})$. The maximum value of J is capped at J_{on} . The actual largest value of J used and the length of the pulse then determine the phase acquired under ZZ evolution. We first analytically evaluate the accumulated ZZ evolution as a function of these parameters around the target of π evolution under ZZ, and then experimentally fine tune the actual accumulated ZZ evolution by executing a Ramsey circuit with a decoupled CPhase evolution in between the two $\pi/2$ rotations. An example of such a calibration measurement is shown in Fig. 5.9k.

CZ phase crosstalk – (Q1, Q2, Q5, Q6 → <30 s; Q3, Q4 → <50 s) – After the exchange pulse is executed, single-qubit phases have to be corrected. We correct these phases on all the qubits, whether participating or not in the two-qubit gate. We calibrate the required phase corrections in a very similar way as done for the single-qubit gate phase corrections. An example of the circuit and measurement is given in Fig. 5.9l-m. The exact calibration run-time depends on the CZ pulse width and can vary by couple of seconds depending on the target qubit.

HEATING EFFECTS

We observed several effects that bear a signature of heating in our experiments. When microwaves (MWs) are applied to the EDSR line of the sample, several qubit properties change by an amount that depends on the applied driving power and the duty cycle of applying power versus no power. This effect has also been observed in other works [47]. We report our findings in Fig. 5.11 and will discuss adjustments made to the sequences of the experiments to reduce their effects. The main heating effects are a reduction of the signal-to-noise ratio (SNR) of the sensing dot and a change of the qubit resonance frequency and T_2^* .

In Fig. 5.11a-d, we investigate the effect of a MW burst applied to the EDSR driving gate, after which the signal of the sensing dot is measured. We observe changes in the background signal and in the peak signal (the electrochemical potential of the sensing dot is not affected, as the peak does not shift in gate voltage). Since the background signal rises more than the peak signal, the net signal is reduced. This reduction depends on the magnitude and duration of the applied MW pulse (Fig. 5.11b). The original SNR can be recovered by introducing a waiting time after the MW pulse. The typical timescale needed to restore the SNR is in the order of 100 μ s (see Fig. 5.11c-d). We added for all (RB) data taken in this paper a waiting of 100 μ s (500 μ s) after the manipulation stage to achieve a good balance between SNR and experiment duration. Spin relaxation between manipulation and readout is negligible, given that no T_1 decay was observed on a timescale of 1 ms within the measurement accuracy. We did not introduce extra waiting times after feedback/CROT pulses in the initialization/readout cycle, as the power to perform these pulses did not limit the SNR.

Fig. 5.11f gives more insight in what makes the background and peak signal of the sensing dots change. The impedance of the sensing dot is measured using RF-reflectometry. The background of the measured signal depends on the inductance of the surface-mount inductor, the capacitance to ground[10, 35, 28] and the resistance to ground of the RF readout circuit. Fig. 5.11f shows the response of the readout circuit under different MW powers (the RF power is kept fixed). A frequency shift (0.5 MHz) and a reduction in quality factor is observed. This can be indicative of an increase in capacitance and dissipation in the readout circuit. Presently the microscopic mechanisms that cause this behavior are unknown.

The second effect is observed when looking at the qubit properties themselves. Fig. 5.11e shows that both the dephasing time T_2^* measured in a Ramsey experiment and the qubit frequency are altered by the microwave radiation. In the actual experiments, we apply a MW pre-pulse of 1-4 μ s before the manipulation stage to make the qubit frequency more predictable, though this comes at the cost of a reduced T_2^* . The pre-pulse can be applied either at the start or at the end of the pulse sequence, with similar effects. This indicates that heating effects on the qubit frequency persist for longer than the total time of a single-shot experiment ($\approx 600 \mu$ s), different from the effect on the sensing dot signal. Also the microscopic mechanisms behind the qubit frequency shift and T_2^* reduction remain to be understood.

PARITY MODE PSB READOUT

Pauli spin blockade (PSB) readout is a method used to convert a spin state to a more easily detectable charge state[37]. Several factors need to be taken into account for this conversion, to enable good readout visibilities. Fig. 5.6a-b shows the energy level diagrams for PSB readout performed in the (1,1) and (3,1) charge occupation. The diagrams use valley energies of 65 μ eV, to illustrate where problems can occur. When looking at Fig. 5.6, we can observe two potential issues:

- The excited valley state with $|\downarrow\downarrow\rangle$ is located below the ground valley state with $|\uparrow\uparrow\rangle$. We assume in the diagram that the (2,0) singlet state ($|S,0\rangle$) is coupled to both the

(1,1) ground valley state and the (1,1) excited valley state. In this case, during the initialisation/readout pulses, population can be moved into the excited valley state. This problem can be solved by working at a lower magnetic field, such that $E_v > E_z$ (panel Fig. 5.6b).

- When operating in the (1,1) charge occupation, the readout window is quite small, as the size is determined by the difference between the valley energy and the Zeeman energy. A common way to prevent this problem is by operating in the (3,1) electron occupation.

With both measures in place, we consistently obtain high visibilities of Rabi oscillations ($\geq 94\%$) on every device tested.

In the following we describe the procedure used to tune up the parity mode Pauli Spin Blockade.

5

1. Find an appropriate tunneling rate at the (3,1) anticrossing. An initial guess of a good tunneling rate can be found using video mode tuning. We use the arbitrary waveform generator to record at high speed frames of the charge stability diagram (5 μ s averaging per frame, $t_{\text{image}} = 200$ ms). While the frames are measured, we vary the tunnel coupling, while looking at the (3,1) \leftrightarrow (4,0) anticrossing until the pattern shown in Fig. 5.6c is observed. This figure shows that depending on the (random) initial state, the transition from (3,1) to (4,0) occurs at either location (i) or location (ii). This is exactly what needs to happen when the readout is performed.
2. Find the readout point. We hold point (1) fixed in the center of the (3,1) charge occupation (Fig. 5.6c). Point (2) is scanned with the AWG along the detuning axis as shown in Fig. 5.6c. We pulse from point (1) to point (2) and measure the state (ramp time of $\sim 2 \mu$ s), then we pulse back to point (1). When plotting the measured singlet probability, a gap is seen between the case where a singlet is prepared versus a random spin state is prepared (Fig. 5.6d). The center of this region is a good readout point.
3. Optimizing the readout parameters. The main optimization parameters are the detuning (ϵ), tunnel coupling (t_c) and ramp time to ramp towards the PSB region. We also independently calibrate the ramp time and tunnel coupling from the readout zone towards the operation point of the qubits. When ramping in towards the readout point, it is important to be adiabatic with respect to the tunnel coupling. We do not need to be adiabatic with respect to spin, as both $|\uparrow\downarrow\rangle$ and $|\downarrow\uparrow\rangle$ relax quickly to the singlet state (faster than we can measure, < 1 ns). When pulsing from the readout to the operation point, more care has to be taken. When using the ramp time which performs well for readout, we notice that we initialize a mixed state, as we are not adiabatic with respect to spin. This can be solved by pulsing the tunnel coupling to a larger value before initiating the initialization ramp (Fig. 5.6g).

We show in the Fig. 5.6e-f, that the histograms for parallel and anti-parallel spin states are well separated, allowing for a spin readout fidelity exceeding 99.97% for both qubits 1-2 and for qubits 5-6. This number could be further increased by integrating the signal for longer, but is not the limiting process. This way of quantifying the spin readout

fidelity is commonly used in the literature but it leaves out errors occurring during the ramp time (mapping of qubit states to the readout basis states). This can be a significant effect, as seen from the measured visibility of the Rabi oscillations.

Post-selection of data When using parity readout on a single qubit pair, ~5% of the runs are discarded on average as part of the initialization procedure (see Fig. 5.1d). In case two outer qubit pairs are used, about ~10% of the data is discarded ($1 - 0.95^2$). When performing experiments on all six qubits, additional initialization steps with post-selection are needed (in Fig. 5.7, runs are post-selected based on 18 measurement outcomes in total), and we discard ~65% of the data set. When we do not discard any runs, the initialization fidelity reduces with ~5-9% for a single qubit pair.

DATA FIGURES AND TABLES

5

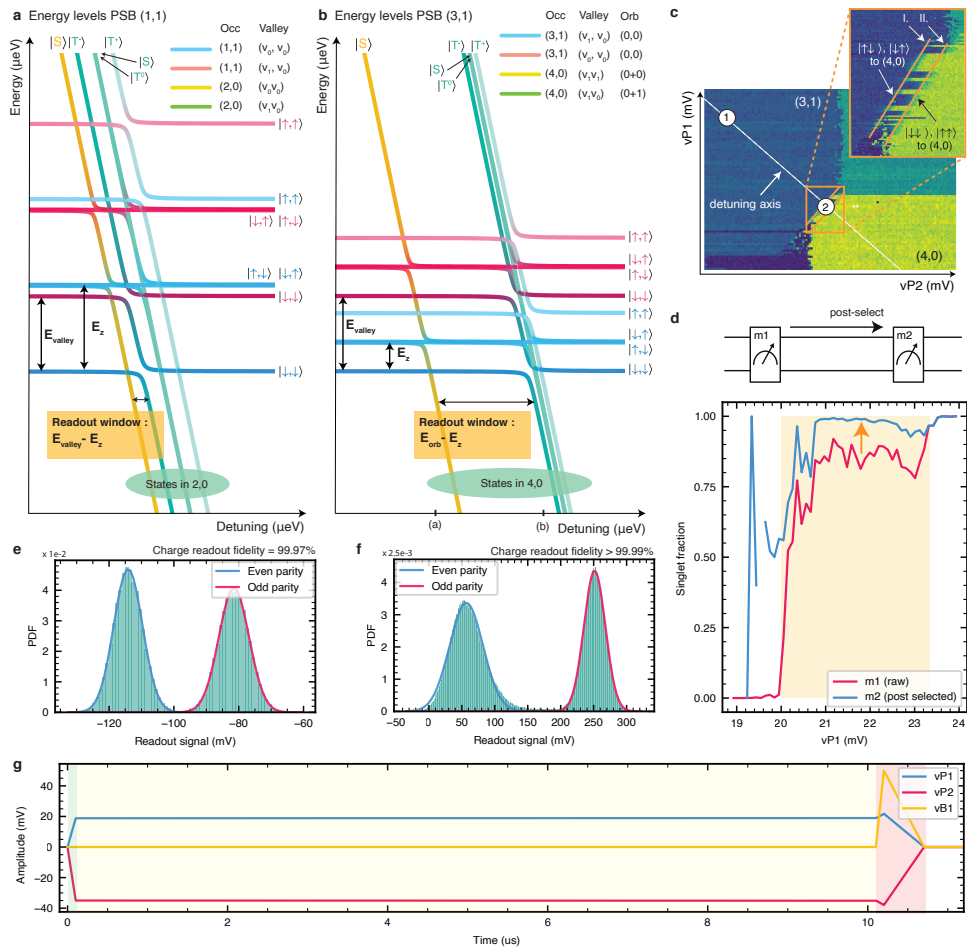


Figure 5.6: **Pauli Spin Blockade readout** **a**, Energy diagram for a double quantum dot as a function of the detuning between the (1,1)/(2,0) charge electron occupation. The Zeeman energy (E_z) for qubit 1/2 is set to 74/75 μeV (18/18.2 GHz) and the valley energy (e_v) of dot 1 is set to 65 μeV . We set e_c for the second dot to a much larger value to shift part of the energy spectrum out of view and simplify the visual analysis. The charge and valley occupations are indicated in the top right of this panel. **b**, Energy diagram in the (3,1)/(4,0) charge occupation. This panel uses identical parameter values as panel **a**, except for the Zeeman energy for qubit 1 and 2, 25/26 μeV (6 and 6.2 GHz). The excited state energy of dot 1 in the (4,0) charge occupation is given by the orbital energy instead of the valley splitting. **c** Experimental charge stability diagram taken at the (3,1)/(4,0) anticrossing for dots 1 and 2. The point indicated with '1' indicates the qubit operation point and the point indicated as '2' indicates the readout point. The inset zooms in on the anticrossing, allowing one to observe the spin selective tunneling for the different input states (the readout zone). **d** In our experiment we initialize via measurement and post-selection. In the plot we can see the effects of two subsequent readouts. First readout 'm1 (raw)' shows the initial singlet fraction (electron spins are not intentionally randomized and by nature of the executed measurement sequence, a singlet state is preserved for next single shot). Second measurement 'm2' shows the outcome from post-selection on the result of 'm1' (realized as per-measurement-point post-processing in software). Within the readout zone (shaded area) the initialized singlet fraction is greatly amplified. **e-f** Probability density function of the PSB readout signal between qubit pairs 12 and 56 (10 μs integration time), recorded in the course of the Rabi oscillations of qubit 1/5 in figure 5.2. The Gaussians are fitted to the two distributions and charge readout fidelities, estimated from their overlap, exceeding 99.9%. No T_1 decay was observed at the readout point ($T_1 \gg 100 \mu\text{s}$). **g**, Gate voltage pulses applied to perform PSB readout on qubit pair 12. The different background colors indicate the ramp towards the readout point (green), measurement at the readout point (yellow) and the adiabatic ramp back to the operating point (red).

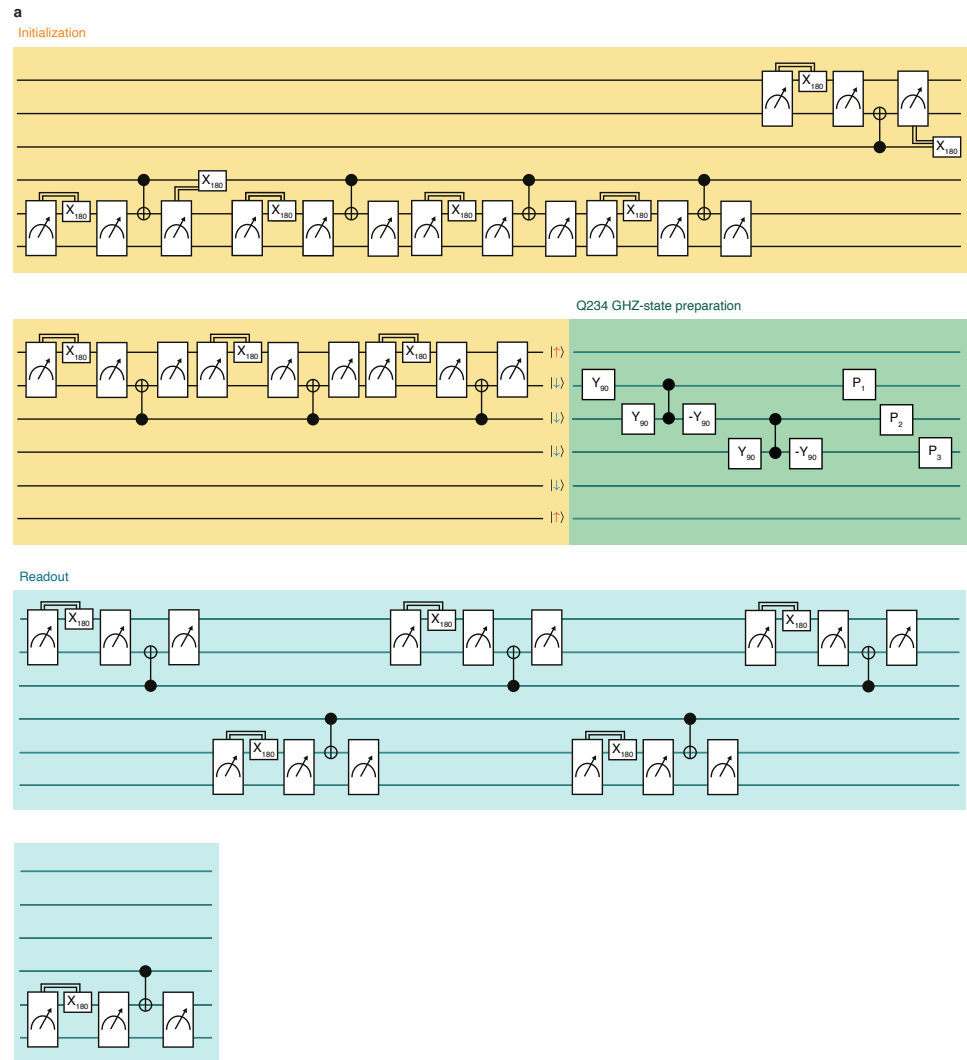
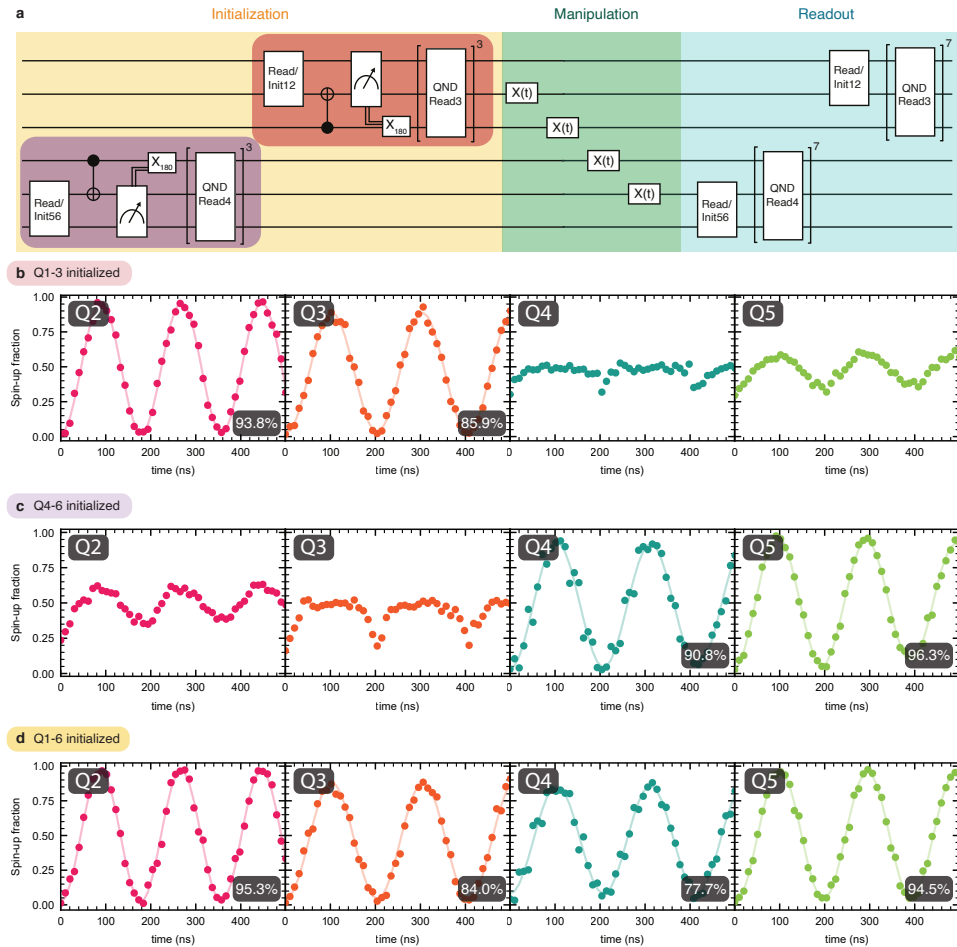


Figure 5.7: **Full quantum circuits.** **a**, This circuit was used to produce the data presented in Fig. 5.5c. The different background colors indicate the different parts of the sequence (yellow – initialization, green – manipulation (including the tomography pulses), blue – readout). The sequence could be made significantly shorter if we would parallelize the readout operations. We did not implement this, since this is not the limiting factor ($t_{read} \ll T_1$).



5

Figure 5.8: Loss in visibility when initializing all qubits. **a**, Gate sequence used to demonstrate the effect of running different qubit initialization routines. Microwave bursts with variable duration are performed sequentially on qubits 2, 3, 4 and 5, as shown in the schematic. In all cases, readout is performed on all the qubits, but we vary which qubits are initialized for a particular experiment. **b-d**, Results of the sequence displayed in panel **a**, when qubit 1-3 (**b**), 4-6 (**c**) or 1-6 (**d**) are initialized. The shaded numbers in the panels indicate the visibility of the measured qubit. With all qubits initialized we observe a visibility loss on qubit 4 and to a lesser extent qubit 3. A visibility loss in principle can originate from a reduced readout or initialization fidelity. We keep the readout sequence identical for **a**, **b**, and **c**. Additionally, we include a 500 μ s waiting time prior to readout, to minimize any effects of MW pulsing during initialization or manipulation stage on the readout performance (see Methods). Although, we cannot be certain that the readout fidelity is unaffected by the initialization of all qubits, we speculate that the majority of the observed visibility loss is due to a reduced initialization fidelity, possibly due to the sensitivity of the CROTs to qubit frequency shifts. This interpretation is consistent with the fact that mostly qubit 4 suffers a lower visibility, as qubit 4 is initialized before qubits 1,2 and 3. If instead we reverse the initialization order, qubit 3 displays lowered visibility (data not shown).

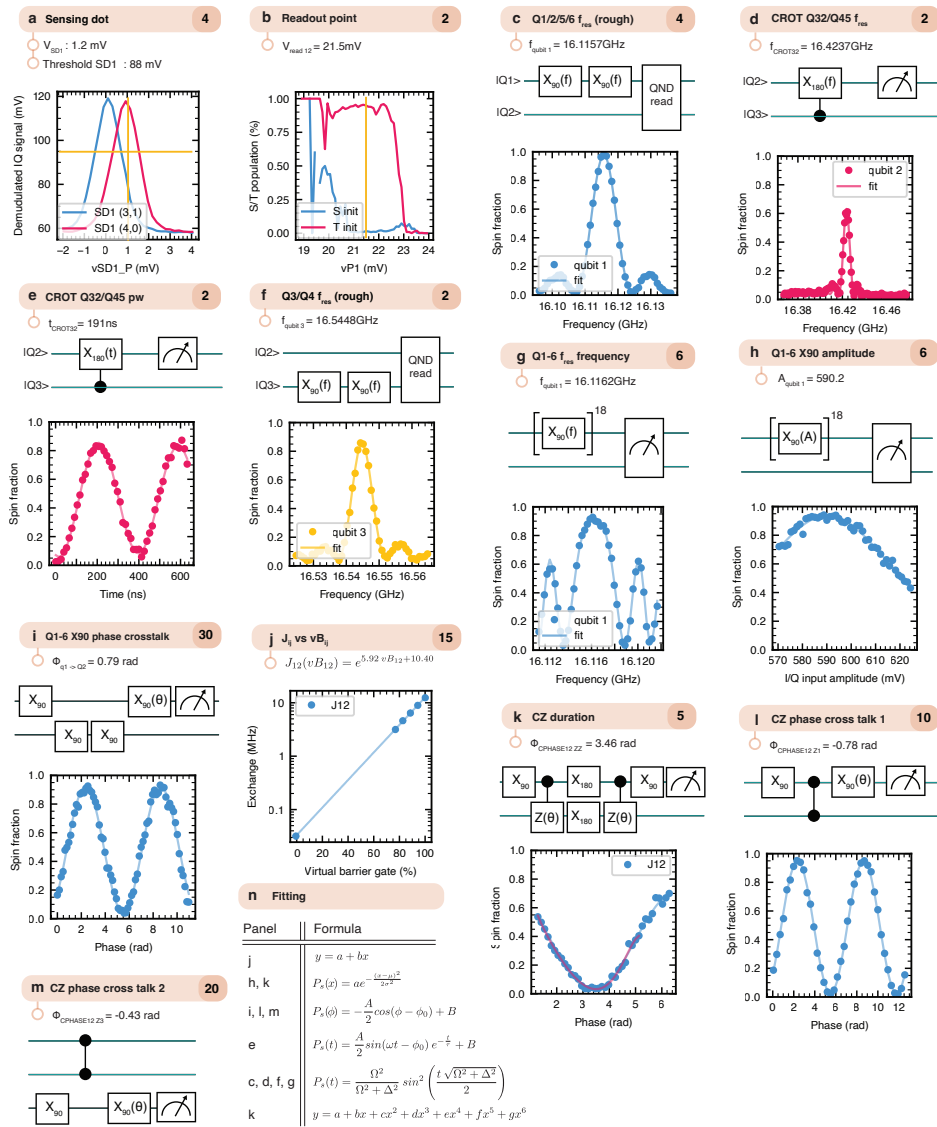


Figure 5.9: **Calibrations a-m** Each panel shows a typical experimental dataset obtained in one of the calibration routines for the relevant experimental parameters. Every panel indicates in the header the calibration name and the corresponding number of calibration parameters. Below the header, the values extracted from the data is indicated. See the methods section for a detailed description. **n**, Table showing the formulas used to fit the data for the indicated figure panels.

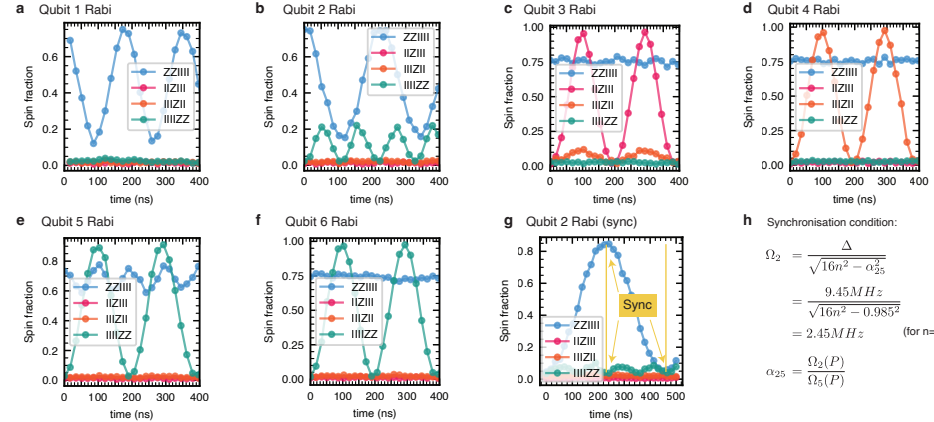


Figure 5.10: Crosstalk a-f. In this experiment all qubits are initialized. We observed the presence of crosstalk by measuring the expectation values of the native observables on the sample. **a-e**, Rabi oscillations executed on different qubits in each panel. Panels b, c and e display coherent oscillations of nominally idle qubits, which are a clear indication of crosstalk at the chosen Rabi frequencies. Qubits 1 and 2 show flipped measurement outcomes due to a miscalibration of sensing dot 1. This bears no influence on the conclusion from this experiment. **g**, Example of qubit 2 driven at the frequency determined by the synchronization condition. In this case the crosstalk to qubit 5 (qubit with the closest resonance frequency) was nullified by design for every multiple of a 90 degree rotation. **h**, Expressions [19] used to calculate the synchronization condition shown in panel **g**.

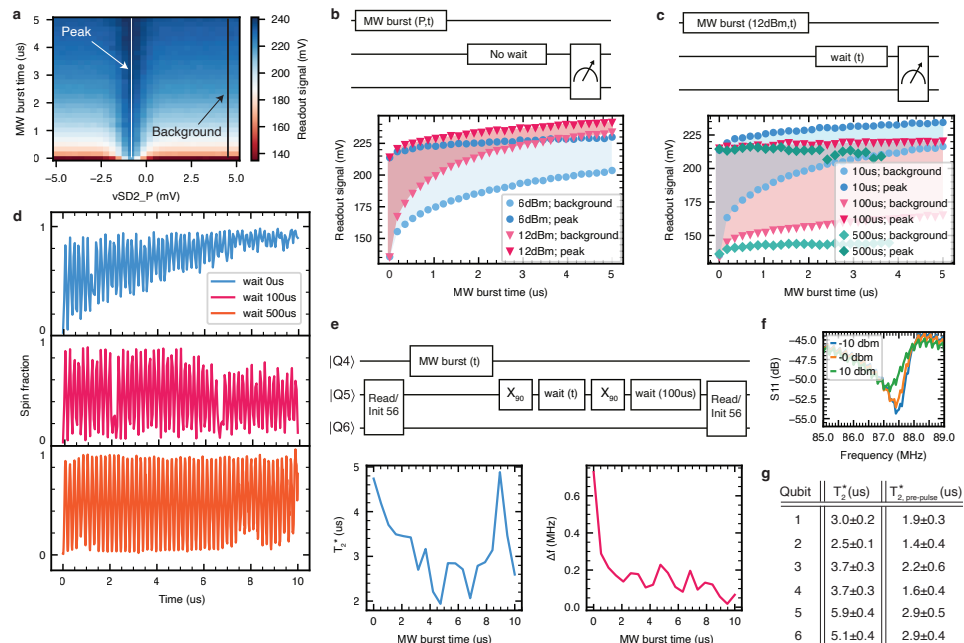


Figure 5.11: **Heating effects** **a**, A microwave burst of 16 GHz at 12 dBm output power and of a variable duration is applied before scanning the sensing dot virtual plunger gate. We observe no shift of the Coulomb peak, indicated by the white line, but the background signal increases significantly. Also the peak signal increases, but by a smaller amount. **b**, Linecut along the Coulomb peak and linecut parallel to the Coulomb peak of panel **a**, showing the peak and background signal as a function of the MW burst duration, for two different powers. The shaded area indicates the net signal, which is smaller the larger the applied power and the longer its duration. **c**, Variation on panel **b**, where we introduce a waiting time after the microwave burst, as indicated in the schematic. The longer the wait time, the more the original SNR is recovered, and the higher the readout fidelity will be. **d**, Rabi oscillations with different waiting times introduced before the qubit readout. The 500 μ s wait time allows for recording long lived Rabi oscillations, while with no wait time prior readout, the contrast vanishes as the perceived spin fraction converge towards 1, due to shifts in the sensing dot signal and background (the threshold for single-shot analysis was kept fixed). **e**, Schematic showing the circuit used to investigate the effect of a pre-pulse (labelled MW burst (t)) on the qubit properties. A microwave burst of 6 dBm is applied before running a Ramsey experiment. We extract the change in T_2^* and Larmor frequency for qubit 5 for different microwave burst times as shown in the plots. **f** Return loss of the RF readout circuit for different powers of continued microwave driving (i.e. driving at the qubit frequencies, not for the RF readout). We observe both a shift in the RF resonance frequency and a degradation of the quality factor with higher power excitation. **g**, Extracted dephasing times T_2^* with and without pre-pulse (4 μ s, 6 dBm), measured as illustrated in **e**.

5

	vB0	vB1	vB2	vB3	vB4	vB5	vB6
$V_{J_{12}}$	-1	1	-1.6	0	0	0	0
$V_{J_{23}}$	0	-0.2	1	-0.5	0	0	0
$V_{J_{34}}$	0	0	-0.3	1	-0.3	0	0
$V_{J_{45}}$	0	0	0	-0.9	1	-0.9	0
$V_{J_{56}}$	0	0	0	-0.2	-0.9	1	0

Table 5.1: **Exchange pulses.** In order to achieve sufficiently high $J_{\text{on}}/J_{\text{off}}$, we use a combination of barrier gate pulses, where we pulse a barrier gate in between the target qubit pair to a more positive voltage and at the same time we pulse the voltage on the barrier gates on the outer side of target qubit pair to a less positive voltage. This pushes the two quantum dots towards each other further enhancing the tunnel coupling.

5.6. CONSIDERATIONS ON SCALING

5.6.1. SCALING LIMITATIONS OF THE METHODS USED IN THE PRESENT WORK

We briefly comment on the scaling limitations of some of the methods used in the present experiment, and mention the key ingredients we believe will be necessary for scaling to larger systems.

Micromagnets for EDSR In the present design, there is frequency selectivity along one axis only (its design requirements are discussed in 5.7). The micromagnet design would need to be modified for small 2D arrays in order to get selectively of the qubit frequencies in two dimensions in combination with a sufficiently strong transverse gradient for driving. No micromagnet patterns have been developed that work well in large two-dimensional arrays. Therefore, we believe that a more fruitful path is to use local arrays of a moderate size (where micromagnets can be used and designed to minimize decoherence gradients) and network them together on the same chip using quantum links.

We furthermore note that a known disadvantage of EDSR with micromagnets is that the artificial spin orbit coupling generated by the micromagnets allows charge noise to cou-

ple to the spin qubits (this is directly connected to the need for frequency selectivity between neighboring qubits). Also, questions remain on how uniform or reproducible the field of a micromagnet can be across a chip with thousands of micromagnets.

Sensing dots Device A had a sensing dot near the middle of the array in addition to two sensing dots at the end of the array. The sensing dots at the end of the array have the maximum sensitivity to interdot transitions, which we were interested in here. Since we found the full 6-qubit array could be tuned up without the third sensing dot alongside the array, we left it out in devices B and C in order to slightly reduce the complexity of fabrication. Such a third sensor would have made it possible to probe PSB directly on the inner pair of dots. For longer one-dimensional arrays, we would place a sensing dot alongside the qubit array every 3 qubit dots [63].

QND Readout QND can be performed sequentially on multiple qubits, such that multiple qubits can be read out that are too far away from the charge sensors to be read out directly. For instance, in a linear array, one can perform QND readout of qubit 4 by mapping its state onto that of qubit 3, and from there onto that of qubit 2, which is in turn read out using the charge sensor. QND readout of qubit 5 can be done by mapping it onto the state of qubit 4, and so on. This would involve linear overhead in the length of the chain. However, the errors from the successive mapping (CROT/CNOT) operations would accumulate for concatenated QND readout. Alternatively, the number of QND repetitions needed to achieve the target readout fidelity would increase, making the overall overhead a bit higher than linear in the distance. This concept works also in 2D, again with overhead. However, the successive QND measurements would increase the total measurement time, which must remain shorter than the coherence time when implementing quantum error correction schemes.

Alternative readout schemes include CCD like concepts where electrons are shuttled to the sensor one after the other [4] or cascade effects are used [12] to propagate spin-dependent charge motion to the charge sensors.

5.6.2. PATH FORWARD TO LARGER SYSTEMS

This constitutes a full research topic in itself, which we have spent considerable time thinking about and published several proposal/design papers. For large dense 2D arrays, we have shown that cross-bar addressing techniques can provide universal control and readout [27]. Proposals also exist for bringing individual wires to every qubit in a dense 2D array [51]. Either way, there will still be limits to how large such 2D arrays will work well, for instance because of the limitations of this approach for parallel operations. To scale beyond, we envision networks of local registers [48, 49], connected together with quantum coherent links. Such links can consist of shuttling channels, or perhaps of superconducting resonators, or other methods. An alternative strategy we have explored conceptually is to use highly sparse 2D arrays instead [7]. Also other groups have given the operation of such on-chip spin qubit networks detailed consideration, see e.g. [11].

5.7. MICROMAGNET DESIGN

Most micromagnets used in spin qubit experiments have been designed to support up to 2 to 3 qubits [40, 61, 13]. In this experiment, a suitable gradient was needed across a six-qubit device. A schematic of the micromagnet design, along with the coordinate system is shown in Fig. 5.12. When designing the magnet, we set the following requirements:

- Target Rabi frequency of 5-10 MHz. The higher the driving speed, the more operations can be completed within the coherence time. We limit the target frequency to 10 MHz as we have found the Rabi frequency to become non-linear in the driving amplitude for higher Rabi frequencies (see also ref. [60]). Based on prior experience, this translates to a target gradient in the transverse component of the micromagnet stray field of at least 1 mT/nm.
- All the qubits are driven by a single gate using frequency multiplexing. Overlap in resonance frequencies must thus be avoided. We target a frequency difference of 100 MHz between different qubits when the micromagnets are fully magnetized. This value is chosen as it results in an acceptable level of crosstalk when driving the qubits at a Rabi frequency of 5-10 MHz.
- Following [60], we aim at a maximal decoherence gradient ($|\frac{\partial B_z}{\partial z}| + |\frac{\partial B_z}{\partial y}|$) of 0.1 mT/nm. In this way, qubit coherence is not impacted assuming an intrinsic qubit linewidth of $\delta f \sim 10$ kHz. We report the decoherence gradient calculated at the center of the quantum dot location.

5

To design the micromagnets, we parametrized a model of the magnets and optimized a number of design parameters (e.g. the magnet-magnet separation, height of the magnets, size and angle of the slanting part and distance from the quantum well). The core of the calculations was based on the python package magpylib [38], which allows for fast analytical solutions of simple magnet geometries (our wrapper can be found at [39]). We assume full magnetization of the micromagnet in our simulations. The result of the optimization is shown in Fig. 5.12 b-f. In panel b-c, one can visually inspect the micromagnet stray magnetic field profile. Panel d-f show line cuts of magnetic properties described above, along the length of the six-qubit array. We are able to satisfy all our design targets.

Fig. 5.12g-i show the measured frequency distributions of the qubits on three samples from different fabrication runs. The measured frequency profile for sample A is comparable to the simulated profile of Fig. 5.12d. For samples B and C, the measured frequencies are very different than expected based on the simulations. The parabolic trend seen in Sample C (the sample discussed in the main text paper) can be roughly reproduced by assuming that the magnet boundary is displaced. The solid white lines in Fig. 5.12j show the bottom and the top of the magnet, indicating that the micromagnet sidewalls are slightly tilted, which indeed effectively displaces the magnet boundary. When simulating the frequency profile with the black dashed line as the magnet boundary (as a rough approximation), we obtain the profile shown in purple in Fig. 5.12i. The qubit frequencies reported in these plots are reproducible between different cooldowns of the same device.

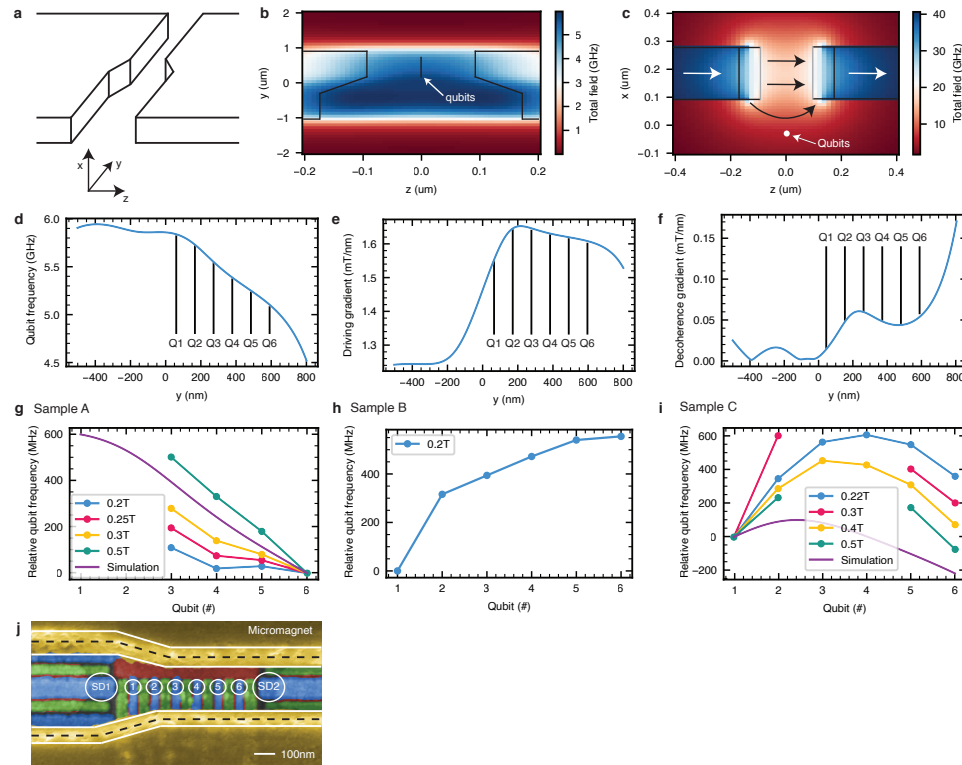


Figure 5.12: Micromagnet simulations and experimental values

a, Sketch of the micromagnet structure in 3D. The micromagnets are magnetized along the z direction, with a magnetization vector of $M = (0 \text{ T}, 0 \text{ T}, 1.5 \text{ T})$ as estimated from the experiments. The maximum magnetisation is reached in the experiment when 0.1–0.2T external field is applied to the magnets.

b, Simulation of the total field generated by the micromagnets in the z,y plane, where the quantum dots reside. A projection of the micromagnets is shown by the black lines overlaid in the figure.

c, Simulation of the total field generated by the micromagnets in the z,x plane.

d, Simulated values for the qubit frequencies (without the contribution of the externally applied magnetic field) along the y axis, with the target qubit positions indicated.

e, Simulated values for the (transverse) driving gradient of the micromagnet ($| \frac{\partial B_x}{\partial z} | + | \frac{\partial B_y}{\partial z} |$) along the y axis, with the target qubit positions indicated.

f, Simulated values of the decoherence gradient of the micromagnet ($| \frac{\partial B_z}{\partial z} | + | \frac{\partial B_z}{\partial y} |$) along the y axis, with the target qubit positions indicated.

g-i, Experimentally measured qubit frequencies for three different samples with the same micromagnet design. All frequencies in the plots are taken in reference to one qubit, to clearly display the difference in qubit frequency distribution versus the different fields applied to the sample. The simulated curve in panel i is computed assuming the magnet boundary is as indicated by the dashed black line in panel j.

j, False colored SEM image of a sample similar to sample C and fabricated in the same fabrication run. The white lines indicates the top and bottom edge of the micromagnet, with inner lines indicating the intended step boundary. The black, dashed line is the average distance between top and bottom edge of the magnets.

5.8. DIFFERENT SAMPLES TESTED FOR THIS EXPERIMENT

	Device A	Device B	Device C
Design			
Number of qubits	6	6	6
Number of sensing dots	3	2	2
Access to reservoir from dots	1, 6	1, 3, 4, 6	1, 6
Dot pitch	100 nm	80 nm	90 nm
Tuning for sufficient t_c	3,1,3,1,3,1	1,1,1,1,1,1	1,1,1,1,1,1
Comment	Right SD unusable due to faulty source contact		
Valley splitting (μeV)			
Substrate [56]	Quantum well A	Quantum well B	Quantum well B
Dot 1	160	118.9	220
Dot 2	130	160.8	140
Dot 3	0	113.4	105
Dot 4	173	160.9	138
Dot 5	–	56.8	220
Dot 6	–	148.4	300
Comment	Valley splitting in dot 3 too low for qubit experiments		
Dephasing time T_2^* (μs)			
Dot 1	12.7	3.0	3.0
Dot 2	5.5	3.2	2.5
Dot 3	3.4	6.0	3.7
Dot 4	7.2	3.0	3.7
Dot 5	–	6.5	5.9
Dot 6	–	6.4	5.1
Hahn echo decay time T_2^h (μs)			
Dot 1	24.8	77	14.0
Dot 2	28.1	47	21.1
Dot 3	–	75	40.1
Dot 4	26.9	48	37.2
Dot 5	–	58	44.7
Dot 6	–	41	26.7
General comment			
	Sample discarded due to low valley splitting in dot 3	Sample discarded due to low EDSR drive quality	Sample used in this experiment

Table 5.2: **Properties of different samples tested for this experiment.** In the course of this experiment, we have modified the sample design to match the requirements set for 6-qubit control. Device A has been discarded due to the low valley splitting in dot 3. Additionally, we could only use 4 out of 6 quantum dots, due to a failure on the right sensing dot. Due to the 100 nm dot pitch, it was necessary to tune the device to the (3,1,3,1,3,1) charge configuration in order to achieve sufficient tunnel coupling t_c between adjacent dots. Device B allowed for 6-qubit operation, however, the EDSR drive quality was poor, with Rabi oscillations decaying within a few periods. We have used Device C with a 90 nm pitch for the data presented in the main text. The reported valley splittings are measured using magnetospectroscopy. Since there are no reservoirs available in the middle of the device, we measure the valley splitting by performing spectroscopy on the anticrossing between the (2,0) and (1,1) at a relatively low tunnel coupling.

5.9. SAMPLE DESIGN

A CAD image of the device design is shown in Fig. 5.15a,b. The samples are designed without a physical mesa. A mesa is often used to prevent leakage at the bondpads where damage by a wirebonder could create a contact to the 2DEG residing below. Instead, we deposit a 200 nm silicon nitride layer underneath the bondpads to prevent leakage to the 2DEG below (Fig. 5.15c). In addition, all the gates in the plunger and barrier gate layer run over a screening gate layer, blocking any current flow between the bondpad and the center of the device, as long as the screening gates are not accumulated (Fig. 5.15d). As a last measure, part of the gate fan-out wiring is reduced to patterned nanowires (Fig. 5.15e), which need higher voltages to accumulate.

We designed an on-chip coplanar waveguide with a characteristic impedance of 50 Ohm to optimize the power delivery of the microwave excitation. For the RF readout, we use a low capacitance design where the readout signal is applied via the source contact [35, 10, 28]. We ensure low parasitic capacitance by placing the source contact close to the center of the device ((Fig. 5.15a)) and wire bond directly to these source contacts. Furthermore, running the accumulation gates over a screening gate prevents the creation of a large capacitance between accumulated 2DEG and the accumulation gate, which helps achieve a good RF readout.

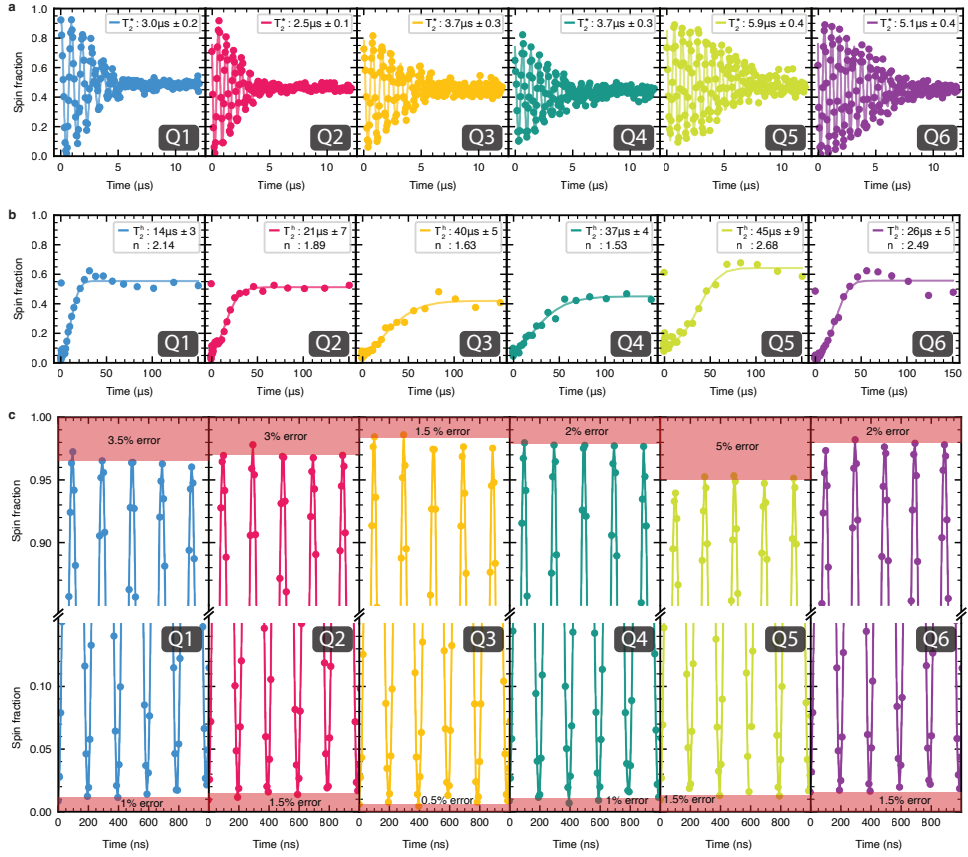


Figure 5.13: T_2^* , T_2^h and visibility measurements **a**, T_2^* measurement for each qubit. These measurements were measured without any pre-pulse and are fitted to a Gaussian decay: $P_S(t) = A\cos(\omega t + \phi)\exp\left(-\frac{t^2}{T_2^{*2}}\right) + B$. **b** T_2^h measurement for each qubit. These measurements are also performed without any pre-pulse and are fitted using: $P_S(t) = A\exp\left(-\frac{t^n}{T_2^{h2}}\right) + B$. **c**, Detailed plots of the Rabi oscillations shown in the main text. The errors contributing to loss of visibility are estimated by eye.

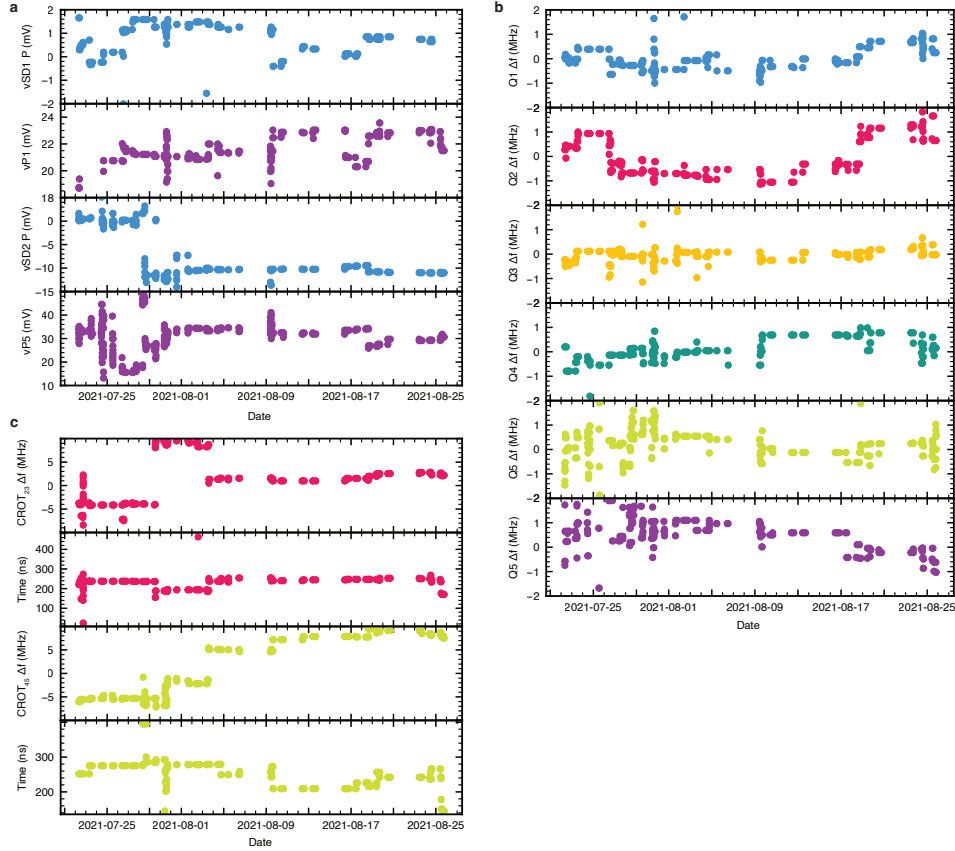


Figure 5.14: Calibration log of the sample during a period of approximately one month. Every data point in the calibration plot represents a result of a calibration measurement **a**, Calibration results of the sensing dot and readout point. The panels with the blue dots show the calibration results of the optimal operating point of SD1 (top) and SD2 (bottom). The purple dots show the readout point used for the parity readout for dot pair 12 (top) and 56 (bottom). **b**, Calibration results for the qubit resonance frequency, one plot per qubit. We plotted the deviation from the average resonance frequency. **c**, Controlled rotation calibration. The calibrated values for the driving frequency and burst duration for $CROT_{23}$ and $CROT_{45}$ are shown.

5

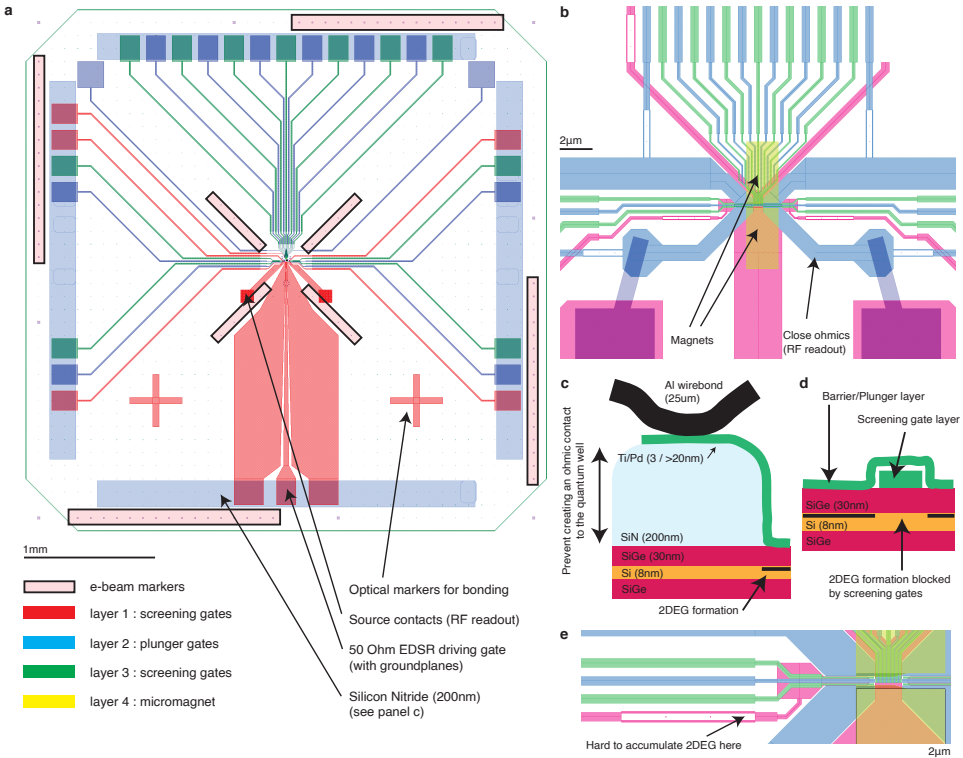


Figure 5.15: **Sample design** **a**, CAD image of the sample layout. **b**, Zoom in of **a**, showing the active region of the device. **c**, Silicon nitride (SiN) below the bondpad prevents punch-through of the bondwire to the quantum well. **d**, Screening gates block current flow below the gates between the bondpads and the active device area. **e**, Narrow segments of the gates increase the accumulation voltage underneath, and thereby also block current flow underneath.

5.10. ENTANGLEMENT WITNESSES

Entanglement witnesses are an efficient means to check whether a state is entangled. A witness is constructed in such a manner that its expectation value is negative in case the state is entangled. When choosing an entanglement witness, usually one needs to balance the number of operators measured versus the possible states that can be detected. Examples for GHZ states include the optimal, stabilizer and Mermin witness [17]. We choose a witness which requires a few more measurements but is able to detect entanglement across a larger part of the space with entangled states:

$$W = III - |\psi_{\text{GHZ}}\rangle \langle \psi_{\text{GHZ}}| . \quad (5.7)$$

This operator can be decomposed into Pauli operators. For three qubits, this results in:

$$\begin{aligned} W = & \frac{3}{8} \langle III \rangle - \frac{1}{8} \langle IZZ \rangle - \frac{1}{8} \langle XXX \rangle + \frac{1}{8} \langle XYY \rangle + \\ & \frac{1}{8} \langle YXY \rangle + \frac{1}{8} \langle YYX \rangle - \frac{1}{8} \langle ZIZ \rangle - \frac{1}{8} \langle ZZI \rangle . \end{aligned} \quad (5.8)$$

We use similar procedures as for the state tomography to remove the SPAM error of the witness operators.

5

5.11. QUANTUM STATE TOMOGRAPHY

Quantum state tomography is used to obtain the density matrices for the qubits. We used the maximum likelihood method to obtain the density matrices reported in this paper.

The concept of quantum state tomography is based on the idea that every density matrix can be decomposed in a set of orthogonal basis states (e.g. Pauli basis):

$$\rho = |\psi\rangle \langle \psi| = \frac{1}{2^N} \sum_i^{4^N} \langle \psi | \hat{V}_i | \psi \rangle \cdot \hat{V}_i , \quad (5.9)$$

where \hat{V}_i is the i^{th} basis state. Here \hat{V}_i are of the form $\{I, X, Y, Z\}^{\otimes N}$, and N is the number of qubits. In the experiment we measure the expectation value M_i of all the possible \hat{V}_i 's; $M_i = \langle \psi | V_i | \psi \rangle$ and reconstruct a first estimate of the density matrix using equation 5.9. To ensure that the obtained density matrix ρ is valid, we take the closest positive semi-definite matrix and ensure that the norm of ρ is one.

The resulting state can be used as input for the Maximum Likelihood Estimation (MLE) [21]. This is procedure to obtain the most likely state for a given set of M_i , using an optimizer for the following cost function:

$$\sum_i^{4^N} |M_i - \text{tr}(\rho V_i)| \quad (5.10)$$

To make this method work well, we use so called T matrices, which is the lower triangular matrix, where every non-zero entry is a variable. The relation to the density matrix is

$\rho = TT^\dagger$. An initial guess of T is obtained by performing a Cholesky decomposition on the density matrix used as input for MLE.

The fidelity of the estimated density matrix can be further increased by taking into account the readout errors of the system. When measuring an observable, the following matrix can be used to describe the measurement process:

$$P_{\text{meas}} = S_k P_{\text{real}} = \begin{pmatrix} F_{k,-1} & 1 - F_{k,+1} \\ 1 - F_{k,-1} & F_{k,+1} \end{pmatrix} P_{\text{real}} \quad (5.11)$$

where P_{meas} are the measured spin spin probabilities for the k^{th} observable (while we are interested in the real probability amplitudes). $P_{\text{real}} F_{k,-1}$ ($F_{k,+1}$) is the corrected for readout error probability to obtain -1 ($+1$) as measurement outcome for the k^{th} observable. These numbers are derived from the visibility of single-qubit Rabi oscillations such as in main text Fig. 2, but taken with the same initialization and readout sequences as are used in the circuits for preparing the density matrix.

The following observables are measured:

5

k	observable
1	ZIIII
2	IZIIII
3	ZZIIII
4	IIZIII
5	IIIZII
6	IIIZI
7	IIIZZ
8	IIIIZZ

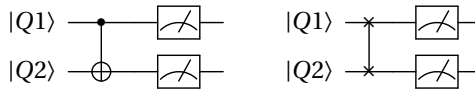
and have their own associated S_k matrix. We decompose other measurement operators we want to measure into elements of this set, for example $ZZZIII$ is decomposed into a combination of the $ZZIIII$ and $IIZIII$ operators, which we can simultaneously measure. The procedure we would use to generate to expectation value would be give by :

$$\langle ZZZIII \rangle = \text{Tr}(ZZ \cdot (S_3 \otimes S_4)^{-1} \cdot P_{\text{meas}}) \quad (5.12)$$

Where P_{meas} is a vector with the probabilities of the four possible measurement outcomes.

A comment needs to be made on the validity of this approach, as the SPAM errors are most likely spread over initialization and readout. The above method of removing readout errors could then artificially result in faulty results (e.g. expectation values above 1) in specific circumstances. As an example, let us assume that initialization and readout are error-prone for one qubit (Q1) and perfect for the other qubit (Q2). Characterization of SPAM errors would give us a matrix S_1 with which to correct the measurement outcomes for Q1.

Now consider performing state tomography after running a CNOT or SWAP operation:



In the first case, correction using the matrix S_1 will accurately remove the SPAM errors from the measured values for Q1. For qubit two, errors have been propagated from Q1, but these errors are not removed by the analysis as there are no SPAM errors on Q2 by itself. In this case, SPAM error removal thus only removes a subset of the errors introduced by SPAM. In the second case, we get for both qubits the wrong results. For Q1 the corrected expectation values could exceed one (which would be non-physical), whereas for Q2 there is no correction even though initialization errors on Q1 have propagated to Q2. In the experiments that are performed in this work, the circuits focus on entangling rather than swapping states. For that reason we believe that we do not introduce non-physical elements by applying the SPAM correction; rather it cannot remove all errors and will tend to worsen the actual fidelity.

5.12. ERROR CHANNELS IN THE EXPERIMENTAL DATA: DEPHASING AND “HEATING”

In order to examine the impact of dephasing on the measured density matrices of main text Figs. 4-5, we compare with the results of two numerical simulations performed according to the following methodology.

5.12.1. STATE TOMOGRAPHY SIMULATIONS

The multi-qubit system is well approximated by the Hamiltonian

$$H = H_{\text{Zeeman}} + H_{\text{Heisenberg}}, \quad (5.13)$$

consisting of the Zeeman interaction

$$H_{\text{Zeeman}} = \sum_{j=1}^6 \frac{g_j \mu_B}{2} \mathbf{B}_j \cdot \boldsymbol{\sigma}_j \quad (5.14)$$

and the isotropic Heisenberg exchange interaction

$$H_{\text{Heisenberg}} = \sum_{\langle j,k \rangle} \frac{J_{j,k}}{4} \boldsymbol{\sigma}_j \cdot \boldsymbol{\sigma}_k. \quad (5.15)$$

Here, $\boldsymbol{\sigma}_j$ is the vector of the Pauli matrices acting on qubit j , $\mathbf{B}_j = (v_{ac,j}(t)\partial B_{x,j} \cos(2\pi f_j), 0, B_{z,j})^T$ is the combined magnetic field, $\partial B_{x,j}$ the micromagnet gradient orthogonal to the qubit array axis (expressed in units of Tesla/V), $v_{ac,j}$ the voltage amplitude applied for driving EDSR, and $J_{j,k} = J_{\text{res},j,k} \exp(2\alpha_{j,k} v_{B,j,k}(t))$ is the exchange interaction between qubit j and k , where $J_{\text{res},j,k}$ is the residual exchange for $v_{B,j,k}(t) = 0$. The sum $\langle j,k \rangle$ runs over all neighboring pairs in the linear array.

For the numerical simulations, we solve the time-dependent Schrödinger equation

$$i\hbar \frac{d}{dt} |\psi(t)\rangle = H|\psi(t)\rangle \quad (5.16)$$

by discretizing $H(t + \Delta t)$ into segments of length Δt taking $H(t)$ constant in the time-interval $[t, t + \Delta t]$. We compute the unitary propagator according to

$$U(t + \Delta t) = e^{-\frac{i}{\hbar} H(t + \Delta t)} U(t), \quad (5.17)$$

where $\hbar = h/(2\pi)$ is the reduced Planck constant. The simulations are performed in the multiply rotating frame which removes the Larmor precession of each qubit around the average external magnetic field $\sum_{j=1}^N B_{z,j}/N$. By making the so-called rotating wave approximation (RWA) we neglect counter-rotating terms such that we can choose $\Delta t = 10$ ps as a sufficiently small time step.

The simulated GHZ states are the final states $\rho_f = U_f \rho_{\text{init}} U_f^\dagger$ obtained by applying the pulse sequence of main text Fig. 5a to the ideal input state ρ_{init} (here U_f is shorthand for the product of the successively applied unitary operations). For simplicity each GHZ simulation is performed on the subspace of only the involved qubits, motivated by the small residual exchange to the other qubits.

Low-frequency noise is included in the simulation via quasistatic fluctuations $H_{\text{Zeeman}} \rightarrow H_{\text{Zeeman}} + \sum \xi_j \sigma_{z,j}$ and averaging the final result over 5000 random initializations. Here ξ_j are Gaussian stochastic variables with mean $\langle \xi_j \rangle = 0$ and variance $\langle \xi_j^2 \rangle = \hbar^2/2(\pi T_{2,j}^*)^2$.

5.12.2. DISCUSSION

In the tables below we present a comparison of the experimental results (RAW data: without SPAM error removal; Processed data: with SPAM error removal) to the outcomes of the two simulations with different input parameters. The first simulation uses the T_2^* values from the table in main text Fig. 2e. The second simulation takes the T_2^* values obtained after a 4 μ s microwave bursts applied off-resonance before the pulse sequence used to measure T_2^* . We find systematically that such a prepulse causes both a shift in the qubit frequency and a reduction in T_2^* , by amounts that depend on the microwave burst duration and power (see Fig. 7). In the actual experiments, prepulses shorter than 4 μ s are used, to strike a balance between saturating the frequency shift and not reducing T_2^* too much. We can thus expect that dephasing reduces the off-diagonal elements in the measured density matrices of Fig. 4-5 by an amount that lies in between the case of the two simulations, with the shorter and longer sets of T_2^* values. Furthermore, the longer the state preparation sequence, the shorter the resulting T_2^* , which is consistent with the fact that the off-diagonal entries are lower for the GHZ states of qubits 2-4 and 3-5 than for GHZ states of qubits 1-3 or 4-6.

The diagonal entries deviate most from the ideal expectation for the GHZ states involving qubits 2-4 and 3-5. State preparation of qubits 1-3 or qubits 4-6 by itself works very well, but we find consistently that state preparation of qubits 4-6 is somewhat degraded when it follows state preparation of qubits 1-3 (see Fig. 3), and vice versa. In the simulations we assume perfect initial states in order to probe only the effects of dephasing.

Finally, the qubit frequency shifts from the prepulses and the pulses applied during state preparation lead to reproducible phase shifts seen in the experimentally prepared GHZ states, deviating from the ideal GHZ state $(|000\rangle + |111\rangle)/\sqrt{2}$.

The frequency shifts and reduced dephasing times generally bear signatures of heating, as in previous reports [54, 47]. Their microscopic origin is at present not well understood.

Generally, we find that the reduced coherence times in the second simulation provides us with state fidelities closely resembling the experimental data after SPAM removal. We neglect the non-ideal phase component in the experimental data when making this comparison, as we have omitted frequency shits and virtual-Z gates in our simulation.

BIBLIOGRAPHY

- [1] S. J. Angus, A. J. Ferguson, A. S. Dzurak, and R. G. Clark. “Gate-defined quantum dots in intrinsic silicon”. *Nano Letters* 7.7 (2007), pp. 2051–2055.
- [2] J. M. Arrazola *et al.* “Quantum circuits with many photons on a programmable nanophotonic chip”. *Nature* 591.7848 (2021), pp. 54–60.
- [3] F. Arute *et al.* “Quantum supremacy using a programmable superconducting processor”. *Nature* 574.7779 (2019), pp. 505–510.
- [4] T. A. Baart, M. Shafiei, T. Fujita, C. Reichl, W. Wegscheider, and L. M. K. Vandersypen. “Single-spin CCD”. *Nature Nanotechnology* 11.4 (2016), pp. 330–334.
- [5] J. Z. Blumoff *et al.* “Fast and high-fidelity state preparation and measurement in triple-quantum-dot spin qubits”. *PRX Quantum* 3.1 (2022), p. 010352.
- [6] M. G. Borselli *et al.* “Pauli spin blockade in undoped Si/SiGe two-electron double quantum dots”. *Applied Physics Letters* 99.6 (2011), p. 063109.
- [7] J. M. Boter *et al.* “The spider-web array—a sparse spin qubit array”. *arXiv preprint arXiv:2110.00189* (2021).
- [8] C. D. Bruzewicz, J. Chiaverini, R. McConnell, and J. M. Sage. “Trapped-ion quantum computing: Progress and challenges”. *Applied Physics Reviews* 6.2 (2019), p. 021314.
- [9] E. T. Campbell, B. M. Terhal, and C. Vuillot. “Roads towards fault-tolerant universal quantum computation”. *Nature* 549.7671 (2017), pp. 172–179.
- [10] E. J. Connors, J. J. Nelson, and J. M. Nichol. “Rapid high-fidelity spin-state readout in Si/SiGe quantum dots via rf reflectometry”. *Physical Review Applied* 13.2 (2020), p. 024019.
- [11] O. Crawford, J. R. Cruise, N. Mertig, and M. F. Gonzalez-Zalba. “Compilation and scaling strategies for a silicon quantum processor with sparse two-dimensional connectivity”. *arXiv:2201.02877* (2022).
- [12] C. J. van Diepen, T.-K. Hsiao, U. Mukhopadhyay, C. Reichl, W. Wegscheider, and L. M. Vandersypen. “Electron cascade for distant spin readout”. *Nature Communications* 12.1 (2021), pp. 1–6.
- [13] N. I. Dumoulin Stuyck, F. A. Mohiyaddin, R. Li, M. Heyns, B. Govoreanu, and I. P. Radu. “Low dephasing and robust micromagnet designs for silicon spin qubits”. *Applied Physics Letters* 119.9 (2021), p. 094001.
- [14] L. Egan *et al.* “Fault-tolerant control of an error-corrected qubit”. *Nature* 598.7880 (2021), pp. 281–286.

- 5
- [15] F. Fedele, A. Chatterjee, S. Fallahi, G. C. Gardner, M. J. Manfra, and F. Kuemmeth. "Simultaneous operations in a Two-Dimensional array of Singlet-Triplet qubits". *PRX Quantum* 2.4 (2021), p. 040306.
 - [16] D. M. Greenberger, M. A. Horne, and A. Zeilinger. "Going beyond Bell's theorem". *Bell's theorem, quantum theory and conceptions of the universe*. Springer, 1989, pp. 69–72.
 - [17] O. Gühne and G. Tóth. "Entanglement detection". *Physics Reports* 474.1-6 (2009), pp. 1–75.
 - [18] P. Harvey-Collard *et al.* "High-fidelity single-shot readout for a spin qubit via an enhanced latching mechanism". *Physical Review X* 8.2 (2018), p. 021046.
 - [19] I. Heinz and G. Burkard. "Crosstalk analysis for single-qubit and two-qubit gates in spin qubit arrays". *Physical Review B* 104.4 (2021), p. 045420.
 - [20] N. W. Hendrickx, W. I. Lawrie, M. Russ, F. van Riggelen, S. L. de Snoo, R. N. Schouten, A. Sammak, G. Scappucci, and M. Veldhorst. "A four-qubit germanium quantum processor". *Nature* 591.7851 (2021), pp. 580–585.
 - [21] Z. Hradil, J. Řeháček, J. Fiurášek, and M. Ježek. "3 maximum-likelihood methods in quantum mechanics". *Quantum state estimation*. Springer, 2004, pp. 59–112.
 - [22] W. Huang *et al.* "Fidelity benchmarks for two-qubit gates in silicon". *Nature* 569.7757 (2019), pp. 532–536.
 - [23] E. Kawakami *et al.* "Electrical control of a long-lived spin qubit in a Si/SiGe quantum dot". *Nature nanotechnology* 9.9 (2014), pp. 666–670.
 - [24] A. Kha, R. Joynt, and D. Culcer. "Do micromagnets expose spin qubits to charge and Johnson noise?" *Applied Physics Letters* 107.17 (2015), p. 172101.
 - [25] W. I. L. Lawrie, M. Russ, F. van Riggelen, N. Hendrickx, S. de Snoo, A. Sammak, G. Scappucci, and M. Veldhorst. "Simultaneous driving of semiconductor spin qubits at the fault-tolerant threshold". *arXiv:2109.07837* (2021).
 - [26] W. I. L. Lawrie *et al.* "Quantum dot arrays in silicon and germanium". *Applied Physics Letters* 116.8 (Feb. 2020), p. 080501. ISSN: 0003-6951. DOI: [10.1063/5.0002013](https://doi.org/10.1063/5.0002013).
 - [27] R. Li *et al.* "A crossbar network for silicon quantum dot qubits". *Science advances* 4.7 (2018), eaar3960.
 - [28] Y.-Y. Liu, S. G. J. Philips, L. A. Orona, N. Samkharadze, T. McJunkin, E. R. MacQuarrie, M. A. Eriksson, L. M. K. Vandersypen, and A. Yacoby. "Radio-frequency reflectometry in silicon-based quantum dots". *Physical Review Applied* 16.1 (2021), p. 014057.
 - [29] M. T. Mądzik *et al.* "Precision tomography of a three-qubit donor quantum processor in silicon". *Nature* 601.7893 (2022), pp. 348–353.
 - [30] J. M. Martinis and M. R. Geller. "Fast adiabatic qubit gates using only σ_z control". *Physical Review A* 90.2 (2014), p. 022307.
 - [31] T. Meunier *et al.* "Experimental signature of phonon-mediated spin relaxation in a two-electron quantum dot". *Physical Review Letters* 98.12 (2007), p. 126601.

- [32] A. R. Mills, C. Guinn, M. Gullans, A. Sigillito, M. Feldman, E. Nielsen, and J. Petta. “Two-qubit silicon quantum processor with operation fidelity exceeding 99%”. *arXiv preprint arXiv:2111.11937* (2021).
- [33] P. A. Mortemousque, E. Chanrion, B. Jadot, H. Flentje, A. Ludwig, A. D. Wieck, M. Urdampilleta, C. Bäuerle, and T. Meunier. “Coherent control of individual electron spins in a two-dimensional quantum dot array”. *Nature Nanotechnology* 16.3 (2021), pp. 296–301.
- [34] A. Noiri, K. Takeda, T. Nakajima, T. Kobayashi, A. Sammak, G. Scappucci, and S. Tarucha. “Fast universal quantum gate above the fault-tolerance threshold in silicon”. *Nature* 601.7893 (2022), pp. 338–342.
- [35] A. Noiri, K. Takeda, J. Yoneda, T. Nakajima, T. Kodera, and S. Tarucha. “Radio-Frequency-Detected Fast Charge Sensing in Undoped Silicon Quantum Dots”. *Nano Letters* 20.2 (2020), pp. 947–952.
- [36] T. Obata, M. Pioro-Ladrière, Y. Tokura, Y.-S. Shin, T. Kubo, K. Yoshida, T. Taniyama, and S. Tarucha. “Coherent manipulation of individual electron spin in a double quantum dot integrated with a micromagnet”. *Physical Review B* 81.8 (2010), p. 085317.
- [37] K. Ono, D. Austing, Y. Tokura, and S. Tarucha. “Current rectification by Pauli exclusion in a weakly coupled double quantum dot system”. *Science* 297.5585 (2002), pp. 1313–1317.
- [38] M. Ortner and L. G. Coliado Bandeira. “Magpylib: A free Python package for magnetic field computation”. *SoftwareX* (2020). DOI: [10 . 1016 / j . softx . 2020 . 100466](https://doi.org/10.1016/j.softx.2020.100466).
- [39] S. G. J. Philips. *uM Simulator for spin qubits*. Version 1. 0. 0. Jan. 2022. DOI: [10 . 5281 / zenodo . 5833197](https://doi.org/10.5281/zenodo.5833197).
- [40] M. Pioro-Ladrière, Y. Tokura, T. Obata, T. Kubo, and S. Tarucha. “Micromagnets for coherent control of spin-charge qubit in lateral quantum dots”. *Applied Physics Letters* 90.2 (2007), p. 024105.
- [41] A. K. Rajagopal and R. W. Rendell. “Robust and fragile entanglement of three qubits: Relation to permutation symmetry”. *Physical Review A* 65.3 (2002), p. 032328.
- [42] D. Ristè, J. G. van Leeuwen, H. S. Ku, K. W. Lehnert, and L. DiCarlo. “Initialization by measurement of a superconducting quantum bit circuit”. *Physical Review Letters* 109.5 (2012), p. 050507.
- [43] M. Russ, D. M. Zajac, A. J. Sigillito, F. Borjans, J. M. Taylor, J. R. Petta, and G. Burkard. “High-fidelity quantum gates in Si/SiGe double quantum dots”. *Physical Review B* 97.8 (2018), p. 085421.
- [44] S. Simmons, R. M. Brown, H. Riemann, N. V. Abrosimov, P. Becker, H.-J. Pohl, M. L. Thewalt, K. M. Itoh, and J. J. Morton. “Entanglement in a solid-state spin ensemble”. *Nature* 470.7332 (2011), pp. 69–72.
- [45] K. Takeda, A. Noiri, T. Nakajima, T. Kobayashi, and S. Tarucha. “Quantum error correction with silicon spin qubits”. *arXiv:2201. 08581* (2022).

- 5
- [46] K. Takeda, A. Noiri, T. Nakajima, J. Yoneda, T. Kobayashi, and S. Tarucha. “Quantum tomography of an entangled three-qubit state in silicon”. *Nature Nanotechnology* (2021), pp. 1–5.
 - [47] K. Takeda *et al.* “Optimized electrical control of a Si/SiGe spin qubit in the presence of an induced frequency shift”. *npj Quantum Information* 4.1 (2018), pp. 1–6.
 - [48] J. M. Taylor, H. A. Engel, W. Dür, A. Yacoby, C. Marcus, P. Zoller, and M. Lukin. “Fault-tolerant architecture for quantum computation using electrically controlled semiconductor spins”. *Nature Physics* 1.3 (2005), pp. 177–183.
 - [49] L. M. K. Vandersypen, H. Bluhm, J. S. Clarke, A. S. Dzurak, R. Ishihara, A. Morello, D. J. Reilly, L. R. Schreiber, and M. Veldhorst. “Interfacing spin qubits in quantum dots and donors—hot, dense, and coherent”. *npj Quantum Information* 3.1 (2017), pp. 1–10.
 - [50] L. M. K. Vandersypen and M. A. Eriksson. “Quantum Computing with Semiconductor Spins”. *Physics Today* 72 (2019), pp. 8–38.
 - [51] M. Veldhorst, H. G. J. Eenink, C.-H. Yang, and A. S. Dzurak. “Silicon CMOS architecture for a spin-based quantum computer”. *Nature Communications* 8.1 (2017), pp. 1–8.
 - [52] M. Veldhorst *et al.* “An addressable quantum dot qubit with fault-tolerant control-fidelity”. *Nature nanotechnology* 9.12 (2014), pp. 981–985.
 - [53] C. Volk *et al.* “Loading a quantum-dot based “Qubyte” register”. *npj Quantum Information* 5.1 (2019), pp. 1–8.
 - [54] T. F. Watson *et al.* “A programmable two-qubit quantum processor in silicon”. *Nature* 555.7698 (2018), pp. 633–637.
 - [55] A. J. Weinstein *et al.* “Universal logic with encoded spin qubits in silicon”. *arXiv:2202.03605* (2022).
 - [56] B. P. Wuetz *et al.* “Atomic fluctuations lifting the energy degeneracy in Si/SiGe quantum dots”. *arXiv:2112.09606* (2021).
 - [57] X. Xue, M. Russ, N. Samkharadze, B. Undseth, A. Sammak, G. Scappucci, and L. M. K. Vandersypen. “Quantum logic with spin qubits crossing the surface code threshold”. *Nature* 601.7893 (2022), pp. 343–347.
 - [58] X. Xue *et al.* “Repetitive quantum nondemolition measurement and soft decoding of a silicon spin qubit”. *Physical Review X* 10.2 (2020), p. 021006.
 - [59] C. H. Yang *et al.* “Silicon qubit fidelities approaching incoherent noise limits via pulse engineering”. *Nature Electronics* 2.4 (2019), pp. 151–158.
 - [60] J. Yoneda *et al.* “A quantum-dot spin qubit with coherence limited by charge noise and fidelity higher than 99.9%”. *Nature nanotechnology* 13.2 (2018), pp. 102–106.
 - [61] J. Yoneda *et al.* “Robust micromagnet design for fast electrical manipulations of single spins in quantum dots”. *Applied Physics Express* 8.8 (2015), p. 084401.
 - [62] D. M. Zajac, T. M. Hazard, X. Mi, K. Wang, and J. R. Petta. “A reconfigurable gate architecture for Si/SiGe quantum dots”. *Applied Physics Letters* 106.22 (2015), p. 223507.

- [63] D. M. Zajac, T. Hazard, X. Mi, E. Nielsen, and J. R. Petta. “Scalable gate architecture for a one-dimensional array of semiconductor spin qubits”. *Physical Review Applied* 6.5 (2016), p. 054013.
- [64] D. M. Zajac, A. J. Sigillito, M. Russ, F. Borjans, J. M. Taylor, G. Burkard, and J. R. Petta. “Resonantly driven CNOT gate for electron spins”. *Science* 359.6374 (2018), pp. 439–442.
- [65] E. J. Zhang *et al.* “High-performance superconducting quantum processors via laser annealing of transmon qubits”. *Science Advances* 8.19 (2022), eabi6690.
- [66] H. S. Zhong *et al.* “Quantum computational advantage using photons”. *Science* 370.6523 (2020), pp. 1460–1463.
- [67] F. A. Zwanenburg, A. S. Dzurak, A. Morello, M. Y. Simmons, L. C. Hollenberg, G. Klimeck, S. Rogge, S. N. Coppersmith, and M. A. Eriksson. “Silicon quantum electronics”. *Reviews of modern physics* 85.3 (2013), p. 961.
- [68] A. M. J. Zwerver *et al.* “Qubits made by advanced semiconductor manufacturing”. *arXiv preprint arXiv:2101.12650* (2021).

6

DEFINING CONTROL ARCHITECTURES FOR SPIN QUBIT EXPERIMENTS

6.1. INTRODUCTION

When executing spin qubit experiments, three elements define how well an experiment can be performed. One is the knowledge about the experiment, one is the quality of the hardware that can be used (e.g. the device¹, the experimental apparatus etc.) and lastly, the software used to control the experiment. Usually a lot of attention is devoted to the first two items, where good software lags behind in priority. Since one of our goals was to expand the number of qubits, it was important that programming the qubits became much easier. In this chapter we introduce several new software libraries, discuss some of the practicalities of operating spin qubit samples (e.g. how to test them?, what do our setups look like?) and the hardware we use for that.

6.2. CHARACTERIZING SPIN QUBIT DEVICES

The fabrication and characterization cycle of spin qubit devices is a long one. Fabrication[4, 7] typically takes two to four weeks and the device characterization a few days (6-8 devices can be tested daily). If the device characterization is successful, one can consider mounting it in a dilution refrigerator. This characterization is designed to check if the devices are electrostatically 'fine' (see next section), as yields can be low (0%-10%). This first characterization is performed at 4K where the semiconducting substrate is non-conductive while also not loosing the time it would take to cool down/warm up the sample to 10mK, which will be needed for the device operation.

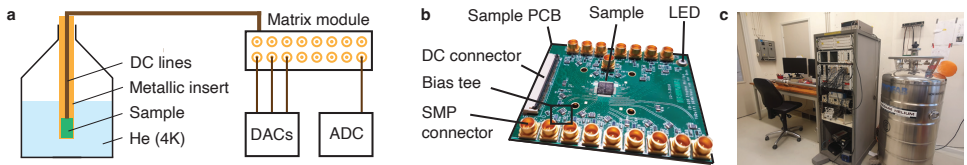


Figure 6.1: **Dipstick characterization setup** | **a**, Schematic of a dipstick setup, where a metallic insert is dipped in liquid *He*, which cools the chip placed on the insert to 4K. A matrix module, DAC's and ADC's are used to perform the transport measurements on the sample (see main text). **b**, Image showing a PCB carrying a sample used for the six-qubit experiments. **c**, Picture of the dipstick setup.

6.2.1. DIPSTICK DEVICE CHARACTERIZATION

The initial characterization of devices is performed at a dipstick setup, as shown in Fig. 6.1. A dipstick is a metal stick on which a device can be mounted, and which can be dipped in liquid helium (boiling point of 4.2 Kelvin). During this characterization we carry out the following tests (see Fig. 6.2).

1. Gate-to-gate leakage (Fig. 6.2a) occurs when two separate gates have a galvanic connection between them. This can be caused by liftoff issues, a bad dielectric

¹Optimizing the device quality is one of the most time consuming processes for spin qubits as the feedback cycle is slow (~2-4 weeks). In this work, double the time was spent on device characterization/optimization and fabrication as compared to device operation.

and/or an electrostatic discharge (ESD) event. An ESD event can happen during the fabrication process (e.g. dicing) or in the process of bonding/sample handling. The latter can be prevented by making the environment ESD safe. We took the following prevention measures:

- Make sure you are always grounded (no gloves) when in contact with the sample.
 - Always use an ionizer during the wire bonding process.
 - Ensure that all the gates are shorted to each other, while handling the PCB and during wire bonding, by connecting a shorting pin to the DC connector² of the sample PCB (Fig. 6.1b).
2. The accumulation of a two-dimensional electron gas (2DEG) (Fig. 6.2b) in the quantum well. Sometimes it can be hard to create a stable 2DEG, some common issues related to 2DEG accumulation are:
- No accumulation is observed, this could indicate a wire bonding problem, a discontinuity in the gate, or a problem with the ohmic contact for example.
 - A large leakage current is observed when activating the gate (as shown in Fig. 6.2b). This can be caused by punching through the oxide of the sample with the bonder. See Fig. 5.15 for details and on how to prevent this from happening.
 - Drift in the 2DEG accumulation voltage (i.e. the voltage at which carriers start to accumulate). A change in the accumulation voltage occurs when carriers move/tunnel from the quantum well into the material layers below the gate (e.g. the Si cap of the wafer). This creates a sheet of static charge that causes an offset in the electric field applied to the quantum well by the gate electrode. This effect can be observed by accumulating a 2DEG using the accumulation gate, then depleting the quantum well and then accumulating it again. Fig. 6.2b shows an example, the first accumulation curve is shown by the solid black curve and the red curve shows the second one. The drift free range is defined by the distance between the point of 2DEG accumulation (red curve) and the maximal applied voltage in the sweep. This range defines the maximal voltage that can be applied beyond the point of accumulation, before additional carriers will tunnel upward and cause an subsequent shift in accumulation voltage. This drift effect can be problematic during device operation as the device properties change during the tune-up of the sample. When we choose a device, we target a drift-free range of at least 300-500mV for every accumulation gate .
 - 3. A pinch-off check (Fig. 6.2c) verifies whether all the gates are able to influence the electrostatic potential in the quantum well at the desired locations. This test is performed by making a 2DEG channel on the device, e.g. through activating multiple gates in the section with the quantum dots or the sensing dots. Then every gate is tested sequentially by turning it off and on. Drift can cause the total current to drop/vanish during the testing. If the transport current cannot be pinched off with

²The samples boards are designed to have two DC connectors where both connectors are connected to the same pins of the sample. This makes it possible to connect the sample to the measurement setup and only afterwards remove the short between all the gates.

one of the gates, it is likely that an error occurred during the wire bonding process, or the metal of one of the gate electrodes is not continuous (e.g. lift-off error).

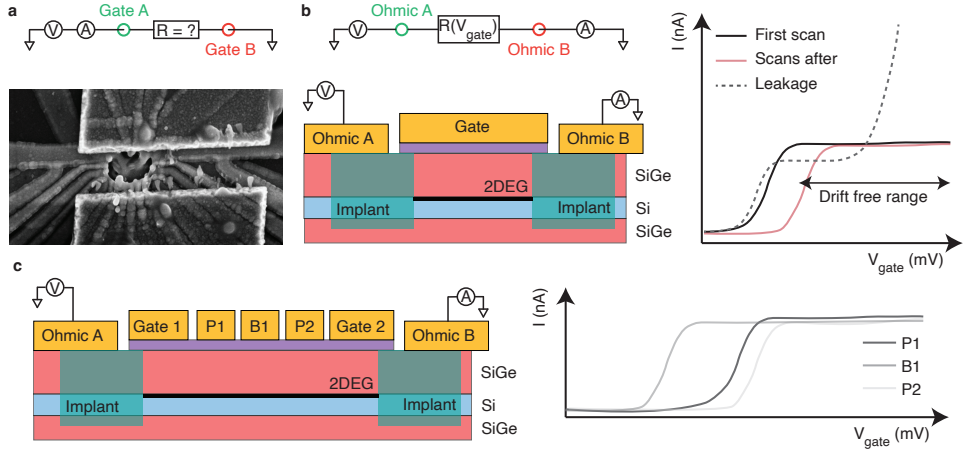


Figure 6.2: Dipstick measurements | a, The measurement circuit used to measure the resistance between a single gate and all other gates. The image below shows a device that suffered from an electrostatic discharge event, causing some of the gates to melt together. **b,** Measurement circuit used to check if the accumulation gate accumulates a 2DEG. The cross section shows how the 2DEG is connected to the outside world via the implanted regions. The graph on the right shows the current through the device as a function of the accumulation voltage (V_{gate}). The black and red curves illustrate the drift effect (see main text). The dashed gray curve shows a measurement indicating leakage. **c,** Schematic showing an accumulated 2DEG channel in the quantum dot region between both terminals of the device. For the pinch-off tests, we sweep the fine gates out and in of accumulation, one by one. The graph on the right shows the expected measurement outcome for these experiments. Due to the background charge disorder, the pinch-off voltages differ between gates that have nominally identical dimensions.

If no leakage, drift, nor pinch-off problems are detected within a single device, a device is deemed 'worthy' to be cooled down to lower temperatures, to form quantum dots and qubits.

For this experiment, a dipstick equipped with DC wiring is needed (schematic in Fig. 6.1a). The voltages for sample characterization are applied by very accurate (18 bit), stable and low noise DC voltage sources (D5a). These sources are battery powered such that the sample is isolated from the noisy main lines.

Currents are measured using a homemade module (M1b) that converts the current into a voltage. This voltage is measured through an isolator (M0) which decouples any back action from the voltage meter (e.g. Keithley 2000) to the experiment.

The details of these experimental tools can be found in [15].

6.3. SPIN QUBIT DEVICE OPERATION AND INSTRUMENTATION

When we want to operate qubits, we cool down our devices to an electron temperature of 50 – 150mK using a dilution refrigerator such as a BlueFors XLD400. We do this because the qubits gain in coherence[14, 13, 17], due to the reduced occupation of thermally excited states ³ and the increase in the signal-to-noise ratio (SNR) when performing readout of the quantum dots.

The setup for a *qubit* experiment is more complicated compared to the dipstick setup due to the additional instrumentation that is needed to control the qubits on nanosecond timescales. This extra equipment is connected using coaxial cables to the setup, which routes the fast signals to the PCB. The PCB combines RF and DC signals using bias tees and connects them to the sample. A complete overview of a setup for qubit experiments is shown in Fig. 6.3, which is the setup used for the six-qubit experiments in chapter 5. A description of the most important instruments is given below:

- Digitizers (DIG) are instruments with a fast ADC (analog-to-digital converter), which digitizes analog voltages to digital values (ns to ms timescales). Digitizers used for spin qubit experiments should be able to digitize a waveform for a specified sample rate and time interval (Elzerman readout) and have a function to average this time trace (PSB readout).
- An arbitrary waveform generator (AWG) is one of the most critical elements of a spin qubit setup, as it dictates what the electrons do. An AWG is a device that outputs every nanosecond (for a sample rate of 1GS/s) a well defined voltage which can be used to create for example the waveform needed to perform a two-qubit gate. Criteria for selecting an AWG are given in section 6.5.
- Microwave (MW) vector sources are used to perform single-qubit gates on our samples. A vector source has two inputs, one for the In-phase (I) and one for the Quadrature (Q) component, which are generated by an AWG. Both components can be used to modulate the carrier wave around its center frequency f_c .

The IQ signal provided to the vector source has the following form :

$$I(t) = \sum_i A_i(t) \sin(2\pi f_{IQ,i} t + \phi_i) \quad (6.1)$$

$$Q(t) = \sum_i A_i(t) \cos(2\pi f_{IQ,i} t + \phi_i) \quad (6.2)$$

Where A_i is the windowing function of the applied microwave signal, with a frequency $f_{IQ,i}$ and a phase ⁴ ϕ_i applied to qubit i . These signals are multiplied (mixed) in the vector source⁵ with the carrier frequency f_c , resulting in the following output

³For example, if one has an excited state (e.g. the valley/orbital state) with an energy smaller than 1.6meV, then there is a ~1% likelihood that the excited state is occupied at 4K (assuming thermal equilibrium). At 100mK, this would occur at energy scale of 40μeV.

⁴The phase controls the rotation axis (xy plane) of the qubit, e.g. adding 90 degrees changes a X gate into a Y gate.

⁵ $MW_{out}(t) = \cos(2\pi f_c t) I(t) + \sin(2\pi f_c t) Q(t)$

:

$$MW_{out}(t) = \sum_i A_i(t) \sin(2\pi(f_{IQ,i} + f_c)t + \phi_i) \quad (6.3)$$

This means that any tone (and also multiple tones at the same time) within the bandwidth limit of the AWG can be produced.

In addition to the IQ modulation, most vector sources also have a pulse modulation option (PM), which allows one to strongly attenuate the output of the vector source when it is not used, reducing the output noise. The PM is controlled using a digital signal (e.g. with the marker output of an AWG). We observed in our experiments that this reduces the electron temperature.

6

- RF generators, amplifiers and downconvertors are used to read-out the state of the qubits, by detecting the impedance of the sensing dot using a method called RF reflectometry [11, 2, 8] (see also chapter 4). The diagram in Fig. 6.3 shows a schematic of a setup with reflectometry. The RF generator ⁶ is used to create an oscillating wave which probes a resonant circuit into which the sensing dot is embedded. We measure the reflected signal by inserting a directional coupler and several amplifiers in the signal chain for the readout. From the reflected signal, we can detect changes in the sensing dot impedance. Specifically, we extract the phase and amplitude difference with respect to the (normalized) probe signal. The phase and amplitude of the signal is acquired by downconverting it in its I and Q components (similar to the up conversion of the vector source).

It is possible to make the setup more compact by using a single AWG channel to generate the probe tones and a single digitizer channel to directly demodulate the signal in the digital domain (not done in our setup since the FPGA image was not yet ready). This can be done for readout frequencies up to ~200MHz, limited by the bandwidth of the digitizer (in our case). The amplifiers are still needed in the signal chain, as low powers are used.

⁶We modulate the amplitude (on/off) of the RF sources using markers from the AWG. This prevents us from sending power to the sample when not required. Note that this might not matter as low powers (e.g. -100dBm) are used for this detection method.

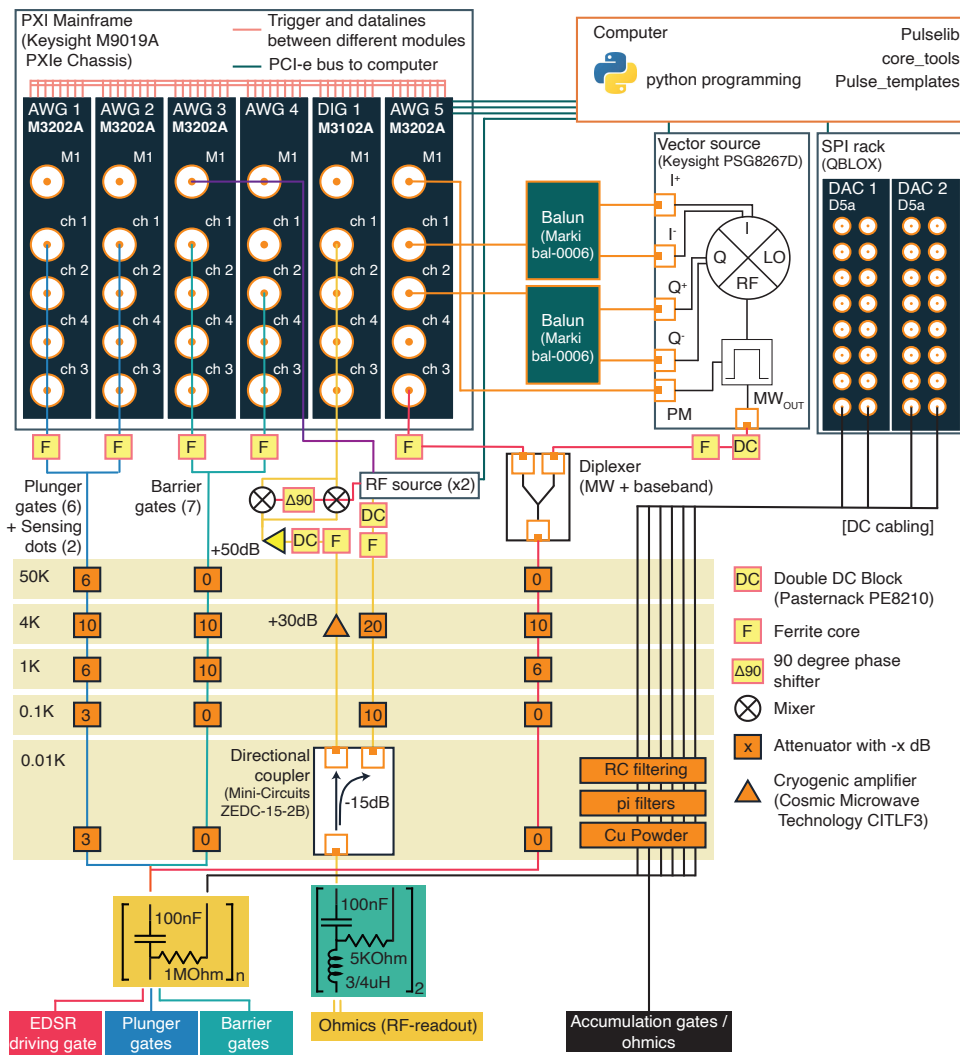
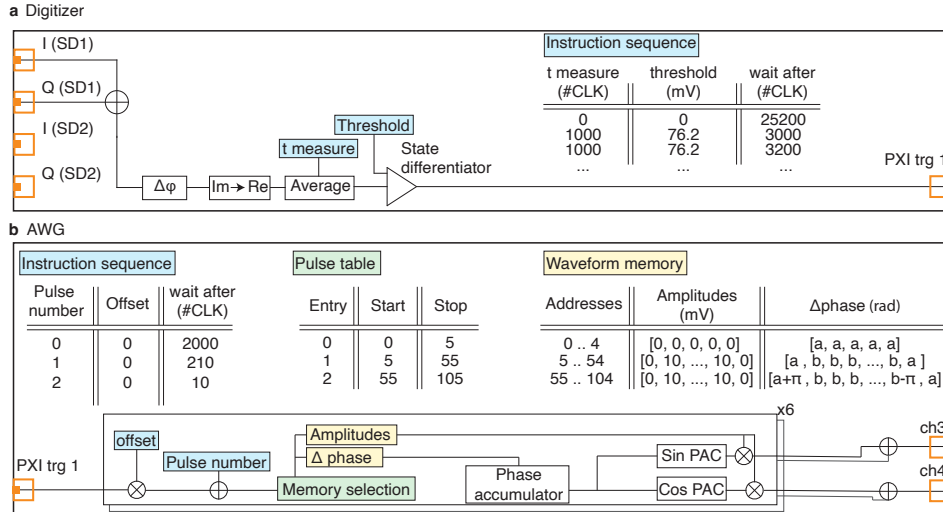


Figure 6.3: **Schematic overview of the experimental setup** | The bulk of the experiment is controlled by Arbitrary Waveform Generators (AWG, Keysight M3202A) and digitizers (DIG, Keysight M3201A) in a PXI chassis (used for synchronization and feedback). The AWGs generate baseband pulses (0-300MHz) used for initialization, readout and two-qubit gates. These baseband signals are provided to all plunger and barrier gates of the quantum dots. Sensing dot plungers are also connected to AWG channels to allow for fully compensated virtual plungers. In addition, we use the AWGs to generate the I/Q input signals for the vector source (Keysight PSG E8267D), used to perform single-qubit gates. Using this source, a large IQ modulation bandwidth (800 MHz) can be obtained by using the differential IQ inputs. The differential signal is generated using Baluns (Marki bal-0006), which reduce the number of AWG channels and ensure excellent timing (AWG channel pairs 1,2 and 3,4 have a larger skew (± 30 ps) compared to just channel 1 and 2). We use a homemade combiner to allow for both baseband and MW control on the EDSR driving gate. Coils with ferrite cores are used to reduce low-frequency noise generated by the instruments. In addition, we use double DC blocks for any RF/MW signal used in this experiment. The schematic shows in yellow the different temperature stages of the dilution refrigerator at which the signals are attenuated and thermalized. All plunger gates have discrete attenuators in the line with a total attenuation of ~ 28 dB, and barrier gates of ~ 20 dB in addition to the attenuation from the coax line itself. The barrier gates have less attenuation because of the large voltage pulses needed to achieve the desired $J_{\text{on}}/J_{\text{off}}$ ratio. We use bias tees on the sample PCB with a RC time constant of 100 ms to combine baseband and microwave signals (for qubit driving) with a static DC voltage. We generate the RF-carrier signal for readout using a homemade RF source (one carrier per sensing dot), which we route into the dilution refrigerator using a combiner. A marker output channel of the AWGs is connected to the RF sources in order to only output RF power during the readout. At the 10 mK stage, we use a directional coupler to separate the reflected signal (S_{11}) from the incoming RF carrier. A coplanar waveguide routing the RF signal on the sample PCB is split in two and connects to bias tees (dark green), each one going to a sensing dot. Bias tees with a low resistance are chosen as it also allows us to perform DC measurements as needed. NbTiN inductors (low C_p , high Q) are wire-bonded directly to the source contacts on the sample [2, 11] (see chapter 4). These inductors form a resonant circuit together with the stray capacitance of e.g. the wire bonds. When the carrier signal reflects from the sensing dots, it passes again through the directional coupler and is amplified both at the 4 Kelvin stage and at room temperature. The signal is fed through two sets of mixers (1 for each SD) to demodulate the signal to baseband. We finally sample the I and Q channels with the digitizer in the PXI chassis. Besides the fast baseband/RF/MW pulses, all the gates of the sample are also connected to battery-powered DACs built in-house, which supply the DC operating voltages.



6

Figure 6.4: **Implementation of real time feedback** **a**, Schematic of the FPGA layout of the digitizer (Keysight M3201A). At the input, one (or two) baseband IQ signals (originating from RF reflectometry) arrive at the input channels of the digitizer. The digitizer rotates the combined I and Q input with an angle $\Delta\phi$ and converts the vector into a scalar by dropping the Q signal. Upon a trigger from the instruction sequence, the signal is averaged for a time $t_{measure}$ and compared with a threshold to infer the qubit state. The result is written both to the DRAM and the PXI trigger line. **b**, Schematic of the FPGA layout of the AWGs (Keysight M3201A) used in our experiments (MW modules). The waveform memory stores the amplitude (envelope) and phase information for all the microwave bursts (e.g. X_{90} , X_{-90} , Y_{90} , ...) used in an experiment, as well as for the necessary single-qubit phase corrections (e.g. Z_{45}). The pulse table contains the start and stop memory addresses of each control pulse present in the waveform memory. For every single-shot experiment, the AWG steps through the instruction sequence, which defines all the single-qubit gate pulses that need to be executed during the experiment. When the offset flag of an instruction in the instruction sequence is 1, the current value on the PXI trigger (0/1) is added to the pulse number that will be played from the pulse table. This bitwise addition implements real-time feedback. When an instruction sequence is ran, the amplitude and phase information are read from the waveform memory for the selected pulse numbers one after the other. The differential phase (Δ phase) is added for every rendered sample to the phase accumulator (which controls the qubit frequency) and is then converted to an in-phase (I) and quadrature (Q) signal by the phase-to-amplitude converters (PAC). These I and Q signals are multiplied with the amplitude envelope of the waveform and are then passed to the outputs of the AWG and from there to the vector source. We can run up to twelve sequencers in parallel in a single AWG.

REAL-TIME FEEDBACK

Initially, we aimed at performing a quantum error correction experiment with real time feedback. While we did not manage to perform these experiments using current devices/methods, we did manage to develop (in collaboration with Keysight) the needed control systems for such experiments. Furthermore, we used the feedback capabilities to initialize the qubits as illustrated in chapter 5. In the following sections the FPGA layout of the AWG and digitizer that allows for this will be discussed.

The real time feedback is implemented by sending data from the digitizer to the AWG, whereby the pulse that the AWG subsequently sends to the sample depends on the measurement outcome (the result of processing the measurement signal in the digitizer card). To facilitate this data transfer we use the PXI trigger lines of the PXI chassis that holds the AWGs and digitizers as shown in Fig. 6.3. We configure the chassis such that the digitizer writes bits of data to the trigger ⁷ lines and which are connected to the AWG input.

The block diagram describing the FPGA layout of the digitizer and AWG is shown in Fig. 6.4. A crucial development for both the AWG and digitizer was a custom instruction sequence table. This table holds the instructions for the AWG and digitizer to be performed at specified times. For the digitizer, the instruction sequence specifies the measurement time ($t_{measure}$), a wait time after the measurement (*wait after*) and a *threshold* to differentiate the qubit state. When the instruction is executed, it directly starts measuring for the specified time, after which the averaged result is compared to a threshold, which returns a value of 0 or 1. This result is written to one of the PXI trigger lines. In addition the outcome is also written to the DRAM of the digitizer (not shown in the schematic), such that the measured result can be easily read out remotely.

The schematic of the block diagram of the AWG is shown in Fig. 6.4b. In this case, the instruction sequence holds table where each entry has a *pulse number*, *offset* and *wait time*.

- The *pulse number* defines which pulse needs to be played. The pulse number corresponds to the entry number in the pulse table. The pulse table holds the start and stop addresses of the waveform memory defining the pulses that need to be played.
- The *offset* is a flag that indicates if a bitwise addition of the pulse number with the value of the PXI trigger needs to be done. This simple addition forms the core of the feedback mechanism in our experiments. For example, if the instruction sequence defines a pulse number 4 and an offset of 1; the 4th entry will be selected if 0 was measured ($4 + 0 = 4$); in case 1 was measured, the 5th entry in the pulse table would be selected ($4 + 1 = 5$). The feedback can be implemented for multiple measurement results by using multiple trigger lines (currently implemented for 2 bits of data) or by storing the bits in a local register.
- The *wait time*, defines how many clock cycles need to be counted before reading the next instruction.

⁷The word trigger line might be misleading in this context, as we don't use them to trigger anything in this case. All we do is set/read a 0 or 1 state.

In our system, this modified FPGA image was developed for the generation of IQ signals but not yet for baseband pulses (e.g. two-qubit gates, readout pulses, ...). For baseband pulses, we upload full waveforms⁸, as no feedback was needed for these channels.

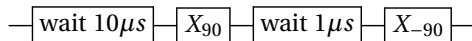
The baseband IQ signal is used to modulate the microwave carrier which generates the signal that drives Rabi rotations on the qubits. When controlling several qubits at different frequencies with a single vector source, the frequency of the driving signal is distributed⁹ between the microwave source (f_c) and the baseband IQ signal (f_{IQ}), for which we ensure the following :

$$f_{qubit}(t) = f_c + f_{IQ}(t) \quad (6.4)$$

As such, we need to keep track of the frequency of every qubit in the FPGA. This is illustrated in the block diagram in Fig. 6.4b.

A separate instruction sequence is implemented for each qubit, hosting its own numerical controlled oscillator (NCO) that tracks the phase of the qubit. The numerically controlled oscillator consists of a phase accumulator and a phase to amplitude converter. Every timestep, a phase $\Delta phase$, is added to the phase accumulator. The phase increment defines the frequency at which the phase accumulator runs ($\Delta phase = \frac{2\pi \cdot f_{acc}}{\text{SAMPLE RATE}}$). The accumulated phase is converted into an amplitude by looking up its value in a sine/-cosine table.

To better understand the capabilities of the AWG, we consider the programming needed for a Ramsey experiment for a single qubit :



The instruction sequence for this experiment can be found in Fig. 6.4b. The sequence start with a $10\mu s$ wait. The wait triggers a short waveform (5ns), after rendering this waveform, the last phase increment is maintained (the FPGA runs at 200MHz). The phase increment, a , of this pulse is chosen such that the numerical oscillator follows the frequency of the idling qubit ($f_{IQ} = f_{qubit} - f_c$).

Next a X_{90} pulse is rendered. The qubit is driven at its driving frequency, defined by a phase increment b . Notice that the first and last entry of the amplitudes ($A(t)$) have a zero amplitude. This allows us to program a phase shift in a single sample (1ns). This is illustrated in pulse number 2 (Fig. 6.4b), a X_{-90} pulse. The phase of the pulse is shifted by 180 degrees by adding this increment to the first $\Delta phase$ entry. The last entry sets the phase back to the starting phase (in the rotating frame). The same method can also be used to implement virtual Z gates.

6.4. SOFTWARE

Over the years, several software packages have been developed that made simulating, programming and running experiments more efficient. Below I give an overview of the

⁸There is nothing stopping us from implementing an instruction set for baseband signals, but time is finite in this universe.

⁹In general it is a good idea to avoid $f_{IQ} = 0[\text{Hz}]$ as the pink noise of the AWG output signal is much stronger at low frequencies.

packages that I developed during my PhD:

- DM_solver : a fast and easy interface to solve the time-dependent Schrödinger equation.
- Core_tools : efficient experimental loops and secure, fast and (non-)local data storage (and more).
- PulseLib : efficient control interface to program pulse sequences for spin qubits.
- SpinQubitTemplates : abstract template library that builds on the functionality of PulseLib. The goal is to easily write quantum circuits in code, i.e. provide the needed abstractions to describe the gates in quantum algorithms.
- uMagLib : library that simulates the magnetic fields of micromagnets.

In the following sections a more detailed description of every library will be given.

6.4.1. DM_SOLVER

DM solver¹⁰ stands for density matrix solver. This package was developed to perform simulations for the algorithms executed on the device described in chapter 3, but can be used to simulate most spin qubit experiments. The goal of this library is to offer an API that allows one to simulate the time-dependent Schrödinger equation using pulses and noise models that mimic the experiments performed in the lab.

6

This library is subdivided into three main components, who each perform a separate function (see Fig. 6.5) :

- The H_channel class creates an Hamiltonian channel object, that describes the amplitude of a specific operator in function of time. This amplitude can also include noise.
- The H_Solver class is the object that collects all the H_channel objects, which defines the total Hamiltonian that needs to be simulated. In addition, a Lindbladian can also be defined at this stage. After the input of simulation is defined, this object is also used to call the H_Calculator class, which solves the Schrödinger equation and can be used to extract the observables.
- The H_Calculator class forms the core of the library. It perform the actual calculation and is written in c++ for performance reasons.

The following sections will discuss each of these components in more detail.

H_CHANNEL

In our experiment, gated pulses are used to enhance/decrease the amplitude of certain parts of the Hamiltonian. This simulator offers similar functionality using the Hamiltonian channels, which are defined by a time-dependent pulse amplitude, $p(t)$, and its corresponding operator \mathcal{O} . Noise, for example 1/f noise, nuclear spin noise, etc. can be

¹⁰https://github.com/stephanphilips/DM_solver

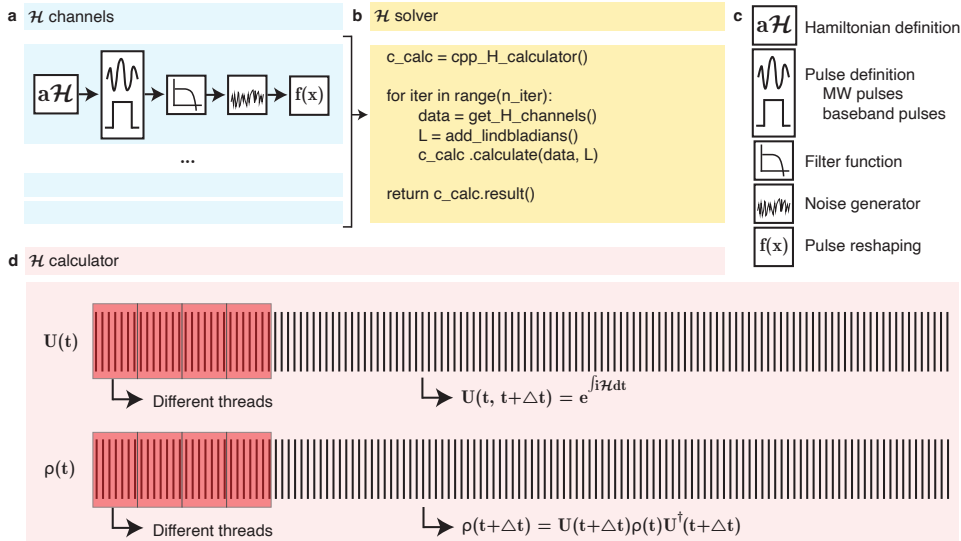


Figure 6.5: **DM_solver architecture** | **a**, Graphical representation of the `H_channel1` class where each blue box represents an instance of `H_channel1`. This class processes the input data as shown by the block diagram (legends in panel **c**). The sequence generates a waveform with the amplitudes of the Hamiltonian in function of time. **b**, Pseudo code showing the function that fetches calculations from the `H_Calculator` class. When sampling noise from a distribution, the problem is repeated for `n_iter` times. For each iteration the Hamiltonian describing the problem is regenerated, noise resampled, and re-calculated. The average density matrix is returned at the end of the calculation. **c**, Symbols describing the operations performed in the `H_channel1` class. **d**, Schematic illustrating the calculation of the unitaries, $U(t)$ and the density matrices, $\rho(t)$. First, the unitaries are calculated. Every black bar represents a slice of the calculated unitary for a discrete time step. The calculation is distributed between the different cores of the CPU. The collection of unitaries is split in groups of one thousand matrices, which are assigned to different threads, as shown in the schematic. A similar principle is used for the calculation of the density matrices, $\rho(t)$ (see main text for details).

added using the noise function $f_{noise}(t)$.

The full definition of a Hamiltonian channel can written as:

$$H_i(t) = f_{reshape,i} \left(f_{signal,i} (p_i(t)) + p_{noise,i}(t) * f_{noise,i}(t) \right) \cdot \mathcal{O}_i \quad (6.5)$$

where $H_i(t)$ is the i^{th} Hamiltonian channel, $f_{signal,i}$ is a function that reshapes the signal amplitudes $p(t)$, e.g. a filter function¹¹. $p_{noise}(t)$ is a function that can modulate the noise generator $f_{noise}(t)$.

The $f_{reshape,i}$ function reshapes the signal as a whole, including the noise. This functionality can for example be used to describe a voltage pulse on the barrier gate of a quantum dot system. When the barrier gate is pulsed, the exchange J increases exponentially. This behavior can be simulated by setting $f_{reshape,i}(x) = e^x$.

In the following, we use an example a single-qubit Hamiltonian to illustrate how the `H_channel` classes works. The Hamiltonian for a single qubit that is driven is given by:

$$\hat{H} = \omega \hat{S}_z + 2\Omega(t) \sin(\omega t + \phi) \hat{S}_x \quad (6.6)$$

Where ω corresponds to the frequency of the qubit, $\Omega(t)$ the Rabi frequency and \hat{S}_z and \hat{S}_x are the spin matrices. The units are in radians.

6

In our experiment, we perform a X_{90} rotation on the qubit. In short, we need to set the resonance frequency (S_z channel) of the qubit (a constant) and describe a pulse that performs the $\frac{\pi}{2}$ rotation (S_x channel). In python code, this would look like:

```
from DM_solver.solver import H_channel, H_solver
from DM_solver.utility.pauli import X,Y,Z

import numpy as np

f_qubit = 1e9 # 1 GHz
f_drive = 5e6 # 5 MHz

# define channel -- Sz hamiltonian. Units of [rad]
Qubit1_Z = H_channel(Z/2)
Qubit1_Z.pulse.add_constant(2*np.pi*f_qubit)

# define channel -- Sx hamiltonian.
Qubit1_X = H_channel(X/2)
# define a pulse from 10 ns to 60ns
Qubit1_X.pulse.add_MW_pulse(10e-9,60e-9, amp=4*np.pi*f_drive, freq=
                           f_qubit, phase=np.pi/2)

# show the pulse
Qubit1_X.plot_pulse(t_end=100e-9, sample_rate=1e11)
```

The pulse and outcome of this experiment is shown in Fig. 6.6.

¹¹Waveform generators have a limited bandwidth, with a specific frequency response. This can lead to ringing effects and defines the rise time of the pulse. When the frequency response is known, these effects can be included in the simulation.

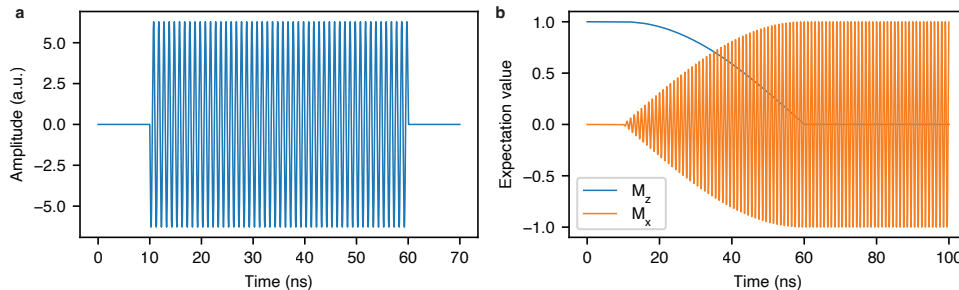


Figure 6.6: **Single qubit Rabi simulation** | **a**, Amplitude $p(t)$ of the S_x channel in function of time. **b**, Expectation values ($M_z = \langle \psi(t) | \hat{S}_z | \psi(t) \rangle$, $M_x = \langle \psi(t) | \hat{S}_x | \psi(t) \rangle$) of the wavefunction during the evolution.

To ensure that most pulses used in spin qubit experiments can be made, the `H_channel.pulse` class is equipped with the following methods (Si units are used), which are very similar to the ones used in the `pulse_lib` library:

- `pulse.constant(amp)`, sets a constant amplitude for the whole sequence. Note that it is still possible to use the other methods on top of this one.
- `pulse.add_block(t_start, t_stop, amp)`, adds a block pulse from `t_start` to `t_stop` with an amplitude `amp`.
- `pulse.add_ramp(t_start, t_stop, start_amp, stop_amp)`, similar to the block function, but adds instead a ramp.
- `pulse.add_function(t_start, t_stop, function)`, adds a pulse that is defined by a function between the given start and stop time (e.g. as used for shaped two-qubit gates).
- `pulse.add_MW_pulse(t_start, t_stop, amp, freq, phase, AM, PM, is_complex)`, adds a microwave pulse to the simulation, with a given start and stop time, frequency and amplitude. It is also possible to specify a phase (=rotation axis) and a amplitude/phase modulation. The amplitude modulation argument supports the `get_window(scipy.signal.windows.get_window)` function. The last argument can be used to add a complex, oscillating signal to the Hamiltonian which is common in transformed Hamiltonians. In this case the signal $\mathcal{O}A(t)\sin(\omega t + \phi(t))$ is represented as $\text{triu}(\mathcal{O})A(t)e^{i\omega t+\phi(t)} + \text{tril}(\mathcal{O})A(t)e^{-i\omega t+\phi(t)}$. Where `triu` (`tril`), is the upper (lower) triangle of the matrix.
- `pulse.add_phase_shift(phase)`, adds a phase shift to all subsequent microwave pulses (e.g. to account for a phase shift due to a Stark shift).

A filter can be applied to the pulse after pulse definition. For example the output filter of the Keysight M3201A AWG:

```
test_channel = H_channel(x/2)

test_channel.pulse.add_block(5e-9, 10e-9, 1)
```

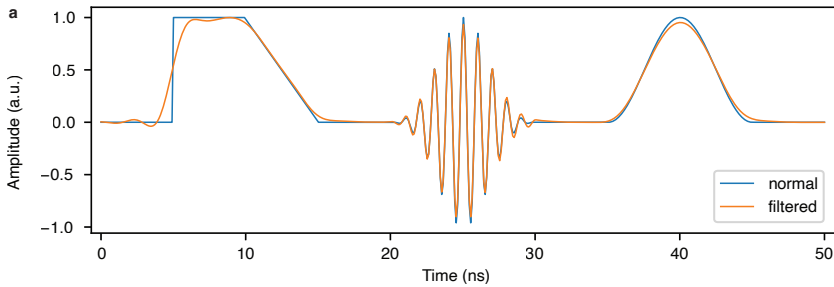


Figure 6.7: **Filter functions** | a, pulse amplitude of the unfiltered ($p(t)$) and filtered ($f_{signal}(p(t))$) pulse represented in the code snipped in the main text.

```

test_channel.pulse.add_ramp( 10e-9, 15e-9, 1, 0)
test_channel.pulse.add_MW_pulse(20e-9, 30e-9, 1, 1e9, AM='blackman')

SineShape = lambda x:(1-np.cos(x*np.pi*2))/2
test_channel.pulse.add_function(35e-9, 45e-9, SineShape)

from DM_solver.pulse_generation.filters import keysight_AntiRing_filter
test_channel.pulse.add_filter(keysight_AntiRing_filter)
test_channel.plot_pulse(50e-9)

```

6

Fig. 6.7 shows the rendered pulse. The filter is applied directly on the baseband pulse elements. For microwave pulses, only the envelope of the pulse is send through the filter, resembling the signal generation with a vector microwave source as used in the experiments.

The previous paragraphs discussed the generation of the pulse $f_{signal}(p(t))$, now we switch gears and explain how noise is generated in the simulations. When adding noise to the simulations the run time increases significantly as one needs to average over the noise distribution(s). A simulation typically has to be averaged 1000-10000 times, where in each iteration, $f_{noise}(t)$ is resampled. Two types of energy conserving noise can be added to a $H_channel$ object:

- **Static noise** is used to simulate slowly varying noise, i.e. a noise source that has a constant value during a single shot of the experiment/simulation (e.g. nuclear spin noise). The noise is added by sampling from a normal distribution for every iteration of the experiment :

$$H_{noise} = p_{noise}(t) * f_{noise}(t)\mathcal{O}_c = p_{noise}(t)\mathcal{N}(0, \sigma)\mathcal{O}_c \quad (6.7)$$

where \mathcal{O}_c is the noise channel operator, $p_{noise}(t)$ a function that can be used to modulate the noise in function of time and $\mathcal{N}(\mu = 0, \sigma)$ is a sample from a normal distribution. The noise can be added to the simulation using the method
 $H_channel.add_noise(generator, pulse_modulation=None),$

```

from DM_solver.noise.noise_sources import static_noise_generator

```

```

sigma_noise = np.sqrt(2)/50e-9 # T2* : 50ns
my_noise    = static_noise_generator(sigma_noise)
Qubit1_Z.add_noise(my_noise, pulse_modulation=None)

```

The quantity of the noise can be set using the relation $\sigma = \frac{\sqrt{2}}{T_2}$ [1].

- The second type of noise acts on faster time scales, which can be well described using a **noise (power) spectral density** $S(f)$. This function is well suited to describe charge noise which can be characterized by the function $S(f) = \frac{1}{f^\alpha}$. If the noise spectral density is known, we can use it to generate traces of noise in function of time[16]. We start by generating white noise in frequency space:

$$\epsilon(f) = \mathcal{N}\left(\mu = 0, \sigma = f_s \frac{\sqrt{S(f)}}{2}\right) + i\mathcal{N}\left(\mu = 0, \sigma = f_s \frac{\sqrt{S(f)}}{2}\right) \quad (6.8)$$

where $\epsilon(f)$ is the noise function and f_s the sample rate. Then we perform an inverse Fourier transformation¹² on $\epsilon(f)$, such that $f_{noise}(t) = FFT(\epsilon(f))$.

An example of the implementation in code is give below:

```

from DM_solver.noise.noise_sources import spectral_noise_generator

S_f = lambda f: 1e8/f #1 over f noise with an amplitude of 1e8
f_cutoff = None

my_noise = spectral_noise_generator(S_f, f_cutoff)
Qubit1_Z.add_noise(my_noise, pulse_modulation=None)

```

One of the limitations of this method is that only the noise power within the range¹³ $[f_{sim}, \frac{f_s}{2}]$ is included. Which means that the amount of noise in the simulation depends on its the length. This problem can be circumvented by defining a cutoff frequency f_cutoff , such that noise is effectively sampled in the range $[f_{cutoff}, \frac{f_s}{2}]$. The additional noise is modeled as static noise with a standard deviation of

$$\sigma_{spect} = \sqrt{2 \int_{f_{cutoff}}^{f_{sim}} S(f) df} \quad (6.9)$$

Such that :

$$f_{noise}(t) = FFT(\epsilon(f)) + \mathcal{N}(\mu = 0, \sigma = \sigma_{spect}) \quad (6.10)$$

When no cutoff frequency is defined, the static noise contribution is neglected.

Noise correlations between different channels can be added by providing a copy of the same noise source to different channels, e.g.:

```

Qubit1_ZI.add_noise(0.5*noise)
Qubit2_IZ.add_noise(1*noise)

```

¹²We set $c(f = 0) = 0$, as this is infinitely large for pink noise.

¹³ $f_{sim} = \frac{1}{t_{sim}}$, where t_{sim} is the total time simulated.

In this case, qubit 1 and 2 will receive identical noise, where the amplitude of the noise on the first qubit is half as large. This can be useful, as sometimes a single fluctuator influences multiple parameters in the Hamiltonian.

At the last stage of the pulse definition, a reshaping function can be added. This function allows one to rescale the pulse and its noise data. For example, an exponential scaling function is appropriate when one wants to describe the exchange interaction between two qubits using gate voltages. In such a case, one could write:

```
EXP = lambda x : np.exp(x)
Channel_B12.add_pulse_modulator(EXP)
```

H_SOLVER

The H_solver class is designed to interact with the c++ code and the input data of the simulation. The solver object is quite simple, as illustrated below

```
from DM_solver.solver import H_solver

calc = H_solver()
calc.add_channels(Qubit1_Z,Qubit1_X)
calc.add_lindbladian(np.matrix([[0,0],[1,0]]), np.sqrt(1/10e-9)) #T1 of
                                                               10ns

psi_0 = np.matrix([[1,0],[0,0]]) #density matrix of the init state
calc.calculate(psi_0, end_time = 100e-9, sample_rate = 1e11, n_iter=1)

# calculate some expectation values and plot
Z_expect, X_expect = calc.return_expectation_values(Z, X)
time = calculation.return_time()
```

6

On creation of an H_solver instance, the different H_channel instances can be added using the add_channels method. The add_lindbladian method adds noise via a Lindblad operator A and amplitude γ (see next section).

At this point, all possible inputs for the simulation are provided and the calculation can be started. The n_iter parameter in the calculate method specifies the number iterations for modeling noise.

At the end of the calculation, expectation values can be calculated (e.g. $tr(\rho \hat{A})$) for the operators (\hat{A}) of interest.

H_CALCULATE

The H_calculate function performs the actual calculation. This function does two things : (1) calculate the **unitaries** describing the time evolution generated by the Hamiltonian (2) calculate the **evolution** of the Hamiltonian.

A single unitary operation describes the evolution of the quantum system during a discrete time step Δt . The unitary is calculated as:

$$U(t, t + \Delta t) = e^{-iH(t)\Delta t} \quad (6.11)$$

The matrix exponential can be calculated using several methods [10] (e.g. Taylor series/Padé approximation). We choose to calculate the matrix exponential using matrix decomposition, which is especially efficient for symmetric matrices. Suppose a matrix A has eigenvectors U and the eigenvalues D ($A = UDU^{-1}$), then the matrix exponential can be evaluated as :

$$e^A = U e^D U^{-1} \quad (6.12)$$

This calculation is performed in c++, as it is efficient and as it has great multithreading libraries (e.g. openMP). For every time step in the calculation, $H(t)$ is known. This means we can parallelize it by splitting it up in several batches of size N , so that the first core of the CPU takes care of the first batch, b_0 , the second core of b_1 and so on ... (see Fig. 6.5). We also calculate the total unitary of every batch ($U_{b_i} = \prod_{j=0}^N U_{b_{i,j}}$). This allows us to parallelize the calculation of the density matrices as well, as it is easy to calculate the initial density matrix for every batch.

The software calculates the evolution of the quantum states using a master equation (either the von Neumann equation or the Lindblad equation). The von Neumann equation is given by:

$$\frac{\partial \rho}{\partial t} = -\frac{i}{\hbar} [H, \rho] \quad (6.13)$$

Which is solved in the software as:

$$\rho(t + \Delta t) = U(t, t + \Delta t) \rho(t) U^\dagger(t, t + \Delta t) \quad (6.14)$$

In case a Lindbladian [9] is added, the evolution of the system is given by :

$$\frac{\partial \rho}{\partial t} = -\frac{i}{\hbar} [H, \rho] + \sum_i \gamma (A_i \rho A_i^\dagger - \frac{1}{2} A_i^\dagger A_i \rho - \rho \frac{1}{2} A_i^\dagger A_i) \quad (6.15)$$

Which is implemented as :

$$\rho(t + \Delta t) = U(t, t + \Delta t) \rho(t) U^\dagger(t, t + \Delta t) + \sum_i \Delta t \gamma \left(A_i \rho(t) A_i^\dagger - \frac{1}{2} A_i^\dagger A_i \rho(t) - \rho(t) \frac{1}{2} A_i^\dagger A_i \right) \quad (6.16)$$

As this equation needs to be executed with the right time ordering, no multithreading can be used here.

6.4.2. CORE_TOOLS

This package¹⁴ is a collection of commonly used tools needed to carry out spin qubit experiments. This entails a storage back-end, graphical user interfaces (GUI's) for video mode plotting, gate voltages, virtual gates and storing variables. It also contains a hardware class which streamlines the process of configuring the experiment, for example, keeping track of settings, linking the DAC voltage with the AWG voltages (AWG channels are attenuated), etc. In the following sections the ideas behind the different parts of the packages will be explained. A more practical usage description can be found in the online [documentation](#).

¹⁴https://github.com/stephanlphilips/core_tools

DATA STORAGE

A new data storage back end was developed to solve some of the issues with the previous solutions :

- Data locality : the data was either stored in a text file (inefficient and hard to sort through) (known as the 'old' QCoDeS format) or in a SQLite database which has a poor performance¹⁵ (the current QCoDeS dataset). Both solutions are not ideal, as it is hard to copy data from one system to another one.
- No overview : all the files are stored on different locations, with an ever growing tree of directories. There is no option to sort/search through them in an efficient way. This is also a problem for the qCoDeS database as only a limited number of experiments can be saved in a single database.

To solve these issues, a different approach to data storage was envisioned where the data of every experiment could be accessed through the cloud. A schematic of such an architecture is shown in Fig. 6.8. Every measurement computer runs a local database that stores the measurements taken on that system. The experimentalist can access the local measurements for liveplotting, inspecting and analyzing data. At the same time, the local database is also synchronized with a remote database in the cloud¹⁶.

As a result, the experimentalist can seamlessly switch from analyzing data on the measurement computer in the lab to another device, as the data availability is device independent. Notice that the remote database holds data from all the experiments performed on the different setups in the lab and allows one to inspect/compare data between the different setups. This can be useful when you measure the same sample in different setups (i.e. in a dipstick and a dilution refrigerator), as it is possible to group the data together.

The data storage solution was realized using a PostgreSQL database. This database has good all around performance and supports¹⁷ storage formats for binary data (numpy arrays) using large binary objects (lobject). This object stores the measured data of the experiment in memory and writes it regularly to the hard drive.

In the following sections the usage of this dataset solution will be explained in more detail. We start by defining a measurement and how we store it in the SQL data tables. Then we look at the different ways the dataset can be inspected.

Defining measurements

A measurement is a collection of outcomes from a measurement apparatus. Several apparatuses can be measured after each other. We often perform these measurements as a function of *setpoint parameters*. A setpoint parameter is a parameter which controls

¹⁵The poor performance is caused by a bad database architecture, rather than issues with the database itself.

¹⁶In the 'cloud' means that the remote database runs on a remote server.

¹⁷In retrospect, this feature might not have been needed, as the data could also be stored using an object storage service, which might facilitate scaling for larger systems (the data does not have to be on the same server as the database) (from discussions with Arthur Newton).

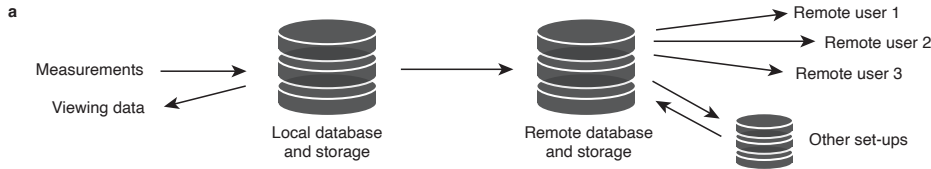


Figure 6.8: **Data storage architecture | a**, the left side of the figure shows the user at a measurement setup interacting with a local database. The user uploads measurements to the local database and inspects them as the data comes in. The local storage is synchronized with a larger, remote database, which holds the data of all the setups in the lab. Several users can connect to this server at the same time and request datasets.

a variable in the experiment, for example, the applied magnetic field, the duration of a microwave pulse, the voltage on a gate,

We say a measurement has zero dimensions (0D), if it does not have a setpoint parameter and 1/2D¹⁸ if it is measured in function of one or two setpoint parameters, for example a charge stability diagram, where two gate voltages (or virtual gate voltages) are the set-point parameters.

We describe our measurements using a simple syntax (based on the QCoDeS one):

```
# register a measurement
from core_tools.data.lib.measurement import Measurement

meas = Measurement("give me a name")

# two setpoint parameters are swept (x (S1), y (S2) axis), with 50
# points on each axis
meas.register_set_parameter(S1, 50)
meas.register_set_parameter(S2, 50)

# we will be measuring 1 parameter that depends both on the value of S1
# and S2
meas.register_get_parameter((M1, M1()), (S1, S1()), (S2, S2()))

# generate the dataset in the context manager
with meas as ds:
    # do sweep on two axes
    for i in range(50):
        S1(i) # set first setpoint
        for j in range(50):
            S2(j) # set seconds setpoint
            # measure + write the results
            meas.add_result(M1, S1, S2)

# get the dataset
dataset = meas.dataset
```

6

In reality this is a long syntax to perform for loops, instead, we usually run functions like :

¹⁸Note that there are no restrictions on the dimensionalality of a measurement.

```
from core_tools.sweeps.sweeps import do0D, do1D, do2D

ds1 = do0D(*m_param).run() #m_param = list of measurement variables
ds2 = do1D(param, start, stop, n_points, delay, *m_param).run()
ds3 = do2D(param_1, start_1, stop_1, n_points_1, delay_1,
           param_2, start_2, stop_2, n_points_2, delay_2, *m_param).run()
```

Notice that the scan function has a `.run()` function at the end. This function runs the scan in the main thread. Alternatively, the scan can also be run in a separate thread using the `.put()` argument, which puts the experiment in an external queue. This functionality is handy as it allows the experimentalist to queue experiments, and analyze data in the same kernel during run time.

6

Structure of a measurement in the database

The measurement data is divided over two tables in the PostgreSQL database. On creation of a measurement, a new entry is made in the `global_measurement_overview` table. This table contains the following entries: `id, uuid, exp_name, set_up, project, sample, created_by, start_time, stop_time, completed, snapshot, metadata, keywords, starred, data_cleared, data_synchronized, table_synchronized and sync_location`. The entries in red hold information about the identity and the state of the measurement (e.g. where and when has it been measured? Is the measurement completed?), the entries in teal hold additional information about the measurement (e.g. a snapshot of the state of the setup, additional metadata (e.g. what AWG pulses were executed), some keywords identifying the measurement and a rating of the measurement). The violet entries hold information about the data synchronization.

When a new record is added to the `global_measurement_overview` table, several new records are written to the `measurement_parameters` table. For every measured parameter, information about the measurement scan needs to be saved. This includes basic information about the parameters (measurement parameter and involved setpoints), like names and units, and information about the storage location of the measured binary data.

Inspecting measurement results

The data sets themselves can be displayed to the user by printing the dataset (e.g. `print(ds)`), which shows an output like:

```
dataset :: my_measurement_name

id    = 1256
uuid = 1225565471200

| idn | label | unit | size |
```

```

| m1      | 'I1'   | 'A'    | (100,100) |
| x       | 'P1'   | 'mV'   | (100,)   |
| y       | 'P2'   | 'mV'   | (100,)   |

| m2      | 'I2'   | 'A'    | (100)    |
| x       | 'P1'   | 'mV'   | (100,)   |

database : vandersypen
set_up : XLD
project : 6dot
sample_name : SQ19

```

The contents of the dataset can be accessed using the following syntax:

- Measurement parameters are denoted as `m1`, `m2` and can be accessed by calling `ds.m1`, `ds.m2`. If multiple measurement variables are present in a single measurement parameter (e.g. IQ trace), the data will be organized as `m1_1`, `m1_2`, `m2`, etc. Alternatively the data can also be accessed using the label of the measured variable (e.g. `ds['I1']`), which allows for better readability of the code.
- The setpoints of the measurement variables can be called by `ds.m1.x`, (or `ds.m1.x`, `ds.m1.y` if there are multiple setpoints)

In addition, it is also possible to slice/average the data set using a syntax similar to the numpy library. Examples of this functionality can be found in the online documentation.

6

The data can be viewed with an application with a graphical user interface, the data browser. The data browser shows an overview of all the measurements run on a particular day (see Fig. 6.9). When clicking on a measurement, it will show the contents of a measurement as a set of graphs/heatmaps (see Fig. 6.10). If the measurement is currently being measured, the plot will update in real time. Many ideas for the GUI were inspired by the PLOTR¹⁹ package, developed/used in the Kouwenhoven lab.

GUI's

Aside from graphical user interfaces used to interact with the data storage, several other GUI's have been developed:

- Parameter viewer (Fig. 6.11a) : used to inspect and set voltages on the sample. The voltages can be changed by scrolling with the mouse or by entering a number.
- Virtual gate matrix (Fig. 6.11b,c) : this is a GUI developed to easily set values in the virtual gate matrix. The invert option allows access to the inverted virtual gate matrix. Updates are direct and affect the parameter viewer in real time. In addition all changes to the virtual gate matrix are saved in a database (no need to save anything when loading a new session). The attenuation tab allows for the conversion of AWG to dac voltages, which allows us to share the virtual gate matrix for both instruments.

¹⁹<https://github.com/toolsforexperiments/plottr>

a

Data Browser					
OVERVIEW		SEARCH			
Project	6dot	Set up	XLD	Sample	603S - SQ20-20-5-18-4
Date	ID	UUID	Time	Name	Keywords
01/12/2020	★ 3846	1606844240036898284	18:37:20	qubit 4 rabi	time, Signal 1
30/11/2020	★ 3845	1606844149704898284	18:35:49	qubit 4 freq search	freq, Signal 1
29/11/2020	★ 3844	1606844064053898284	18:34:24	qubit 4 freq search	freq, Signal 1
28/11/2020	★ 3843	1606843950398898284	18:32:30	qubit 4 rabi	time, Signal 1
27/11/2020	★ 3842	1606843819656898284	18:30:19	adiabatic sweep qubit 3 and 4	Frequency, Signal 1
26/11/2020	★ 3841	1606843806745898284	18:30:06	psb test coherent pulses	✓P1, Frequency, Signal 1
25/11/2020	★ 3840	1606843742086898284	18:29:02	adiabatic sweep qubit 3	Frequency, Signal 1
24/11/2020	★ 3839	1606843652090898284	18:27:32	psb test coherent pulses	✓P1, Signal 1
23/11/2020	★ 3838	1606843617904898284	18:26:57	psb test coherent pulses	✓P1, Signal 1
20/11/2020	★ 3837	1606843552669898284	18:25:52	psb test coherent pulses	✓P1, Signal 1
19/11/2020	★ 3836	1606843518037898284	18:25:18	psb test coherent pulses	✓P1, Signal 1
<input checked="" type="radio"/> Local Connection		<input checked="" type="radio"/> Remote Connection		Enable liveplotting	

Figure 6.9: **Data Browser | a**, Graphical user interface used to browse through the datasets. The data is sorted by default on project, setup and sample. The measurements are displayed per date. When the enable liveplotting toggle is enabled, a new measurement window appear (Fig. 6.10) whenever a new measurement is started. The search functionality is not implemented at the time of writing.

6

- Video mode : user interface to tune devices by continuously taking 1D or 2D scans with an arbitrary waveform generator (see Fig. 6.12a). Similar to the developments of the video mode in the qtt package²⁰, but with a single window for 1/2D scans (axes can be changed), a settings tab and the option for compensated video mode scans (see Fig. 6.12b).
- Variable explorer : an interface that can be used to keep track of variables in the experiment, e.g. the amplitude required to perform a Rabi oscillation at 5MHz, the voltages for the readout point, ... (see Fig. 6.12c). The user can update the variables by hand or by programming (e.g. for calibrations). Every change of the variables is saved to a database, such that a full history is always available.

²⁰<https://qtt.readthedocs.io/en/latest/>

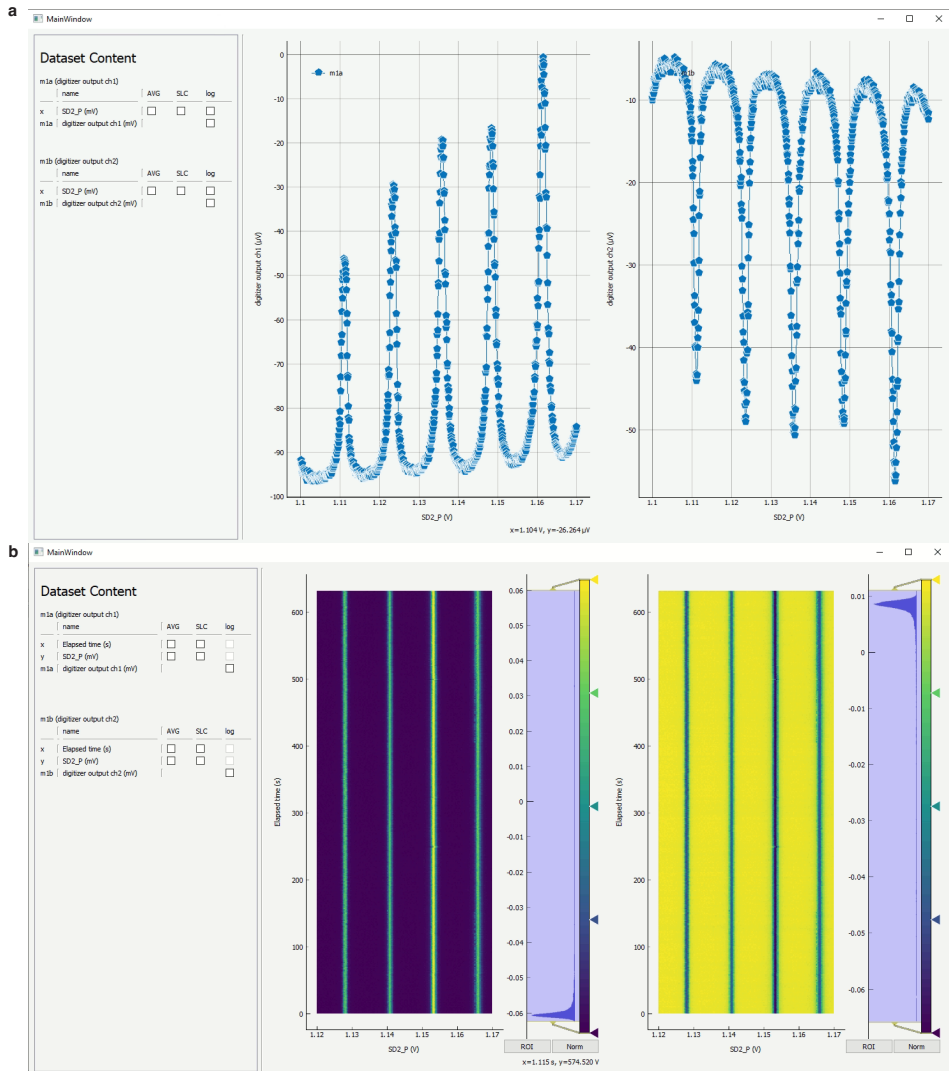


Figure 6.10: Data Viewer | a, Layout of the data viewer for 1D measurements. **b**, Layout of the data viewer for 2D measurements. This measurement can be averaged/sliced along the x or y direction to obtain a 1D plot. The log option allows one to plot the data on a logarithmic scale.

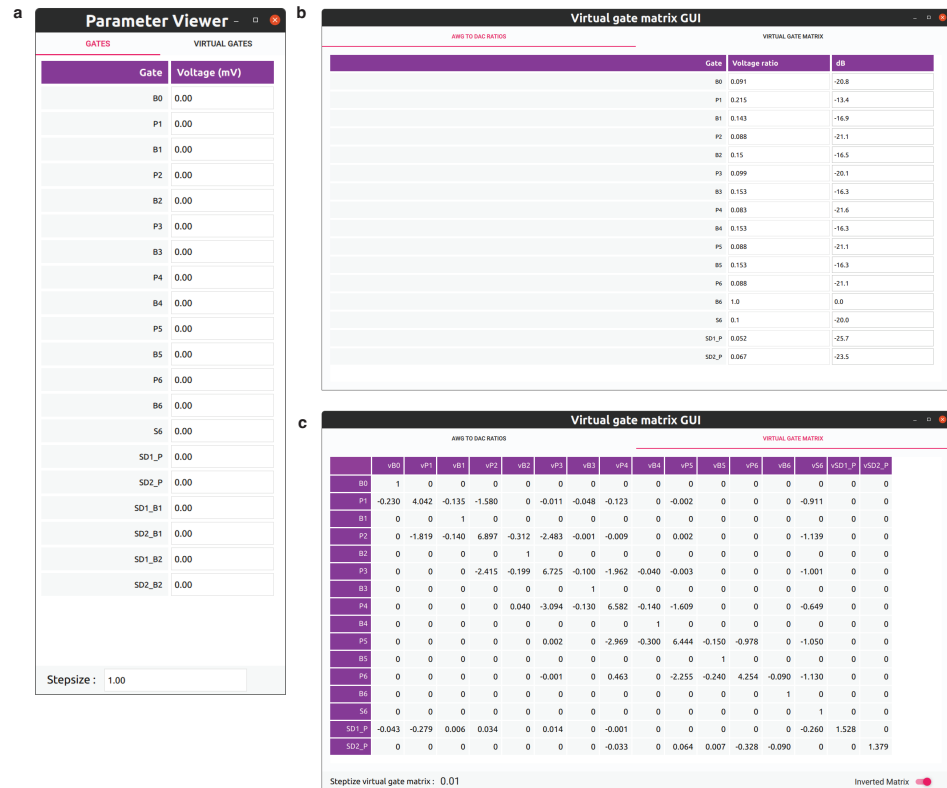


Figure 6.11: **a**, Parameter viewer showing the voltages applied to the gates of a device. For most of the gates, there also exists a virtual gate (in the virtual gates tab). Which can be modified, just like the real gates. **b**, User interface to set the AWG to DAC ratio. This is important, as it is needed to ensure that 1 mV with the DAC's is equal to 1 mV with the AWG on the sample (in addition it is also needed to ensure that the virtual gate matrix is valid for operating both the DACs and AWGs. **c**, Virtual gate matrix graphical user interface. This interface is used to update values of the virtual gate matrix.

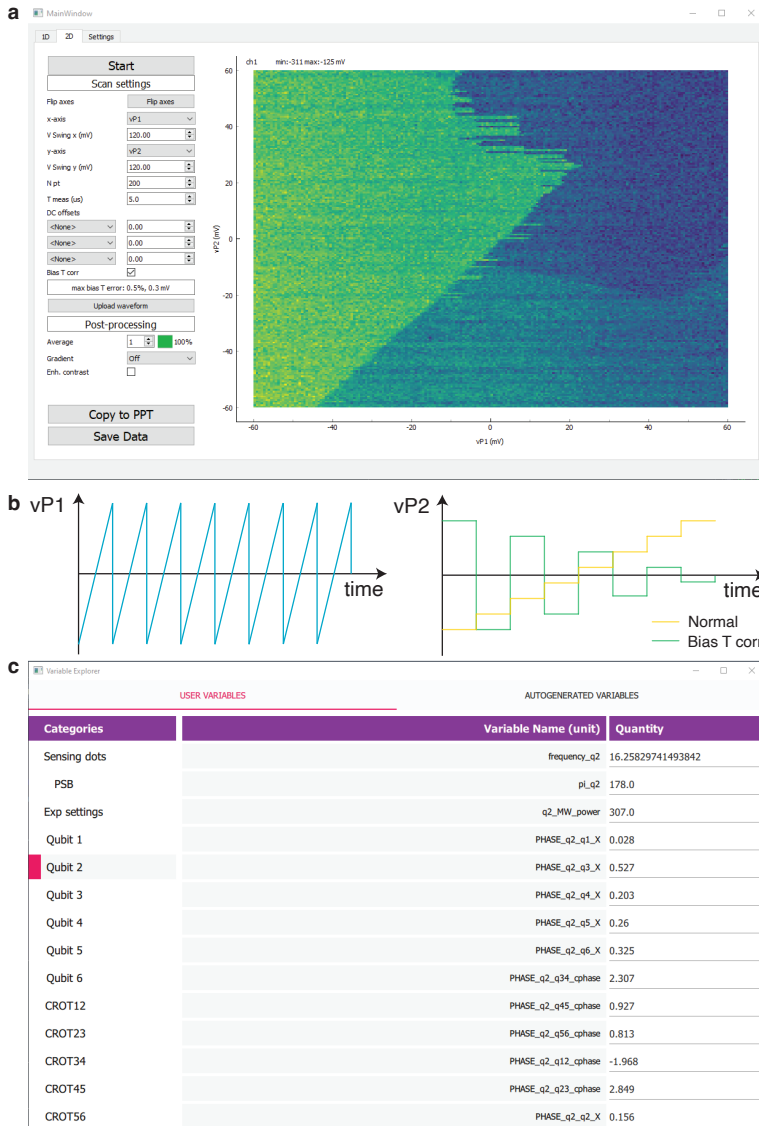


Figure 6.12: **a**, Screenshot of the video mode GUI. The 1D/2D tabs define the type of scan. The left part of the window allows the user to define the properties of the scan. **b**, The bias T corr option in the video mode plotting GUI (panel a) allows one to reduce the charging effects of the bias tee, increasing the integration time that can be used in the scan. This correction is implemented by uploading a modified pulse (green curve) to the AWG that defines the y-axis of the plot. **c**, Screenshot of the variable manager. The left column shows the variables categories, the right column displays the variables in this category.

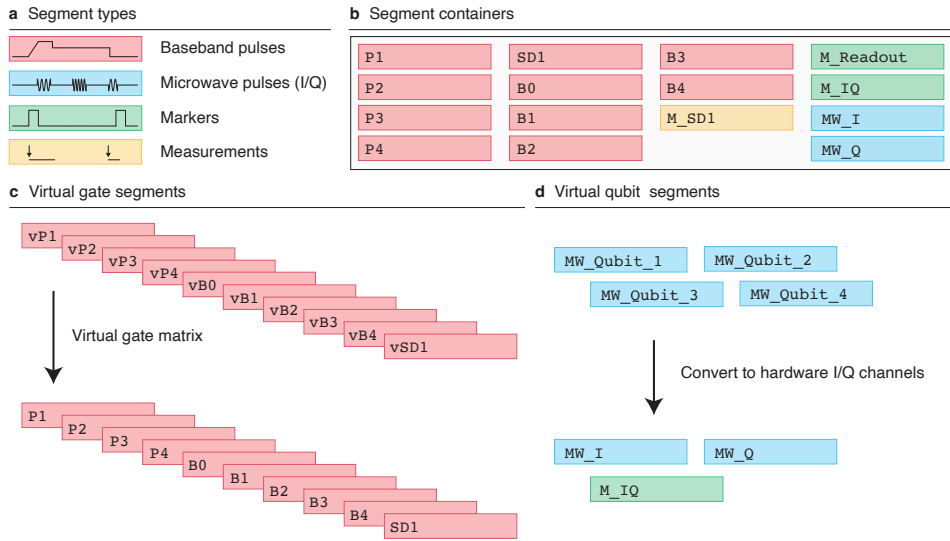


Figure 6.13: **Segments in PulseLib** | **a**, The four types of segments that can be used to build pulses. Each AWG channel is linked to a single segment type, as they are all designed to be connected to a particular instrument. **b**, Graphical illustration of a segment container. A segment container holds segments of all the gates, including virtual segments. The user can access individual segments using this object. **c**, A virtual gate matrix can be supplied which links the ‘real’ gates with the ‘virtual’ gates. **d**, A virtual qubit channel can be constructed to operate qubits at their operating frequency, e.g. one could add a microwave pulse at 12.4GHz, with a well defined phase. Because the frequency of the microwave vector source is known, it can automatically convert it to the appropriate I and Q signals. For each qubit, a virtual channel can be made, which tracks the qubit frequency. It is possible to add a marker to this channel, which will enable the pulse modulation during the microwave pulses (with optional padding).

6

6.4.3. PULSELIB

PulseLib is a library developed with a very simple end goal, namely to make the construction of pulse sequences for quantum experiments as easy as possible. Easy-to-use software usually originates from a well designed code structure. In the following, we introduce segments and segment containers which are essential structural elements in the pulse construction. We also discuss mechanisms for looping and how different back ends can be implemented.

SEGMENTS AND SEGMENT CONTAINERS

A segment is defined as an object that holds instructions describing a pulse on a single channel. A segment container is a collection of segments for the different channels.

A more or less complete description of spin qubit experiments can be created by introducing the four segment types shown in Fig. 6.13a. **Baseband segments** can contain block pulses (adiabatic transitions), ramps (adiabatic transitions) and more complex shapes (i.e. as needed for two-qubit gates). This type of segment is typically used to move charges about (initialization, readout and two-qubit gates). **Microwave segments**

are used to describe single-qubit gates, performed by ESR or EDSR. These segments allow for precise frequency ($f(t)$), amplitude ($A(t)$) and phase control ($\phi(t)$), similar as described in the [DM_solver](#) section [6.4.1](#).

Some of the experimental equipment requires triggering by digital signals (low/high voltage). **Marker segments** are introduced for this. Qubit measurement acquisitions are defined using the **measurement segment**. This segment type specifies when the digitizer needs triggering and the length of the data acquisition.

Segment containers allow one to access all the AWG channels of the experiment (see Fig. [6.13b](#)), which is convenient when programming pulses. In addition to these channels, it is also possible to define virtual segments in a segment container. There are two types of virtual segments, virtual gates and virtual qubit channels (Fig. [6.13c,d](#)). Virtual gates are made by supplying a virtual gate matrix to the pulse library, usually this will be the same matrix as used in core-tools^{[21](#)} environment for the DACs. Virtual and real gates can be used interchangeably in the software.

A single (physical) gate can drive Rabi oscillations on several qubits, for which we use a single microwave source controlled by one IQ output pair of the AWG. To help control the microwave radiation applied to each qubit, we define virtual qubit channels. Every channel keeps track of its own clock at the resonant frequency of the qubit. After the user defines its single-qubit gates on each of these channels, they are all converted into a single I/Q signal that is sent to the vector source.

In the following, an example of the syntax for generating pulses with segments in a segment container is given :

```
# example 1
seg_container = pulse.mk_segment()
seg_container.vP1.add_block(0, 50, 50) #start stop Amp
seg_container.P1.add_block(5, 15, -10)
seg_container.vP2.add_ramp(20, 50, 50) #start stop Amp0 Amp1
seg_container.reset_time()
seg_container.vP2.add_block(0, 10, 30)
seg_container.reset_time()
```

Notice that the `reset_time()` command resets the time reference. This allows one to easily keep building waveforms without the need for manually counting time or making a new segment each time.

When pulsing several gates at once, pulses can also be defined at the level of the segment container:

```
# example 2

gates = ('vP1', 'vP2')
_11 = (0,0)
_11_02_anti = (8,-10)
_02 = (14,-18)
```

²¹Note that pulselib only stores a reference to the matrix, as a result any update of the matrix by the GUI is also an update for pulse lib.

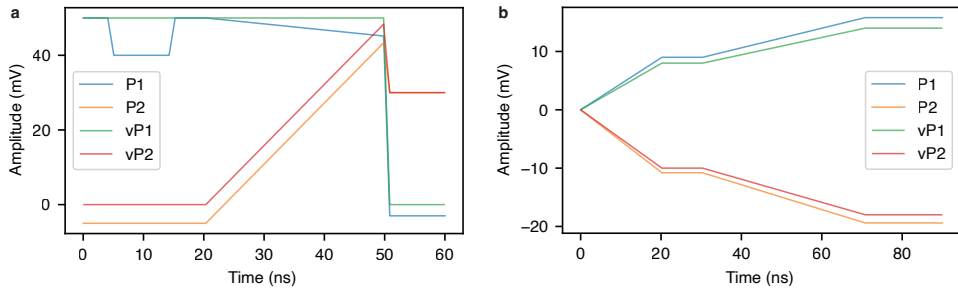


Figure 6.14: **a**, Rendering of example 1. A dummy virtual gate matrix is added to show the effect of programming with virtual gates. **b**, Rendering of example 2.

```
seg_container.add_ramp_ss( 0, 20, gates, _11, _11_02_anti, reset_time=True)
seg_container.add_ramp_ss( 0, 40, gates, _11_02_anti, _02, reset_time=True)
seg_container.add_block(0, 20, gates, _02, reset_time=True)
```

This syntax offers a convenient way to pulse in between charge states. A graphical representation of these pulses is shown in Fig. 6.14.

6

Looping over variables is one of the most used functionalities of a pulse library. Loops are created by placing a loop object instead of a normal variable (e.g. double) as argument. An example of such a loop is shown in the following example (see Fig. 6.15):

```
# example 3
import pulse_lib.segments.utility.looping as lp

t_sweep = lp.linspace(10, 50, n_steps = 5, axis = 0, name = 'Time',
                      unit = 'ns')

seg_container.P1.add_block(10, t_sweep, 20)
seg_container.P1.reset_time()
seg_container.P1.add_block(0, 30, 40)
```

The main advantage of this method is that no strings need to be defined in the pulse instructions. Other libraries (e.g. qupulse²², broadbean²³) typically use a syntax like:

```
my_single_channel_pulse.add_block(10, 't_sweep', 20)
```

Where before uploading, one needs to set the `t_sweep` variable (e.g. using a sweep). This is less convenient, as it forces the user to define variables in two locations.

The waveform generation is independent of the back end – it does not matter which waveform generator you are using. New back ends can be added by defining an

²²<https://github.com/qutech/qupulse>

²³<https://github.com/QCoDeS/broadbean>

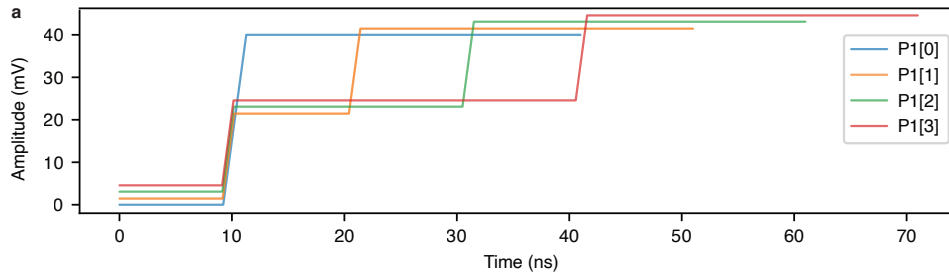


Figure 6.15: Rendering of example 3, the index i of $\text{P1}[i]$, indicates which trace is rendered. An artificial offset is given to the different indices to more clearly display each trace.

.add_upload_job() and a .play() method in the AWG driver. Currently Keysight, Qblox and Tektronix AWGs are supported, in addition, digitizers from Keysight, Spectrum, QBLOX and AlazarTech are also supported.

The link to quantum assembly languages (QASM) (e.g. OpenQASM [3]) can be made using libraries that build on top of this one. For our experiments we added these abstractions using the spin qubit Templates library (next section).

A more extensive overview of all the features of pulselib can be found on the [GitHub](#) repository.

6.4.4. SPINQUBITTEMPLATES

PulseLib is great for describing pulses on a low level, but when programming quantum circuits, it is not a convenient description. To solve this problem, the SpinQubitTemplates²⁴ library was developed.

The SpinQubitTemplates library implements template definitions on two levels :

- a pulse template : this is a parametrized abstraction of a qubit operation, for example a single-qubit gate.
- a gate set : this is a set of related instructions. For example, a single-qubit gate set contains the $X90$, $X180$, $Y90$, $Y180$, $Z90$, $Z180$, $Z(\theta)$ gates. When a pulse template for a $X90$ gate is provided to this set, it automatically generates the other gates by shifting phases/repeating the $X90$ gate. For two-qubit gates, similar sets are available.

Once all the gate sets are created on the device, they can be grouped in one object (here my_QP). An example of the syntax for the operation of a device with templates is given below :

```
my_QP = generate_get_sets()
```

²⁴<https://github.com/stephanphilips/spin-qubit-operations>

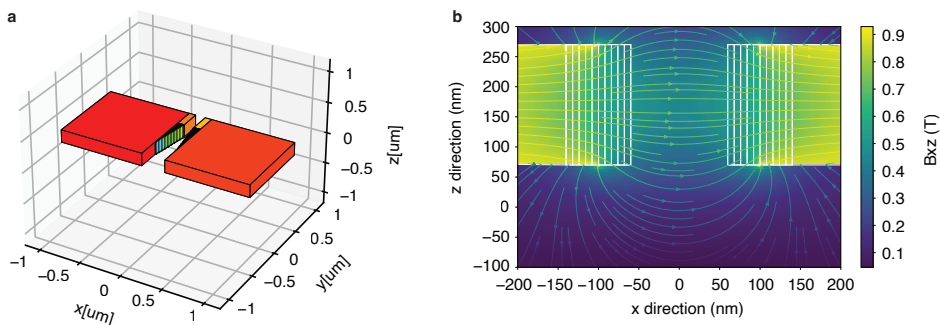


Figure 6.16: **a**, Schematic showing the structure of a micromagnet in 3D. To build the magnet, several cubes and triangular pieces of magnet were added to the simulation. **b**, Fields (B_{zx}) of the magnet created in **a**.

```

my_QP.Q1.X90.add(seg)
# loops still can be accessed, place an argument in the add function of
# the template.
my_QP.Q2.X90.add(seg, t_pulse = lp.linspace(30,80, 50))
my_QP.Q12.cphase.add(seg)
my_QP.Q1.X90.add(seg)

my_QP.read_Q1(seg)

```

6

A lot of control of the pulses is still available as all the template arguments (pulse lengths, amplitudes, ramp times, ...) can be overwritten when the pulses are added to the segment container. The combination of the short gate syntax and a great parameter flexibility allows for an efficient tuning of qubits.

6.4.5. MICROMAGNET SIMULATOR

Micromagnets are used to create the field gradients which we use for driving Rabi oscillations. The micromagnets can also be designed to make the qubits addressable. As these parameters need to be designed well, we designed a package²⁵ that makes this process easier.

The field of the micromagnets is simulated by breaking it down into a description of rectangular building blocks (Fig 6.16a). The fields originating from each magnet block are calculated using the magpylib [12] package. We then calculate the total field and its derivatives, typically the driving and decoherence gradient (Fig 6.16b).

It is also possible to provide an array of parameters (like in pulselib) for which to calculate the fields. This is useful to optimize/better understand how different parameters effect the micromagnet performance. A guide on how this works can be found [here](#)²⁶.

²⁵https://github.com/stephanphilips/MM_sim

²⁶<https://micromagnet-simulator.readthedocs.io/en/latest/>

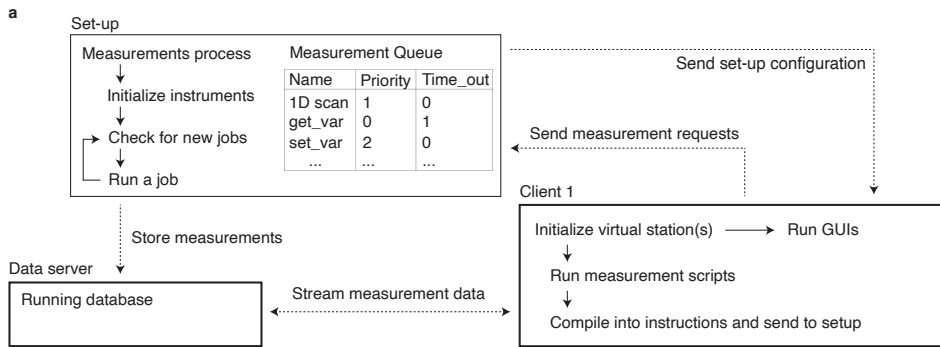


Figure 6.17: **a**, Software scheme for a multi-user measurement setup. Every square indicates the different functions of each computer/server (setup, data server, clients), the lines between boxes indicate the flow of data.

6.4.6. NEXT GENERATION SOFTWARE?

As qubit chips get larger, the amount of experiments that can be executed on a single chip increases significantly. One could imagine that if a device is sufficiently stable, it would be beneficial if multiple people could operate that device at the same time. Fig. 6.17 shows a blueprint of a software architecture that would support this.

One would need to imagine a setup where the measurement computer only performs measurements, but where the operator does no more analysis nor scripting of the experiments on this computer. The scripting of experiments would be done on an external device (the client device), which runs a virtual setup. The client programs locally his/her experiments which are then send to a queue on the measurement computer. While the experiments in the queue get executed, the data is saved in a remote database which allows the client to inspect the data in real time.

6.5. EXTRA : CHOOSING AN AWG

When choosing an AWG for spin qubits, the following things should be considered :

- The upload speed. When we perform experiments, we often sweep one or more variables that define a pulse. For example the duration of a microwave segment to measure a Rabi oscillation. In practice, this means that the AWG has to play a different waveform for every iteration of the variable(s). To avoid significant overhead from the upload of the waveforms to the AWG, the speed of the interaction with the computer and AWG is preferably faster or on a similar timescale as the execution time of the experiment²⁷.

Fully rendered waveforms for the duration of a single shot experiment form a large amount of data to be uploaded to the instrument. Some newer AWGs come with an instruction set to generate and manipulate short waveforms. The amount of data needs to be uploaded for the instructions and short waveforms is much smaller.

- The number of channels. As the number of qubits increases in experiments, many channels are needed that can be operated synchronously.
- Architecture of the AWG. There are two popular AWGs architectures: one is based on the idea that one sequencer²⁸ controls the whole experiment (many AWGs). In the other one, every AWG channel runs its own sequencer(s).

In the first architecture this translates to a master-slave architecture. The master (separate module) sends commands using keywords to the slaves (AWGs). Each keywords signals which waveform needs to be played by the slave. This type of architecture is for example used in the Zurich instruments AWGs.

In the second architecture, each AWG is its own master and runs its own sequencer. This is accomplished by synchronizing²⁹ the clocks of all the AWGs before the start of the sequence. It is possible to send data from one sequencer (e.g. digitizers) to another one, which allows for decision making (feedback) in the experiments. In our case, we went for the this approach as at the time of ordering our instruments, no systems with fast upload speeds using a master slave architecture were available.

For the current experimental needs, both architectures are equivalent. When thinking about scaling qubits systems, in a bruteforce way, the second architecture seems better as less communication (keywords) is needed between the modules. In general it would be best to strive towards scaling methods that do not require the usage of AWGs at all. This statement is based on the idea that every AWG has an information bandwidth of ~2GB/s, which is significantly higher than the actual information bandwidth needed to describe the qubit operations using digital signalling (S, Clifford and CNOT gates).

²⁷For the 6-qubit experiments, timescales for thousand single shot experiments are in a range of 20ms-200ms

²⁸A sequencer is an object that holds a list of instructions related to the operation of the AWG(s) and that can execute them. An instruction could be anything, e.g. turn on channel 1 of AWG1, start to play waveform x, perform a loop, perform a measurement,

²⁹Technically one could say that the AWG that triggers the start command is the master. Note that similar clock synchronization is needed with the master slave architecture. The typical precision of the this synchronization (channel skew) is in the order of 20 to 150ps.

- Capabilities of the AWG sequencer. Nearly all sequencers are able to play waveforms defined by a set of 16 bit integers which are stored in memory. This method works well for controlling a few qubits, but once more qubits get into play, some considerations need be made to make this process more efficient. Most waveforms can be decomposed into a set of ramps, waits, IQ signals and short, complex waveforms (e.g. two-qubit gates). All these signals can be represented in the AWG in a abstract form, e.g. a ramp can be represented by a start voltage, stepping voltage and duration. The decomposition of large pulses in small instructions also enables real-time feedback in experiments (crucial for IQ signals, see further), which could be used for quantum error correction³⁰ experiments or for the initialization of qubits (see chapter 5).

The gate model introduced in chapter 2 can run fully on the FPGA inside the AWG module. This means that one just needs to upload all the instructions defining a gate model. The user can then run any quantum circuit by just uploading a new sequence by listing which instructions (gates) should be executed at what times. This model of operation fits quite well with a more industrial operation and is supported by most modern AWG solutions.

- Voltage swing, noise temperature, sample rate and number of bits of DAC. Aside from the quality of the programming of the AWG, the analog properties of the AWG matter.

The signal output of the AWGs goes from 300K to 20mK, where the spin qubit chip is located. As one goes down in temperature, thermal noise reduces. The noise temperature of the signal can be reduced accordingly by placing attenuators at the different temperature stages in the dilution refrigerator³¹ (see Fig. 6.3). One would need ~42dB of attenuation to reduce the noise temperature from room temperature close to base temperature. We did not put as much attenuation for our experiments, as our samples are not very sensitive to high frequency radiation (e.g. transmons) and because with more attenuation, the AWGs cannot provide the required pulsing range. It is important to note in this discussion that the amplifiers of the AWGs have a noise temperature greater than room temperature ($> 10^5$ K), as such it is debatable how much the attenuation³² of the signal matters.

The discussion of the required voltage swings of an AWG is not straightforward due to the elements outlined above. In our experience, for an overlapping gate Si/SiGe device such as the one from chapter 5, one should be able to produce at

³⁰This can be done, but is not required[5] and does not necessarily improve the performance of the error correcting code.

³¹The noise spectral density of a resistor is given by, $S_f(T) = 2k_B T R$, where k_B is the Boltzmann constant, T the temperature and R the resistance (50Ohm). As such, the recommended attenuation at each plate in the dilution refrigerator is $10 * 10 \log \left(\frac{T_2}{T_1} \right)$ [dB], where T_2 is the temperature of the higher temperature plate. It is also possible to add bandpass/high frequency filters at the lower temperature (10mK) stage to further reduce noise, this is especially useful as the classical approximation of $S_f(T)$ is not frequency independent for relevant operating frequencies at low temperatures [6].

³²The attenuators also serve a second function in the dilution refrigerator, as they thermalize the center of the coaxial cable to the temperature of the cooling stage. For this reason it is recommended to spread the attenuators among the different temperature stages. Note that $> 3dB$ attenuation can also be quite useful to suppress standing waves in coaxial cables.

least 100mV(300mV) voltage swing for the plungers (barrier) gates. In our current experiments we are content with an AWG output swing of 3V, which permitted 28dB (20dB) of attenuation on the plunger (barrier) gates. The total swing can be smaller if the attenuation in the dilution refrigerators is reduced and high frequency filters are placed. The output swing should not be a strong criteria when selecting an AWG but rather the noise spectral density of the AWG in function of the output voltage.

The sample rate of the AWG is directly related to the bandwidth ³³ ($\sim \frac{\text{sample rate}}{3}$) of the signal. The available bandwidth needed for experiments generally depends on the strength of the interactions; e.g. for driving a qubit at $\Omega_r = 100\text{MHz}$, a sample rate of 1GS/s might be rather low, certainly if one needs to be careful with the (a)diabaticity of the pulse. In our case, the maximal qubit-qubit interaction strength was about 10MHz, translating in gate durations of 25ns to 100ns. A 1ns timing resolution was sufficient for us. In addition to pulses in the time domain, also RF pulses for the IQ modulation are needed (more information in next section). Using a 1GS/s AWG, 600MHz of RF-bandwidth (twice the normal bandwidth) is available, which will be the maximal frequency spread that can be targeted with a single vector source. The channel skew and clock instability is also important in spin qubit experiments and should be minimal.

³³Theoretically the bandwidth is given by the Nyquist frequency, which is half the sample rate. In reality the output signal is filtered to reduce the harmonics in the signal, reducing the effective bandwidth.

BIBLIOGRAPHY

- [1] A. Abragam. *The principles of nuclear magnetism*. 32. Oxford university press, 1961.
- [2] E. J. Connors, J. J. Nelson, and J. M. Nichol. “Rapid high-fidelity spin-state readout in Si/SiGe quantum dots via rf reflectometry”. *Physical Review Applied* 13.2 (2020), p. 024019.
- [3] A. W. Cross, L. S. Bishop, J. A. Smolin, and J. M. Gambetta. “Open quantum assembly language”. *arXiv preprint arXiv:1707.03429* (2017).
- [4] J. P. Dodson *et al.* “Fabrication process and failure analysis for robust quantum dots in silicon”. *Nanotechnology* 31.50 (2020), p. 505001.
- [5] A. G. Fowler, M. Mariantoni, J. M. Martinis, and A. N. Cleland. “Surface codes: Towards practical large-scale quantum computation”. *Physical Review A* 86.3 (2012), p. 032324.
- [6] S. Krinner, S. Storz, P. Kurpiers, P. Magnard, J. Heinsoo, R. Keller, J. Luetolf, C. Eichler, and A. Wallraff. “Engineering cryogenic setups for 100-qubit scale superconducting circuit systems”. *EPJ Quantum Technology* 6.1 (2019), p. 2.
- [7] W. I. L. Lawrie *et al.* “Quantum dot arrays in silicon and germanium”. *Applied Physics Letters* 116.8 (2020), p. 080501.
- [8] Y.-Y. Liu, S. G. J. Philips, L. A. Orona, N. Samkharadze, T. McJunkin, E. R. MacQuarrie, M. A. Eriksson, L. M. K. Vandersypen, and A. Yacoby. “Radio-frequency reflectometry in silicon-based quantum dots”. *Physical Review Applied* 16.1 (2021), p. 014057.
- [9] D. Manzano. “A short introduction to the Lindblad master equation”. *Aip Advances* 10.2 (2020), p. 025106.
- [10] C. Moler and C. Van Loan. “Nineteen dubious ways to compute the exponential of a matrix, twenty-five years later”. *SIAM review* 45.1 (2003), pp. 3–49.
- [11] A. Noiri, K. Takeda, J. Yoneda, T. Nakajima, T. Kodera, and S. Tarucha. “Radio-Frequency-Detected Fast Charge Sensing in Undoped Silicon Quantum Dots”. *Nano Letters* 20.2 (2020), pp. 947–952.
- [12] M. Ortner and L. G. C. Bandeira. “Magpylib: A free Python package for magnetic field computation”. *SoftwareX* 11 (2020), p. 100466.
- [13] L. Petit, H. Eenink, M. Russ, W. Lawrie, N. Hendrickx, S. Philips, J. Clarke, L. Vandersypen, and M. Veldhorst. “Universal quantum logic in hot silicon qubits”. *Nature* 580.7803 (2020), pp. 355–359.
- [14] L. Petit *et al.* “Spin lifetime and charge noise in hot silicon quantum dot qubits”. *Physical review letters* 121.7 (2018), p. 076801.

- [15] R. Schouten. *QuTech Electronic equipment*. URL: <https://qwork.tudelft.nl/~schouten/>.
- [16] J. Timmer and M. Koenig. “On generating power law noise.” *Astronomy and Astrophysics* 300 (1995), p. 707.
- [17] C. H. Yang *et al.* “Operation of a silicon quantum processor unit cell above one kelvin”. *Nature* 580.7803 (2020), pp. 350–354.

7

CONCLUSION AND OUTLOOK

7.1. CONCLUSIONS

When I started this thesis, the first single and two-qubit experiments were just performed on silicon quantum dot devices [57, 58, 24]. This thesis expands further on these works, by (1) increasing the number of qubits, (2) improving the operation fidelities and (3) designing a framework that makes the operation of qubits easier.

In the following, the different experiments performed in the chapters of this thesis are reviewed:

- In chapter 3, we operated the first two-qubit quantum processor in silicon. We created Bell states and ran algorithms like Grover's and the Deutsch–Jozsa algorithm. These demonstrations were encouraging because it meant we could run several quantum operations sequentially, without problem. On the other hand, several improvements were needed for larger or deeper algorithms :
 - **Material** : the sample was fabricated on natural Si/SiGe quantum well, which limited the coherence time to $T_2^* \approx 1\mu s$ [24, 70, 60]. The coherence time and the qubit operation fidelities can be increased by isotopically purifying the silicon quantum well [73, 23, 63].
 - In addition, the mobility (quality metric) of the substrate was rather limited ($\mu_e < 5 \cdot 10^4 \frac{\text{cm}^2}{\text{Vs}}$), which led to challenges in tuning the device as the electron positions were defined not only by the electrostatic gate potential, but also by the disorder in the substrate. This material challenge was largely tackled in future works by Giordano Scappucci's group [62, 61] and was one of the key enablers to make the quantum dot array shown in chapter 5.
 - **Device design** : a double layer gate pattern (stadium style) was used to define the quantum dots on this device. The lithographic location of the quantum dots were spaced too far from each other, which together with the substrate

non-uniformities made it hard to couple the two dots to each other. Denser gate patterns are required to increase the number of dots [69].

The micromagnet design was not ideal. The frequency difference between the qubits was very large ($>1\text{GHz}$) and the design could only be used for a few qubits [68]. We introduce a modified micromagnet design that supports a larger array of qubits in chapter 5.

- **Setup and device operation :** the software to control the experiments was rather tedious, as several scripts with more than 1000 lines were needed to run the experiments. This becomes a problem when performing larger experiments. The software libraries introduced in chapter 6 were built to resolve this issue.

The data acquisition was quite slow in this experiment¹. The readout signal of the sensing dot (DC) was amplified at room temperature, which limited both the signal-to-noise-ratio (SNR) and bandwidth that could be achieved. This, in combination with long waveform upload times, limited the rate at which we could run experiments. Using the methods, hardware and software developed in chapters 4 and 6, we improved the execution rate of experiments by 2 to 3 orders of magnitude.

- In chapter 4, we optimize the detection of the readout signal, addressing the slow readout encountered in chapter 3. Fast readout ($\sim 1\text{MHz}$ bandwidth) was first achieved in GaAs devices with the RF-readout method[42]. Silicon (accumulation mode) devices have much larger parasitic capacitances² compared to the GaAs (depletion mode) devices, which did not allow us to just copy the design. To perform fast readout, we used the large capacitance of the accumulation gate with the 2DEG to directly couple the RF signal into the 2DEG. Leakage to the ohmic contacts is prevented by making a resistive channel in the path to the contacts, before the implantation region.

7

We were able to detect the presence/absence of a single electron within one microsecond, with a fidelity greater than 99.9%. Similar results of other groups were published in [37, 11].

- Chapter 5 discusses the operation of a six-qubit quantum processor. To accomplish this goal, we implemented many of the improvements listed before. The most important ones were the design and optimization of the fabrication process, introducing RF-readout, a $^{28}\text{Si}/\text{SiGe}$ substrate [61] with a high uniformity ($> 10^5 \frac{\text{cm}^2}{\text{Vs}}$) and high valley splittings ($> 50\mu\text{eV}$) and a redesigned hardware/software stack.

The culmination of all these improvements was to operate the quantum dot array as a quantum processor. We showed that we were able to perform single- and two-qubit gates on all³ six electrons on the device. We performed qubit measurements using parity readout[46] and quantum nondemolition measurements[64, 35]. This control allowed us to prepare entangled GHZ states of three neighboring qubits, at

¹A single shot experiment took about 10ms, which means ~ 10 seconds were needed to acquire a single data point, averaging over 1000 single-shot measurements.

²More specifically the parasitic capacitance between the accumulation gate and its 2DEG below.

³Sequentially, without removing the electrons.

all possible locations on the device. In order to entangle more electrons, a new set of problems would need to be solved. The most prevalent problem was a heating effect we observed.

Aside from that, a more robust design/fabrication process for the micromagnet is needed to improve the addressability of the qubits. In addition, the coherence time of the qubits is shorter than expected[63, 49]. We suspect that this is caused by the gradients of the micromagnets.

- The technology presented in chapter 6, forms the basis for the experiments executed on the six-qubit quantum processor. A new type of AWG allowed us to perform our experiments more quickly, in combination with an extensive software framework that made the programming of experiments easier, enabling more complex experiments.

7.2. OUTLOOK

The ultimate goal of the quantum computing field is to build a machine that is fault tolerant. This fault tolerance can be achieved by implementing a quantum error correction (QEC) code[9]. This code largely defines the architecture of a quantum computer. The minimal requirements to run the much-studied surface code are[9, 51, 17, 31]:

- **Fidelity** : Gate operations need to be executed with a fidelity⁴ greater than 99.9%, assuming 1000-10000 qubits are used to define a single logical qubit with an error rate of 10^{-15} [41, 17].
- **Connectivity** : A qubit connectivity in two dimensions (or greater).
- **Measurement** : Running error correcting codes requires massive measurement capabilities. For example, a quantum computer with two million physical qubits (i.e. a 1000 logical qubits) and an error cycle time of $1\mu s$, needs to perform $\sim 10^{12}$ qubit measurements per second!
- **Speed** : Gate operations should be sufficiently fast, i.e. with a logical cycle time $< 10\mu s$, such that quantum algorithms can be completed within a reasonable amount of time [31]. The logical cycle time for the surface code is given by : $(4t_{gate} + 2t_{meas})d$, where t_{gate} and t_{meas} is the time needed to execute a gate and a measurement. d is the distance of the error correcting code, for example, if 1000 physical qubits represent a logical qubit, the distance would be $d = \sqrt{1000} = 31$.

7

What makes this list so challenging are the fast and high-fidelity gates that need to be achieved in combination with a high qubit count. In the coming sections each of these requirements are treated in more detail, for spin qubits specifically.

⁴Note that these numbers depend on the error correcting code that is considered. The numbers in this example are given for the surface code. The fidelity reported here is different from the code threshold ($\sim 99\%$), as the threshold only indicates when the code outperforms the physical qubit.

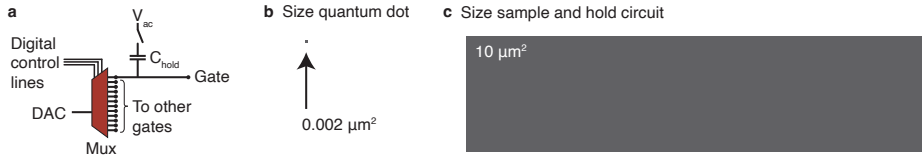


Figure 7.1: **a**, Schematic of a sample-and-hold circuit. The MUX is used to connect the DAC to one of the gate lines. While the DAC is connected to this gate, it charges the capacitor C_{hold} , which stores the voltage applied to the gate. While one capacitor is charging, the other gates are disconnected from ground, which maintains the charges on the capacitor (details in [6]). The MUX switches periodically through all the gates to adjust for small leakage currents. **b-c**, The difference in size between a single quantum dot and the area needed to store a voltage for a single gate (size estimate based on the design footprints in [6]).

7.2.1. FIDELITY

Recently, there have been several demonstrations of high-fidelity qubit operations (~99.5%) in silicon devices[63, 36, 34]. These fidelities are less than one order of magnitude away from the practical requirement for a QEC implementation. It is likely that we can breach the 99.9% boundary with further optimization of the devices, for example by reducing charge noise and increasing coherence times. In addition, we also need to obtain these fidelities consistently on the whole chip, preferably without a lengthy tuning process.

7

In the lab, a lot of time is spent on tuning the gate voltages of our devices, such that a good operating regime is reached for the qubits. The need for this extensive tuning originates from disorder that we need to compensate for. This disorder comes from various sources, for example, variation in the g-factors of the quantum dots, the (rough) potential landscape of the quantum dots $V(x, y, z)$, the valley splittings, and the stray fields created by the micromagnets (if applicable).

With current technologies, it is hard to imagine a spin qubit device where all the qubits are controlled with identical voltages. We need to make the assumption that a separate control line is needed for every qubit or gate operation. In practice this causes wiring issues [18] for larger chips. This problem can be mended using sample-and-hold circuits [55, 6], which store the local voltage of a gate in a capacitor as shown in Fig. 7.1. This significantly reduces the amount of IO needed. An area of $\sim 10 \mu\text{m}^2$ is needed to store the voltage for a single gate, assuming a precision of $1 \mu\text{V}$ is required[6]. As such, we need to target sparse qubit arrays and design our gate operations such that a minimum number of unique gate voltages are required.

In the following paragraphs I review the current state of the essential gate operations and propose improvements over the current experiments. At the end of each paragraph attention is given to the question, "can we make the tuning of qubit operations easier?", preferably by using as few control lines as possible.

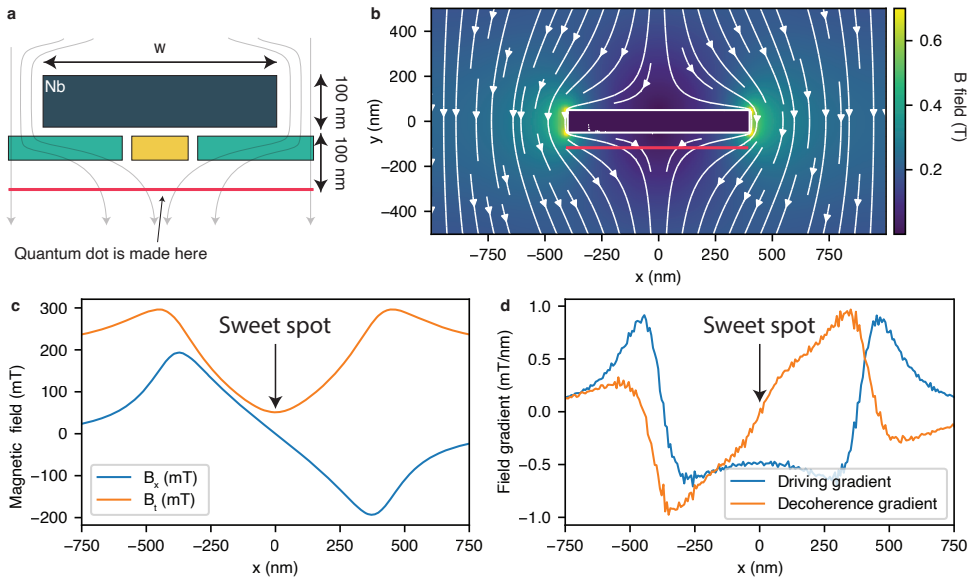


Figure 7.2: **a**, A superconductor (niobium) is placed on top of a quantum dot gate stack. The red line indicates the 2DEG (also in panel **b**). The magnetic field lines are sketched in gray. **b**, Simulation of the magnetic field around the superconducting slab. The superconductor is simulated as a diamagnetic material (see main text), which is placed in an external field of 180mT. The magnetic field lines are drawn in white. **c**, Magnetic field experienced in the plane of the qubits (red line in panel **a** and **b**). **d**, The driving gradient is used to drive the qubits ($\frac{dB_x}{dx}$). The decoherence gradient, ($\frac{dB_t}{dx}$), can limit the lifetime of the qubit [66].

7

SINGLE-QUBIT GATES

Single-qubit gates are performed by driving the spins with either an alternating electric (EDSR) or an alternating magnetic (ESR) field. When designing for either method, we want well defined qubit frequencies, an efficient driving mechanism that does not impair the coherence and a low cross-talk (see chapter 2). Using both methods, good fidelities can be achieved (> 99.9%) [66, 65], however demonstrations for more than three qubits are rather limited [27, 40] and can prove to be challenging, as discussed in the following.

With our current devices (based on EDSR), we had difficulties in creating reproducible field gradients for the qubits using micromagnets. The reason for this non-uniformity is not well understood. Perhaps the micromagnet shape and size was different than intended, or the magnetic domains at the edges might not be homogeneously magnetized. A more detailed investigation is needed to better understand the exact fields produced by the micromagnets.

One could either try to solve this problem by further optimizing the magnets or by a change in methodology. For the latter one, one could imagine using a superconductor (SC). When a SC is placed in a magnetic field, the Meissner effect causes the mag-

netic field lines to curve around the superconductor, creating local gradients as shown in Fig. 7.2. The width of the superconductor, together with the applied field (B_0), controls the resonance frequency of the qubit. The properties of the magnetic field gradient at the sweet spot are shown⁵ below:

Superconductor width (nm)	B field (mT)	Driving gradient (mT/nm)
200	118 (=3.3GHz)	0.65
400	79 (=2.2GHz)	0.65
600	60 (=1.7GHz)	0.55
800	51 (=1.4GHz)	0.5

The simulated field gradients are have similar magnitude as the gradients generated with micromagnets (factor ~ 2 lower). This would allow for driving the qubits with a Rabi frequency greater than 5MHz. This estimate is based on the Rabi frequencies achieved in experiments with micromagnets (see chapter 5). Note that these results are only valid if the superconducting slab is sufficiently long.

Just as for micromagnets, this method suffers from strong decoherence gradients when moving away from the sweet spot (see Fig. 7.2d). The decoherence gradients created by the superconductor have a similar magnitude to the ones created by the micromagnet(s).

The main reason to try this superconducting slab approach over the micromagnets one, would be to increase the field uniformity. This is expected because the edges of the superconductor are relatively far from the quantum dots and small non-uniformities at these edges should have little effect on the fields experienced by the qubits.

Alternatively, it might also be interesting to look towards introducing ESR antennas[14] on Si/SiGe heterostructures, as they don't introduce any decoherence gradients. However, the g-tensor and its relation to the applied electric field is currently unknown and well worth investigating!

Furthermore, I would propose to use an ESR antenna with a U shape as shown in Fig. 7.3, as it eliminates the need to rely on g-factor differences for qubit addressability. When a DC current is pulsed through the antenna, a linear magnetic field gradient between the qubits is created (Fig. 7.3b). Assuming a current density⁶ of $5 \cdot 10^{10} \frac{\text{A}}{\text{m}^2}$ ($I_{\text{antenna}} = 2\text{mA}$), a frequency difference⁷ of $\Delta f = \sim 20\text{MHz}$ can be expected between adjacent qubits. This

⁵The simulations were carried out with FEniCS[1] (FEM solver), where I solved for $\nabla \mu A_z = 0$. The superconductor was considered as a diamagnetic material ($\mu \approx 0$). More accurate simulations can be obtained by solving the London equations. The applied external field was 0.18T, which is the field where Nb transitions from a type I into a type II superconductor [44]. For niobium, the London penetration depth is $\lambda_L \approx 40\text{nm}$ [32].

⁶When using copper, current densities up to $5 \cdot 10^{10} \frac{\text{A}}{\text{m}^2}$ can be applied at room temperature before failure modes via electromigration appear. Using superconductors, we measured current densities up to $7 \cdot 10^{10} \frac{\text{A}}{\text{m}^2}$ for NbTiN.

⁷Estimated by performing a FEM simulation, with the sizes given in 7.3.

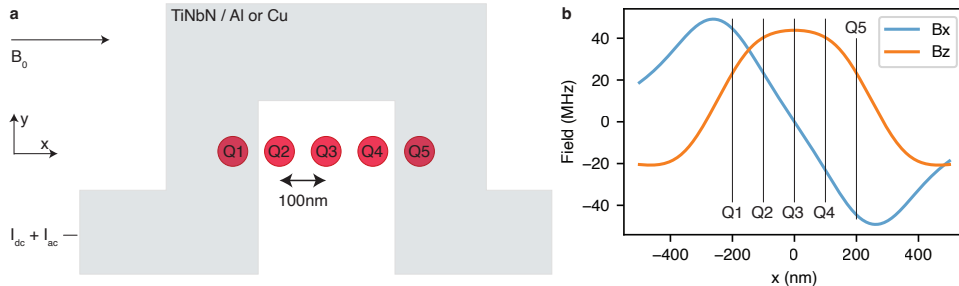


Figure 7.3: **a**, Topview of the transmission line antenna. The dots below the antenna represent the different qubits, with a pitch of 100nm. The thickness of the antenna is 200nm. **b**, Field produced when a DC current is send through the antenna. The qubits are located 100 nm below the antenna.

antenna design allows for the implementation of Z gates in software and hardware, performing \sqrt{SWAP} gates and testing PSB readout in the absence of a magnetic field gradient[46]. The mode of operation proposed here is similar to the one proposed for the cross bar architecture [28].

One of the biggest problems with current approaches is that they are not designed to scale, but rather to illustrate the principle of driving a qubit. For example, it is hard to drive many qubits with a single transmission line (magnetic drive) or to use (artificial) spin orbit coupling to drive many of them electrically. The latter requires extensive tuning to reach a sweet spot, the right Rabi and resonance frequency for each qubit. In an ideal world, the g-factor is not tunable, such that the resonance frequency is only determined by the local magnetic field (e.g. as in [28]) and insensitive to defects in the material stack. In this way, a control methodology can be designed where the number of unique control signals is a constant ($\mathcal{O}(1)$), irrespective of the number of qubits.

Efforts have been made towards this direction, for example by using a global alternating magnetic field [53, 54]. This method is challenging as the magnetic mode needs to deliver a homogeneous field across the whole die (several mm), at sufficiently high powers. More research is needed to establish if this is a valid methodology.

Alternatively, one could try to tackle this problem by removing the need to drive qubits with an alternating field. This can be done by setting the resonance frequency of all qubits to 0Hz (the qubits are operated at 0T). In this case, the spin is rotated by applying a local magnetic field [29]. The direction of the applied magnetic field defines the rotation axis of the qubit. An example of structures that accomplish this is shown in Fig. 7.4.

This method offers several advantages; (1) the possibility to avoid tuning single-qubit gates for every qubit on the device, (2) no single-qubit phase corrections are needed when shuttling or performing two-qubit gates (see next section), (3) no microwave signals are needed, simplifying the design of the quantum chip, (4) two-qubit gates (\sqrt{SWAP}) and PSB readout can still be performed using the usual methodologies.

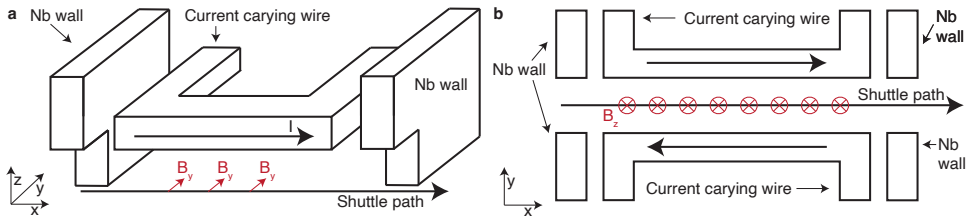


Figure 7.4: Structures for performing single-qubit gates (for example in the spider web array [6] architecture), when the external magnetic field is set to 0T. The electron is shuttled from the left to the right as indicated in each panel. The shuttling averages the local magnetic field (motional narrowing) and thus increases the precision of the rotation. The niobium walls shield the magnetic fields of the current carrying wires such that the cross-talk in the other operating zones (idling, two-qubit gates and readout) is low. **a**, Structure that performs qubit rotations around the y-axis. Any rotation axis in the xy-plane can be obtained by using a rotated structure. **b**, Structure used to generate a magnetic field that rotates the spin around the z-axis.

There are however also some disadvantages; (1) the qubit does not have a well defined quantization axis, thus the qubit dephases in all directions; (2) one needs to be able to apply a local magnetic field that is uniform enough to reach the desired fidelity, (3) the g-factor variation⁸ must be small in order to meet condition (2).

It should not go unstated that the heating effects discussed in chapter 6 are another important challenge to overcome in future. Unpublished work from Undseth et al. suggest that these effects are mainly due to physical heating of the qubits and illustrate that this problem disappears when the qubits are operated at higher temperatures ($> 200\text{mK}$). The mechanism that causes these effects still needs to be elucidated.

7

TWO-QUBIT GATES

Current demonstrations of high fidelity two-qubit gates[63, 36, 34] are shown on devices with a magnetic field gradient in between the qubits. In this case, the CPhase gate is the native two-qubit gate. Alternatively, when no gradient is present, the native gate is a $\sqrt{\text{SWAP}}$ gate [39]. Because of its simplicity, I think the $\sqrt{\text{SWAP}}$ is a worthwhile gate to further explore, as such I will motivate this statement and discuss its practical implementation.

The achievable fidelity of a two-qubit gate ultimately depends on the degree of charge noise and the coherence times of the qubits, considering that the gate is performed with a perfectly well tuned pulse[43]. This can be improved by reducing two-level fluctuators in the material. The ease of tuning the gate goes hand in hand with the boringness of the Hamiltonian. For the $\sqrt{\text{SWAP}}$ gate, the evolution of the gate is described⁹ by the exchange interaction J , as such, we only need to control the magnitude or length of the interaction, irrespective of the pulse shape. A ZZ interaction (CPhase gate) can be recovered by decoupling the XX and YY components of the exchange interaction, for example

⁸It could be interesting to explore different materials for this, for example electrons confined on top of a dielectric like He or Ne [30, 72, 10] which are expected to have a longer coherence time and a much weaker spin orbit coupling than silicon.

⁹Assuming the resonance frequencies of both qubits are identical.

by applying a Z gate (not virtual!) in between two \sqrt{SWAP} instances. To practically implement the \sqrt{SWAP} gate, the design introduced in Fig.7.3 could be used.

When comparing this gate to the CPhase gate, the Hamiltonian is given by: $\hat{H} = \frac{\mu_b g_1}{\hbar} B_1(J) \hat{S}_{z,1} + \frac{\mu_b g_2}{\hbar} B_2(J) \hat{S}_{z,1} + J \hat{S}_1 \otimes \hat{S}_2$, where in addition to the exchange, two additional variables are needed, the single-qubit phases generated on each qubit, which are unique per gate, require calibration and need to be compensated¹⁰. An adiabatic pulse shape must be used to avoid coherent errors during the execution of the gate [43].

The best scaling one can hope for, is one unique gate voltage per two-qubit gate instance. This voltage is used to set the tunnel coupling to a precise value, under the assumption that the frequencies of the two qubits remain identical to each other and are not affected by the gate voltage pulse and that the device uniformity is good enough to operate around the symmetry point without tuning additional gate voltages.

INITIALIZATION AND READOUT OF QUBITS

Efficient initialization and readout are crucial in any error correcting scheme. Currently, there exist two methods that can be used to initialize and readout spin qubits : Elzerman readout and Pauli spin blockade (PSB). On large scale systems, PSB readout seems to be more favorable as it involves simpler signal processing, is faster, has a larger operating window (energy scale : $\epsilon_{orbital}$ versus ϵ_{Zeeman}) and does not need a reservoir.

More research is needed to obtain a better understanding of PSB readout itself. Fairly detailed studies have been performed on errors occurring during the charge readout process [22], but errors during the spin to charge conversion are less well studied [46]. For example, in our experiments we noticed a relaxation path from the $|\uparrow, \uparrow\rangle$ to the $|S, 0\rangle$ state which we could not explain¹¹. A deeper understanding of these types of error would allow for a further increase of the readout fidelities!

7

7.2.2. CONNECTIVITY

Linking one or two-dimensional qubit arrays to each other is a daunting task. This link should have a lengthscale¹² of $5\text{-}100\mu\text{m}$, a high fidelity ($> 99.9(9)\%$), and a high transfer speed ($\ll 100\text{ns}$).

Coherently shuttling spins seems to be one of the most promising approaches to accomplish this[33, 67, 74, 47]. It remains challenging to shuttle adiabatically with respect to the valley energy [26]. Current valley splittings ($\sim 100\mu\text{eV}$) allow for transfer rates of $\sim 10\frac{\mu\text{m}}{\mu\text{s}}$ (theoretical estimate for 99.9% transfer fidelity). In practice, we would like to achieve faster transport times ($> 100\frac{\mu\text{m}}{\mu\text{s}}$) such that they don't dominate the error correction cycle time. More research has to be performed on longer arrays to estimate what

¹⁰It is also possible to remove the single-qubit phases by dynamically decoupling the CPhase gate.

¹¹One could explain this by the presence of the artificial spin orbit coupling created by the micromagnet, but in that case relaxation from the $|\downarrow, \downarrow\rangle$ to the $|S, 0\rangle$ state would be expected as well.

¹²These length scales are determined by the CMOS components on the chip (for multiplexing of static gate voltages, switching of signals (pulsing/readout) and the readout amplifiers).

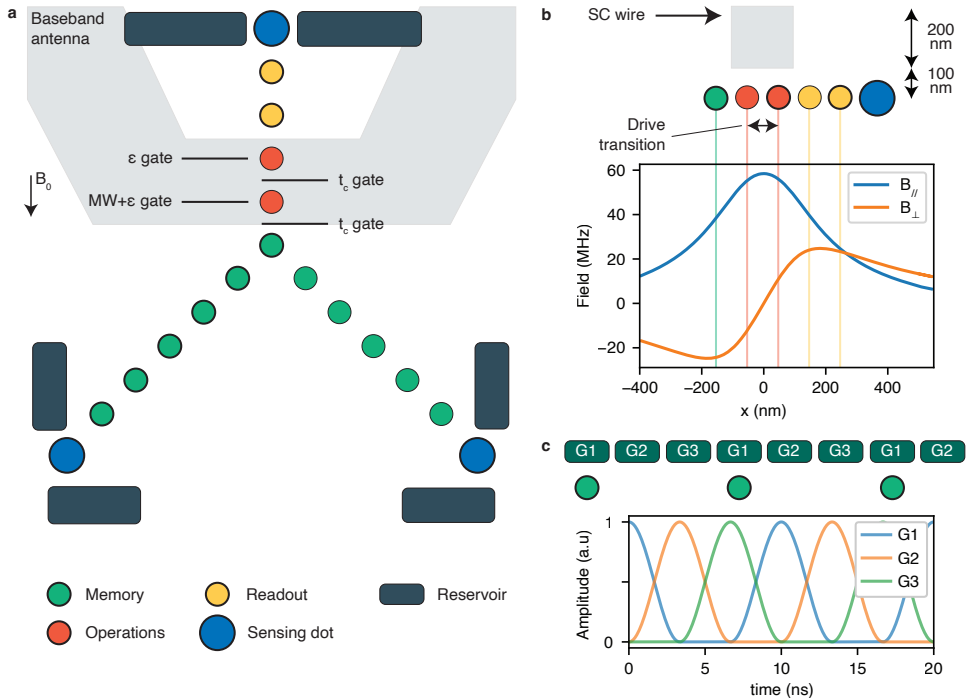


Figure 7.5: **a**, Device concept for the error correction experiment proposed in the main text. The device hosts up to 6 data qubits and a single ancilla qubit (S/T qubit). The gray overlay shows the footprint of the baseband antenna (deposited NbTiN on top of the device). This antenna generates the magnetic fields required for driving the qubits and Z gates. **b**, Frequency distribution at the quantum dots locations when a current ($J = 5e10 \frac{A}{m^2}$) is pulsed through the superconducting antenna. The external field B_0 is subtracted from this field. The qubits are driven using flopping mode EDSR, at the location labeled "drive transition". **c** Modified design for the data qubit array[26, 47]. The gates are driven using a sine-like wave, where the signal on G1,G2,G3 have phase offsets of $\frac{2\pi}{3}$, as shown in the graph below. It is recommended to have a separate bias-tee for each gate, such that disorder can be tuned away.

7

shuttling rates may be realized experimentally.

The integration of shuttling operations with other qubit operations is something important to investigate. Therefore I propose an (ambitious) experiment that demonstrates this integration by running an error correction experiment, similar to the architecture in [6]. A sketch of the quantum dot layout is shown in Fig. 7.5a. Three linear qubit arrays are used, where the three ends are connected to each other. Two of these arrays are used as a quantum memory, which can be occupied by six electrons (half filled). The gate layout of the quantum memory is slightly different from the layout used in the six-qubit project, as an extra gate needs to be added to enable conveyor mode shuttling. For the shuttling itself I would propose to use the pulse shape shown in Fig. 7.5c. This shape increases the electric field experienced by the electrons in the quantum dots on average, resulting in a potentially increased valley and orbital splitting.

The operation and readout zone both contain two dots, with a gate design comparable to the six-qubit device used in chapter 5. The two dots in the readout zone are used for Pauli spin blockade readout. The gradient line (baseband antenna), allows one to choose the eigenbasis of the ancilla qubit ($|S\rangle / |T\rangle$ or $|\downarrow\uparrow\rangle / |\uparrow\downarrow\rangle$).

The gate labeled "MW gate", in the operation zone, is used to drive single-qubit gates electrically using the "flopping mode" mechanism (Fig. 7.5a) [45, 2]. Taking into account the field applied by the superconducting wire and assuming that the wavefunction fully delocalizes while driving, Rabi frequencies greater than 10 MHz may be achievable (Fig. 7.5b).

The gradient line can also be used to apply Z gates in hardware, which in combination with two \sqrt{SWAP} gates can be used to create a CPhase gate. The \sqrt{SWAP} gate can be applied¹³ by pulsing one of the t_c gates.

The table below shows the expected gate times :

Gate type	time (ns)
X90	25
Z180	25
\sqrt{SWAP}	5-10
Shuttling by one position	10
Readout	1000

Considering these numbers, a parity measurement of four data qubits can be performed in $\sim 1.5\mu s$, which is well below the T_2^{Hahn} of the qubits. This time is dominated by the readout time of the ancilla qubit.

7

Alternatively, research has also focused on making a link via coherent spin-photon coupling [4, 20]. We will not consider this method here, as the resonators are hard to integrate in large scale system due to the extensive cross talk [21], the large length scales (0.1-1mm), and the need for frequency tunability of the qubits with respect to the resonator frequency. Other methods also exist, but are less actively researched, a good overview can be found in [8].

7.2.3. MEASUREMENT AND SPEED

In my opinion, the measurement problem is the most challenging of all challenges that need to be tackled on the path to fault tolerance. As previously introduced, there is a need for measuring many, many qubits in parallel and fast. Ideally, one places a state detector next to each ancilla qubit that converts the measured state ($|\downarrow\rangle / |\uparrow\rangle$) into a classical bit. Preferably, this whole process can be performed within hundreds of nanoseconds[31], which requires a SNR greater than two at a measurement bandwidth of 10MHz. The state detector with the required on-chip electronics, should occupy a small amount

¹³In order to achieve great on/off ratio's for J, it is recommended to first deposit the barrier layer and then the plunger layer on the device.

of space ($<10 \times 10 \mu\text{m}^2$), to limit the sparsity of the qubits.

The charge state of a quantum dot can be measured using an electrometer or using gate-based dispersive readout. The impedance of an electrometer¹⁴ can be tuned such that it depends on the presence/absence of nearby charges. One can measure the impedance by measuring the current through the electrometer at a fixed applied voltage bias. When using room temperature equipment, the measurement bandwidth is typically limited to 100kHz, due to the line capacitance and the input impedance of the amplifier.

This bandwidth can be increased by lowering the noise temperature of the amplifier, reducing the input impedance [3], or by placing the amplifier closer to the quantum chip [59, 52], which reduces the line capacitance. More research is needed to quantify the performance of baseband CMOS state detection circuits, residing next to the qubits.

Alternatively the impedance can be measured using RF readout (see chapter 4). Measurement bandwidths up to $\sim 2\text{MHz}$ have been achieved using this method, while maintaining a good SNR¹⁵. Current impedance measurements are typically limited by the bandwidth of the resonator, which can be increased by placing the resonator on chip, reducing the inductance and (parasitic) capacitance of the matching circuit [25].

When sensing is performed dispersively[48, 13], a resonator is connected to the plunger gate of a double dot[71] or to the plunger gate of single-electron box[5]. Both methods measure a change in quantum capacitance, created by the movement of a single electron. The SNR depends on the quality factor of the resonator, the curvature of the dispersion and the lever arm of the resonator to the dot. State of the art results show that it is possible to achieve charge readout in $1\mu\text{s}$ with a SNR exceeding 100 [5]. While this result is great, more investigation is needed to answer if the usage of resonators is practically feasible, as their size is large ($100 \times 100 \mu\text{m}^2$) and complex amplification chains are needed to digitize the signals. As the measurement time needs to be kept short, it is unlikely that time-multiplexing changes the numbers significantly.

7

7.3. LOOKING AHEAD, FROM A PERSONAL PERSPECTIVE

The current landscape of quantum computing is plagued by (1) disorder, leading to complex designs and (2) a non-trivial implementation of quantum error correction (said as a non-expert). I often wonder "what is the correct path forward?" and "how many non-idealities in a qubit system should we be willing to accept?".

The optimist might say : "with enough engineering and effort, you can probably make it work".

The realist, idealist or pessimist (depending on your perspective) might argue that more emphasis is needed on exploring new, better¹⁶ qubit types rather than focusing all our

¹⁴For example a sensing dot or quantum point contact.

¹⁵Assuming the sensing dot is operated in the strong response regime [38].

¹⁶A better qubit is defined here as a qubit that is easy to operate (i.e. with voltage pulses that don't need to be precise (as for Majorana's)), with qubit properties that are fully defined during the fabrication process, a qubit that is physically movable and whose fidelities are sufficiently high such that no more than a few dozen

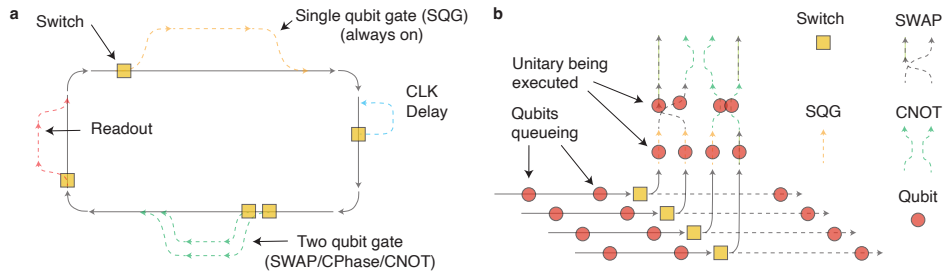


Figure 7.6: **a**, Hypothetical quantum dot device, where qubits are continuously shuttled along the path indicated by the gray line. Gate operations are performed by toggling the switches, which alter the path of the qubits into the single-qubit gate, two-qubit gate, CLK delay or readout zone. The CLK delay can be used to change the position of electrons relative to each other in the array. The switch element is treated in Fig. 7.7d. **b**, Extension of the concept shown in panel **a**. In this case, multiple qubits can undergo simultaneous operations. Such a structure could for example be used to perform parity measurements on the qubits.

effort on slowly improving the existing ones. This is however a risky path to walk, as research in this direction does not guarantee success nor security (which is desired by many researchers).

Which approach will work best in the end is unclear, but I'm sure large scale quantum computing will become a reality one day as there are only practical obstacles hindering its development.

Lastly, I would like to share two more ideas:

1. The architectural proposals for spin qubits submitted¹⁷ so far [50, 56, 28, 7, 12, 19, 55, 6] have in common that all qubits are stationary(-ish) and have their own control signals, which allows one to locally perform the single- and two-qubit gates. This choice has the advantage that one can parallelize many gate operations, which increases the number-of-operations-to-coherence-time ratio. Though, for most algorithms, large parts need to be executed in a serial fashion (e.g. QFT). As such, one could divide the qubits into two groups, an active qubit group and an idling one. The idling qubits are operated as a quantum memory (i.e. all qubits undergo the same operations). The active qubits undergo unitary gate operations and additional error correction.

Keeping these ideas in mind, one could design an architecture that makes this distinction. A simplistic (non-error corrected) example is shown in Fig. 7.6a. A circular quantum dot array is used to hold spin qubits, which are continuously shuttled around. This array could be seen as the quantum memory.

An idling qubit can be converted into an active qubit, by toggling one of the switches, which causes a change in the path of the targeted qubit, performing a unitary operation.

To better quantify the speed of this system, let's suppose the circular qubit array

of qubits are needed make a logical qubit.

¹⁷By the best my knowledge, with exception of [16] (quantum computation with levitons).

(e.g. with 50 qubits) is operated at a shuttling frequency of 100MHz, resulting in a gate-execution-rate of \sim 2MHz. This rate is similar to the one found in a linear or 2D qubit-array, without sacrificing qubit-to-qubit connectivity and while strongly reducing the number of variables to tune.

For larger qubit systems, one could imagine routing/controlling several qubits in tandem (e.g. belonging to one logical qubit), as shown in Fig. 7.6b.

2. From an engineering perspective, the challenge of the extensive, parallel readout needed for QEC can be addressed by devising a scheme where the error decoding and correction is performed on chip and where the digitization step is removed from the readout procedure. This can be done by performing the needed classical logic with single electrons. This does require however that the decoding of the error correcting code is sufficiently simple. An example of how one could design such a scheme for the repetition code is shown in Fig. 7.8 (see Fig. 7.7 for the practical implementation of the logic gates). Note that this scheme is quite extensive and by far not an ideal solution, but it might be useful as an inspiration for better ideas.

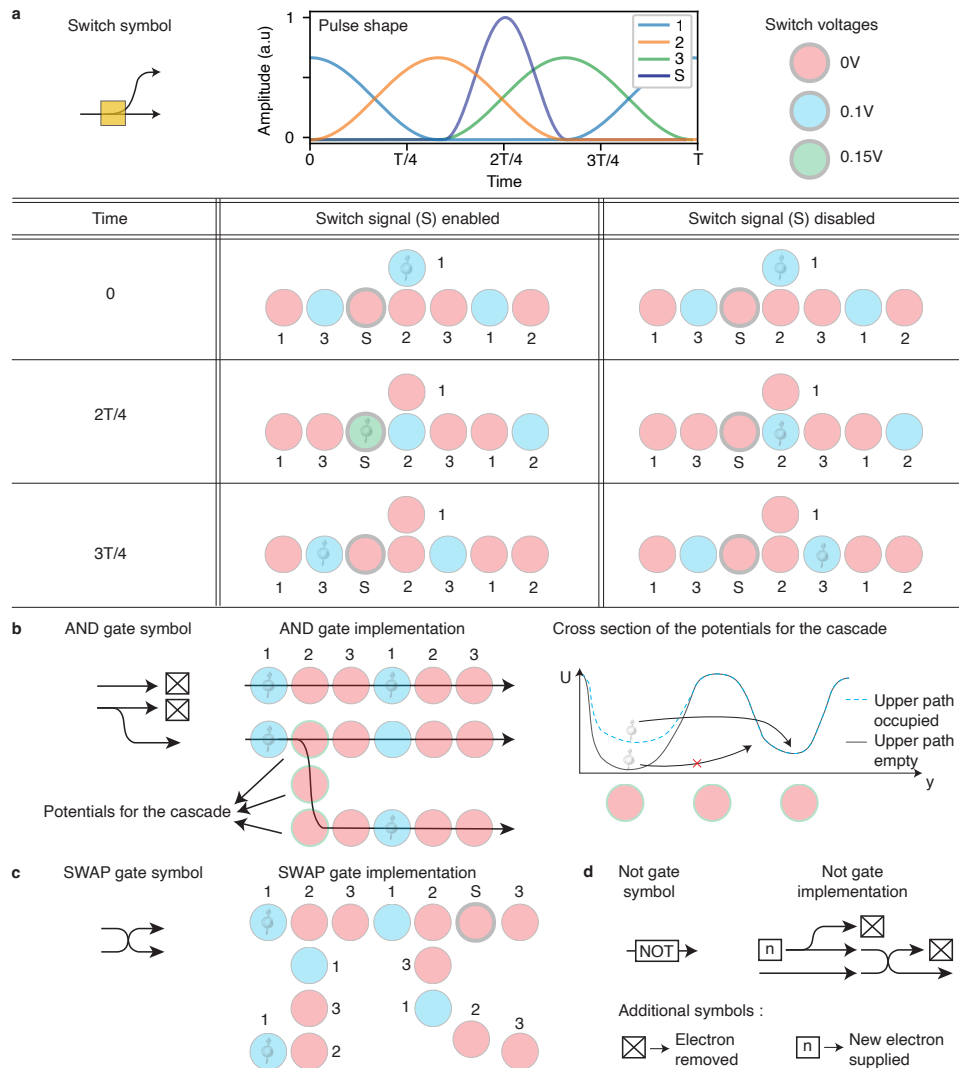
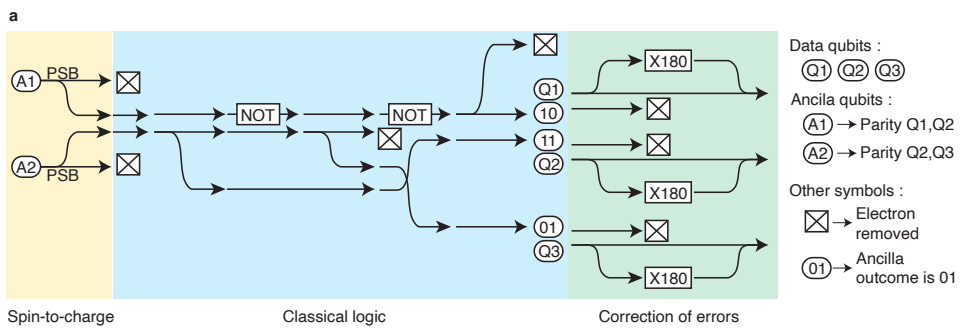


Figure 7.7: **a**, Schematic illustrating the operating principle of the switching element. Each dot represents a physical gate whereon one of four signals (1, 2, 3 or S) is applied. The signals are shown in the top graph. It takes a single clock cycle (i.e. one period, T) for an electron to pass through the switch. Approximate voltages, applied at different operating stages, are shown in the right-top of the figure. **b**, Operating principle of an AND gate for single electrons. The AND gate relies on the cascade effect (see [15]), which occurs at $t = \frac{T}{3}$. The graph on the right describes this effect more in detail. The electrostatic potential over the three vertical quantum dots (QD) is shown for two cases, (1) an electron is present in the upper path, which affects the potential of the surrounding QDs, causing the electron to tunnel in the lower path (quantum dot), (2) no electron is present in the upper path, the second electron remains in the same QD and continues to travel horizontally. **c**, SWAP element which interchanges the path of two electrons. The switching signal (S) is used to route the electrons along the correct path, taking advantage of the different arrival times. **d**, Implementation of the NOT gate using circuit elements previously shown.



7

Figure 7.8: **a**, Feedback implementation of the repetition code, with single electrons. The input states of the circuit are prepared by performing a spin-to-charge conversion with PSB readout. The readout outcome is used as input state ($\{00, 01, 10, 11\}$) for the area labelled "Classical logic". The "Classical logic" section converts these states into the following output states : $\{000, 100, 001, 010\}$. The 0/1 indicates the absence/presence of an electron. The location of these bits is indicated by : $\{\textcircled{10}, \textcircled{11}, \textcircled{01}\}$. The error correction is performed by applying AND gates between the bits of the output states and the corresponding data qubits. When an electron is present in the output states, it causes a single-qubit gate to be applied to the data qubit, correcting the logical qubit ($\{Q1, Q2, Q3\}$).

BIBLIOGRAPHY

- [1] M. S. Alnaes *et al.* “The FEniCS Project Version 1.5”. *Archive of Numerical Software* 3 (2015).
- [2] M. Benito, X. Croot, C. Adelsberger, S. Putz, X. Mi, J. R. Petta, and G. Burkard. “Electric-field control and noise protection of the flopping-mode spin qubit”. *Physical Review B* 100.12 (2019), p. 125430.
- [3] H. Bohuslavskyi, M. Hashisaka, T. Shimizu, T. Akiho, K. Muraki, and N. Kumada. “Fast time-domain current measurement for quantum dot charge sensing using a homemade cryogenic transimpedance amplifier”. *Applied Physics Letters* 121.18 (2022), p. 184003.
- [4] F. Borjans, X. Croot, X. Mi, M. Gullans, and J. Petta. “Resonant microwave-mediated interactions between distant electron spins”. *Nature* 577.7789 (2020), pp. 195–198.
- [5] F. Borjans, X. Mi, and J. Petta. “Spin digitizer for high-fidelity readout of a cavity-coupled silicon triple quantum dot”. *Physical Review Applied* 15.4 (2021), p. 044052.
- [6] J. Boter *et al.* “Spiderweb array: A sparse spin-qubit array”. *Physical Review Applied* 18.2 (2022), p. 024053.
- [7] B. Buonacorsi *et al.* “Network architecture for a topological quantum computer in silicon”. *Quantum Science and Technology* 4.2 (2019), p. 025003.
- [8] G. Burkard, T. D. Ladd, J. M. Nichol, A. Pan, and J. R. Petta. “Semiconductor Spin Qubits”. *arXiv preprint arXiv:2112.08863* (2021).
- [9] E. T. Campbell, B. M. Terhal, and C. Vuillot. “Roads towards fault-tolerant universal quantum computation”. *Nature* 549.7671 (2017), pp. 172–179.
- [10] Q. Chen, I. Martin, L. Jiang, and D. Jin. “Electron spin coherence on a solid neon surface”. *Quantum Science and Technology* 7.4 (2022), p. 045016.
- [11] E. J. Connors, J. J. Nelson, and J. M. Nichol. “Rapid high-fidelity spin-state readout in Si/SiGe quantum dots via rf reflectometry”. *Physical Review Applied* 13.2 (2020), p. 024019.
- [12] O. Crawford, J. R. Cruise, N. Mertig, and M. F. Gonzalez-Zalba. “Compilation and scaling strategies for a silicon quantum processor with sparse two-dimensional connectivity”. *arXiv:2201.02877* (2022).
- [13] A. Crippa *et al.* “Gate-reflectometry dispersive readout and coherent control of a spin qubit in silicon”. *Nature communications* 10.1 (2019), pp. 1–6.
- [14] J. P. Dehollain, J. Pla, E. Siew, K. Tan, A. Dzurak, and A. Morello. “Nanoscale broadband transmission lines for spin qubit control”. *Nanotechnology* 24.1 (2012), p. 015202.

- [15] C. J. van Diepen, T.-K. Hsiao, U. Mukhopadhyay, C. Reichl, W. Wegscheider, and L. M. Vandersypen. “Electron cascade for distant spin readout”. *Nature Communications* 12.1 (2021), p. 77.
- [16] H. Edlbauer *et al.* “Semiconductor-based electron flying qubits: review on recent progress accelerated by numerical modelling”. *EPJ Quantum Technology* 9.1 (2022), p. 21.
- [17] A. G. Fowler, M. Mariantoni, J. M. Martinis, and A. N. Cleland. “Surface codes: Towards practical large-scale quantum computation”. *Physical Review A* 86.3 (2012), p. 032324.
- [18] D. Franke, J. S. Clarke, L. M. Vandersypen, and M. Veldhorst. “Rent’s rule and extensibility in quantum computing”. *Microprocessors and Microsystems* 67 (2019), pp. 1–7.
- [19] M. F. Gonzalez-Zalba, S. de Franceschi, E. Charbon, T. Meunier, M. Vinet, and A. Dzurak. “Scaling silicon-based quantum computing using CMOS technology”. *Nature Electronics* 4.12 (2021), pp. 872–884.
- [20] P. Harvey-Collard, J. Dijkema, G. Zheng, A. Sammak, G. Scappucci, and L. M. Vandersypen. “Coherent spin-spin coupling mediated by virtual microwave photons”. *Physical Review X* 12.2 (2022), p. 021026.
- [21] P. Harvey-Collard, G. Zheng, J. Dijkema, N. Samkharadze, A. Sammak, G. Scappucci, and L. M. Vandersypen. “On-chip microwave filters for high-impedance resonators with gate-defined quantum dots”. *Physical Review Applied* 14.3 (2020), p. 034025.
- [22] P. Harvey-Collard *et al.* “High-fidelity single-shot readout for a spin qubit via an enhanced latching mechanism”. *Physical Review X* 8.2 (2018), p. 021046.
- [23] W. Huang *et al.* “Fidelity benchmarks for two-qubit gates in silicon”. *Nature* 569.7757 (2019), pp. 532–536.
- [24] E. Kawakami *et al.* “Electrical control of a long-lived spin qubit in a Si/SiGe quantum dot”. *Nature nanotechnology* 9.9 (2014), pp. 666–670.
- [25] D. Keith, M. House, M. Donnelly, T. Watson, B. Weber, and M. Simmons. “Single-shot spin readout in semiconductors near the shot-noise sensitivity limit”. *Physical Review X* 9.4 (2019), p. 041003.
- [26] V. Langrock, J. A. Krzywda, N. Focke, I. Seidler, L. R. Schreiber, and Ł. Cywiński. “Blueprint of a scalable spin qubit shuttle device for coherent mid-range qubit transfer in disordered Si/SiGe/SiO₂”. *arXiv preprint arXiv:2202.11793* (2022).
- [27] W. I. L. Lawrie, M. Russ, F. van Riggelen, N. Hendrickx, S. de Snoo, A. Sammak, G. Scappucci, and M. Veldhorst. “Simultaneous driving of semiconductor spin qubits at the fault-tolerant threshold”. *arXiv:2109.07837* (2021).
- [28] R. Li *et al.* “A crossbar network for silicon quantum dot qubits”. *Science advances* 4.7 (2018), eaar3960.
- [29] D. Loss and D. P. DiVincenzo. “Quantum computation with quantum dots”. *Physical Review A* 57.1 (1998), p. 120.

- [30] S. Lyon. "Spin-based quantum computing using electrons on liquid helium". *Physical Review A* 74.5 (2006), p. 052338.
- [31] B. M.E. *et al.* "Assessing requirements to scale to practical quantum advantage". *arXiv preprint arXiv:2211.07629* (2022).
- [32] B. Maxfield and W. McLean. "Superconducting penetration depth of niobium". *Physical Review* 139.5A (1965), A1515.
- [33] A. R. Mills, D. Zajac, M. Gullans, F. Schupp, T. Hazard, and J. Petta. "Shuttling a single charge across a one-dimensional array of silicon quantum dots". *Nature communications* 10.1 (2019), pp. 1–6.
- [34] A. Mills, C. Guinn, M. Gullans, A. Sigillito, M. M. Feldman, E. Nielsen, and J. R. Petta. "Two-qubit silicon quantum processor with operation fidelity exceeding 99%". *Science Advances* 8.14 (2022), eabn5130.
- [35] T. Nakajima *et al.* "Quantum non-demolition measurement of an electron spin qubit". *Nature nanotechnology* 14.6 (2019), pp. 555–560.
- [36] A. Noiri, K. Takeda, T. Nakajima, T. Kobayashi, A. Sammak, G. Scappucci, and S. Tarucha. "Fast universal quantum gate above the fault-tolerance threshold in silicon". *Nature* 601.7893 (2022), pp. 338–342.
- [37] A. Noiri, K. Takeda, J. Yoneda, T. Nakajima, T. Kodera, and S. Tarucha. "Radio-Frequency-Detected Fast Charge Sensing in Undoped Silicon Quantum Dots". *Nano Letters* 20.2 (2020), pp. 947–952.
- [38] N. Oxtoby, H. M. Wiseman, and H.-B. Sun. "Sensitivity and back action in charge qubit measurements by a strongly coupled single-electron transistor". *Physical Review B* 74.4 (2006), p. 045328.
- [39] L. Petit, M. Russ, H. Eenink, W. Lawrie, J. Clarke, L. Vandersypen, and M. Veldhorst. "Design and integration of single-qubit rotations and two-qubit gates in silicon above one Kelvin". *Nature communications materials* 3.82 (2022).
- [40] S. Philips *et al.* "Universal control of a six-qubit quantum processor in silicon". *Nature* 609 (2022), pp. 919–924.
- [41] R. Raussendorf, J. Harrington, and K. Goyal. "A fault-tolerant one-way quantum computer". *Annals of physics* 321.9 (2006), pp. 2242–2270.
- [42] D. Reilly, C. Marcus, M. Hanson, and A. Gossard. "Fast single-charge sensing with a rf quantum point contact". *Applied Physics Letters* 91.16 (2007), p. 162101.
- [43] M. Rimbach-Russ, S. Philips, X. Xue, and L. Vandersypen. "Simple framework for systematic high-fidelity gate operations". *arXiv preprint arXiv:2211.16241* (2022).
- [44] K. Saito *et al.* "Critical field limitation of the niobium superconducting RF cavity". *The 10th Workshop on RF Superconductivity, Tsukuba, Japan*. 2001, pp. 583–587.
- [45] N. Samkharadze, G. Zheng, N. Kalhor, D. Brousse, A. Sammak, U. Mendes, A. Blais, G. Scappucci, and L. Vandersypen. "Strong spin-photon coupling in silicon". *Science* 359.6380 (2018), pp. 1123–1127.
- [46] A. E. Seedhouse *et al.* "Pauli blockade in silicon quantum dots with spin-orbit control". *PRX Quantum* 2.1 (2021), p. 010303.

- [47] I. Seidler, T. Struck, R. Xue, N. Focke, S. Trelenkamp, H. Bluhm, and L. R. Schreiber. "Conveyor-mode single-electron shuttling in Si/SiGe for a scalable quantum computing architecture". *npj Quantum Information* 8.1 (2022), pp. 1–7.
- [48] J. Stehlik, Y. Liu, C. Quintana, C. Eichler, T. Hartke, and J. R. Petta. "Fast charge sensing of a cavity-coupled double quantum dot using a Josephson parametric amplifier". *Physical Review Applied* 4.1 (2015), p. 014018.
- [49] T. Struck *et al.* "Low-frequency spin qubit energy splitting noise in highly purified 28Si/SiGe". *npj Quantum Information* 6.1 (2020), pp. 1–7.
- [50] J. M. Taylor, H. A. Engel, W. Dür, A. Yacoby, C. Marcus, P. Zoller, and M. Lukin. "Fault-tolerant architecture for quantum computation using electrically controlled semiconductor spins". *Nature Physics* 1.3 (2005), pp. 177–183.
- [51] B. Terhal. "Quantum error correction for quantum memories". *Reviews of Modern Physics* 87.2 (2015), p. 307.
- [52] L. Tracy, D. R. Luhman, S. M. Carr, N. C. Bishop, G. A. Ten Eyck, T. Pluym, J. R. Wendt, M. P. Lilly, and M. S. Carroll. "Single shot spin readout using a cryogenic high-electron-mobility transistor amplifier at sub-Kelvin temperatures". *Applied Physics Letters* 108.6 (2016), p. 063101.
- [53] E. Vahapoglu *et al.* "Coherent control of electron spin qubits in silicon using a global field". *npj Quantum Information* 8.1 (2022), pp. 1–6.
- [54] E. Vahapoglu *et al.* "Single-electron spin resonance in a nanoelectronic device using a global field". *Science Advances* 7.33 (2021), eabg9158.
- [55] L. M. K. Vandersypen, H. Bluhm, J. Clarke, A. Dzurak, R. Ishihara, A. Morello, D. Reilly, L. Schreiber, and M. Veldhorst. "Interfacing spin qubits in quantum dots and donors—hot, dense, and coherent". *npj Quantum Information* 3.1 (2017), pp. 1–10.
- [56] M. Veldhorst, H. G. J. Eenink, C.-H. Yang, and A. S. Dzurak. "Silicon CMOS architecture for a spin-based quantum computer". *Nature Communications* 8.1 (2017), pp. 1–8.
- [57] M. Veldhorst *et al.* "A two-qubit logic gate in silicon". *Nature* 526.7573 (2015), pp. 410–414.
- [58] M. Veldhorst *et al.* "An addressable quantum dot qubit with fault-tolerant control-fidelity". *Nature nanotechnology* 9.12 (2014), pp. 981–985.
- [59] I. Vink, T. Nooitgedagt, R. Schouten, L. Vandersypen, and W. Wegscheider. "Cryogenic amplifier for fast real-time detection of single-electron tunneling". *Applied Physics Letters* 91.12 (2007), p. 123512.
- [60] T. F. Watson *et al.* "A programmable two-qubit quantum processor in silicon". *Nature* 555.7698 (2018), pp. 633–637.
- [61] B. P. Wuett *et al.* "Atomic fluctuations lifting the energy degeneracy in Si/SiGe quantum dots". *arXiv:2112.09606* (2021).
- [62] B. Wuett *et al.* "Reducing charge noise in quantum dots by using thin silicon quantum wells". *arXiv preprint arXiv:2209.07242* (2022).

- [63] X. Xue, M. Russ, N. Samkharadze, B. Undseth, A. Sammak, G. Scappucci, and L. M. Vandersypen. "Quantum logic with spin qubits crossing the surface code threshold". *Nature* 601.7893 (2022), pp. 343–347.
- [64] X. Xue *et al.* "Repetitive quantum nondemolition measurement and soft decoding of a silicon spin qubit". *Physical Review X* 10.2 (2020), p. 021006.
- [65] C. H. Yang *et al.* "Silicon qubit fidelities approaching incoherent noise limits via pulse engineering". *Nature Electronics* 2.4 (2019), pp. 151–158.
- [66] J. Yoneda *et al.* "A quantum-dot spin qubit with coherence limited by charge noise and fidelity higher than 99.9%". *Nature nanotechnology* 13.2 (2018), pp. 102–106.
- [67] J. Yoneda *et al.* "Coherent spin qubit transport in silicon". *Nature communications* 12.1 (2021), pp. 1–9.
- [68] J. Yoneda *et al.* "Robust micromagnet design for fast electrical manipulations of single spins in quantum dots". *Applied Physics Express* 8.8 (2015), p. 084401.
- [69] D. M. Zajac, T. Hazard, X. Mi, E. Nielsen, and J. R. Petta. "Scalable gate architecture for a one-dimensional array of semiconductor spin qubits". *Physical Review Applied* 6.5 (2016), p. 054013.
- [70] D. M. Zajac, A. J. Sigillito, M. Russ, F. Borjans, J. M. Taylor, G. Burkard, and J. R. Petta. "Resonantly driven CNOT gate for electron spins". *Science* 359.6374 (2018), pp. 439–442.
- [71] G. Zheng, N. Samkharadze, M. L. Noordam, N. Kalhor, D. Brousse, A. Sammak, G. Scappucci, and L. M. Vandersypen. "Rapid gate-based spin read-out in silicon using an on-chip resonator". *Nature nanotechnology* 14.8 (2019), pp. 742–746.
- [72] X. Zhou *et al.* "Single electrons on solid neon as a solid-state qubit platform". *Nature* 605.7908 (2022), pp. 46–50.
- [73] A. M. J. Zwerver *et al.* "Qubits made by advanced semiconductor manufacturing". *Nature Electronics* 5.3 (2022), pp. 184–190.
- [74] A. Zwerver, S. Amitonov, S. de Snoo, M. Małzik, M. Russ, A. Sammak, G. Scappucci, and L. Vandersypen. "Shuttling an electron spin through a silicon quantum dot array". *arXiv preprint arXiv:2209.00920* (2022).

SUMMARY

Physicist have been entertaining the idea of a quantum computer for quite a while. The theoretical foundations of this idea are well understood and it is clear that certain calculations can be performed significantly faster compared to the classical computer. Consequently, research in quantum computation is seen as a promising and valuable endeavor.

The fundamental building block of a quantum computer is the qubit. A qubit represents the basic unit of information, which is encoded in the states of a quantum mechanical object. Qubits can be realized through diverse implementations, for example, by utilizing the spin states of an electron (up or down), the polarization of a single photon (horizontally or vertically), the orbital states of an electron orbiting an atom (ground or excited orbital state).

While there is a wide range of qubit types that allow one to encode and manipulate information, not all of them scale easily. Ideally, qubits are operated with low error rates, while also allowing one to increase the qubit count without excessive overhead. However, determining which qubit types possess these qualities remains an active and central area of research.

In this work, the spin of a single electron is used as the unit of information of a quantum computer. We accurately control the state of single electrons by confining them in quantum dots on a silicon chip.

The objective was to scale up the qubit count from two to a handful (six) of qubits, while maintaining or improving qubit quality. Although this may appear as a modest step, the scaling process posed several technical challenges. Major challenges included (1) the fabrication of the qubits chips, (2) introducing new hardware and software for the operation of larger quantum chips and (3) acquiring expertise in operating larger qubit devices.

(1) The first significant challenge was to optimize the fabrication process of the qubit chips. It became evident that denser gate patterns¹⁸ and substrate improvements were necessary. The disorder in the old sample generations made it difficult to precisely manipulate the position of individual electrons, making it hard to place several electrons in a controlled fashion next to each other. It took several years of optimization before we could place arrays of electrons successfully.

¹⁸A denser gate pattern allows us to control voltages in smaller spaces, increasing the amount of disorder in the substrate that we can handle. An example of the metallic gate pattern is shown on the cover of this thesis. The metal lines of this pattern have a radius that is roughly a million times smaller than the trunk of a tree.

(2) The hardware and software infrastructure had to be redesigned to support larger experiments. We needed hardware that was capable of sending many electrical signals in parallel to the sample, as well as an efficient means of uploading¹⁹ instructions to the equipment that controls the qubits. Software improvements we needed as well to efficiently program, run and calibrate the experiments. These enhancements significantly improved the speed at which we could perform experiments. We also strongly reduced the readout duration of the quantum bits by improving on the readout technique.

(3) Operating larger qubit devices presented its own set of challenges. For example correcting for all the cross-talk that occurs when tuning electrons in a linear array, ensuring high fidelities qubit operations and correcting for all kinds of drift that occur throughout time.

By integrating all these improvements, we achieved the main goal of this work, i.e. being able to operate a handful of qubits. We managed to operate this array with better fidelities as obtained in earlier, smaller experiments, indicating a successful step in the scaling progress of electron spin qubits in silicon.

Stephan Philips

¹⁹This was quite slow, leading to long experiments.

SAMENVATTING

Fysici dromen al geruime tijd over het idee van een kwantumcomputer. De theoretische fundamenteen zijn wel bekend en het is duidelijk dat bepaalde berekeningen aanzienlijk sneller kunnen worden uitgevoerd dan met een klassieke computer. Zo doende wordt het onderzoek naar kwantumcomputers gezien als een veelbelovende en waardevolle onderneming.

De fundamentele bouwsteen van een kwantumcomputer is een qubit, een quantum-mechanisch object waarin informatie kan worden geëncodeerd door het in een specifieke kwantumtoestand²⁰ te brengen. Voorbeelden van zulke toestanden zijn onder andere de spin-toestanden van een elektron (omhoog of omlaag), de polarisatie van een enkel foton (horizontaal of verticaal) en de orbitale toestanden van een elektron dat om een atoom cirkelt (grondtoestand of aangeslagen toestand).

Hoewel er veel qubit-typen zijn waarin de kwantuminformatie kan worden geëncodeerd en gemanipuleerd, betekent dit niet zo zeer dat ze gemakkelijk schalen. Idealiter kan men qubits met een kleine kans op fouten manipuleren, en explodeert de complexiteit van de kwantum computer niet wanneer het aantal qubits wordt verhoogd. Momenteel zijn we in een fase waarin er actief onderzoek wordt gedaan om te kijken welke qubit-typen hieraan voldoen.

In dit werk wordt de spin van een enkel elektron gebruikt als de informatiedrager van een kwantumcomputer. De toestand van deze elektronen kunnen we nauwkeurig controleren door ze in een kwantumdot te plaatsen op een silicium chip.

Het doel was om het aantal qubits op te schalen van twee naar een handvol (zes) qubits, met behoud of verbetering van de qubit-kwaliteit. Hoewel dit misschien een bescheiden stap lijkt, bracht het schalingsproces verschillende technische uitdagingen met zich mee. Belangrijke uitdagingen waren (1) de fabricage van de qubit-chips, (2) de introductie van nieuwe hardware en software om de grotere kwantumchips te bedienen en (3) het verwerven van een expertise in het bedienen van deze kwantumchips.

(1) De eerste grote uitdaging was het optimaliseren van het fabricageproces van de qubit-chips. Het was duidelijk dat fijnere gate-patronen²¹ en verbeteringen aan het substraat noodzakelijk waren. De wanorde in de oude sample generaties maakte het moeilijk om de positie van de individuele elektronen nauwkeurig te manipuleren, waardoor het lastig

²⁰Een qubit heeft twee toestanden, vergelijkbaar met de klassieke bit. Het verschil is dat de quantum bit in beide toestanden ter gelijkertijd kan zijn.

²¹Een fijner gate-patroon laat ons toe de positie van de elektronen beter te controleren, hierdoor kunnen we omgaan met meer wanorde in het substraat. Een voorbeeld van een gate-patroon wordt getoond op de omslag van deze thesis. De metalen gates in deze illustratie hebben een straal die ongeveer een miljoen keer kleiner is dan de stam van een boom.

was om meerdere elektronen gecontroleerd naast elkaar te plaatsen. Het kostte een aantal jaren aan optimalisatie voordat we succesvol een rijtje elektronen konden plaatsen.

(2) De hardware- en software-infrastructuur moest opnieuw worden ontworpen om grotere experimenten te ondersteunen. We hadden hardware nodig die in staat was om vele elektrische signalen in parallel naar de kwantumchip te sturen, evenals een efficiënte manier om instructies van de apparatuur die de qubits bestuurt, te uploaden. Ook waren softwareverbeteringen nodig om de experimenten efficiënt te programmeren, uit te voeren en te kalibreren. Deze verbeteringen hebben de snelheid waarmee we experimenten uitvoeren aanzienlijk verbeterd. We hebben ook de uitleesduur van de toestand van de kwantum bits sterk gereduceerd door de uitleestekniek te verbeteren.

(3) Het bedienen van grotere qubit-chips bracht zijn eigen uitdagingen met zich mee. Bijvoorbeeld het corrigeren van de overspraak die optreedt bij het plaatsen van elektronen in een rijtje, het tunen van qubit-operaties met een kleine foutenmarge en het corrigeren van diverse soorten drift die in de loop der tijd op de chip optreden.

Door al deze verbeteringen te integreren, hebben we het hoofddoel van dit werk bereikt, namelijk het bedienen van een handjevol qubits. We hebben een rijtje van 6 qubits gebouwd en dit met een betere qubit kwaliteit in vergelijking met onze eerdere, kleinere experimenten. Dit is een succesvolle stap in de voortgang voor het schalen van spin qubits in silicium.

Stephan Philips

ACKNOWLEDGEMENTS

Over the years, I have been fortunate to cross paths with numerous people, both within and outside of QuTech, who helped me grow as a person and also significantly contributed to the successful completion of this thesis.

Lieven, you are a good listener who dares to trust his students and gives them the chance to pursue their dreams. Throughout the years you have always known when to give nudge that would push us in the right direction, for example enforcing Elzerman readout. I'll always be thankful for your small nudges, guidance in improving my writing, and above all, for always being there when help was needed (and also for your impressively fast email responses).

Luca, my former roommate! I have always enjoyed our scientific and non-scientific conversations, our late dinners at home after sports and your kind nature. I'm impressed by your attention to detail and how fast you can pick things up (also in the gym). I see you as one of the most honourable persons that I know which also has a very well oriented internal compass. I always valued your advice, it's has been helpful on every level.

Hanifa, you are a wonderful person and scientist with a strong and unique character. A random reference which I might or might not get is usually not far away. Your support has helped me through the last parts of my thesis. It meant a lot to me that you always had the trust that I will be able to finish the project well. You are also one of the people that helped me develop a lot as a person.

Thomas, you know how to make things work, even if the sample has other ideas about that. You were the first to introduce me to the measurement of qubits. Thank you for being patient when explaining things while also at the same time giving me time to figure out how things work. You are a friendly giant and I'll always remember our fun night out in Sheffield! **Nima**, we started the 6dot project together. You are a detail oriented person who is easy going and nice to work with. It was a pity the time was not yet mature for the project to take off, but we certainly learned a lot! Thanks for the nice personal conversations and advice on life.

Toivo, you are an inspiring person, who has a very widespread knowledge and also knows how to explain things in an approachable manner to people. I really appreciated you guiding me through my first months and also in helping with the planning of the 6dot project.

Christian, you were the second person to join the 6dot project. I enjoyed measuring

a lot of samples together. We went through some tough times as things did not really want to work, but I thank you for always having hope and to keep on pushing for results. **Sergey**, you are one of the few people that uses Linux as his default operating system, this made me instantaneously like you (together with your two halve keyboards). You have an inquisitive mind that makes fab processes somehow just work better! I always enjoyed our conversations and your easy-going-ness.

Mateusz, you are one of the most relaxed persons I know and a master at tuning. Somehow you seem to be able to transfer that relaxedness very well to samples, such that they behave well and are not too jumpy. I also wanted to thank you for helping me to see the light at the end of the tunnel while performing the experiments. I wish you all the best at Intel!

Andrea, you have been a very nice experimental set-up neighbour with an impressive apparatus knowledge. Thanks for the many nice conversations, bouldering sessions and for inviting me to your wedding in Italy, it was beautiful! **Marco**, you are always relaxed and in a good mood! Thanks for the many fun times during bouldering and during skiing!

JP, you have a vast all-round knowledge and are always to the point. **Udit**, you are a contagious bomb of laughter that is always ready to explode. Thanks for always being joyful. You are by far the fastest interpreter of charge stability diagrams I have ever met. I also wanted to thank you for the nice times in Montpellier!

7

PHC, you have a very deep knowledge of spin qubit physics and a deep love for the things you do! But what I'll always remember most will be the screams that we echoed during the countless after-trainings of our bouldering sessions. Keep strong! **Guoji**, you are one of the most talented PhDs I have met. I'm also amazed by your unparalleled skill in detecting (and smuggling) free food (e.g. the free hot dogs in Ikea!). **Nodar**, you are a very relaxed and down to earth person. I always like the creativity with which you approach problems and the ease with which you can communicate. **Jurgen**, you are an extremely hardworking person, keep up the good work, I'm sure good things will keep coming out. I was happy to hear that your qubits started swapping!

AM, you always bring a lot of energy and positivity with whatever you do, be it in shuttling electrons, editing movies, organizing events or eating some m&m's after helping each other out! I hear you have some exciting next steps prepared, I wish you the best of luck! **Tobias**, you always had a nice sense of humour! **Jelmer**, you are one of the most organized people I know. **Maxim**, it's nice to have a fellow Belgian PhD student in the lab, make us proud! **Yuta**, success with the experiments!

Max, you are one of the kindest and most modest persons that I know. You have a very deep knowledge of physics and you are always ready to explain any theoretical physics question in such a way that the other person will understand. Thank you for the many nice walks and talks.

Delphine and **Amir**, you both made it possible that the fab could be carried out efficiently for the 6dot project (and many others). Thanks for the many brainstorms and the flexibility. **Lara**, you and Sergey created the last generation of samples that worked really well! This was crucial in the success of our project :).

Xiao, you read a lot of papers and remember them all, that's impressive. At the same time you also seem to have a good feeling of which experiments need to be done when and where, leading to a long trail of impressive papers! Now you have become an expert in qubits, qubits at a distance and integration of qubits with CMOS, I'm curious to see what is next! **Kostas**, you are a person that perseveres and gets results. Looking forward to seeing you again! **Florian**, you are getting close to end, success with the last steps!

Sjaak, you are a master of precision, that focuses on understanding things in every detail. I always liked your kindness, openness to ideas and the help when needed. **Tzu-Kan**, you are a very patient and knowledgeable person. I'm curious to see both SAW and germanium together! **Steven**, I liked the enthusiasm with which you programmed the scripts for simulating certain features of charge stability diagrams.

Pablo, you have a great reservoir of positivity and energy, which you combine with a great interest in fundamental physics. I really enjoyed our trip in Australia. You are a fantastic conversational partner whether it is just to discuss physics, the intrinsics of life or what's there for breakfast. I hope that your devices do want to work with you, you will for sure do exciting experiments with them! **Daniel**, you started when I started rolling out of the lab, I always liked your sense of humor! **Liza**, you are a person that goes straight to the point, I appreciate that! Liza and **Xin**, success with the quantum simulations and the ST-qubits!

Brennan, you are like a train that has a steady course and never stops. You continuously figure things out in full depth, deliver great results and then go to the next stop. I'm curious to see how you will shape the bi-linear arrays into a reality. **Eline**, my old friend from Belgium, you took a brave step to switch into the field of quantum physics for your postdoc! You are a down to earth person that is very true to yourself. I'm happy you were one of the successors of the 6dot project and confident that you will keep pushing out great results (certainly since almost everything has improved compared to my time ;)). **Irene**, you ask yourself and others a lot of questions, this is a sign of a great scientist! **Oriol**, you are a person that pushes hard for results, this will get you far.

Marcel, I always liked our little discussions! **Chien-An**, you always produce very nice results. **GJ**, I have never met a person who can make that many associations at the same time when it comes down to song texts. **Nico**, you are impressive on all fronts. **Luka**, you are always optimistic. It is cool to see you operate a record number of quantum dots! **Will**, you are both emotionally and scientifically intelligent and have a nice Australian humor! Thanks for helping us out with the samples when we needed it direly and of course also for the many nice conversations over the years. I always enjoyed them! **Al-**

berto, I admire how you manage to do a great multitude of projects at the same time! You always manage to persevere through your positive view on life. **Brian**, you are like the wafer manager of the lab, always coming around to check with us what can be improved. I liked your many visits and talks (and our trip to the US). Microsoft is lucky to have you managing and improving their material stack! **Mohammad**, you always have a high attention to detail. Success with the writing of the thesis!

LaReine, you are one of my first friends in Delft. You are a very strong person that pushed hard to set up the initial characterization routines for Hall bars. Thanks for the many nice dinners and hosting Pablo and me in Australia!

Sander, you are an amazing programmer and always strive to do things well. I admire the patience with which you manage to help everyone in the lab and solve their problems. As we both like programming, we always have something to talk about. But as it happens you are also a person that is interested in nearly everything and always up for an interesting conversation!

A part of a PhD is of course the possibility to supervise and learn from master students. **Stefano**, you are an independent, critical thinker and a person that picks things up really quickly. Your addition of the Lindbladians is still used in people their simulation code today! **Vincent**, you are a person who likes detail. Thanks for all the efforts in exploring all possible pulse shapes! **Zhongyi**, your project was a bit more hands-on than we initially thought since we did not have many samples. Many thanks for helping us figure out some of the problems we had with the fab stack.

7

Mohamed and **Maarten**, we did a lot of homework together for the courses in our first year! This was always fun (and also the trips to Rotterdam :)).

Our experiments wouldn't be running as well as they do without the help of the technicians and administrative staff. **Raymond (S)**, **Raymond (V)**, **Marijn**, **Roy** thanks for always being ready at a moment notice and helping us with your extensive knowledge and experience. **Olaf** and **Matt**, thanks for helping us solve many fridge issues and learning us a lot about it in the process. **Ricardo**, you were the first to teach me about fridges, thanks! **Hans**, **Nicolas** and **Berend**, thanks for designing the PCB of the 6dot project, we used them a lot! Also thanks to **Siebe**, **Jelle** and **Roy** for ensuring that the lab is a pleasant place and ensuring that the fridges keep cold! **Nico**, thanks for the fast and reliable machining of copper parts! **Marja** and **Chantal**, thanks you for the quick responses, organizing the summer BBQ's, Christmas parties and Kavli days!

I also want to thank (in arbitrary order), **Thijs**, **Ramiro**, **Niels**, **Christian**, **Xiang**, **Marios**, **Peter**, **Matteo**, **Maximilian**, **Norbert**, **Nicolas**, **Sjoerd**, **Connor**, **Chris**, **MG**, **Julia**, **Lukas**, **Filip**, **Willemijn**, **James**, **Daniel**, **Damaz**, **Pieter**, **Luc**, **Floor**, **Francesco**, **Cécile**, **Sasha**, **Valentin**, **Job**, **David**, **Roy**, **Davide**, **Mario**, **Diego**, **Luigi**, **Deepika**, **Ramon** for random talks or hi's in the corridors or other places.

I also thank the funding agencies which made this work possible. Thanks to the Marie Skłodowska-Curie Actions and the ARO program for funding.

During these years, life was not only spent in QuTech, so I would also like to thank my friends outside the lab who supported me during this period. **Sona**, thank you for keeping me accountable, **Nicole**, you always know what to say, **Quentin**, you have a kind heart, **Stefan**, I love that you are always up for passionate scientific talks, **Nina**, you are so dedicated! **Deniz**, you always radiate a welcoming feeling, **Milan**, you have a lovely witty way about you. **Raj**, you were a great temporary roommate and conversation partner. **Tina**, you are very kind, **Theo**, you are always good fun! **Manon**, you embody the idea, work hard, play hard. Thanks for introducing me to the latter!

Gerd, we had a lot of amazing climbing sessions together and many nice conversations! Good luck with your next steps in Munich! **Fabio**, we had quite some good nights out! You are always very relaxed, understanding and just a nice friend.

Maarten, you were always ready to help when things were not looking up. Thanks a lot for the support, listening and the retreats from science!

Mama, Nicolas and Raymond, thank you for always standing behind me and supporting me throughout the lengthy PhD process!

CURRICULUM VITAE

Stephan Georges Jozef PHILIPS

1993/01/13	Born in Leuven, Belgium.
2011-2014	BSc in Biochemistry and Biotechnology , <i>minor in chemistry</i> . KU Leuven, Belgium <i>Thesis</i> : Nonlinear optics with fluorescent proteins.
2014-2016	MSc in Nanoscience and Nanotechnology , <i>major in nanophysics</i> . KU Leuven, Belgium <i>Thesis</i> : Directional emission of NV ⁻ centers using plasmonic nanoantenna's.
2015	Research intern . Imec, Belgium Study of thin material layers via ellipsometry and XRR.
2016-2022	PhD physics . TUDelft, Netherlands <i>Thesis</i> : Scaling a spin qubit quantum processor from two to six qubits.

PUBLICATIONS

1. T.F. Watson, **S.G.J. Philips**, E. Kawakami, D.R. Ward, P. Scarlino, M. Veldhorst, D.E. Savage, M.G. Lagally, M. Friesen, S.N. Coppersmith, M.A. Eriksson, L.M.K. Vandersypen, *A programmable two-qubit quantum processor in silicon*, **Nature** 555, 633–637 (2018).
2. W.I.L. Lawrie, H.G.J. Eenink, N.W. Hendrickx, J.M. Boter, L. Petit, S.V. Amitonov, M. Lodari, B.P. Wuertz, C. Volk, **S.G.J. Philips**, G. Droulers, N. Kalhor, F. van Riggelen, D. Brousse, A. Sammak, L.M.K. Vandersypen, G. Scappucci, M. Veldhorst, *Quantum dot arrays in silicon and germanium*, **APL**, 116(8), 080501 (2020)
3. L. Petit, H.G.J. Eenink, M. Russ, W.I.L. Lawrie, N.W. Hendrickx, **S.G.J. Philips**, J. S. Clarke, L.M.K. Vandersypen, M. Veldhorst, *Universal quantum logic in hot silicon qubits*, **Nature** 580, 355–359 (2020).
4. Y.Y. Liu*, **S.G.J. Philips***, L.A. Orona, N. Samkharadze, T. McJunkin, E.R. MacQuarrie, M.A. Eriksson, L.M.K. Vandersypen, A. Yacoby, *Radio-Frequency Reflectometry in Silicon-Based Quantum Dots*, **PRA**, 16(1), 014057 (2021).
5. **S.G.J. Philips***, M.T. Mądzik*, S.V. Amitonov, S.L. de Snoo, M. Russ, N. Kalhor, C. Volk, W.I.L. Lawrie, D. Brousse, L. Tryputen, B.P. Wuertz, A. Sammak, M. Veldhorst, G. Scappucci, L.M.K. Vandersypen, *Universal control of a six-qubit quantum processor in silicon*, **Nature** 609, 919–924 (2022).
6. M. Rimbach-Russ, **S.G.J. Philips**, X. Xue, L.M.K. Vandersypen, *Simple framework for systematic high-fidelity gate operations*. arXiv preprint arXiv:2211.16241 (2022).
7. B.P. Wuertz, M.P. Losert, S. Koelling, L.E.A. Stehouwer, A.M.J. Zwerver, **S.G.J. Philips**, M.T. Mądzik, X. Xue, G. Zheng, M. Lodari, S.V. Amitonov, N. Samkharadze, A. Sammak, L.M.K. Vandersypen, R. Rahman, S.N. Coppersmith, O. Moutanabbir, M. Friesen, G. Scappucci, *Atomic fluctuations lifting the energy degeneracy in Si/SiGe quantum dots*, **Nature Communications**, 13(1), 1–8. (2022).
8. B. Undseth, O. Pietx-Casas, E. Raymenants, M. Mehmandoost, M.T. Mądzik, **S.G.J. Philips**, S.L. de Snoo, D.J. Michalak, S.V. Amitonov, L. Tryputen, B.P. Wuertz, V. Fezzi, D.D. Esposti, A. Sammak, G. Scappucci, L.M.K. Vandersypen, *Hotter is easier: unexpected temperature dependence of spin qubit frequencies*, arXiv preprint arXiv:2304.12984v2 (2023).

*These authors contributed equally.